



Tesis de doctorado en Física

Metallic nanostructures prepared by a solid state dewetting process with potential applications in nanophotonics

Juan Agustín Badán Núñez

Orientador: Enrique A. Dalchiele

Co-orientador: Daniel Ariosa

2021

Abstract

Preparing metallic nanostructures with applications in photonics and/or optoelectronics is the main objective of this work. For this, a reliable manufacturing technique has been developed. It is based on Solid State Dewetting (SSD) process which consists in a restructuration of thin films or layers into a set of separated objects. The material (a metal) remains in the solid state during the process which is activated by a thermal treatment (TT) and occurs at a temperature much lower than that of melting. The thin films and layers were deposited by thermal vacuum evaporation. The challenge is to be able to control the manufacturing parameters so as to obtain nanostructures with the desired optical properties. An exhaustive characterization of morphology, structure and optical properties was performed on all prepared samples. This allowed us to make the link between manufacturing parameters and the observed structural and optical properties.

After adapting and optimizing the evaporation and annealing configurations, 2D silver NP arrays were prepared on glass substrates by SSD process. To study the evolution of NP synthesis, the interrupted annealing method was used. It was observed that the SSD dynamic was not compatible with the usual capillarity approaches and, to explain this, the polycrystalline character of the films has been taken into account. The mean lateral size of NPs varies with Ostwald ripening and increases with time until recrystallization occurs to obtain an equilibrium shape for NP. Surface plasmon resonance (SPR) has been recognized in transmittance spectra. SPR wavelengths show clear dependencies on the ratio between NP mutual distances and NP sizes. Therefore, by controlling the TT parameters and the initial thickness of the thin film, we were able to obtain 2D arrays with the desired properties.

The ZnO (NW) nanowires were decorated with Ag NPs using the SSD technique. Unlike 2D arrays obtained on plane substrates, they constitute 3D hybrid structures (metal-semiconductor). In this case, the initial Ag layers coated the NWs. The photoluminescence (PL) spectra of ZnO NWs shows bands in different regions of the spectrum. One of these bands is the so-called near band edge (NBE) emission, generally attributed to excitons. Other bands, in the visible region, correspond to defects. The NBE emission relative to defect ones is slightly enhanced when naked NWs are subjected to TT, but the NBE photoluminescence efficiency of ZnO is generally low. The most noticeable result that we observe is a strong increase in NBE emissions relative to the defects ones for ZnO NWs / Ag and ZnO NWs / Ag after TT. One reason for this is that Ag NPs harvest electron and energy from defects. The electrons excited by the SPR can be transferred to the ZnO conduction band and become available for the NBE transition.

Resumen

El principal objetivo de este trabajo de tesis es preparar nanoestructuras con aplicaciones en fotónica y optoelectrónica, para lo cual se ha desarrollado un método confiable basado en el proceso conocido como "des-mojado" o Solid State Dewetting (SSD) en inglés. Este proceso consiste en la re-estructuración de películas delgadas o recubrimientos en un conjunto de objetos separados. Es activado por un tratamiento térmico (TT), ocurre a una temperatura más baja que la temperatura de fusión y el material (metal) permanece en estado sólido durante el mismo. Las películas delgadas y recubrimientos fueron depositados por evaporación térmica en vacío. El desafío es poder controlar los parámetros de fabricación para obtener nanoestructuras con las propiedades ópticas deseadas. Por esta razón, todas las muestras fueron caracterizadas morfológicamente, estructuralmente y ópticamente de forma exhaustiva y los resultados fueron correlacionados con los parámetros de fabricación.

Después de adaptar y optimizar las configuraciones de la evaporación y del tratamiento térmico, se prepararon arreglos 2D de nanopartículas de plata sobre substratos de vidrio. Para estudiar la evolución de la síntesis de las nanopartículas, se utilizó el método del tratamiento térmico interrumpido. Se observó que la dinámica del SSD no es compatible con los modelos históricos basados en la capilaridad y para explicarla se debe tener en cuenta la naturaleza poli-cristalina de los films. El tamaño medio lateral de las nanopartículas varía de acuerdo con la maduración de Ostwald y se incrementa con el tiempo hasta que ocurre una re-cristalización para obtener una forma de equilibrio. En los espectros de transmitancia óptica de las muestras se reconoce la resonancia de plasmón superficial. Las longitudes de onda de la resonancia del plasmón superficial muestran dependencias claras con la razón entre las distancias medias entre las nanopartículas y los tamaños medios. Por lo tanto, controlando los parámetros del TT y el espesor inicial de la película delgada, se pueden obtener arreglos 2D con las propiedades ópticas deseadas.

También, se decoraron nanohilos de ZnO (NH de ZnO) con nanopartículas de Ag usando la técnica SSD. Constituyen estructuras híbridas 3D, distintas a los arreglos 2D obtenidos sobre un substrato. La fotoluminiscencia (PL) de los NH de ZnO muestran bandas en diferentes zonas del espectro. Una de esas bandas es conocida como la emisión de borde de banda (NBE por sus siglas en inglés), atribuida al excitón. Otras bandas, en la región del visible, corresponden a defectos puntuales. La emisión de la banda NBE relativa a las de los defectos, aumenta cuando los nanohilos de ZnO sin recubrimiento son sometidos a un tratamiento térmico. Pero la eficiencia de la fotoluminiscencia de la NBE sigue siendo baja para el ZnO. Un resultado es que se observa un fuerte incremento de la emisión NBE relativa a las de los defectos puntuales, para los nanohilos de ZnO recubiertos con plata y para los ZnO decorados con nanopartículas de plata. Una razón es que estas últimas colectan electrones y energía de los defectos. Los electrones excitados por la resonancia superficial del plasmón pueden ser transferidos a la banda de conducción del ZnO y pasan a estar disponibles para la transición NBE.

Agradecimientos

A mi familia, por su apoyo constante a lo largo de estos años.

A los orientadores Enrique A. Dalchiele y Daniel Ariosa por su paciencia y dedicación para que este trabajo llegase a buen puerto. Sentí que pude trabajar en forma independiente, pero también recibiendo sus valiosos aportes y sugerencias.

A la Universidad de la República y al Instituto de Física de Facultad de Ingeniería (IFFI).

Al PEDECIBA-Física.

A la CAP (Comisión Académica de Posgrado), CSIC (Comisión Sectorial de Investigación Científica) y ANII (Agencia Nacional de Investigación e Innovación).

A los integrantes del Grupo de Física de Estado Sólido, Facultad de Ingeniería, Instituto de Física.

A Antonio Saez y Joaquín Fernández del Taller de Mecánica Fina, Jorge Fernández del Taller de Electrónica y Liber Dovat del Soporte Informático del IFFI.

A Judith Castillo, de la Universidad Católica de Chile.

A Ana Laura Reyes de la Unidad de Microscopía de la Facultad de Ciencias, Universidad de la República y a la Dra Rocío Romero de la Universidad de la Universidad de Málaga, España por sus colaboraciones con las imágenes de SEM y de FE-SEM, así como a la Dra. Elena Navarrete (Universidad de Málaga) por las medidas de XPS.

Symbols and abbreviations

A_e: Surface area of the evaporation source

A_s: Substrate area

AFM: Atomic Force Microscopy

Ag: silver

Al: aluminium

B: Intrinsic width corrected from instrumental contribution

B_M: Measured width of the sample diffraction peak

B_S: Measured width of the standard sample diffraction peak

C_{abs}: Absorption cross section

C_{ext}: Extinction cross section

C_{scatt}: Scattering cross section

d: Film thickness

d_0: Biggest thickness of the film

d*: Thickness of a sample whose transmittance is measured

d_{CC}: Average distance between centres of nearest neighbours NPs

d_{planes}: Distance between crystallographic planes

D: Lateral size, in plane diameter of the NP

D_C: Crystallite size obtained by Scherrer equation

D_g: In plane grain diameter

D_S: Diffusion coefficient

E: Young modulus

E_A: Characteristic activation energy

E_B: Electron binding energy

E_C: Energy of the bottom of conduction band

E_d: the diffusion barrier for the species transporting mass

E_{deff}: Energy of the defect level

E_{eff}: Effective activation barrier

E_F: Fermi energy 3

E_{form}: formation energy barrier to extract the diffusing species from a cluster, and attach them to another

E_g: Band-gap energy 6

E_k: Kinetic energy 3

E_{SPR}: Surface plasmon resonance energy

$E_{T1}\ and\ E_{T2}$: Electron transfer processes

E_V: Energy of the maximum of the valence band

E_{vac}: Energy of the vacuum level

EDX: Energy Dispersion X Ray Analysis

$\overrightarrow{E_{dip,i}}$: Sum of the electric fields on particle i generated by others dipoles

$\overrightarrow{E_{inc,i}}$: Electric field of the incident wave on the i particle

$\overrightarrow{E_{loc,i}}$: Local electric field on the i particle

f_0: Intrinsic frequency of the quartz crystal

FEG: Field Emission Gun

FE-SEM: Field Emission Scanning Electron Microscopy

FFT: Fast Fourier Transform

FTO: Fluor tin oxide

FWHM: Full Width at Half Maximum

h: Planck constant

h_H: Supported hemispheroid height

H: Entalpy

ICL: Initial coating Layer

I_{band_i}: integrated intensity of the PL emission band i

$I_{band_norm_i}$: normalized integrated intensity of the PL emission band i

I_{NBE}: Integrated PL intensity of the NBE band

I_{def}: Integrated PL intensity of defects

j_S: Net flux away from a curved surface

k: Wave number2

$\vec{k}$: Wave number vector

$\overrightarrow{k_d}$: X ray diffracted wave vector

$\overrightarrow{k_i}$: X ray incident wave vector

$\overline{M_e}$: Total evaporated mass

$\overline{M_s}$: Total mass deposited on the substrate

N: Number of measurement

N_A: Avogadro number

NBE: Near Band Edge

NP: Nanoparticle

NW: Nanowire

OPC: Out of plane crystallite

P_e: Equilibrium pressure at a given temperature

P_h: Hydrostatic pressure

$\vec{p}$: Dipolar moment

PL: Photoluminescence

Q_{abs}: Absorption cross section relative to geometrical section

Q_{ext}: Extinction cross section relative to geometrical section

Q_{scatt}: Scattering cross section relative to geometrical section

Q_S: Activation energy for surface diffussion

r: NP radius

r_{ev}: distance between the evaporation source and a point of the substrate 3

r_g: In plane grain radius

r_{min}: Minimum radius associated to the formation of a nanoparticle

R: Ideal gas constant

R_{av}: Average island radius

R_C: Critic radius of the grain

R_H: Supported hemispheroid in plane radius

$R_{NBE-def}$: Relation between I_{NBE} and I_{def}

R_{before}: $R_{NBE-def}$ before the TT

R_{after}: $R_{NBE-def}$ after the TT

$\overrightarrow{r_{ij}}$: Vector from i-particle position to j-particle position

SEM: Scanning Electron Microscopy

SSD: Solid State Dewetting

SP: Surface Plasmon

SPR: Surface Plasmon Resonance

S_C: Spreading Coefficient

T_{exp}: Experimental measured optical transmittance

T: Absolute temperature

$T_m(0)$: Melting temperature of the bulk material

$T_m(r)$: Melting temperature of a particle with radius r

TEM: Transmission Electron Microscopy

TT: Thermal Treatment

UV-Vis: Ultra-violet Visible

V_C: Condensed phase volume

V_V: Vapour volume

XPS: X ray Photoelectron Spectroscopy

ZnO: zinc oxide

α: Polarizability

α_{abs}: Absorption coefficient

α_{array}: Polarizability of the array

α_{exp}: Experimental absorption coefficient=$\alpha_{abs}d^*$

α_e: Evaporation coefficient

α_S: Polarizability of an isolated small sphere particle (quasi-static limit)

α_{sphere}: Polarizability of an isolated large sphere (out of the quasi-static limit)

α_{Ag}^{expan}, $\alpha_{SiO_2}^{expan}$: Expansion coefficient of silver and SiO_2

β: kinetic coefficient

γ_f: Surface energy per area of the material of the particle

γ_{gb}: Grain boundary energy

γ_i: Surface energy per area of the interface between the particle and the substrate

γ_s: Surface energy per area of the substrate

γ_{HW}: Half width of the resonance (one half of the Drude width)

γ_{liquid}: Surface free energy of the liquid

γ_{solid}: Surface free energy of the solid

γ_{CS}: Surface energy per area unit of interface crystal-substrate

γ_{CV}: Surface energy per area unit of interface crystal-substrate

γ_{PS}: Surface energy per area unit of interface particle-substrate

γ_{PV}: Surface energy per area unit of interface particle-vapor

γ_{SV}: Surface energy per area unit of interface substrate-vapor

Γ_e: Uniform mass evaporation rate

δ: Energy barrier associated to a step in the surface

ΔF: Free energy change

ΔH_e: Molar heat

$\Delta\sigma$: Change in stress

ε: Dielectric function

ε_0: Vacuum dielectric function

ε_m: Surrounding media dielectric function

ε_{sub}: Substrate dielectric function

ε_{error}: Standard error

ε_z: Out of plane strain

ε_x: In plane strain

ε_{subs}: Dielectric function of the substrate

ϵ: Mechanical strain

θ_{ij}: Angle between $\overrightarrow{r_{ij}}$ and polarization direction

λ: Light wavelength

λ_0 : Free space light wavelength

λ_{array}: SPR wavelength of the array of particles

λ_{isol}: Surface plasmon resonance wavelength of an isolated NP

λ_{sphere}: SPR wavelength of the isolated sphere

μ: Chemical potential

ν: Photon frequency

ρ: density of the deposit

ρ_{quartz}: Density of the quartz crystal

ρ_{liquid}: Density of the liquid phase

ρ_{solid}: Density of the solid phase

σ: Mechanical stress

σ_{dev}: Standard deviation

σ_x: In plane stress

Φ: Work function

Φ_e: Rate of evaporation

ϕ_{eff}: Effective work function

ω_p: Plasma frequency

ω_{SPR}: Surface plasmon frequency of the isolated particle

Ω: Atomic volume

Contents

Abstract....1

Resumen....2

Agradecimientos....3

Symbols and abbreviations....4

Contents....10

Chapter 1: Introduction....13

1.1 References....16

Chapter 2: Theoretical background....18

2.1 Plasmonics theory....18

2.1.1 Quasi-static approximation (sub-wavelength metal particles)....18

2.1.2 Mie theory....20

2.1.3 Plasmonics properties of metal hemisphere or hemispheroid placed on a dielectric substrate....23

2.1.4 Interaction among the particles....25

2.2 Solid State Dewetting Process....28

2.2.1 Mechanism of solid state dewetting....30

2.2.1.1 Induction process....30

2.2.1.2 Holes formation....32

2.2.1.3 Holes propagation....33

2.2.1.4 Sintering....37

2.3 Equilibrium Shapes....39

2.4 References....44

Chapter 3: Experimental methods....46

3.1 Samples preparation....46

3.1.1 Vacuum thermal evaporation....46

3.1.1.1 Deposition geometry....48

3.1.1.2 Evaporation sources and materials.....51

3.1.1.3 Monitoring rate and thickness: quartz crystal monitor.....52

3.1.2 ZnO NWs.....54

3.2 Characterizations..... 54

3.2.1 X-ray diffraction.....54

3.2.1.1 Strain and stress.....57

3.2.2 Chemical surface analysis: X ray photoelectron spectroscopy (XPS).....59

3.2.3 Scanning Electron Microscopy (SEM).....61

3.2.4 Energy Dispersion X ray Analysis (EDX).....63

3.2.5 Optical characterizations.....63

3.2.5.1 Optical UV-Vis transmittance.....63

3.2.5.2 Photoluminescence.....66

3.3 References.....69

Chapter 4: Preliminary studies.....71

4.1 Oblique angle deposition.....71

4.1.1 Oblique evaporation on Al thin films substrates.....71

4.1.2 ZnO nanorods decorated with Al nanoparticles.....78

4.2 Conclusions.....80

4.3 References.....80

Chapter 5: Silver nanoparticles grown by Solid State Dewetting onto glass substrates.....81

5.1 Morphological studies.....82

5.1.1 Effects of the initial thin film thickness and of the working temperature.....82

5.1.2 Effects of the final ramp temperature and of the annealing plateau time.....91

5.2 Structural studies: X ray diffraction analysis.....110

5.2.1 Effects of the initial thin film thickness and of the working temperature.....110

5.2.2 Effects of the final ramp temperature and of annealing plateau time.....115

5.3 Optical properties (Transmittance).....119

5.3.1 Effects of the initial thin film thickness and of the working temperature.....119

5.3.2 Effects of the final ramp temperature and of annealing plateau time.....125

5.4 Conclusions.....133

5.5 References.....135

Chapter 6: ZnO nanowires decorated with silver nanoparticles through the solid state dewetting process.....139

6.1 Morphological Studies.....141

6.1.1 Silver NPs size distribution.....150

6.2 Structural studies.....151

6.2.1 X-rays diffraction analysis.....154

6.3 Optical properties.....158

6.3.1 UV-Vis optical transmittance.....158

6.3.2 Room temperature photoluminescence studies.....160

6.3.2.1 Evolution of the different emission bands.....160

6.3.2.2 ZnO NBE PL emission band energy analysis and its relation with the Ag SPR coupling.....184

6.5 Conclusions.....187

6.6 References.....189

Chapter 7: General conclusions.....192

Chapter 8: Perspectives.....195

8.1 References.....195

Chapter 9: Publications.....197

1 Introduction

In the field of optical technology, nanophotonic systems have great potential and they are promising replacement for microscale devices [1] [2] [3]. Among the applications, we found different areas: photovoltaics [4], optical data processing [5], super resolution microscopy in biology [6] and treatment of oncological diseases in medicine [7]. Nanophotonic systems are usually composed of resonant nanoparticles (NPs), which allow to control the electric and magnetic components of optical waves.

Scattering light generated by metallic NPs due to localized surface plasmon resonance (LSPR) has been recognized as a promising approach for effective light trapping in thin film solar cells [8]. Stuart et al. demonstrated improved photocurrent generation of a silicon-on-insulator photodetector structure with dense NP arrays placed on top of the device [9]. But the applications of plasmonic scattering to photovoltaics appeared only after 2005, with several experimental photocurrent enhancements in silicon solar cells [10] [11], supported by theoretical works [12] [13].

The interaction of light with the metallic NPs at the plasmonic resonance can result in near field enhancement, far field scattering and absorption of light. In the case of solar cells, the efficient scattering of light over a broad wavelength range of the solar spectrum, produces a larger path of the light inside the photovoltaic material. Therefore, it increases the probability to generate photo carriers by the absorption of scattered photons. On the other hand, all scattering elements, in particular metallic NPs, generate parasitic absorption. Hence, a part of the absorbed incident sunlight does not contribute to the photocurrent [14] [15]. As the optical properties of the NPs are strongly dependent on their geometry and on the refractive index of the surrounding medium, the challenge is to optimize the NPs for (i) maximized scattering and minimized absorption (ii) broad spectral response (iii) broad angular distribution of scattered light and (iv) weak dependence on polarization and angle of incidence.

In the last decade, several methods to produce photonic nanostructures have been developed, leading to the creation of resonant particles with an accurate control over size and position. Among them, ion beam milling, multistage e-beam and nanolithography coupled with etching are some methods which allow preparing photonic nanostructures with precise control [16] [17] [18], for example of the nanoparticles size and of their position in an array. However, their low throughput and high cost make them not suitable for large scale production.

To be directly applicable, the NP fabrication method needs to be reliable, low cost, and scalable up to square meter sizes. One of the promising methods which overcome these obstacles is the spontaneous Solid State Dewetting (SSD). SSD is a spontaneous phenomenon where a thin film on a surface re-structure into an ensemble of separated objects [19] and a

schematic view is shown in **Figure 1.1**. Controlling it would open the possibility to obtain objects with a pre defined statistical size and spatial distribution.

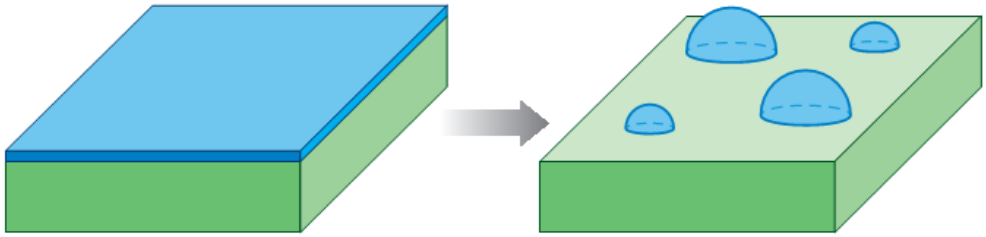


Figure 1.1: Schematic diagram of the solid state dewetting process [19]

Usually, the SSD process is induced by thermal annealing or laser irradiation. Furthermore, it is also outstanding that the dewetting of a thin film can result in the formation of spherical or faceted particles that are impossible to produce via all top down lithography based techniques [19].

The hallmarks of the dewetting process are cost effectiveness and simplicity of creation of almost disordered nanostructures over a large surface area. Moreover, to fabricate disordered nanostructures, the dewetting process can be performed in a single step.

In fact, due to its simplicity, the SSD process has been used extensively to produce subwavelength and nano-scale patterns that are useful for various photonic applications, including colour generation, sensing, photovoltaics and nonlinear light frequency conversion (see **Figure 1.2**) [20].

The first step in the SSD process is the formation of a thin film onto the substrate of interest. A way to prepare it, is the physical vapor deposition (PVD). PVD implicates the production of a vapor flux and its condensation in the form of a thin film on a substrate in a vacuum chamber. Many techniques including thermal and electron beam evaporation, sputtering and laser ablation are considered as PVD and they are characterized by the generation of the vapor flux. This flux can be generated by one or more target or evaporation sources. Gases can also be introduced into the vacuum chamber to change chemically the vapor species or the thin film. A great variety of thin films, from decorative optical coatings to high temperature superconducting films, could be prepared by this technique. Furthermore, inorganic materials (metal, alloys, compounds and mixtures) as well as some organic materials can be deposited. The thickness values of the layers can go from a few angstroms to several millimeters, and very high deposition rates can be reached. A careful monitor is necessary to achieve good structural control at the micrometer and or nanometer length scales.

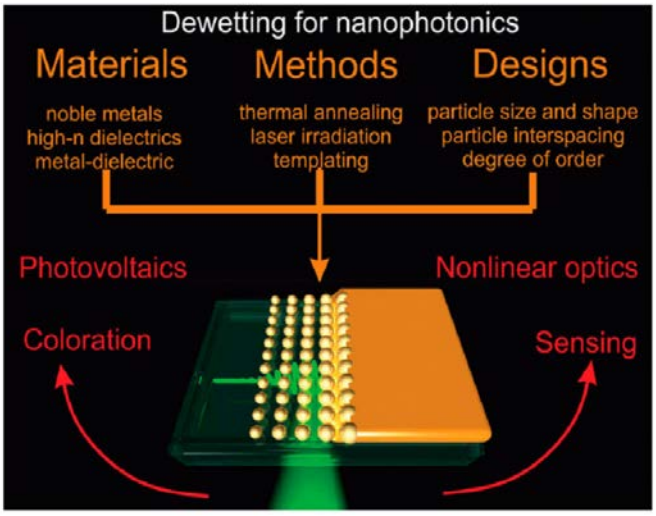


Figure 1.2: Schematic panel of enhanced optical response from nanostructures obtained by dewetting process where the basic optimizing parameters and applications are depicted [20].

The objectives of this Thesis are:

i) Prepare metallic nanostructures with applications in photonics, some of them constituting hybrid nanostructures (metallic-semiconductor), by the Solid State Dewetting process.

ii) Study and control of the dynamic of the SSD, varying the initial thickness of the metallic layer and the thermal treatment parameters.

iii) Setup and optimization of the vacuum thermal evaporation to control the metal deposit

iv) Study the prepared samples by morphological, structural and optical characterizations. Correlate the results with thermal treatment parameters and the initial metal layer thickness.

This doctoral Thesis is organized in the following way:

- Chapter 1: Introduction
- Chapter 2: Theoretical background
- Chapter 3: Experimental methods
- Chapter 4: Preliminary studies
- Chapter 5: Silver nanoparticles grown by Solid State Dewetting onto glass substrates.
- Chapter 6: ZnO nanowires decorated with silver nanoparticles through the solid state dewetting process.

- Chapter 7: General conclusions

- Chapter 8: Perspectives

1.1. References

[1] Atwater, H. A. and Polman, A. Plasmonics for improved photovoltaic devices. *Nature Materials* **2010**, 9, 205–213.

[2] Schuller, J. A. , Barnard, E. S. , Cai, W. , Jun, Y. C. , White, J. S. , and Brongersma, M. L. Plasmonics for extreme light concentration and manipulation. *Nature Materials* **2010**, 9, 193–204.

[3] Brongersma, M. L. , Halas, N. J. , and Nordlander, P. Plasmon-induced hot carrier science and technology. *Nature Nanotechnology* **2015**, 10, 25–34.

[4] Ferry, V. E. , Munday, J. N. , and Atwater, H. A. Design Considerations for Plasmonic Photovoltaics. *Advanced Materials* **2010**, 22, 4794–4808.

[5] Guo, R. , Decker, M. , Setzpfandt, F. , Staude, I. , Neshev, D. N. , and Kivshar, Y. S. Plasmonic Fano Nanoantennas for On-Chip Separation of Wavelength-Encoded Optical Signals. *Nano Letters* **2015**, 15, 3324–3328.

[6] Wertz, E. , Isaacoff, B. P. , Flynn, J. D. , and Biteen, J. S. Single-Molecule Super-Resolution Microscopy Reveals How Light Couples to a Plasmonic Nanoantenna on the Nanometer Scale. *Nano Letters* **2015**, 15, 2662–2670.

[7] O'Neal, D. P. , Hirsch, L. R. , Halas, N. J. , Payne, J. D. , and West, J. L. Photo-thermal tumor ablation in mice using near infrared-absorbing nanoparticles. *Cancer Letters* **2004**, 209, 171–176.

[8] Jang, Y. H. , Jang, Y. J. , Kim, S. , Quan, L. N. , Chung, K. , and Kim, D. H. Plasmonic Solar Cells: From Rational Design to Mechanism Overview. *Chemical Reviews* **2016**, 116, 14982–15034.

[9] Stuart, H. R. and Hall, D. G. Island size effects in nanoparticle-enhanced photodetectors. *Applied Physics Letters* **1998**, 73, 3815–3817.

[10] Pillai, S. , Catchpole, K. R. , Trupke, T. , and Green, M. A. Surface plasmon enhanced silicon solar cells. *Journal of Applied Physics* **2007**, 101, 093105.

[11] Catchpole, K. R. and Polman, A. Plasmonic solar cells. *Optics Express* **2008**, 16, 21793.

[12] Beck, F. J. , Mokkapati, S. , and Catchpole, K. R. Light trapping with plasmonic particles: beyond the dipole model. *Optic Express* **2011**, 19, 25230.

[13] Temple, T. L. and Bagnall, D. M. Broadband scattering of the solar spectrum by spherical metal nanoparticles: Broadband scattering of the solar spectrum. *Progress in Photovoltaics: Research and Applications* **2012**, n/a-n/a.

[14] Schuster, C. S. , Morawiec, S. , Mendes, M. J. , Patrini, M. , Martins, E. R. , Lewis, L. , Crupi, I. , and Krauss, T. F. Plasmonic and diffractive nanostructures for light trapping—an experimental comparison. *Optica* **2015**, 2, 194.

[15] Morawiec, S. , Holovský, J. , Mendes, M. J. , Müller, M. , Ganzerová, K. , Vetushka, A. , Ledinský, M. , Priolo, F. , Fejfar, A. , and Crupi, I. Experimental quantification of useful and parasitic absorption of light in plasmon-enhanced thin silicon films for solar cells application. *Scientific Reports* **2016**, 6, 22481.

[16] Coenen, T. , Groep, J. van de , and Polman, A. Resonant Modes of Single Silicon Nanocavities Excited by Electron Irradiation. *ACS Nano* **2013**, 7, 1689–1698.

[17] Bottein, T. , Wood, T. , David, T. , Claude, J. B. , Favre, L. , Berbézier, I. , Ronda, A. , Abbarchi, M. , and Grosso, D. "Black" Titania Coatings Composed of Sol-Gel Imprinted Mie Resonators Arrays. *Advanced Functional Materials* **2017**, 27, 1604924.

[18] Huang, J.-S. , Callegari, V. , Geisler, P. , Cristoph, B. , Johannes, K. , Prangsma, J. C. , Wu, X. , Feichtner, T. , Ziegler, J. , Weinmann, P. , Kamp, M. , Forchel, A. , Biagioni, P. , Sennhauser, U. , and Hecht, B. Atomically flt single-crystalline gold nanostructures for plasmonic nanocircuitry. *Nature Communications* **2010**, 1, 1–8.

[19] Thompson, C. V. Solid-State Dewetting of Thin Films. *Annual Review of Materials Research* **2012**, 42, 399–434.

[20] Ye, J. , Zuev, D. , and Makarov, S. Dewetting mechanisms and their exploitation for the large-scale fabrication of advanced nanophotonic systems. *International Materials Reviews* **2019**, 64, 439–477.

2 Theoretical background

2.1 Plasmonic theory

2.1.1 Quasistatic aproximation (subwavelength metal particles)

As discussed in detail by Stefan A. Maier in [1], localized surface plasmons are non-propagating excitations of the conduction electrons. **Figure 2.1** shows a schematic diagram of metallic nanoparticles (NPs) coupled to an electromagnetic field. The curved surface generates an effective restoring force which acts on the driven electrons. Therefore, a resonance can occur, and it generates field amplifications, both inside and in the near field zone outside the particle. This resonance is called the localized surface plasmon resonance SPR.

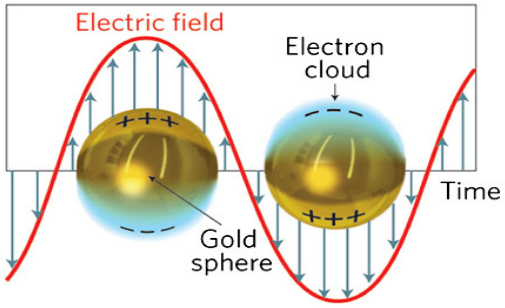


Figure 2.1: Oscillation of a metal particle electron cloud in response to the electric field [2].

Let's recall the main results of [2] within the simplest geometry: an homogeneous isotropic sphere of radius a localized at the origin in an uniform static electric field $\vec{E} = E_0\hat{z}$

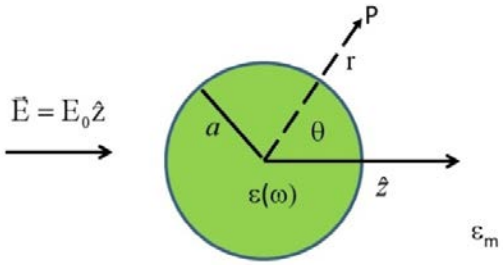


Figure 2.2: Schematic diagram of a spherical particle with radius a and dielectric function $\varepsilon(\omega)$. It is embedded in an isotropic and non absorbing medium with dielectric constant ε_m and it is submitted to a $\vec{E} = E_0\hat{z}$ electric field. θ is the angle between the position vector $\vec{r}$ at a point P and the z-axis.

The sphere is embedded in an isotropic and non-absorbing medium with dielectric constant ε_m. Far from the sphere, the field lines are parallel to the z-axis. The dielectric response of the sphere is described by a dielectric function $\varepsilon(\omega)$.

Within an electrostatic approach, the solution of the Laplace equation for the potential ($\nabla^2\Phi = 0$), allow us to calculate the electric field $\vec{E} = -\nabla\Phi$. The boundary conditions to be imposed are as follows:

i) the potential must be finite at the origin,

ii) the tangential components of the electric field and the normal component of the displacement fields must be the same on both sides of the sphere's surface ($r = a$)

iii) far from the sphere ($r \to \infty$) the electric field limit is the applied field $\vec{E} = E_0\hat{z}$.

Using these conditions, we obtain [1]:

$$\Phi_{in} = -\frac{3\varepsilon_m}{\varepsilon+2\varepsilon_m} E_0 r\cos(\theta) \quad \textbf{2.1}$$

$$\Phi_{out} = -E_0 r\cos(\theta) + \frac{\varepsilon-\varepsilon_m}{\varepsilon+2\varepsilon_m} E_0 a^3 \frac{\cos(\theta)}{r^2} \quad \textbf{2.2}$$

Φ_{out} can be write introducing the dipolar moment $\vec{p}$ as [1]:

$$\Phi_{out} = -E_0 r\cos(\theta) + \frac{\vec{p}.\vec{r}}{4\pi\varepsilon_0\varepsilon_m r^3} \quad \textbf{2.3}$$

$$\vec{p} = 4\pi a^3 \frac{\varepsilon-\varepsilon_m}{\varepsilon+2\varepsilon_m} \varepsilon_0\varepsilon_m \overrightarrow{E_0} \quad \textbf{2.4}$$

The polarizability α is defined by $\vec{p} = \varepsilon_0\varepsilon_m\alpha\overrightarrow{E_0}$. If α is expressed in terms of dielectric functions and radius, we obtain

$$\alpha = 4\pi a^3 \frac{\varepsilon-\varepsilon_m}{\varepsilon+2\varepsilon_m} \quad \textbf{2.5}$$

This is the polarizability of a small sphere whose diameter is smaller than the wavelength. In this, the electric field has not substantial variation across the particle, thus the electrostatic approximation is valid. The polarizability undergoes a resonant enhancement when $|\varepsilon + 2\varepsilon_m|$ is minimal. If $Im[\varepsilon]$ is small or slowly varying around the resonance, the condition simplifies to:

$$Re[\varepsilon(\omega)] = -2\varepsilon_m \quad \textbf{2.6}$$

Equation 2.6 is called the Fröhlich condition and the associated mode the dipole surface plasmon of the metal nanoparticle. For a metallic sphere in air, the Fröhlich criterion is met at the frequency $\omega_0 = \frac{\omega_p}{\sqrt{3}}$, where ω_p is the plasma frequency of the metal. Also, the SPR frequency depends on the dielectric environment and has a red shift when ε_m increases. The corresponding electric fields read as:

$$\overrightarrow{E_{in}} = \frac{3\varepsilon_m}{\varepsilon+2\varepsilon_m}\overrightarrow{E_0} \quad \textbf{2.7}$$

$$\overrightarrow{E_{out}} = \overrightarrow{E_0} + \frac{3\vec{n}(\vec{n}.\vec{p})-\vec{p}}{4\pi\varepsilon_0\varepsilon_m r^3} \quad \textbf{2.8}$$

where $\vec{n}$ is the unit vector in the direction of the point P (see **Figure 2.2)**.

A small sphere ($a \ll \lambda$) can be considered as an ideal dipole in the quasi-static regime. Spatial retardations inside the particle volume are neglected. Under plane wave illumination with $\overrightarrow{E(\vec{r},t)} = \overrightarrow{E_0}e^{-i\omega t}$, an oscillating dipole $p(t) = \varepsilon_0\varepsilon_m\alpha\overrightarrow{E_0}e^{-i\omega t}$ is generated. The resulting scattering of the plane wave by the sphere can be considered as the radiation by a point dipole. The resonant polarization α (**2.5**) enhances both scattering and absorption of light by the nanoparticle. The corresponding cross sections for scattering and absorption C_{sca} and C_{abs} are [2]:

$$C_{sca} = \frac{k^4}{6\pi}|\alpha|^2 = \frac{8\pi k^4 a^6}{3}\left|\frac{\varepsilon+\varepsilon_m}{\varepsilon+2\varepsilon_m}\right|^2 \quad \textbf{2.9}$$

$$C_{abs} = kIm(\alpha) = 4\pi k a^3 Im\left[\frac{\varepsilon-\varepsilon_m}{\varepsilon+2\varepsilon_m}\right] \quad \textbf{2.10}$$

2.1.2 Mie Theory

In practice, the above calculations provide a qualitatively good approximation for small spherical and ellipsoidal particles. The quasi- static approach fails in the case of appreciable variations of the driving field over the particle volume. This approach is known as Mie theory. In this theory, internal and scattered fields are depicted by a set of normal modes described by vector harmonics.

For larger particles, Mie theory yields for the polarizability of a sphere of volume V [1,3]:

$$\alpha_{sphere} = \frac{1-\frac{1}{10}(\varepsilon-\varepsilon_m)x^2+O(x^4)}{\left(\frac{1}{3}+\frac{\varepsilon_m}{\varepsilon-\varepsilon_m}\right)-\frac{1}{30}(\varepsilon+10\varepsilon_m)x^2-i\frac{4\pi^2\varepsilon_m^{3/2}}{3}\frac{V}{\lambda_0^3}+O(x^4)}V \quad \textbf{2.11}$$

where $x = \frac{\pi a}{\lambda_0}$ is the size parameter, relating the radius to the free-space wavelength.
Compared with the simple quasi-static solution, additional terms appear in the numerator and denominator of **equation 2.11**. As discussed by Maier et al. [1], each term has a different physical meaning. The term quadratic in x in the numerator is due the effect of retardation of the exciting field over the volume of the sphere, generating a shift in the plasmon resonance. The quadratic term in the denominator also causes an energy shift of the resonance. This is due to the retardation of the depolarization field inside the particle. In the case of Drude and noble metals, the overall shift is towards smaller energies: the spectral position of the dipole resonance red shifts with increasing particle size. The quadratic term in the denominator also increases the magnitude of the polarization, and thus decreases the influence of the absorption due to the imaginary part of ε. However, this increase in strength is attenuated by the third,

completely imaginary term in the denominator, which accounts for radiation damping. Plots of absorption and scattering cross section are shown in **Figure 2.3.**

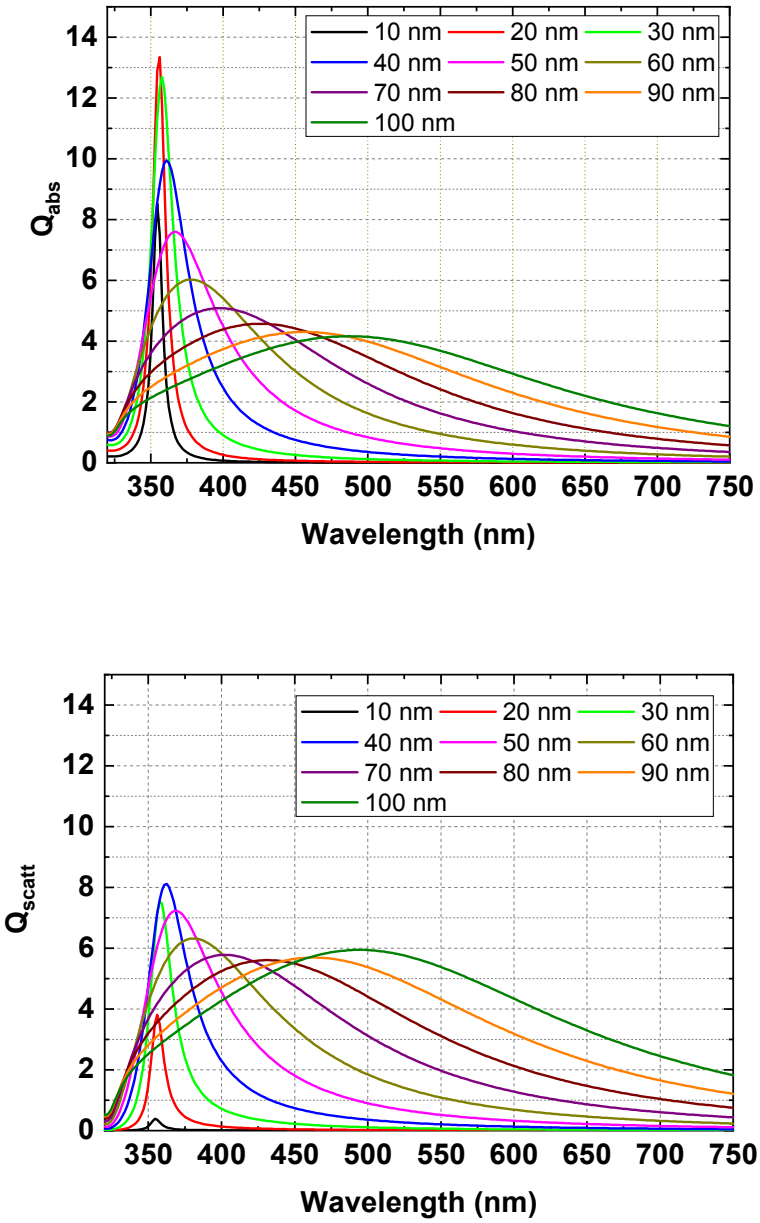


Figure 2.3: Calculated a) absorption cross section and b) scattering cross section for Ag spherical particles of different radius using **equation 2.9** and **2.10**. Both sections are relative to geometrical sections

Kuwata et al. [3] proposed a generalization of **equation 2.11** to a non spherical object:

$$\alpha \approx \frac{V}{\left(L+\frac{\varepsilon_m}{\varepsilon-\varepsilon_m}\right)+A\varepsilon_m x^2+B\varepsilon_m^2 x^4-i\frac{4\pi^2\varepsilon_m^{3/2}}{3}\frac{V}{\lambda_0^3}} \quad \textbf{2.12}$$

The size effect consists fundamentally in the reduction of the depolarization field due to retardation. Hence, the relevant dimension for the size parameter for a spheroidal particle is the diameter along the polarization of the incident light. So, if it is polarized along the direction perpendicular to the revolution axis (z-direction), as shown in **Figure 2.4**, $x = \frac{2\pi a}{\lambda}$.

The strength of the depolarization field depends also on the depolarization L. Considering an oblate with the z-axis as the rotational axis, L_z is given by [4]:

$$L_Z = \frac{1}{e^2}\left(1 - \frac{\sqrt{1-e^2}}{e} arcsin(e)\right) \quad \textbf{2.13}$$

$e = 1 - \left(\frac{c}{a}\right)^2$, where a and c are the quantities specified in **Figure 2.4**. The remaining factors $L_x = L_y$ can be determined by using the sum rule $L_x + L_y + L_z = 1$.

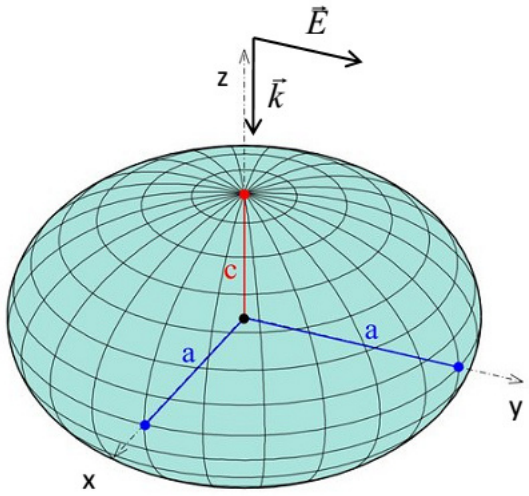


Figure 2.4: An oblate spheroid (volume constructed by a revolution of an ellipsis about its minor axis) with the dimension a and c. The incident electric field is perpendicular to the revolution axis.

A and B in **equation 2.12** are parameters to be determined. These parameters are expected to depend on ε and L. However Kuwata et al. [3] concluded that they are insensitive to the material (Ag or Au) and they depend only on L. Related plots of absorption and scattering cross section are shown in **Figure 2.5 and Figure 2.6 .**

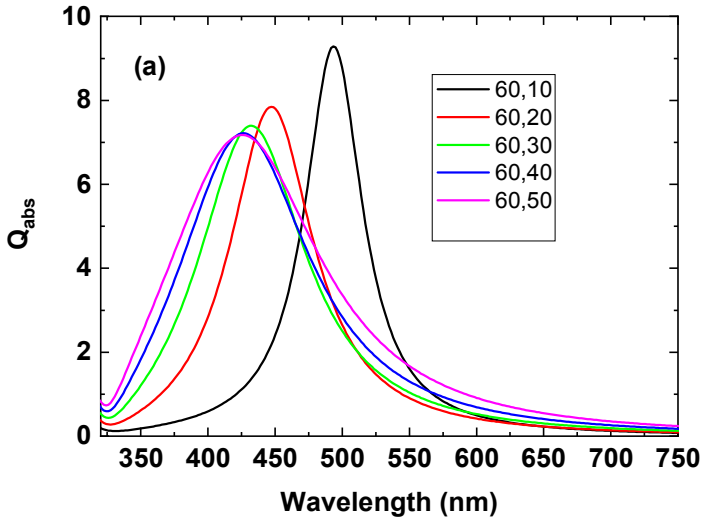


Figure 2.5: Absorption cross section relative to geometrical section curves for silver oblate spheroids. The numbers in legend correspond to $\boldsymbol{a}$ and $\boldsymbol{c}$, respectively.

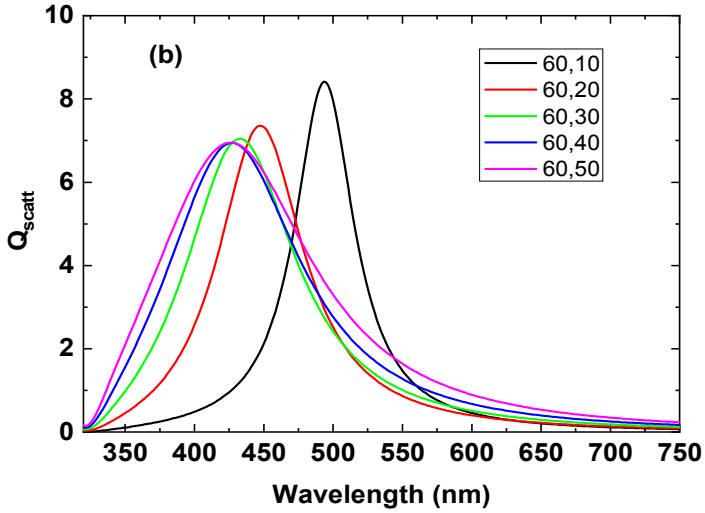


Figure 2.6: Scattering cross section relative to geometrical section for silver oblate spheroids in vacuum. The numbers in legend correspond to $\boldsymbol{a}$ and $\boldsymbol{b}$, respectively.

2.1.3 Plasmonic properties of metal hemisphere or hemispheroid placed on a dielectric substrate (after Scherbak et al. [5] [6])

To describe plasmonics properties of a particle, it is usually enough to find its polarizability. For free standing spherical or spheroidal nanoparticles, analytical solutions allow us to find the SPR frequency. But many relatively simple shapes of metal NPs need numerical techniques to obtain their polarizability. Scherbak et al. [6] made a semi-numerical

analysis of the SPR of a metal hemisphere or hemispheroid situated on a dielectric substrate as shown in **Figure 2.7**.

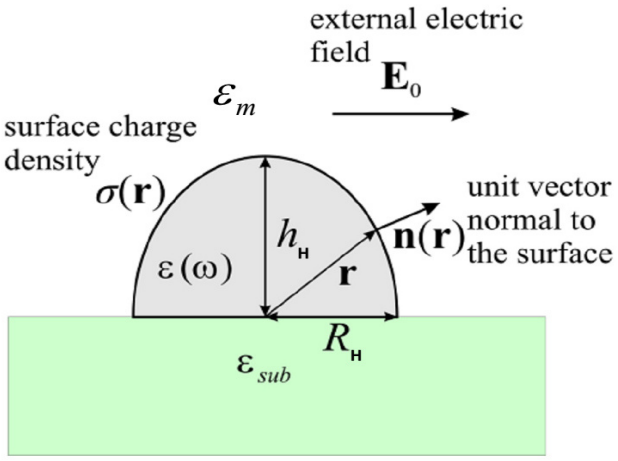


Figure 2.7: Hemispheroidal particle supported on a substrate, with height h_H and a radius in the plane of the substrate R_H. The dielectric function of the particle is $\varepsilon(\omega)$, the dielectric constant of the substrate is ε_{sub} and the upper medium one is ε_m. The polarization of the external electric field $\overrightarrow{E_0}$ is horizontal (parallel to the plane of the interface between the particle and the substrate). $\sigma(\vec{r})$ is the surface charge density and $\vec{n}(\vec{r})$ is unit vector normal to the surface [6].

The external electric field E_0 is directed along the substrate surface and the metal NPs are much smaller than the light wavelength. For this reason, the retardation effects are ignored and the problem is in the quasi-static approximation. The polarizability obtained by Scherbak et al. in this situation, keeping the resonant term only, is [6]:

$$\alpha(\omega) = AR_H^3 \frac{\frac{\varepsilon(\omega)}{\varepsilon_m} - 1}{\frac{\varepsilon(\omega)}{\varepsilon_m} - \varepsilon_{res}} \qquad \textbf{2.14}$$

where the scale coefficient A and the resonant dielectric constant ε_{res} depends on the specific problem geometry and substrate permittivity ε_{subs}. R_H^3 is a dimensional factor. $\varepsilon(\omega)$ and ε_m are the dielectric function of the metal NP and of the surrounding media respectively. If the imaginary part of the dielectric function is small, it is sufficient to calculate the resonant dielectric permittivity. The resonant condition can be written as [6]:

$$Re\left(\frac{\varepsilon(\omega)}{\varepsilon_m} - \varepsilon_{res}\right) = 0 \qquad \textbf{2.15}$$

In the case of hemispherical particle in a homogeneous medium $\varepsilon_{subs} = \varepsilon_m$ and for a glass substrate $\frac{\varepsilon_{subs}}{\varepsilon_m} = 2.25$, the respective polarizabilities obtained by Scherbak et al. are [6] :

$$\alpha(\omega) = 0.63R_H^3 \frac{\frac{\varepsilon(\omega)}{\varepsilon_m} - 1}{\frac{\varepsilon(\omega)}{\varepsilon_m} + 3.95} \qquad \textbf{2.16}$$

$$\alpha(\omega) = 0.52R_H^3 \frac{\frac{\varepsilon(\omega)}{\varepsilon_m}-1}{\frac{\varepsilon(\omega)}{\varepsilon_m}+6.61} \qquad \textbf{2.17}$$

This method was also used to find the polarizability and the SPR wavelengths of axysimmetrical hemispheroids. For example a red shift of 50 nm occurs after the decrease in the aspect ratio from 1.5 to 0.7 as shown in **Figure 2.7** [6]. .

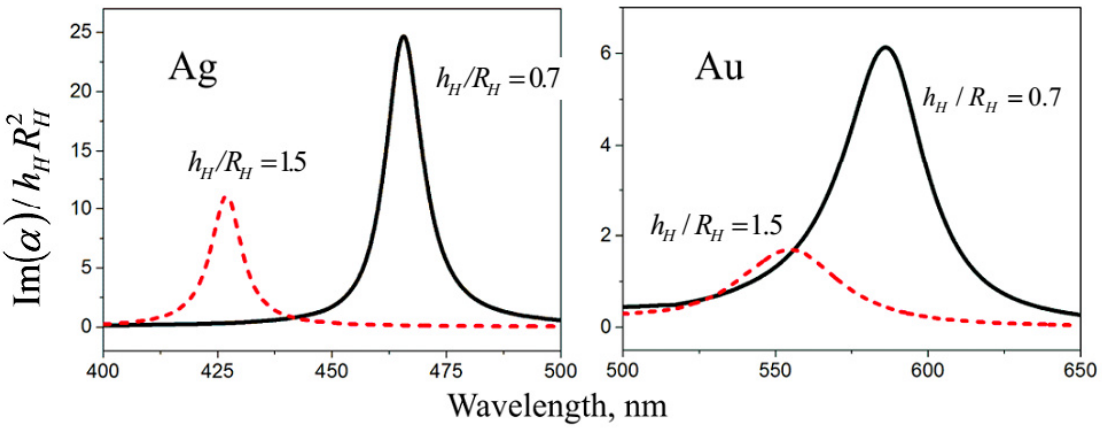


Figure 2.8: Imaginary part of the polarizability relative to the dimensional factor h_H/R_H^2 of silver (left) and gold (right) hemispheroids, with different aspect ratios h_H/R_H on a glass substrate ($\boldsymbol{\varepsilon_{sub} = 2.25}$). h_H and R_H are defined in **Figure 2.7** [6].

2.1.4 Interaction among the particles

Based in the works of Zou et al. [7], Zhao et al.[8] and Ben et al. [9] the basics of the interaction among the particles is presented in this section. Consider a system of nanoparticles which are electromagnetically coupled. In this case, the frequency of the SPR changes because the induced local electric field of adjacent nanoparticles generates other forces.

Now, let's consider a 2D array of N particles as shown in **Figure 2.9** whose positions and polarizabilities are $\vec{r_i}$ and α_i respectively. The induced dipole $\vec{P_i}$ in each particle due to an applied plane wave field is $\vec{P_i} = \alpha_i \overrightarrow{E_{loc,i}}$

$\overrightarrow{E_{loc,i}}(\vec{r_i})$ is the sum of the incident plane wave $\overrightarrow{E_{inc,i}} = \vec{E_0}\exp(i\vec{k}.\vec{r} - i\omega t)$ and the retarded fields of the other N-1 dipoles [7] [8]:

$$\overrightarrow{E_{loc,i}} = \vec{E_o}\exp(i\vec{k}.\vec{r}_{ij}) - \sum_{j\neq i} A_{ij} \cdot \vec{P_j} \quad i = 1,2,\ldots..,N \qquad \textbf{2.18}$$

where E_0 is the amplitude and, for the wavelength λ, $k = \frac{2\pi}{\lambda}$ is the wave vector of the incident wave. The dipole interaction matrix A obeys the following expression [7]:

$$A_{ij} \cdot \vec{P}_j = k^2 exp(i\vec{k}.\vec{r}_i) \frac{\vec{r}_{ij} \times (\vec{r}_{ij} \times \vec{P}_j)}{r_{ij}^3} + exp(i\vec{k}.\vec{r}_{ij})(1 - \vec{k}.\vec{r}_{ij}) \times \frac{[r_{ij}^2 \vec{P}_j - 3\vec{r}_{ij}(\vec{r}_{ij} \cdot \vec{P}_j)]}{r_{ij}^5}$$

$$(i = 1,2, \dots, N,\ j = 1,2, \dots . N, j \neq i) \qquad \textbf{2.19}$$

where $\vec{r}_{ij}$ is the vector from dipole i to dipole j.

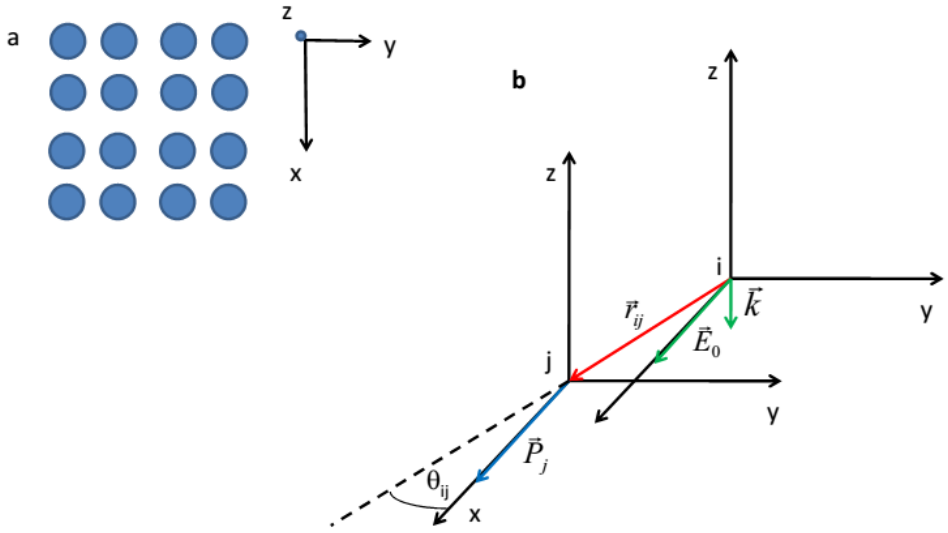


Figure 2.9: a) A 2D array in the x-y plane b) Schematic diagram of the particle $\boldsymbol{i}$ and $\boldsymbol{j}$. $\vec{\boldsymbol{r}}_{\boldsymbol{ij}}$ is distance vector between the particles. $\vec{\boldsymbol{P}}_{\boldsymbol{j}}$ is polarization of the particle $\boldsymbol{j}$ and $\boldsymbol{\theta_{ij}}$ is the angle between $\vec{\boldsymbol{P}}_{\boldsymbol{j}}$ and $\vec{\boldsymbol{r}}_{\boldsymbol{ij}}$. The electric field propagates in the $\vec{\boldsymbol{k}}$ direction and it is polarized in the x-y plane.

The terms which have a $\frac{1}{r}$ dependence on the interparticle spacing are associated to radiative interactions between the particles, while terms with $\frac{1}{r^3}$ correspond to electrostatic coupling.

The polarization vectors are obtained by solving 3N linear equations of the form:

$$\widetilde{A'}\tilde{P} = \tilde{E} \qquad \textbf{2.20}$$

where the off diagonal elements of the matrix $\widetilde{A'}$ ($\widetilde{A'}_{ij}$) are the same as A_{ij}, and the diagonal elements $\widetilde{A'}_{ii}$ are α_i^{-1}. $\tilde{P}$ and $\tilde{E}$ are the N-dimensional vectors constructed with $\vec{P}_j$ and $\vec{E}_{loc,i}$ as components, respectively.

After obtaining the polarization vectors, we can calculate the extinction cross section using [7]:

$$C_{ext} = \frac{4\pi k}{|\boldsymbol{E}_0|^2} \sum_{j=1}^{N} Im(\vec{E}^*_{inc,j} \cdot \vec{P}_j) \qquad \textbf{2.21}$$

A simple analytical solution to **equation 2.21** can be obtained in the case of an infinite array of particles and for a wave in normal incidence. Therefore, p and s polarization are identical

for infinite arrays and we can choose the polarization to be along an axis that corresponds to the smallest inter-particle spacing. However, because all of the arrays considered have a large number of particles, the results of averaging over in plane polarization direction are nearly identical

By assuming that the induced polarization in each array element is the same. This leads to the following expression for the polarization of each particle [7]:

$$P = \frac{\alpha_S E_0}{1-\alpha_S S} \qquad \textbf{2.22}$$

and the extinction cross section is:

$$C_{ext} = 4\pi N k Im(P/E_0) \qquad \textbf{2.23}$$

where S is the retarded dipole sum

$$S = \sum_{j\neq i}\left(\frac{(1-i\vec{k}.\vec{r}_{ij})(3\cos^2\theta_{ij}-1)exp(i\vec{k}.\vec{r}_{ij})}{r_{ij}^3} + \frac{k^2\sin^2\theta_{ij}exp(i\vec{k}.\vec{r}_{ij})}{r_{ij}}\right) \qquad \textbf{2.24}$$

θ_{ij} is the angle between r_{ij} and the polarization direction. The last equation provides a simple way to understand the effect of coupling between the particles on the plasmon resonance line shape. For a small spherical particles close to resonance, the polarizability α_S is approximately $-\frac{A}{(\omega-\omega_p+i\gamma_{HW})}$ where in the Drude model A is $\frac{1}{2}\omega_{SPR}a^3$, ω_{SPR} is the surface plasmon frequency for the isolated particle, a is the sphere radius and γ_{HW} is the half width of the resonance (one half of the Drude width). If this value of α_S is substituted into **equation 2.22**, P is given by [7]:

$$P = \frac{-AE_0}{\omega-\omega_{SPR}+i\gamma_{HW}+AS} = \frac{-AE_0}{\omega-\{\omega_{SPR}-ARe\{S\}\}+i\{\gamma_{HW}+AIm(S)\}} \qquad \textbf{2.25}$$

which means that the real part of the lattice sum S determines whether the plasmon resonance frequency red-shifts or blue-shifts, and the imaginary part determines the change in the width.

Ben et al. [9] express the effective polarizability of the infinite periodic 2D array as:

$$\alpha_{\text{array}} = \frac{\alpha_{\text{sphere}}}{1-S\alpha_{\text{sphere}}} \qquad \textbf{2.26}$$

where the size dependent function α_{sphere} is given by **equation 2.11.**

$\left|\text{Re}\left(\frac{1}{\alpha_{\text{sphere}}(\lambda_{\text{sphere}})} - \text{S}(\lambda_{\text{array}})\right)\right|$ corresponds to the relative LSPR wavelength shift between the array and the single sphere $\Delta\lambda = \left|\lambda_{array} - \lambda_{sphere}\right|$ [9].

2.2 Solid State Dewetting Process

Based on the excellent review of C.V. Thompson [10], we present in this section some basic concepts about the Solid State Dewetting (SSD) process. It is possible that thin metallic films dewet or agglomerate to form arrays of islands, as depicted in **Figure 2.10**, when they are heated to temperatures where the mobility of the atoms is big enough. The reason is that the state of the initial metallic thin film can be unstable or meta-stable. As indicated by the name of the process, the material (for example, a metal) remains in the solid state during it. Furthermore, it can occur at a temperature well below the melting one. The driving force is the minimization of the total energy of the system. It includes film surface energy, substrate energy and film-substrate interface energy. SSD is enhanced when the film thickness decreases. Hence, the temperature at which SSD occurs decreases with film thickness.

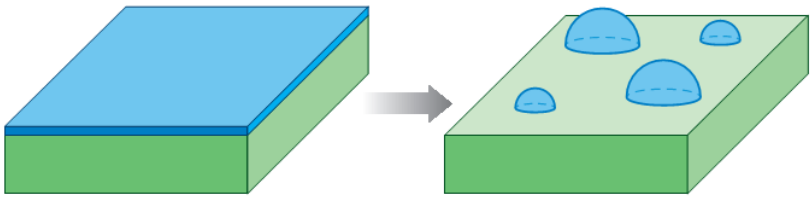


Figure 2.10: Schematics of solid state dewetting process. Thin films dewet to form islands. This occurs while the material remains in solid state [10].

Suppose an island with isotropic surface energy per unit area, γ_f, on a rigid substrate with surface energy per unit area γ_s as shown in **Figure 2.11**.

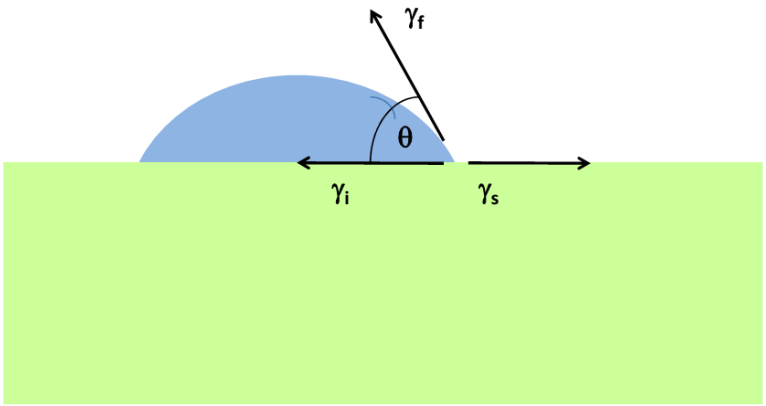


Figure 2.11: Island on a substrate, showing different surface energies per unit area which correspond to the energies per unit area used in **equation 2.27**. $\boldsymbol{\gamma_f}$ is the isotropic surface energy per unit area of the island, $\boldsymbol{\gamma_s}$ is the one of the rigid substrate and $\boldsymbol{\gamma_i}$ is the energy per unit area of the island-substrate interface.

If the volume is kept constant, the energy minimization leads to the Young-Laplace equation [10] .

$$\gamma_s = \gamma_i + \gamma_f \cos\theta \quad \textbf{2.27}$$

where γ_i is the energy per unit area of the island-substrate interface and θ is the equilibrium contact angle. If $\gamma_s > \gamma_i + \gamma_f$, a film is stable and the dewetting does not occur. Therefore, the film will dewet when the last condition is not fulfilled and the rates of the necessary kinetic process are large enough.

A very important parameter for the dewetting process is the spreading coefficient [11]:

$$S_C = \gamma_f(\cos\theta - 1) \quad \textbf{2.28}$$

where γ_f is the surface energy per unit area of the film and θ is the contact angle of the film on the substrate. When $S_C = 0$, the substrate is completely wetted and when $S_C < 0$ dewetting is energetically favorable. When $S_C \ll 0$, nanoparticles with large contact angle are formed.

The free energy change ΔF, due to the conversion of a volume V of the film (thickness d and initial area before dewetting S) into a spherical shaped particle which has a contact angle θ with substrate, is given by:

$$\Delta F = \pi r^2\left[2f(\theta)\gamma_f + \gamma_i - \gamma_s\right] + S\left(\gamma_s - \gamma_f - \gamma_i\right) \quad \textbf{2.29}$$

where

$$f(\theta) = \frac{1+\cos\theta}{\sin^2\theta} \quad \textbf{2.30}$$

γ_f, γ_s and γ_i are the surface energy per unit area of the film, substrate one and interfacial one respectively. The volume conservation gives the following equation:

$$Sd = \frac{2}{3}\pi r^3 g(\theta) \quad \textbf{2.31}$$

with

$$g(\theta) = \frac{1+\cos\theta}{2\sin^3\theta}[1 + \cos\theta + \sin^2\theta] \quad \textbf{2.32}$$

Therefore, the minimum radius associated to the formation of a nanoparticle is obtained from the condition $\Delta F < 0$. It is

$$r_{min} = \frac{3}{2}Kd \quad \textbf{2.33}$$

with $K = \frac{2f(\theta)\gamma_f + \gamma_i - \gamma_s}{g(\theta)(\gamma_i - \gamma_s + \gamma_i)}$ for spherical shaped island. The corresponding island density thus writes as:

$$\rho = \frac{1}{S} \approx \frac{4}{9K^3\pi g(\theta)}d^2 \quad \textbf{2.34}$$

The main factors that play on the morphology of the dewetted state and the kinetics of dewetting for a given couple f/s (film/substrate) [12] are :

- the initial film thickness d
- the annealing temperature T
- the annealing time t
- the annealing atmosphere
- the spreading coefficient which essentially depends on the couple f/s, that may be modified by a foreign adsorption or by strain
- the kinetic coefficient β, sensitive to adsorption and/or strain by means of diffusion coefficient D_S and γ (see **equation 2.46)**
- the nature and the number of the defects in the film that act as nucleation centres for spontaneous void opening
- the crystallographic orientations of the dewetting edges and the faceting properties of the rim that influence the stability condition of a dewetting front
- The specific properties of the triple line, for instance due to local adsorption and/or local pinning to defects that may affect the mobility of the dewetting front.

2.2.1 Mechanism of solid state dewetting

It is possible to identify different steps in the evolution of dewetting

- induction process
- holes formation
- holes propagation
- sintering of disconnected objects

2.2.1.1 Induction process

During induction, some selected grains enlarge more than their neighbours as it is seen in **Figure 2.12**. They are going to be the particles which are observed at the end of dewetting. Although, there are not changes in the substrate covering, many transformations occur. Presland et al. [13] observed the formation of hillocks with SEM and suggested that they are a consequence of stress relaxation which occurs at the interface. It is due to the difference of thermal expansion between film and substrate [12].

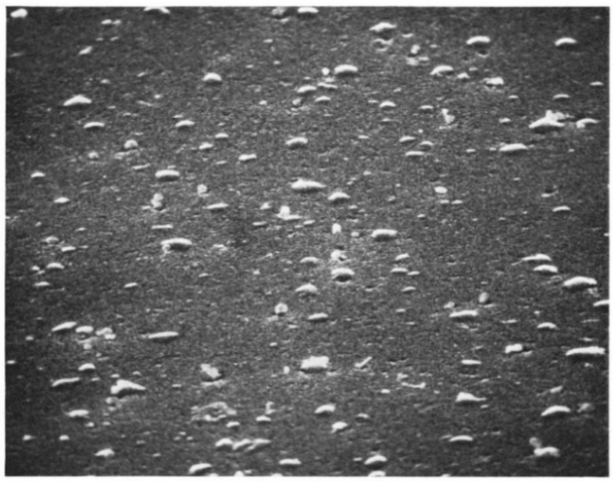


Figure 2.12: SEM micrograph of a metal film surface, at the end of induction period. Hillock can be observed [13].

Hillock growth was observed as the first stage in the agglomeration of silver films, which was found to occur in oxygen atmospheres. Transfer of material to the hillocks resulted in under covered surrounding areas and eventually the remaining material began to be removed from the substrate.

Differential thermal expansion will produce a stress in the film. In the case of silver on a glass substrate, the resultant stress for silver films under the annealing can be calculated from the expression of Pennebaker [13] for the change in stress $\Delta\sigma$ on expansion:

$$\Delta\sigma = \left(\alpha_{Ag}^{expan} - \alpha_{SiO_2}^{expan}\right)\Delta T\left(\frac{E}{1-\nu}\right) \qquad \textbf{2.35}$$

where α_{Ag}^{expan} and $\alpha_{SiO_2}^{expan}$ are the expansion coefficient of silver and SiO_2, respectively. E is the Young modulus and ν is the Poisson ratio. For ΔT=300°C , $\Delta\sigma$=12.5x10^8 N/m^2. The initial stress for silver films, deposited on glass substrates at room temperature, is tensile. Values reported are 3x10^7. N/m^2. Hence at 325°C, the net stress in the film is 12.2x10^8 N/m^2 (compressive). Removal of material, to hillocks above the film surface, will reduce this stress.

The compressive stress occurs regardless the atmosphere, but rapid hillock growth was only observed in the presence of oxygen. However, the increment in the surface self diffusion coefficient D_s by a factor of about 100 in oxygen, is not sufficient to account for hillock formation. Besides the diffusion, a significant crystallographic reorganization and grain formation is observed during induction. Indeed, even if all out of plane orientations are present, the (111) facets are dominant. This fact is in agreement with the hierarchy of the surface energies γ of silver which grows in the following order: γ(111) < γ(100) < γ(110) [14].

2.2.1.2 Holes formation

Following the conclusion reached, that stress in the film is the most likely driving force for hillock formation, an analogy was drawn with stress relief by grain boundary void growth, inside a material in tension.

The nucleation of holes is generally mediated by in-homogeneities at the surface of a film or a substrate. Particles or protrusions on the substrate surface, pits on the film surface, bubbles and grain boundaries have been suggested as in-homogeneities that mediate the nucleation of holes in thin films.

Grain boundaries and grain boundary triple junctions can have an important influence in the hole formation inside polycrystalline films [10]. Suppose that grains are sections of cylinders as shown in **Figure 2.13**.

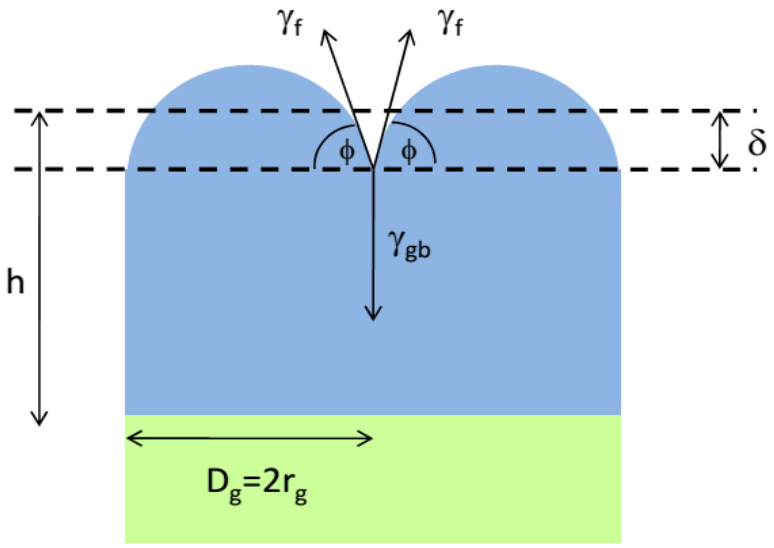


Figure 2.13: Schematic diagram of the cross sectional view of polycrystalline film on a rigid substrate. The in-plane grain diameter is $D_g=2r_g$. In its equilibrium shape, the film's surface will develop grooves with roots angles $\boldsymbol{\phi}$. The depth of groove is $\boldsymbol{\delta}$, and h is the thickness of the initial film. $\boldsymbol{\gamma_{gb}}$ is the grain boundary energy and $\boldsymbol{\gamma_f}$ is the surface energy per unit of area [10].

The grain boundaries have energies γ_{gb} and their size is D=2R. For isotropic γ_f, the angle ϕ is obtained by a force balance at the point at which the grain boundary and surface meet.

$$\phi = \sin^{-1}\left(\frac{\gamma_{gb}}{2\gamma_f}\right) \qquad \textbf{2.36}$$

When this condition is fulfilled, a groove forms at the boundary, with depth δ under the original planar film surface. The magnitude of δ is given by

$$\delta = r_g \frac{(2-3\cos\phi+\cos^3\phi)}{3\sin^3\phi} \qquad \textbf{2.37}$$

For the case that δ is bigger than the film thickness h, the grooves will contact the substrate. Thus, it can grow as a hole to initiate dewetting. The film will therefore break only if:

$$r_g > R_C = \frac{3\sin^3\phi}{(2-3\cos\phi+\cos^3\phi)h} \qquad \textbf{2.38}$$

As grain boundaries have different energies, not all of them will form holes. Holes formation will be most likely at high energy boundaries. The number of holes will also increase when h and γ_f are small and γ_{gb} and r_g are large.

In our case, independently on the pathway of silver diffusion (at surface or interface), the successive reorganization of grains is the main source for grooving. It happens through the appearance of new contact angles, instead of a continuous transformation.

Since reduction of the total energy of the system is the main driving force for grain reorganization, configurations closer to the equilibrium state at the triple line are promoted. As explained above, since this equilibrium drastically depends on atmosphere, different morphologies are expected between vacuum and oxygen. This explains the appearance of many holes in oxygen atmosphere: induction favours deep grooves in this atmosphere.

2.2.1.3 Holes propagation

Historically, the first model was based on capillarity approaches. It is inspired by liquid dewetting, which ignores the crystalline nature of the film. The driving force for agglomeration is the reduction of surface area as presented in **Figure 2.14**. It is assumed that morphological changes occur via surface diffusion driven by surface minimization.

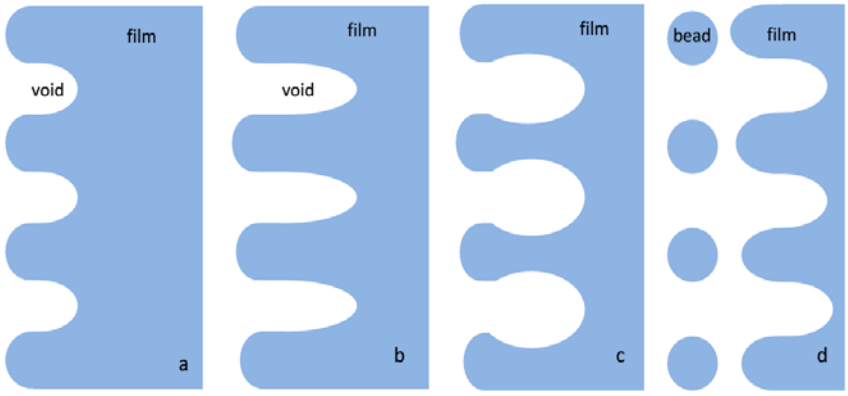


Figure 2.14: a) A series of fluctuations which have penetrated the thickened edge, b) Finger of materials left behind by the growing void cells, c) The fingers lower their surface area by rounding off and thickening, d) The thickened tip detached forming a bead.

The surface is considered as homogeneous and isotropic; the local curvature and the associated chemical potential gradient is suggested to be the driving force of the material transport. In the model developed by Jiran et al [15], thickness of the receding front is constant and equal to the initial film thickness d. The void only propagates through thin areas

of the film. So the material removed from the substrate is deposited at stationary areas to either side of the moving tip of the void as shown in **Figure 2.15**.

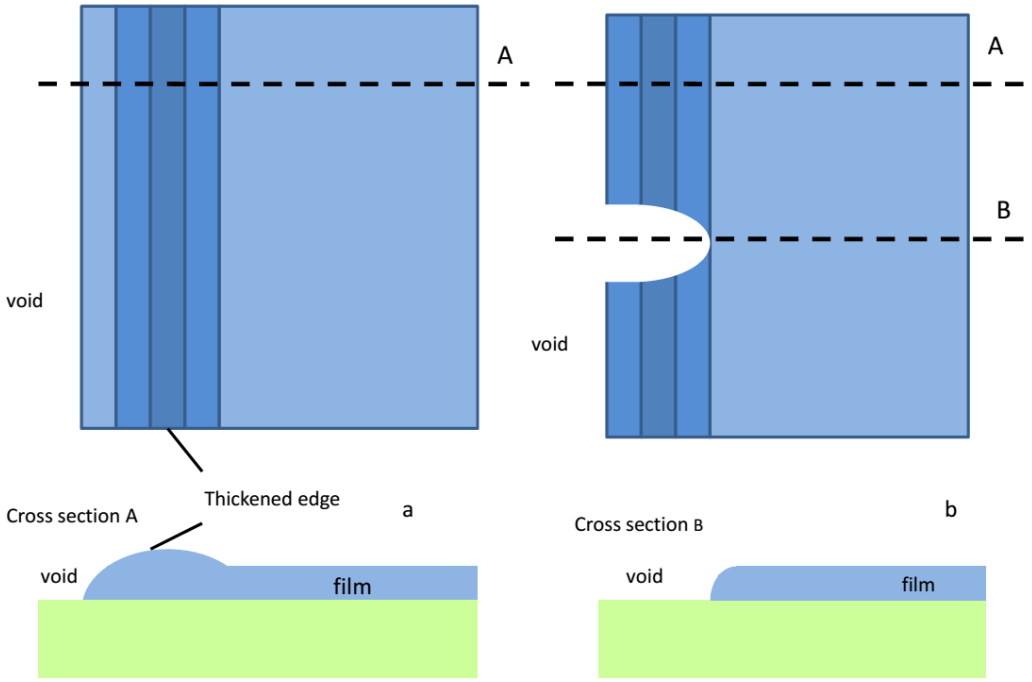


Figure 2.15: a) The edge thickness as it recedes and slows down, b) A fluctuation penetrates the build up and thus grows faster than the rest of the edge.

The edge of the film can be described by two models, one was made by Brandon and Bradshow, the other by Jiran [15]. Both models are shown in **Figure 2.16**. In **Figure 2.16 b**, the edge is a quarter circle whose radius is equal to the film thickness. It is modelled as contacting the substrate at a ninety degrees angle. Atoms will flow from this curved surface and the net flux away j_s is:

$$\overrightarrow{J_S} = -\frac{D_S}{kT}\frac{\partial \mu}{\partial s} \qquad \textbf{2.39}$$

D_S is the surface diffusivity, $\frac{\partial \mu}{\partial s}$ is the chemical potential change over an element of arc length s, k is the Boltzmann constant and T is the temperature (in K). The chemical potential change between the curved portion of radius d and in plane radius r'(see **Figure 2.17**), with a flat area of the film, is given by the following expression:

$$(\mu_A - \mu_B) = -\Omega\gamma_S\left(\frac{1}{d} - \frac{1}{r\prime}\right) \qquad \textbf{2.40}$$

where Ω is the atomic volume and γ_s is the surface tension. r' can be large compared with d so that

$$\Delta\mu \cong -\frac{\Omega\gamma_s}{d} \qquad \textbf{2.41}$$

where $r' \gg d$

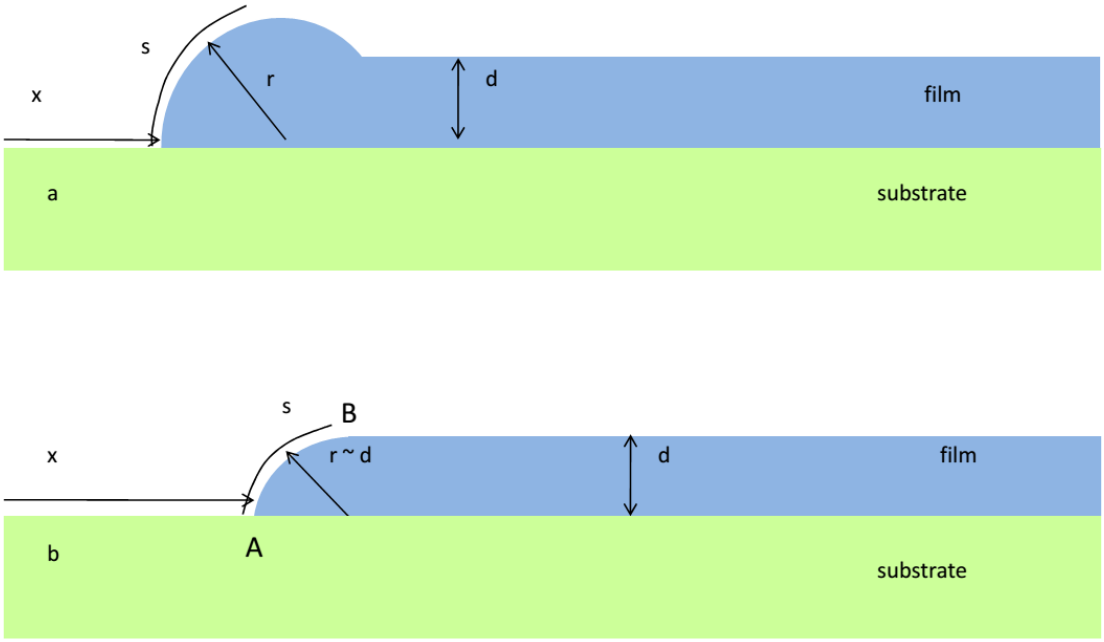


Figure 2.16: Profiles of the receding edge according to: a) Brandon and Bradshaw, b) the proposed model by Jiran et al. [15]. d is the initial thickness of the film, s is the arc length, x is the direction of propagation of the hole, A is the contact point of the receding edge with the substrate and B is the final point of the arc.

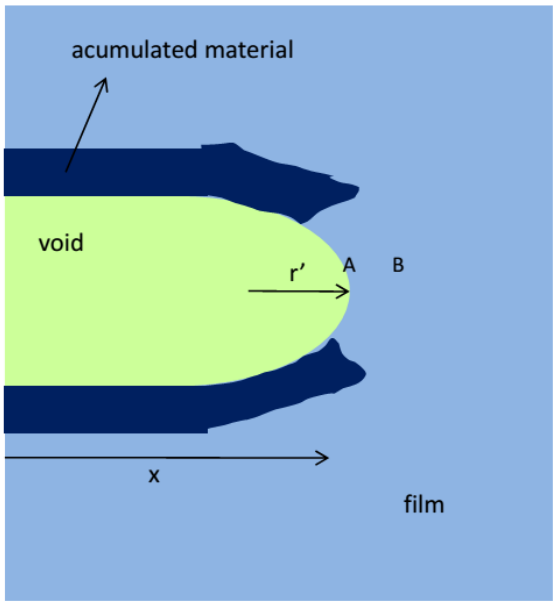


Figure 2.17: A close up view of an edge in **Figure 2.16** b).r' is the in plane radius, A and B are the same as the Figure 2.16.

The distance along the surface where the change $\Delta\mu$ occurs, is $\Delta s = \frac{\pi d}{2}$. The rate of volume transfer $\frac{dV}{dt}$ is equal to the surface flux multiplied by the total length of the advancing interface and the atomic volume Ω:

$$\frac{dV}{dt} = j_S l\Omega \qquad \textbf{2.42}$$

The velocity of the interface, $\frac{dx}{dt}$, is given by:

$$\frac{dx}{dt} = \frac{\Delta \mathrm{x}}{\Delta \mathrm{t}} = \frac{1}{\mathrm{dl}}\frac{\Delta \mathrm{V}}{\Delta \mathrm{t}} \qquad \textbf{2.43}$$

Using **equation 2.42**, $\frac{dV}{dt}$ is substituted by $j_S l\Omega$

$$\frac{\Delta x}{\Delta t} = \frac{j_s}{d}\Omega \qquad \textbf{2.44}$$

Using **equation 2.39**, js is substituted by $-\frac{D_S}{kT}\frac{\partial \mu}{\partial s}$. Also $\Delta\mu$ is given by $\Delta\mu \cong -\frac{\Omega\gamma_s}{d}$ and $\Delta s = \frac{\pi d}{2}$. Thus $\frac{\Delta x}{\Delta t}$ is obtained as:

$$\frac{\Delta x}{\Delta t} = \frac{D_s}{kT}\frac{\Omega^2\gamma_s}{\pi}\frac{2}{d^3} \qquad \textbf{2.45}$$

The material removed from the substrate is assumed to be deposited to each side of the moving tip as in **Figure 2.17.** Atoms diffuse first in the direction of the movement of the tip and the subsequent redistribution to the sides is relatively fast. For this reason, the equation is independent of the tip width. Substituting for D_S in **equation 2.45**, $\frac{\Delta x}{\Delta t}$ is expressed as follows:

$$\frac{\Delta x}{\Delta t} = 2\frac{D_0\gamma_s\Omega^2}{kT\pi d^3} exp\left(-\frac{Q_s}{kT}\right) = \beta\frac{exp(-Q_s/(kT))}{kTd^3} \qquad \textbf{2.46}$$

Observing this equation, we conclude that the growth rate of the hole is constant in time. The slope of an Arrhenius plot of $\frac{\Delta x}{\Delta t}(kT)$ vs $\frac{1}{kT}$ is Q_S, the activation energy for surface diffusion. D_0 can be obtained by the intercept. Also **equation 2.46,** gives the thickness dependence of the void growth rate which is inverse cubic.

Other factors, such as film crystallography and orientation of its edges, play an important role on the morphology of the final dewetted state and on kinetics. Experiments show that i) edge with different in-plane orientation retract at different rates ii) a faceted rim may induce new regimes as, for instance, a layer by layer dewetting mode. For example Jacquet et al. [16] concluded, that during hole propagation, none rim movement is involved. According to their experiments, surface coverage decreases only due to the disappearance of the small grains which are located on the dewetting front. They shrink in favour of selected ones. Grains drastically reorganize, during induction. But they also conclude that oxygen

impacts the evolution by facilitating the creation of holes. It is probably caused by lowering the surface energy of silver and promoting grain boundary grooving. By narrowing the selection of growing grain, oxygen leaves more possibilities for holes. But understanding the origin of grains selection is a subject of future work.

2.2.1.4 Sintering

The droplets originated from dewetted films are often not stable. Hence, they can sinter at later times. The reduction of the total surface free energy of the total system is the driving force of the sintering. The chemical potential measures how unstable a surface atom on a supported metal is, with respect to the bulk metal. When it increases, the atom will experience an acceleration of sintering [17]. The process stops when the thermodynamic equilibrium is reached or when other competing phenomena, such as the crystallization, start after a lag time. Supported nanoparticles evolve to equilibrium shape defined by Winterbottom construction [18], which is the modified Wulff construction by the adhesion energy E_{adh} [19], [20], [21]. Typically, the dependence of the droplet lateral size vs time, follows a power law, whose exponent depends on the underlying mechanism of energy dissipation [22].

Dai et al. [17] mention two different pathways of sintering as depicted in **Figure 2.18**: i) coalescence and ii) Ostwald ripening. For the coalescence process, two or more metal nanoparticles move on the substrate like in a Brownian motion until they meet and merges into large particles. Instead, for Ostwald ripening process, individual metal atoms leave the surface of one nanoparticle to join another nanoparticle via surface diffusion across the substrate. The largest particles are more favoured for growth at the expense of others because their chemical potential is smaller. Whereas, smallest ones exhibit a decrease of their size and eventually disappear. This process causes the sintering of the metal nanoparticles which are well separated.

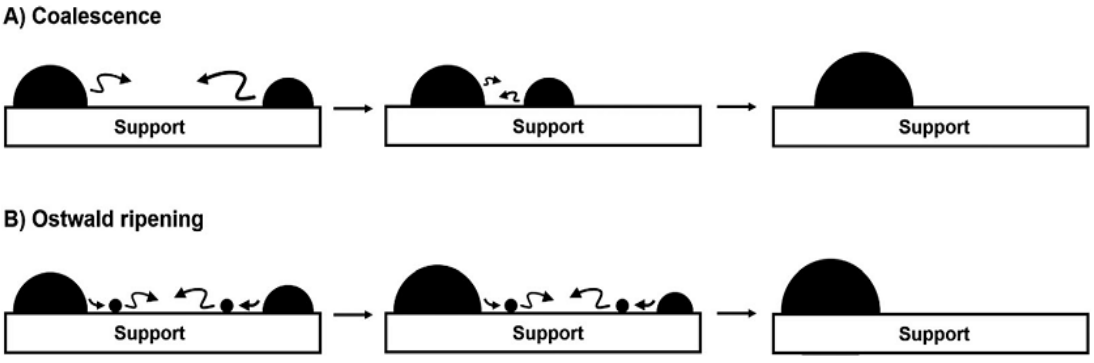


Figure 2.18: Schematic illustration of the two principal sintering mechanism or pathways for inter particle sintering: A) coalescence B) Ostwald ripening [17].

Discrimination among these two sintering mechanism is not an easy task, because sintering may be influenced by both, either simultaneously or alternatively. Coalescence

always produces a decrease of the particle density, while Ostwald ripening is characterized by a fixed particle number density at the early stage.

The rate of sintering has a strong correlation with temperature. Both mechanisms require the breaking of bonds between metal atoms or between metal atoms and the support surface. The temperature at which sintering starts can be roughly estimated using the semi empirical Huttig and Tamman temperatures [23]:

$$T_{Huttig} = 0.3T_{melting} \quad \textbf{2.47}$$

$$T_{Tamman} = 0.5T_{melting} \quad \textbf{2.48}$$

$T_{melting}$ is the melting temperature. The Huttig temperature is the one where atoms start to exhibit mobility. While at Tamman temperature, the atoms from the bulk become mobile and the diffusion is observable. The values of T_{Tamman} for the different metals, calculated from melting points are shown in **Figure 2.19**.

This method neglects the metal/support adhesion energy, which affects dramatically the sintering kinetics. In considering the sintering temperature, it is worth emphasizing that the melting point of a metal nanoparticle is much lower than the one of bulk material, as discussed in [17]:

$$\frac{T_m(r)}{T_m(0)} = 1 - \frac{2}{\rho_{solid} L_{heat}} \left\{ \gamma_{solid} - \gamma_{liquid} \left(\frac{\rho_{solid}}{\rho_{liquid}} \right)^{2/3} \right\} \frac{1}{r} \quad \textbf{2.49}$$

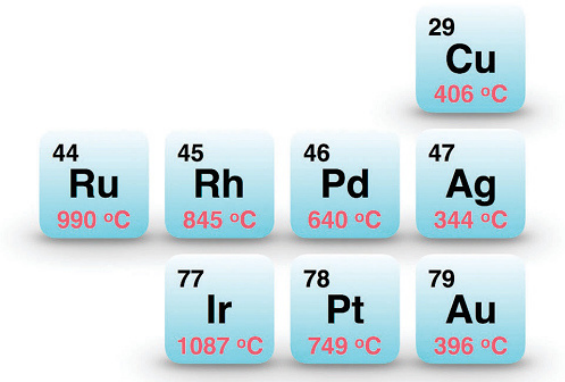


Figure 2.19: Comparison of the Tamman temperature (°C) for different metals [17].

where $T_m(r)$ is the melting point of a particle with radius r; $T_m(0)$ is the melting point of the bulk material. ρ_{solid} and ρ_{liquid} are the densities of the solid and liquid phases, respectively. γ_{solid} and γ_{liquid} are the surface free energy of the solid and liquid phases respectively and L_{heat} is the molar heat of fusion [17].

Thiel et al. [24] made a theoretical study of sintering. They concluded that there are two extremes regimes for Ostwald ripening kinetics. The first one is the diffusion limited transport (DL). The attachment and detachment of particles at the cluster boundaries is fast, compared to the diffusion. Thus, diffusion is the limiting process and it depends strongly on their local environment. There is not a significant barrier for attachment to cluster edges. The second one is attachment-detachment limited transport (AD). In this regime, the attachment and detachment at the cluster boundaries are slower compared to the diffusion in the matrix. The decay or growth of clusters are determined by the average cluster size. Hauβer et al. [20] made simulations and indicated that the average island radius is described by a t^a power law. The generic results for the evolution of the average island radius is:

$$R_{av}(t) \approx R_{av}(0)\left(1+\frac{t}{\tau}\right)^n \quad \textbf{2.50}$$

$\tau = \tau_0 exp\left[E_{eff}/(kT)\right]$ and for Ostwald ripening $n = \frac{1}{(\xi+2)}$

k is the Boltzmann constant, T is temperature and E_{eff} is the effective activation barrier given by:

$$E_{eff} = E_d + E_{form} + \delta \quad \textbf{2.51}$$

E_d is the diffusion barrier for the species transporting mass. E_{form} is the formation energy barrier to extract the diffusing species from a cluster, and attach them to another. δ is the energy barrier associated to a step in the surface where the diffusion is made [24][25].

For longer times $R_{av} \propto t^{\frac{1}{\xi+2}}$ and

$$R_{av} \sim t^{1/2} \text{ for AD } (\xi = 0) \quad \textbf{2.52}$$

2.3 Equilibrium shapes

An equilibrium crystal shape (ECS) of an isolated particle in a homogeneous environment, which is also known as Wulff shape, is shown in **Figure 2.20 a**. It can be obtained from a polar plot, whose construction is based on the orientation dependence of surface energy $\gamma(\hat{n})$. $\hat{n}$ is an unit vector normal to the surface, defined in the crystal coordinate system [19].

$$\vec{r} = \gamma(\hat{n})\hat{n} \quad \textbf{2.53}$$

The Wulff shape is constructed by placing a plane perpendicular to $\hat{n}$ at each point on the surface defined by $\vec{r}$. All the points in the interior of these tangent planes, constitute the Wulff shape. Faceted and curved (atomically rough orientation) surfaces are found in the ECS. Facets occur at orientations which correspond to cusps in the γ plot. All orientations are stable when facets are connected by curved parts. Instead, some orientations will be unstable

if facets have a sharp connection as observed in **Figure 2.20 b**. An example is shown in **Figure 2.20 c**. It consists in an ECS for a face centred cubic (fcc) with only three stable orientations: {100}, {110} and {111}.

It is obvious that if γ_{sl} is isotropic, the Wulff shape is a sphere, coinciding with the polar plot. For anisotropic materials, there is a competition between two shapes: a sphere which has the minimum area and a polyhedron whose facets correspond to lowest energy orientations. The equilibrium shape is a compromise between these two extremes.

Wulff shows that the equilibrium shape should be such that [18]

$$\gamma_{hkl} = \lambda h_{hkl} \qquad \textbf{2.54}$$

The perpendicular distance h_{hkl} of the surface (hkl) from the center of the body (referred to as the Wulff point) is directly proportional to the surface tension γ_{hkl} of that surface [24].

The Winterbottom construction on a flat substrate is shown in **Figure 2.21**. The γ plot is drawn in red. Thin black lines are drawn for discrete values of interface orientation and are perpendicular to the gamma vectors for each orientation

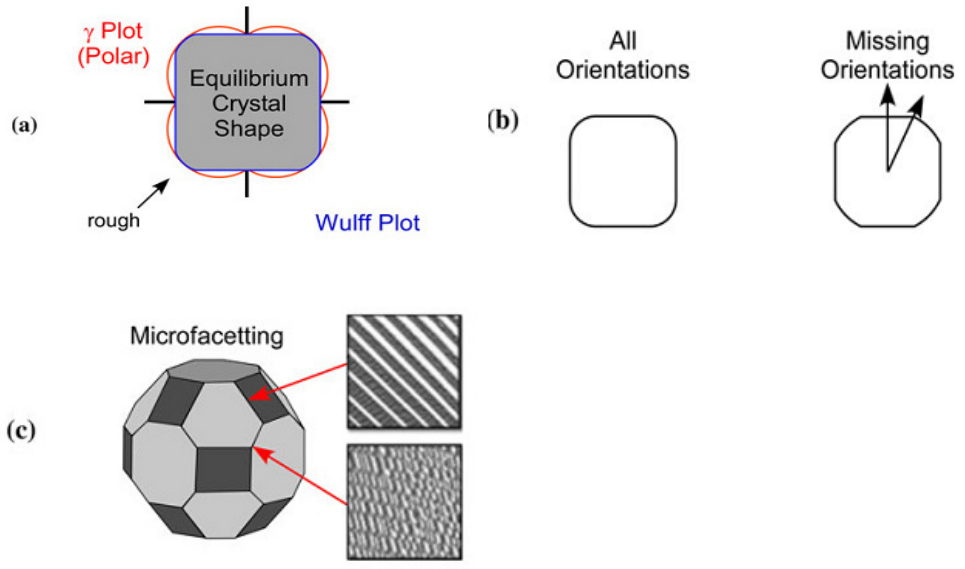


Figure 2.20: Equilibrium shapes and faceting: a) 2D γ plot and equilibrium shape of a crystal b) two 2D equilibrium shapes, the left one with all orientation and the right one with missing orientations where the shape has singularities. c) 3D equilibrium shape of an fcc crystal with only three types of stable orientations ([111], [100], [110]). Two AFM micrographs show micro-faceting of unstable orientation between two stable facets or three stable facets [19].

.

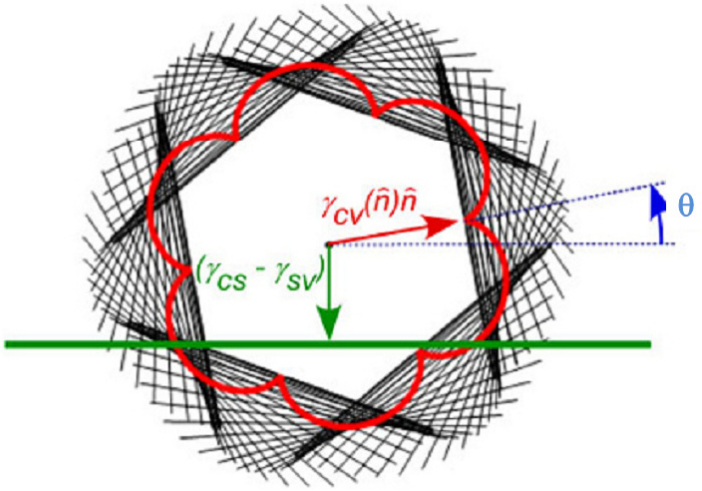


Figure 2.21: Winterbottom construction of a crystal on a flat substrate [19]. γ_{CS} is the surface energy per unit area of the interface crystal- substrate, γ_{SV} is the surface energy per unit area of the interface substrate-vapour (environment). $\gamma_{CV}(\hat{n})$ is the surface energy per unit area, which depends on the direction $\hat{n}$.

Suppose that the substrate is isotropic and flat. To this γ plot, an additional surface energy must be superposed. It represents the interfacial energy for the particle/substrate and substrate/vapor interfaces. It reduces to a γ interfacial vector with magnitude:

$$\Delta = \gamma_{PS} - \gamma_{SV} \qquad \textbf{2.55}$$

However, the derivation of this construction cannot apply in some cases. For example, when Wulff shape does not have a unique centre. It is observed in a crystal which the point group lacks an inversion centre.

On the basis of the shape theory developed for the model described above, it is convenient to classify the possible substrate particle configurations into four types [19]. The classification which is shown in **Figure 2.22** and **2.23** is based on the value of the quantity $(\gamma_{PS} - \gamma_{SV})$ which provides a measure of the binding or the degree of wetting between the particle and the substrate.

a) Non wetting, $(\gamma_{PS} - \gamma_{SV}) \geq \gamma_{PV}$

Under these conditions, the construction yields equilibrium shapes which correspond exactly to that of the free particle and free droplet.

b) Partial wetting, $\gamma_{PV} > (\gamma_{PS} - \gamma_{SV}) > 0$

The Wulff point is in the equilibrium shape.

c) Partial wetting$-\gamma_{PV} < (\gamma_{PS} - \gamma_{SV}) \leq 0$

The Wulff point is out of the equilibrium shape

d) Complete wetting $(\gamma_{PS} - \gamma_{SV}) \leq -\gamma_{PV}$

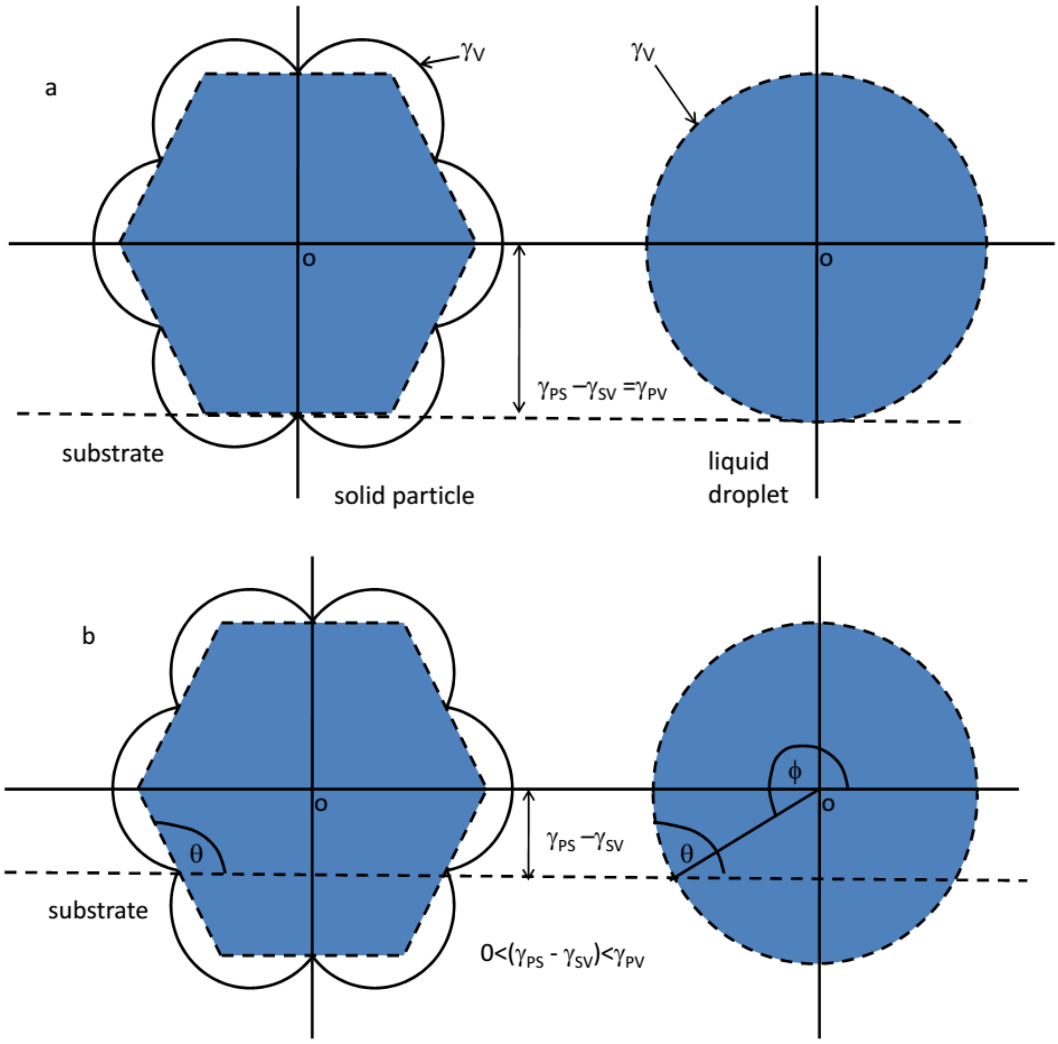


Figure 2.22: γ plots and corresponding equilibrium shapes for a two dimensional solid and liquid a) non wetting b) partial wetting (γ_{PS}-γ_{SV})>0. γ_{PS} is the surface energy per unit area of the interface particle-substrate, γ_{SV} is the one of the interface substrate-vapour (environment) and γ_{PV} is the energy per unit area of the interface particle-vapour (environment). θ is the contact angle.

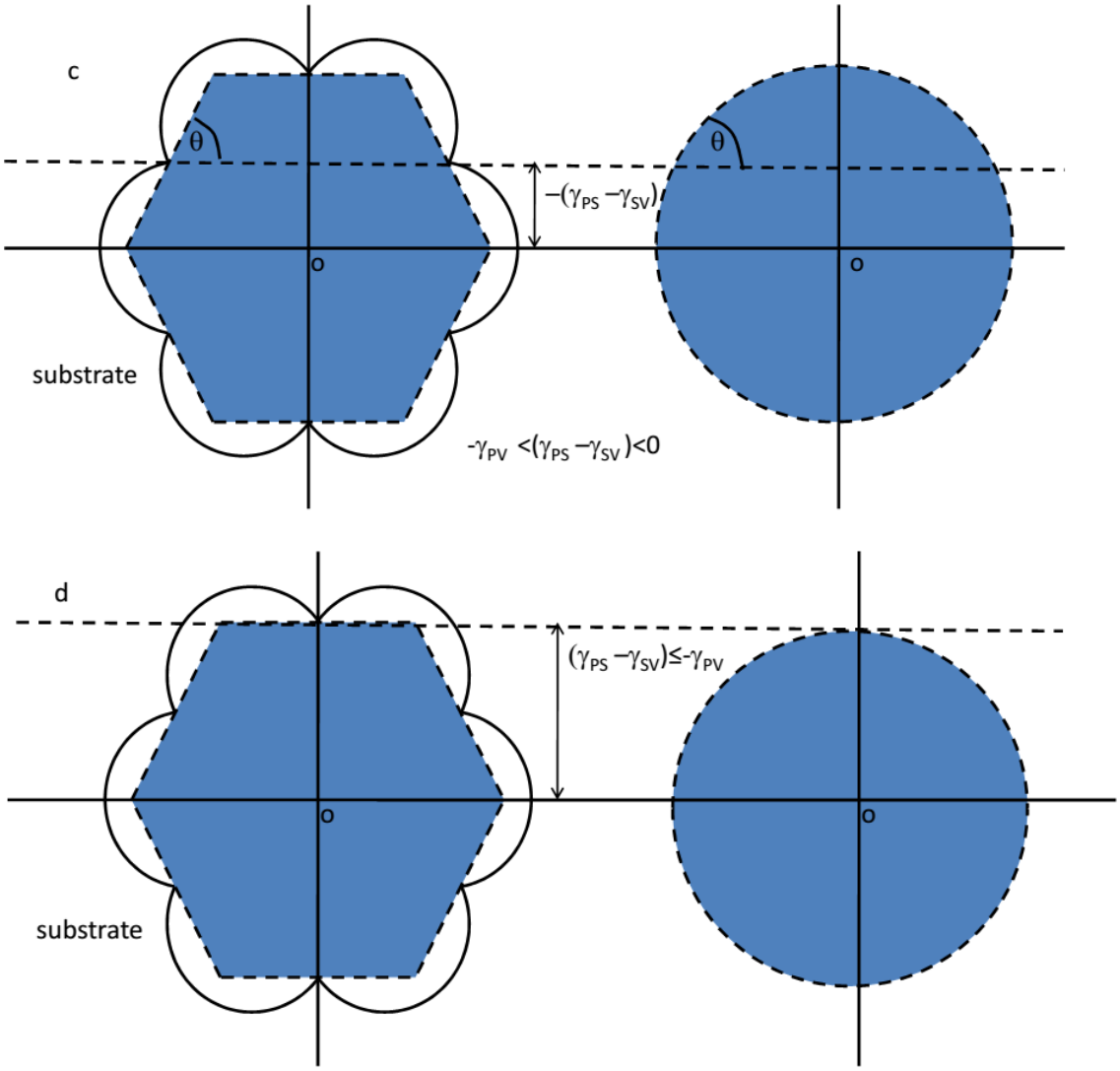


Figure 2.23: γ plots and corresponding equilibrium shapes for a two dimensional solid and liquid: c) partial wetting (γ_{PS}-γ_{SV})<0 d) complete wetting. $\boldsymbol{\gamma_{PS}}$ is the surface energy per unit area of the interface particle-substrate, $\boldsymbol{\gamma_{SV}}$ is the one of the interface substrate-vapour (environment) and $\boldsymbol{\gamma_{PV}}$ is the energy per unit area of the interface particle-vapour (environment). $\boldsymbol{\theta}$ is the contact angle.

This limiting condition for wetting is always characterized by zero angle contact.

In many context, particles show different interfaces. The equilibrium shape must minimize the sum of each total interfacial energy, maintaining other variables constraint such as particle volume. The simplest example is a deformable particle with a fixed volume on a planar interface. In addition to the interfacial energy between particle and its environment in the absence of substrate (γ_{PV}), there are two additional interfacial energies. They correspond to the interface between the substrate and the particle (γ_{PS}) and to the interface between the substrate and environment (γ_{SV}). For the isotropic case, minimization produces spherical cap

that intersects the substrate with an uniform wetting angle θ, for the particle on the substrate with

$$\theta = \cos^{-1}\frac{\gamma_{SV}-\gamma_{PS}}{\gamma_{PV}} \quad \textbf{2.56}$$

The Young equation is independent of particle size, but the curvature of the spherical cap is determined by the particle volume. Consider the geometry of the shape in W-space, the centre of the spherical gamma surface for the particle/exterior interface (with radius γ_{PV}) sits a distance $(\gamma_{SV} - \gamma_{PS})$ above the substrate. If $(\gamma_{SV} - \gamma_{PS})$ is negative, then most of sphere is discarded and only a small cap remains. This is the Winterbottom construction for an isotropic particle. Winterbottom showed that the $\gamma = 0$ point will be a distance $(\gamma_{SV} - \gamma_{PS})$ above the substrate, not only for isotropic particles, but for a particle with a general Wullf shape.

2.4 References

[1] Maier, S. A. Plasmonics: Fundamentals and Applications. Springer US: New York, NY 2007.

[2] Liang, Z. , Sun, J. , Jiang, Y. , Jiang, L. , and Chen, X. Plasmonic Enhanced Optoelectronic Devices. *Plasmonics* **2014**, 9, 859–866.

[3] Kuwata, H. , Tamaru, H. , Esumi, K. , and Miyano, K. Resonant light scattering from metal nanoparticles: Practical analysis beyond Rayleigh approximation. *Applied Physics Letters* **2003**, 83, 4625–4627.

[4] Moroz, A. Depolarization field of spheroidal particles. *Journal of the Optical Society of America B* **2009**, 26, 517.

[5] Scherbak, S. A. and Lipovskii, A. A. Plasmonic properties of metal nanoislands: Practical guide. *Journal of Applied Physics* **2016**, 119, 163106.

[6] Scherbak, S. A. and Lipovskii, A. A. Plasmonic properties of metal nanoislands: surface integral equations approach. *Journal of Physics: Conference Series* **2016**, 741, 012120.

[7] Zou, S. and Schatz, G. C. Narrow plasmonic/photonic extinction and scattering line shapes for one and two dimensional silver nanoparticle arrays. *The Journal of Chemical Physics* **2004**, 121, 12606.

[8] Zhao, L. , Kelly, K. L. , and Schatz, G. C. The Extinction Spectra of Silver Nanoparticle Arrays: Influence of Array Structure on Plasmon Resonance Wavelength and Width †. *The Journal of Physical Chemistry B* **2003**, 107, 7343–7350.

[9] Ben, X. and Park, H. S. Size Dependence of the Plasmon Ruler Equation for Two-Dimensional Metal Nanosphere Arrays. *The Journal of Physical Chemistry C* **2011**, 115, 15915–15926.

[10] Thompson, C. V. Solid-State Dewetting of Thin Films. *Annual Review of Materials Research* **2012**, 42, 399–434.

[11] Kojima, Y. and Kato, T. Nanoparticle formation in Au thin films by electron-beam-induced dewetting. *Nanotechnology* **2008**, 19, 255605.

[12] Leroy, F. , Borowik, Ł. , Cheynis, F. , Almadori, Y. , Curiotto, S. , Trautmann, M. , Barbé, J. C. , and Müller, P. How to control solid state dewetting: A short review. *Surface Science Reports* **2016**, 71, 391–409.

[13] Presland, A. E. B. , Price, G. L. , and Trimm, D. L. Hillock formation by surface diffusion on thin silver films. *Surface Science* **1972**, 29, 424–434.

[14] Jacquet, P. , Podor, R. , Ravaux, J. , Teisseire, J. , Gozhyk, I. , Jupille, J. , and Lazzari, R. Grain growth: The key to understand solid-state dewetting of silver thin films. *Scripta Materialia* **2016**, 115, 128–132.

[15] Jiran, E. and Thompson, C. V. Capillary instabilities in thin films. *Journal of Electronic Materials* **1990**, 19, 1153–1160.

[16] Jacquet, P. , Podor, R. , Ravaux, J. , Lautru, J. , Teisseire, J. , Gozhyk, I. , Jupille, J. , and Lazzari, R. On the solid-state dewetting of polycrystalline thin films: Capillary versus grain growth approach. *Acta Materialia* **2018**, 143, 281–290.

[17] Dai, Y. , Lu, P. , Cao, Z. , Campbell, C. T. , and Xia, Y. The physical chemistry and materials science behind sinter-resistant catalysts. *Chemical Society Reviews* **2018**, 47, 4314–4331.

[18] Winterbottom, W. L. Equilibrium shape of a small particle in contact with a foreign substrate. *Acta Metallurgica* **1967**, 15, 303–310.

[19] Kaplan, W. D. , Chatain, D. , Wynblatt, P. , and Carter, W. C. A review of wetting versus adsorption, complexions, and related phenomena: the rosetta stone of wetting. *Journal of Materials Science* **2013**, 48, 5681–5717.

[20] Haußer, F. and Voigt, A. Ostwald ripening of two-dimensional homoepitaxial islands. *Physical Review B* **2005**, 72, 035437.

[21] Thiel, P. A. , Shen, M. , Liu, D.-J. , and Evans, J. W. Coarsening of Two-Dimensional Nanoclusters on Metal Surfaces. *The Journal of Physical Chemistry C* **2009**, 113, 5047–5067.

[22] Gentili, D. , Foschi, G. , Valle, F. , Cavallini, M. , and Biscarini, F. Applications of dewetting in micro and nanotechnology. *Chemical Society Reviews* **2012**, 41, 4430.

[23] Prieto, G. , Tüysüz, H. , Duyckaerts, N. , Knossalla, J. , Wang, G.-H. , and Schüth, F. Hollow Nano- and Microstructures as Catalysts. *Chemical Reviews* **2016**, 116, 14056–14119.

[24] Thiel, P. A. , Shen, M. , Liu, D. J. , and Evans, J. W. Coarsening of two-dimensional nanoclusters on metal surfaces. *Journal of Physical Chemistry C* **2009**, 113, 5047–5067.

[25] Schwoebel, R. L. and Shipsey, E. J. Step Motion on Crystal Surfaces. *Journal of Applied Physics* **1966**, 37, 3682–3686.

3 Experimental methods

3.1. Sample preparation

3.1.1. Vacuum thermal evaporation

A liquid or a solid evaporates at a certain temperature. It occurs when the number of emitted particles at equilibrium vapour pressure, is larger than the number of particles which return. Hence, the rate of evaporation from a liquid or a solid surface is [1]:

$$\Phi_e = \frac{\alpha_e N_A (P_e - P_h)}{(2\pi MRT)^{1/2}} \quad \textbf{3.1}$$

where Φ_e is the evaporation flux in number of atoms (or molecules) per unit area and per unit time, M (kg/mol) is the molar mass, R is the ideal gas constant, T (K) is the absolute temperature (K), P_e (Pa) is the equilibrium pressure at a given temperature and P_h (Pa) is the hydrostatic pressure acting on the liquid or solid. N_A is the Avogadro number and α_e is the coefficient of evaporation, which has a value between 0 and 1. The maximum evaporation rate is reached when $\alpha_e = 1$ and $P_h = 0$.

The temperature has a very big impact on the equilibrium vapour pressures. Thus, it is the most important variable which affects the evaporation rate. To show the dependence of vapour pressure on temperature, the Clausius-Clapeyron equation is the most suitable starting point. It is valid for both solid-vapour and liquid-vapour equilibrium [1]:

$$\frac{dP}{dT} = \frac{\Delta H(T)}{T\Delta V} \quad \textbf{3.2}$$

The changes of the enthalpy $\Delta H(T)$ and the volume ΔV allude to differences between vapour (V) and the particular condensed phase (C). T is the transformation temperature. As $\Delta V = V_V - V_C$ and the volume of vapour is normally much bigger than one of the condensed phase, we can use that $\Delta V \cong V_V$. If the gas is considered as ideal $V_V = {RT}/{P}$, the **equation 3.2** results in [1]:

$$\frac{dP}{dT} = \frac{P\Delta H(T)}{RT^2} \quad \textbf{3.3}$$

Now, as a first approximation, we use that $\Delta H(T)$ is the molar heat ΔH_e. So, after an integration, we obtain [1]:

$$\ln P \cong -\frac{\Delta H_e}{RT} + 1 \quad \textbf{3.4}$$

$$P = P_0 \exp\left(-\frac{\Delta H_e}{RT}\right) \quad \textbf{3.5}$$

Equation 3.5 describes the temperature dependence of the vapour pressure in many materials. However, it is valid only in a narrow temperature range. Therefore, to make it widen, the temperature dependence of $\Delta H(T)$ must be taken into account. For example, the vapor pressure of liquid Al obeys [1]:

$$\log P(torr) = -\frac{15.993}{T} + 12.409 - 0.999\log T - 3.52 \times 10^{6} T \qquad \textbf{3.6}$$

The Arrhenius characteristics of $\log P$ vs $1/T$ are basically kept by the first two terms on the right hand side. The other terms are small corrections. Vapour pressure data for many other metals have been obtained by the same way.

In practice, evaporation can be classified in two different modes. They depend on the source in which the vapour is generated: liquid or solid source. If the vapour pressure at its melting point is not greater than 10^{-3} torr, the material must be molten to obtain an effective film deposition. The majority of the metals belongs to this category. On the other hand, elements such as Cr, Ti, Mo, Fe, and Si reach sufficiently high vapour pressures below the melting point and therefore sublime. The evaporation system used in this work is shown in **Figure 3.1**.

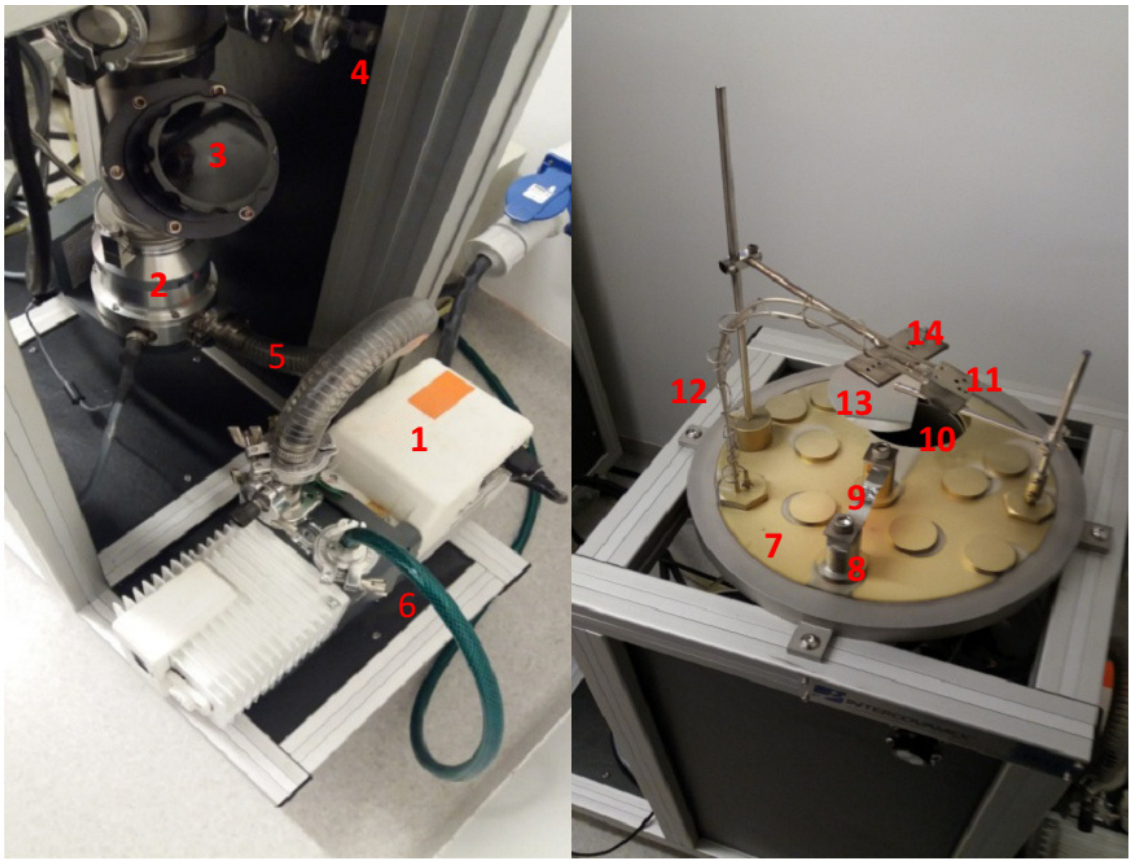


Figure 3.1: 1) Mechanical pump 2) Turbo pump, 3) Valve 4) Venting valve 5) Hose which connects the mechanical pump with the turbo pump 6) Exhaust hose 7) Base plate 8) Current contact electrode 9) Evaporation source 10) to the turbo pump 11) Quartz monitor head 12) Electrical wires and water tubes of quartz monitor 13) Shutter and 14) Substrate holder.

A Pyrex bell jar sealed with a rubber gasket is placed on the base plate, so that all the elements described in **Figure 3.1** remain inside. In addition, the inner part of the bell, is covered with an aluminium foil to prevent deposits of evaporants onto the Pyrex surface. The vacuum is supplied by an Adixen Pascal SD mechanical pump and Adixen ATP 80 turbo pump. The minimum pressure for which the turbo pump is allowed to switch on is $5x10^{-2}$ torr. This vacuum is supplied by the mechanical pump. Usually, the base pressure is 1 $x10^{-6}$ torr. Two pressure gauges were used: an HPS Series 947 Digital Convection Enhanced Pirani for high pressure (higher than $1x10^{-3}$ torr) and HPS Series 243 Digital Cold Cathode for low pressures. The maximum speed of the turbo pump is 27000 rpm. When the evaporation is being made, the pump can work in the standby mode at a reduced speed of 13000 rpm.

The substrate is placed on the substrate holder. It allows us to vary the distance from source and the angle between the substrate normal and the vertical. The thickness of the deposit and its rate are measured with a quartz monitor. Its operation will be described later.

3.1.1.1. Deposition geometry

The simplest geometry is realized for the evaporation from a point source, as shown in **Figure 3.2**. Particles evaporate from an infinitesimally small region (dA_e) of a spherical source of surface area A_e. Also, we consider an uniform mass evaporation rate Γ_e. The total evaporated mass $\overline{M_e}$, is then given by a double integral:

$$\overline{M_e} = \int_0^t \int \Gamma_e \, dA_e \, dt \qquad \textbf{3.7}$$

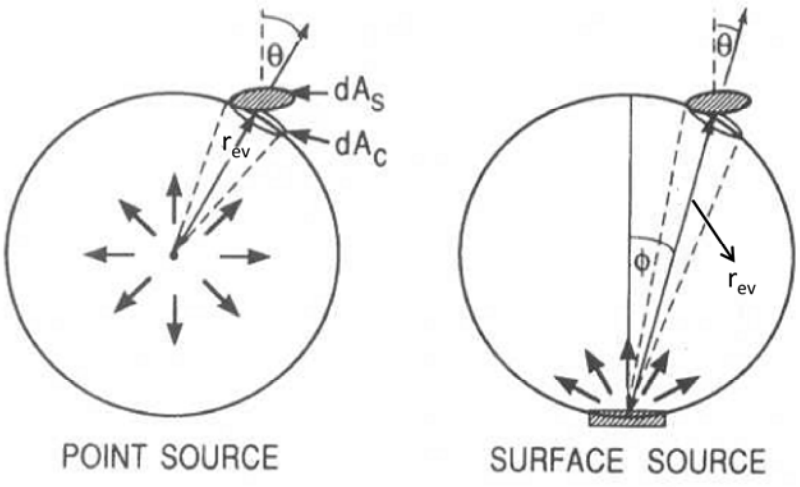


Figure 3.2: Point source and surface source. r_{ev} is the radius of the sphere centred in the point source, dA_S is the area of the substrate and dA_C is the projected area on the sphere. $\boldsymbol{\theta}$ is the angle between r_{ev} and the normal to dA_S, $\boldsymbol{\phi}$ is the evaporant emission angle between r_{ev} and the vertical direction [1].

A mass $d\overline{M_s}$ is deposited on the substrate of area dA_s. As the projected area dA_s on the surface of the sphere is dA_c, with $dA_c = dA_s\cos\theta$, the proportionality can be expressed as:

$$\frac{d\overline{M_s}}{\overline{M_e}} = \frac{dA_c}{4\pi r_{ev}^2} \qquad \textbf{3.8}$$

Finally

$$\frac{d\overline{M_s}}{dA_s} = \frac{\overline{M_e}\cos\theta}{4\pi r_{ev}^2} \qquad \textbf{3.9}$$

is obtained. θ is the angle between the radial vector from the origin and the substrate normal, r_{ev} being the radius of the sphere centred in the point source. We can observe that the deposition varies with the geometric orientation of the substrates and with the inverse square of the source-substrate distance.

The evaporation from an extended area or surface source, which is shown in **Figure 3.2**, can be modelled using the kinetic theory by **equation 3.10.** It consists in a cosine distribution law which has been verified experimentally. In this case, the deposited mass per unit area is given by: [1]

$$\frac{d\overline{M_s}}{dA_s} = \frac{\overline{M_e}\cos\phi\cos\theta}{\pi r_{ev}^2} \qquad \textbf{3.10}$$

which is dependent on two angles: the evaporant emission angle ϕ and the deposition or receiving angle θ. Also, this equation indicates that there is no emission in the $\phi = 90°$ direction. The extended source is considered, as a superposition of many points that strongly contribute to the vapour stream. In practice, boat filaments and wide crucibles containing a pool of molten which are considered as surface sources.

A $\cos^n\phi$ evaporation law is more realistic in many situations [1], where n is associated to the evaporation crucible geometry and scales directly with the ratio of the melt depth to the melt surface area. When n is large, the vapour flux is highly directional. The corresponding deposition equation for such sources is [1]:

$$\frac{d\overline{M_s}}{dA_s} = \frac{\overline{M_e}(n+1)\cos^n\phi\cos\theta}{2\pi r_{ev}^2}\ ,\ n \geq \mathbf{0} \qquad \textbf{3.11}$$

Therefore, the receiving surface area which is effectively exposed to the evaporant, become smaller (i.e. $4\pi r_{ev}^2, \pi r_{ev}^2, 2\pi r_{ev}^2/(n+1)$ for point , $\cos\theta$ and $\cos^n\theta$ respectively) as the source transforms into a more directional one.

Keeping thin film thickness uniformity is always wanted. Now, we consider the evaporation from point and surface sources on flat substrates. The film thickness d is given by $\frac{d\overline{M_s}}{dA_s}/\rho$ where ρ is the density of the deposit. For the point source [1]:

$$d = \frac{\overline{M_e}\cos\theta}{4\pi\rho r_{ev}^3} = \frac{\overline{M_e}h_{ev}}{4\pi\rho r_{ev}^3} = \frac{\overline{M_e}h_{ev}}{4\pi\rho\left(h_{ev}{}^2+l^2\right)^{3/2}} \quad \textbf{3.12}$$

We consider $r_{ev} = (h_{ev}^2 + l^2)^{1/2}$ as shown in **Figure 3.3**. The thickest deposit d_0 occurs at $l = 0$ in this case $d_0 = \overline{M_e}/(4\pi\rho h_{ev}^2)$ and thus

$$\frac{d}{d_0} = \frac{1}{\left\{1+\left(\frac{l}{h_{ev}}\right)^2\right\}^{3/2}} \quad \textbf{3.13}$$

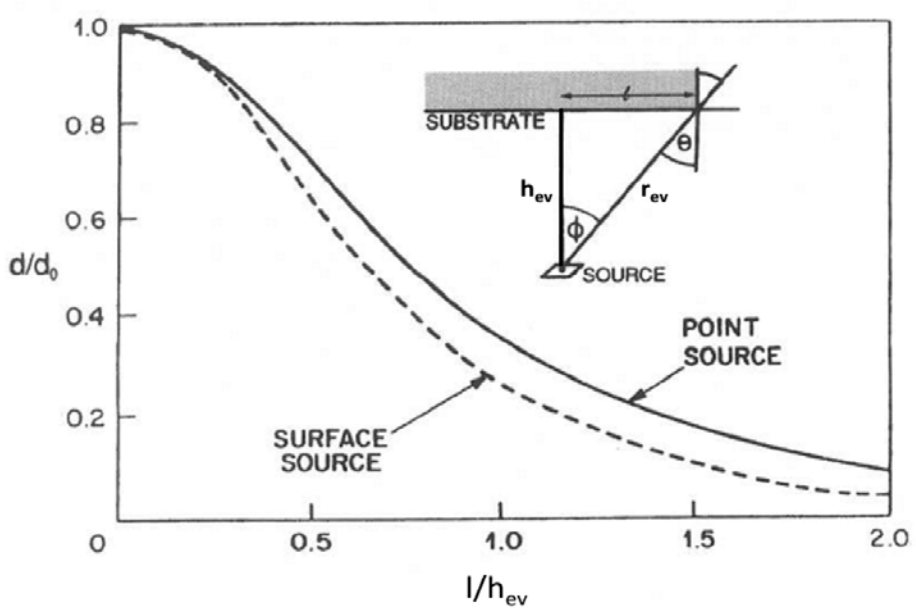


Figure 3.3: Film thickness uniformity for point and surface sources [1]. d is the thickness of the film and d_0 is the thickest one. $\boldsymbol{h_{ev}}$, l, r_{ev}, $\boldsymbol{\theta}$ and $\boldsymbol{\phi}$ are the quantities indicated in the inset of this figure.

Similarly, for the surface source:

$$d = \frac{\overline{M_e}\cos\theta\cos\phi}{\pi\rho r_{ev}^2} = \frac{\overline{M_e}}{\pi\rho r_{ev}^2}\frac{h_{ev}}{r_{ev}}\frac{h_{ev}}{r_{ev}} = \frac{\overline{M_e}h_{ev}^2}{\pi\rho\left(h_{ev}^2+l^2\right)^2} \quad \textbf{3.14}$$

since $\cos\theta = \cos\phi = h_{ev}/r_{ev}$

When normalized to the thickest dimension or $d_0 = \frac{\overline{M_e}}{\pi\rho h_{ev}^2}$

$$\frac{d}{d_0} = \frac{1}{\left\{1+\left(\frac{l}{h_{ev}^2}\right)^2\right\}^2} \quad \textbf{3.15}$$

Inspecting **equation 3.15**, when h_{ev} is constant and l increases, $\frac{d}{d_0}$ decreases. Whereas if l is constant and h_{ev} increases, $\frac{d}{d_0}$ increases. Thus, to obtain a better thickness uniformity of a sample with length l, the substrate holder has to be arranged as far as possible from the source**.**

3.1.1.2. Evaporation sources and materials.

The material to evaporate is placed in the evaporation source which is suspended and connected between the copper electrodes. These electrodes provide the high current generated by the power supply. The source heats and evaporates the material by the Joule effect and it must not contaminate, react or alloy with it. Also, it should not release gases such as oxygen, nitrogen or hydrogen at the evaporation temperature. Evaporation sources can be divided into the following important categories: tungsten wire sources, refractory metal sheet sources, sublimation furnaces and crucibles sources. An image of different types of evaporation sources is shown in **Figure 3.4.**

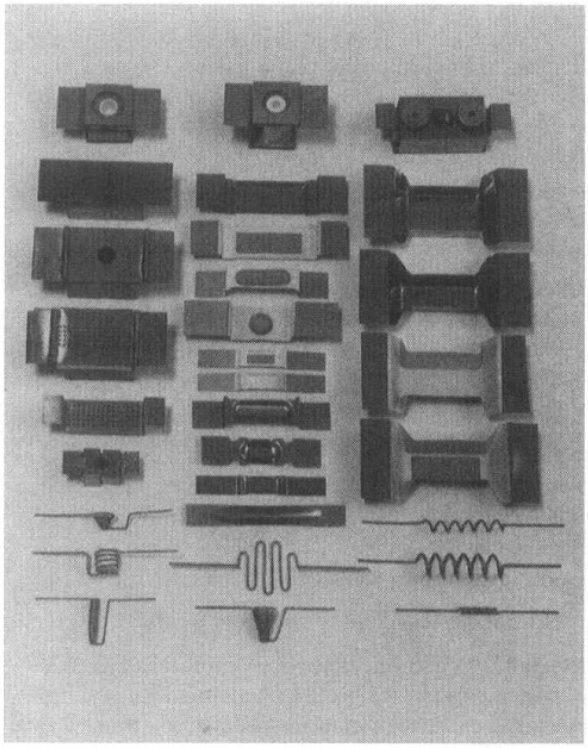


Figure 3.4: Images of different types of evaporation sources [1].

The first are in the form of individual or multiple wires twisted into helical or conical shapes. They are used for metals that wet tungsten readily. For example, a metal evaporation wire is enclosed or suspended by the tungsten wires and the molten drops of metal are retained by surface tension forces. Tungsten filaments can be operated up to about 2000 K before they begin to fail rapidly.

The second type are tungsten, tantalum, and molybdenum sheet metal sources, they are also resistance heaters that require high current power supplies. A great variety of shapes can be found including dimpled strip, boat, canoe and deep folded configurations. Deep folded boat sources have been used to evaporate powder mixtures of metals and metal oxides for coating ophthalmic lenses [1].

In this work, two evaporation sources were used. The first one was a basket heater: refractory metal (tungsten) wires are shaped into an inverted conical basket. Larger pieces of material can be inserted into the cone. It was used to evaporate Kurt Lesker aluminium (Al) wires and pellets, because this metal wet tungsten and the molten beads of metal are retained by surface tension forces. The chemical purity of the wires was 99.999% and the chemical purity of the pellets was 99.99%. The second one was a source with a boat shape. It is made with a sheet of thin, flat tungsten or molybdenum. It was used to evaporate Ted Pella 99.99% silver pieces because it does not wet tungsten as well as Al.

3.1.1.3. Monitoring rate and thickness: quartz crystal monitor

The rate and the thickness were controlled using an Inficon STM 2 USB Thin film rate/Thickness Monitor. Ten measurements are taken per second while achieving a resolution of 0.037 Å per measurement. The measurement frequency range was from 5.0 Hz to 6.0 Hz. The front load single sensor connected to it, allows an insertion of the quartz crystal. To obtain thermal stability, the head is refrigerated with water. When the substrate holder is moved up and down, we have to move the head to measure adequately. Thus, the length of the water tubes, inside the bell jar, is adjustable with compression fittings. Quartz crystals with an intrinsic frequency of 6 MHz and gold electrodes were used. The principle of the QCM is that a frequency shift will be introduced when evaporated materials are deposited on the crystal. It follows [2]:

$$dm = -c\left(\frac{1}{f_0^2}\right)df \qquad \textbf{3.16}$$

where dm is the mass of the deposited materials.

f_0 =intrinsic frequency of the quartz crystal

df = frequency variation

$c = N_q \rho A$

N_q = intrinsic constant of the quartz crystal

ρ_{quartz} = density of the quartz crystal

A = area of the quartz crystal in cm^2

If f_0 is big enough, the mass of deposited material (dm) has a linear relationship with the frequency shift (df). Crystals with f_0 of several megahertz are usually selected. It can also be seen from **equation 3.16** that when the quartz crystal frequency is higher, the

measurement is more sensitive. But if f_0 is too high, thin quartz crystal pieces will break easily. The sensitivity and accuracy will increase if the frequency stability is increased. It is mostly determined by the circuit stability and ambient temperature variations. For this reason, the crystal is maintained at constant temperature.

Using **equation 3.11**, I begun to calibrate the quartz monitor. A certain curvature was given to water tubes, placing the head of the monitor very near of the substrate holder. Also, with this curvature, the head was arranged such as $\phi \approx 0$ and $\theta \approx 0$. If it happens, $\overline{M_s}$ is proportional to r_{ev}^2. For this reason, the vertical distance h_{ev} between source and substrate holder was varied. The length of water tubes inside the bell jar was also changed to stay always very near of substrate holder. In **Figure 3.5**, plot of thickness measured by quartz monitor vs $\frac{1}{r_{ev}^2}$ is presented. A linear fit was made, and its correlation coefficient was 0.99658, which shows a strong linear relation between thickness and $\frac{1}{r_{ev}^2}$. Thus, the head is oriented, such the angle ϕ and θ have no influence.

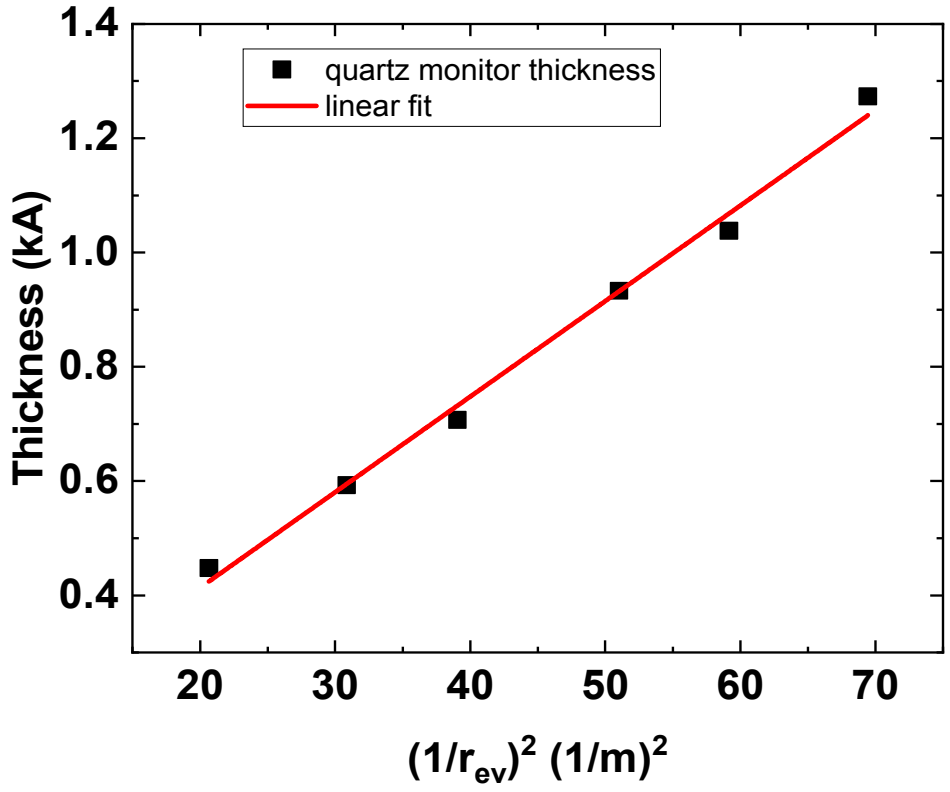


Figure 3.5: Plot of thickness measured by the quartz monitor vs $\frac{1}{r_{ev}^2}$. In this case r_{ev} coincides with the vertical distance between the source and the substrate (l=0). The film thickness d is given by $\frac{d\overline{M_s}}{dA_s}/\rho$ where $\frac{d\overline{M_s}}{dA_s}$ is the mass deposited per unit area and ρ is the density of the deposit.

3.1.2. ZnO Nanowires

The ZnO nanowires were prepared by electrodeposition in our Lab. The process is described in detail in some published papers of our Group [3], [4], [5].

3.2. Characterizations

3.2.1. X ray diffraction (XRD)

X-ray diffraction (XRD) measurements were made in the Bragg-Brentano $\theta - 2\theta$ (or specular) geometry configuration as shown in **Figure 3.6.** Standard $\theta - 2\theta$ scans were performed on a Philips PW1840 diffractometer (30 kV, 40 mA, Cu Kα radiation with λ = 1.5406 Å, Ni filter and variable slit).

In this configuration, the X ray tube is fixed, while the sample and the detection system are mobile. To make measurements in this geometry, the sample and the detection system rotate at rates of θ/min and 2θ/min respectively, both with respect to an axis contained in the sample plane and perpendicular to the incident and the diffracted beams. It allows to change the incident angle θ and to measure the intensity at an angle 2θ with respect to the direction of the incident beam.

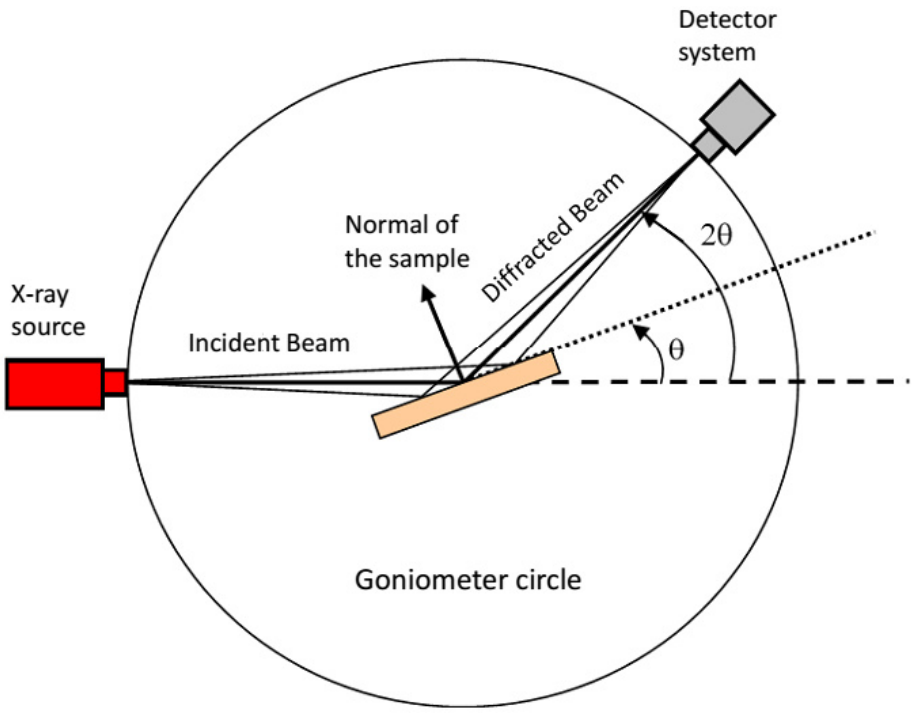


Figure 3.6: Schematic diagram of the Bragg-Brentano $\boldsymbol{\theta - 2\theta}$ geometry configuration.

Now, consider a plane wave with wave vector $\overrightarrow{k_\iota}$, which is incident on an infinite crystalline material. The diffracted wave vector is $\overrightarrow{k_d}$ (with $\left|\overrightarrow{k_d}\right| = \left|\overrightarrow{k_\iota}\right|$) and d_{planes} is the distance between consecutive unit cells (atomic planes for monoatomic crystal) parallel to the surface, as shown in **Figure 3.7**.

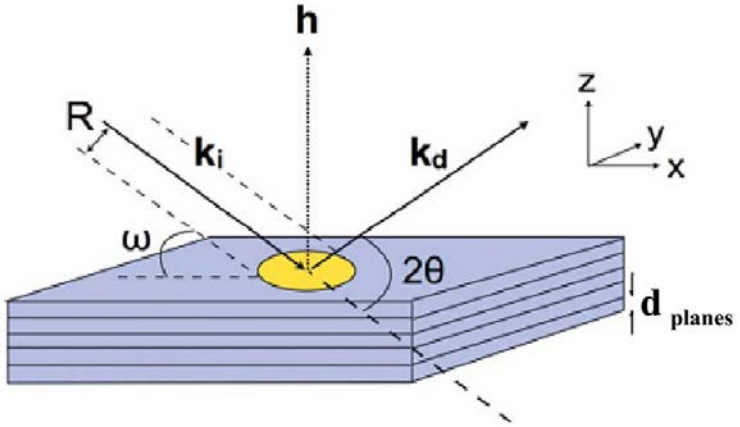


Figure 3.7: Geometry for $\boldsymbol{\theta - 2\theta}$ scan of a thin film For simetric reflections $\boldsymbol{\omega = \theta}$, the reciprocal lattice vector $\vec{\boldsymbol{h}} = \overrightarrow{\boldsymbol{k_d}} - \overrightarrow{\boldsymbol{k_\iota}}$ h is parallel to the normal direction [6].

The path difference between rays scattered by two consecutive planes is $2d_{planes}\sin(\theta)$. The constructive interference occurs when the path difference is an integer number of wavelengths λ, generating a sharp maximum of the intensity. This condition is known as the Bragg's law:

$$2d_{planes}\sin(\theta) = n\lambda \qquad \textbf{3.17}$$

In this derivation, a perfect infinite crystal and an incident beam composed of perfectly parallel and monochromatic radiation were considered. These are ideal conditions, so effects of the departure from them, have to be considered in the diffraction. A very important one is that the width of the diffraction curve increases as the thickness of the crystal decreases [7], as depicted in **Figure 3.8.**

The Scherrer formula relates the peak width B with crystallite size D_C in the direction normal to the surface sample [6,7]:

$$D_c = \frac{c\lambda}{B\cos\theta_B} \qquad \textbf{3.18}$$

The constant c depends on the geometry but is quite close to unity. The intrinsic peak width is obtained by correcting the measured peak width B_M by the instrumental one B_S. If the diffraction peak has a Gaussian shape, B is obtained using equation 3.19 [7]:

$$B^2 = B_M^2 - B_S^2 \qquad \textbf{3.19}$$

B_M is the FWHM (full width at half maximum) of the diffraction peak for the sample, while B_S is the same for a silicon standard, which is 0.14°. Equation 3.18 will be used to extract the crystallite size from the peaks widths in our samples.

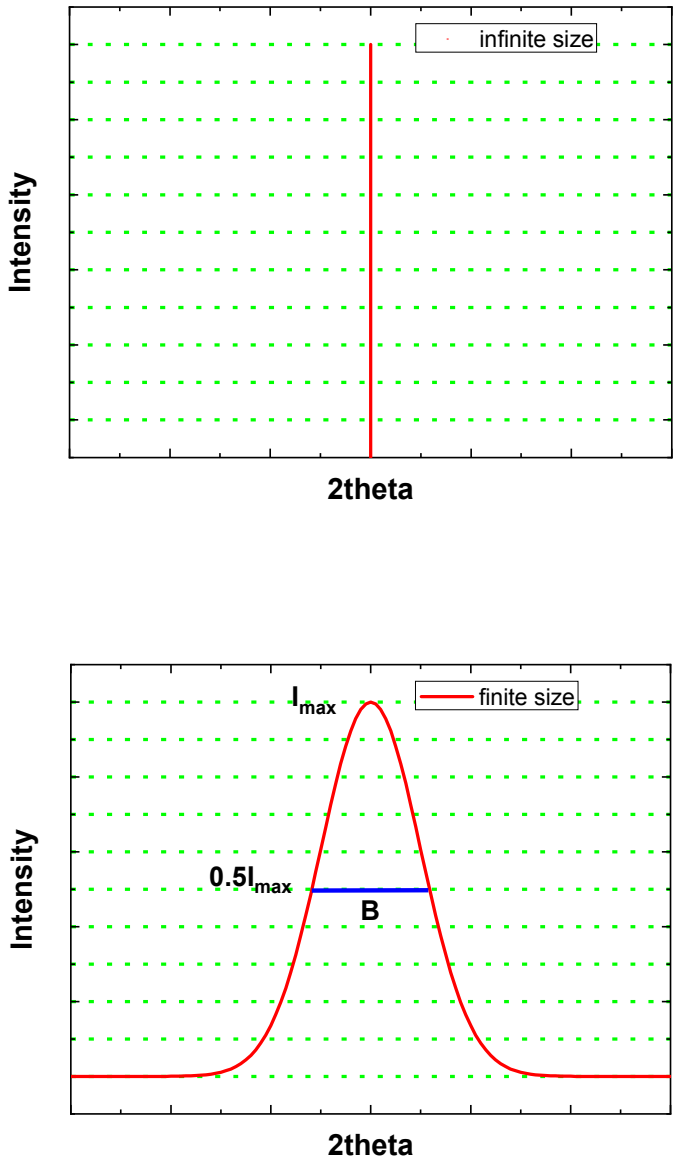


Figure 3.8: Effect of the crystallite size on diffraction curve [7].

3.2.1.1. Strain and Stress

When a polycrystalline piece of metal is practically deformed, grains change their shape, becoming flattened and elongated. The change in shape of any grain is determined, not only by the forces applied to the piece as a whole, but also by the fact that each grain retains contact on its boundary surfaces with all its neighbours. As a result, a plastically deformed grain, in a solid aggregate, usually has regions of its lattice in an elastic bent or twisted condition. More rarely, it is in a state of uniform tension or compression.

A metal can contain residual stress. Stresses of this kind are also called micro-stresses since they vary from one grain to another, or from one part of a grain to another part, on a microscopic scale. On the other hand, the stress may be quite uniform over large distances and it is referred to as macro-stress.

Figure 3.9 presents a schematic illustration of a lattice with and without strain. The effect of it, both uniform and non-uniform, in the x ray diffraction is shown in **Figure 3.10**.

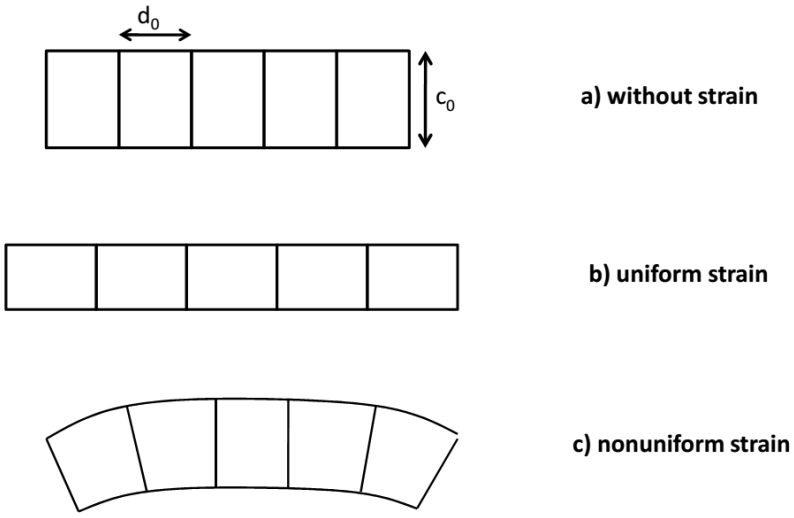


Figure 3.9: Schematics of Lattice without strain and with uniform and nonuniform strain.

A portion of unstrained grains appears in **Figure 3.9 a** and the planes have their equilibrium in-plane spacing d_0 and the out of plane spacing c_0 everywhere. If the film suffers an uniform in-plane tensile strain as shown in **Figure 3.9 b**, their in plane spacing becomes larger than d_0, and the out of plane smaller than c_0. The corresponding diffraction line, in Bragg-Brentano geometry, shifts to higher angles as shown in **Figure 3.10** [7].

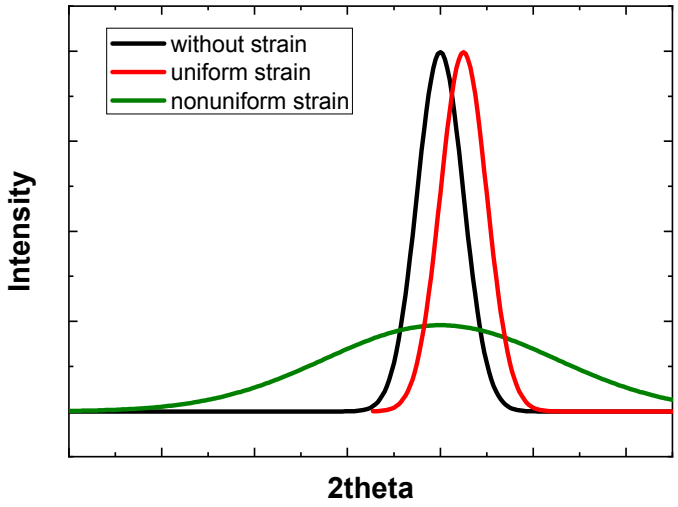


Figure 3.10: Effect of strain on line width and position

In **Figure 3.9 c**, the film is bent, and the strain is not uniform. On the top side, the planar spacing variations are opposite to the bottom side ones. Somewhere in the middle, the lattice is unchanged respect to the relaxed one. These regions contributes with various different diffraction lines. Their sum, each slightly displaced from the other, generates a broadened diffraction line centred at the original position, as shown in **Figure 3.10**.

Differentiating the Bragg law, we obtain:

$$\Delta d_{planes} = -\frac{n\lambda\cos(\theta)\Delta\theta}{\sin^2(\theta)} \qquad \textbf{3.20}$$

and the strain is:

$$\epsilon = \frac{\Delta d_{planes}}{d_{planes}} = -\frac{\Delta\theta}{\mathrm{tg}(\theta)} \qquad \textbf{3.21}$$

Assuming in-plane stress condition in the film ($\sigma_z = 0$) and an equi biaxial stress state in the plane ($\sigma_x = \sigma_y$), the in-plane strain can be calculated as a function of the measured out-of-plane strain as follows:

$$\epsilon_x = -\frac{(1-\nu_P)}{2\nu_P}\epsilon_z \qquad \textbf{3.22}$$

where ν_P is the Poisson ratio and ϵ_z is the out of plane strain calculated using XRD peak shift and the Bragg's law.

The in plane stress can be calculated as follows:

$$\sigma_x = M_{hkl}\epsilon_x \quad \textbf{3.23}$$

where M_{hkl} is the biaxial modulus for a given crystallographic orientation [8].

3.2.2. Chemical surface analysis: X ray photoelectron spectroscopy (XPS)

XPS is a technique for a quantitative analysis of surface composition. All elements with the exception of hydrogen and helium can be identified by the detection of their binding energies. Since it has a very high resolution in energy, it is a good technique to identify elements, their chemical state, and discriminate between oxidation states.

Photoelectron spectroscopy is a general term that refers to all those techniques based on application of the photoelectric effect. When light is incident on a sample, an electron can absorb a photon and escape from the material with a maximum kinetic energy:

$$E_k = h\nu - E_B - e\Phi \quad \textbf{3.24}$$

where ν is the photon frequency, E_B electron binding energy and Φ work function, which gives the minimum energy required to remove a delocalized electron from the surface of metal.

XPS being a "photon in, electron out" technique, photo-emitted electrons can undergo multiple inelastic interactions within the solid, all of which reduces drastically the number of escaping photoelectrons. The detected photoelectrons are mostly coming from the first atomic planes below the sample surface, which makes XPS a surface analysis tool.

The surface of a solid has different chemical composition and physical properties from the interior of the solid. An intense beam of ultraviolet or X ray light ionizes molecules or atoms. **Figure 3.11** shows schematically how the energy level diagram and the energy distribution of photo-emitted electrons related each other. The solid sample has core levels and a valence band. In the case of a metal, the Fermi energy E_F is at the top of the valence band and has a separation ϕ from the vacuum level E_{vac}. If photoabsorption takes place in a core level with binding energy E_B .($E_B = 0$ at E_F), the photoelectrons can be detected with kinetic energy $E_k = \hbar\omega - \phi - |E_B|$ in the vacuum. If the energy distribution of the emitted electrons is plotted (see **Figure 3.11)**, their number per energy interval often gives a replica of the electron energy distribution in the solid. It is able to provide us information on the electron energy distribution in a material. In actual data accumulation, the reference point for molecules and atoms is taken to be E_{vac}, while in solid E_F is taken as natural zero. However, in general, the abscissa of the plots is E_B instead E_k.

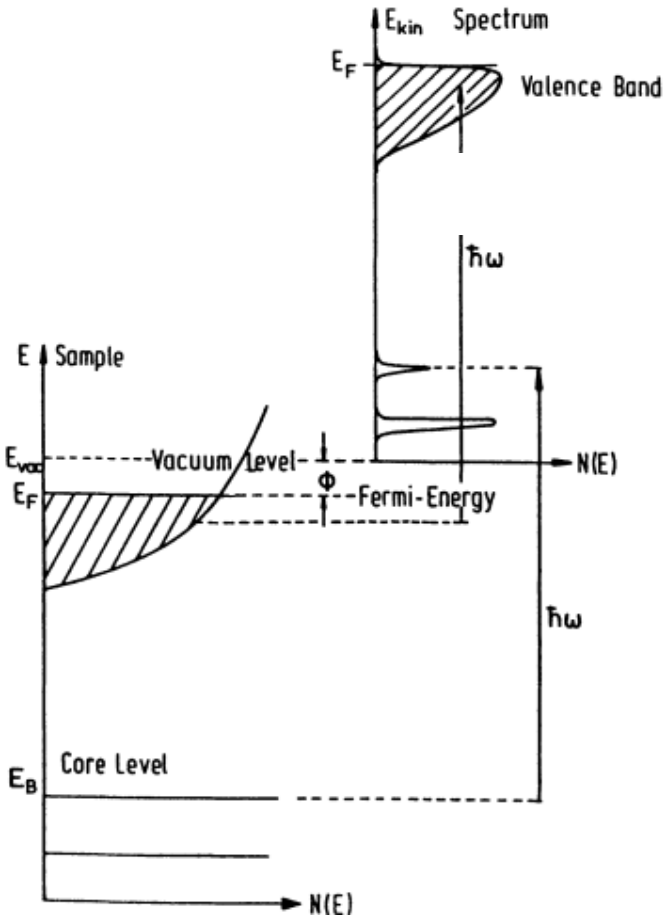


Figure 3.11: Relation between the energy levels in a solid and the electron distribution produced by photons of energy $\hbar\omega$. The natural abcissa for the photoelectrons is the kinetic energy with its zero at the vacuum level of the sample ($E_k = \hbar\omega - |E_B| - \phi$). Experimenters generally prefer to use E_B as the abcissa. E_B is so called binding energy of electrons, which in solids is generally referred to the Fermi level and in free atoms or molecules to the vacuum level [9].

Each element produces a characteristic set of XPS peaks at characteristic binding energy values that directly identify each one. These peaks correspond to the electron configuration of the electrons within atoms: 1s, 2s, 2p, 3s, etc. In each orbital, electrons have a characteristic binding energy E_B, the minimum energy needed to eject them to infinity. **Figure 3.12** shows a spectrum taken with $\hbar\omega = 1487\ eV$ (Al Ka) from a surface of polycrystalline gold. The Au 5d valence band is clearly seen near E_F and at larger binding energies the 5p and 4f core levels are visible.

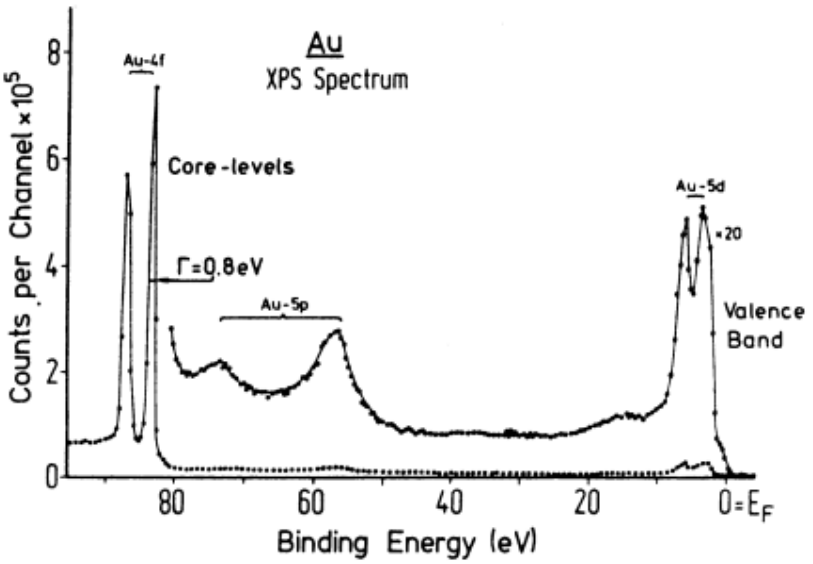


Figure 3.12: XPS spectrum ($\hbar\omega = 1487\ eV$) of polycrystalline Au for $0 \leq E_B \leq 100eV$ [9].

3.2.3. Scanning Electron Microscopy (SEM)

The basic principle of SEM is that a finely focused beam of electrons is moved or scanned from point-to-point on the specimen surface. Different types of electron guns can be used: thermionic electron guns, Schottky electron guns and field emission guns (FEG). The last, compared with thermionic one, provides an extremely focused electron beam and it can work with low (1 keV) as well as high energy. These characteristics generate an improvement of the spatial resolution and the minimization the charging effect in non conductive samples. If the electrons remain on the sample, they will repel electrons from the incoming beam. This effect usually looks like blurring. A schematic diagram of energy barriers for different guns is shown in **Figure 3.13**.

In thermionic emission, electrons from the Fermi level E_F of the cathode material overcame the work function ϕ_w by thermionic excitation. The maximum gun brightness is proportional to the electron energy E, which hinders the use of thermionic cathodes at low energies of the order of 1 keV in low voltage SEM [10]. Thus, if we want to work in this low energy with high gun brightness we have to use Schottky or field emission cathodes.

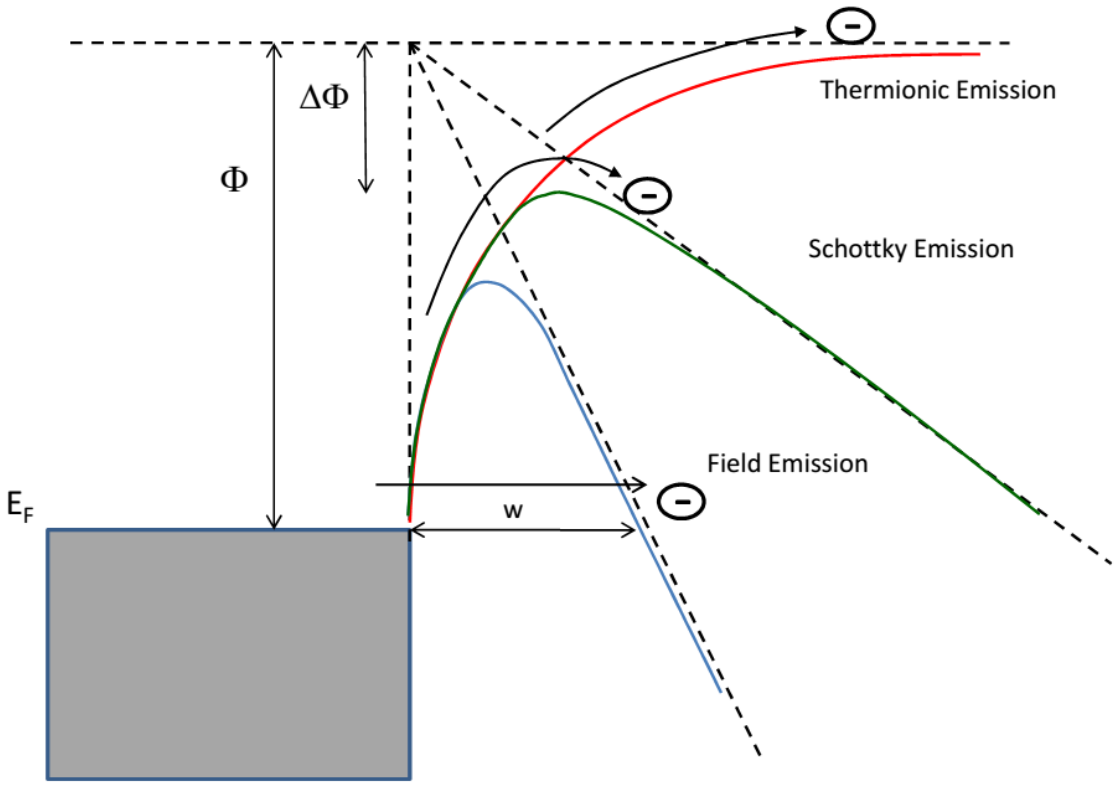


Figure 3.13: Schematic diagram of energy barriers for different guns [10].

For Schottky electron guns the field strength is not sufficient for the wave mechanical tunnelling effect. Although the potential barrier is lowered by ΔΦ, electrons have to overcome the barrier by their thermal energy.

When the field strength E at the cathode is increased, the work function [10].

$$\Phi_{eff} = \Phi - \Delta\Phi = \Phi - e\sqrt{\frac{e|E|}{4\pi\varepsilon_0}} \qquad \textbf{3.25}$$

is decreased. This decrease can be neglected in normal thermionic cathodes. When using a Schottky cathode with radius $r \leq 1\ \mu m$ at the tip, the electric field $|E| \approx \frac{U}{r}$ at the cathode is strongly increased and a field strength of the order of 106 V/m results in decrease of

$$\Delta\Phi \approx 0.4\ eV \qquad \textbf{3.26}$$

In the field emission guns, high fields decrease the width w of the potential wall, in front of the cathode to a few manometers. So electrons from the Fermi level E_F can penetrate the potential barrier by the wave mechanical tunneling effect.

The main advantages of FEG are the very substantially higher gun brightness, $\beta \approx 10^8 - 10^9\ A/cm^2$ at $E = 20\ keV$, and the smaller diameter of the virtual source of the order of 3-5 nm, so that only one de-magnifying lens is needed to get electron probe

diameters below 1 nm. The lifetime of a field emission cathode can be some years while lifetime of tungsten cathodes (40-200 h) is limited by evaporation of the cathode material, which results in a break when part of the wire become too thin [10].

3.2.4. Energy Dispersion X Ray Analysis (EDX)

EDX is an analytical technique used to identify the elemental composition of surfaces. When EDX systems are attached to Scanning Electron Microscopy (SEM) or Transmission Electron Microscopy (TEM), they provide elemental analysis on areas as small as manometers in diameter. The incident beam electron can scatter with an electron of an atomic shell. It causes the ejection of the electron from the atom and the ionized atom is left with a vacancy. This energy state can be lowered through the transition of an electron from more energetic shell to fill the vacancy. This process can create X rays which carry the inter-shell transition energy. As the last one is a characteristic of each element, we can identify its presence.

The EDX technique is non-destructive and specimens of interest can be examined in situ with little or no sample preparation. It also can be qualitative, semi-quantitative, quantitative and also provide spatial distribution of elements through mapping. The last one was used in this work to analyze the distribution of Ag and Zn atoms in a ZnO nanowires (NWS) decorated with silver nanoparticles (NPs).

3.2.5. Optical characterizations

Optical properties were studied by UV-Vis transmittance and room temperature photoluminescence.

3.2.5.1. Optical UV-Vis transmittance

Optical transmittance spectra were obtained using a homemade lab setup which is shown in **Figure 3.14 a**. For transmittance measurements, the optical excitation was provided by an halogen lamp Ocean Optics (OO) HL 2000. Light travels through an optical fiber whose diameter was 600 μm to an OO 74 VIS collimating lens. The collimated light had normal incidence on the sample. The transmitted light is collected by an another optical fiber, coupled to an OO S2000 spectrometer. The diameter of the last fiber was 100 μm. A schematic diagram of the setup is shown in **Figure 3.14 b.**

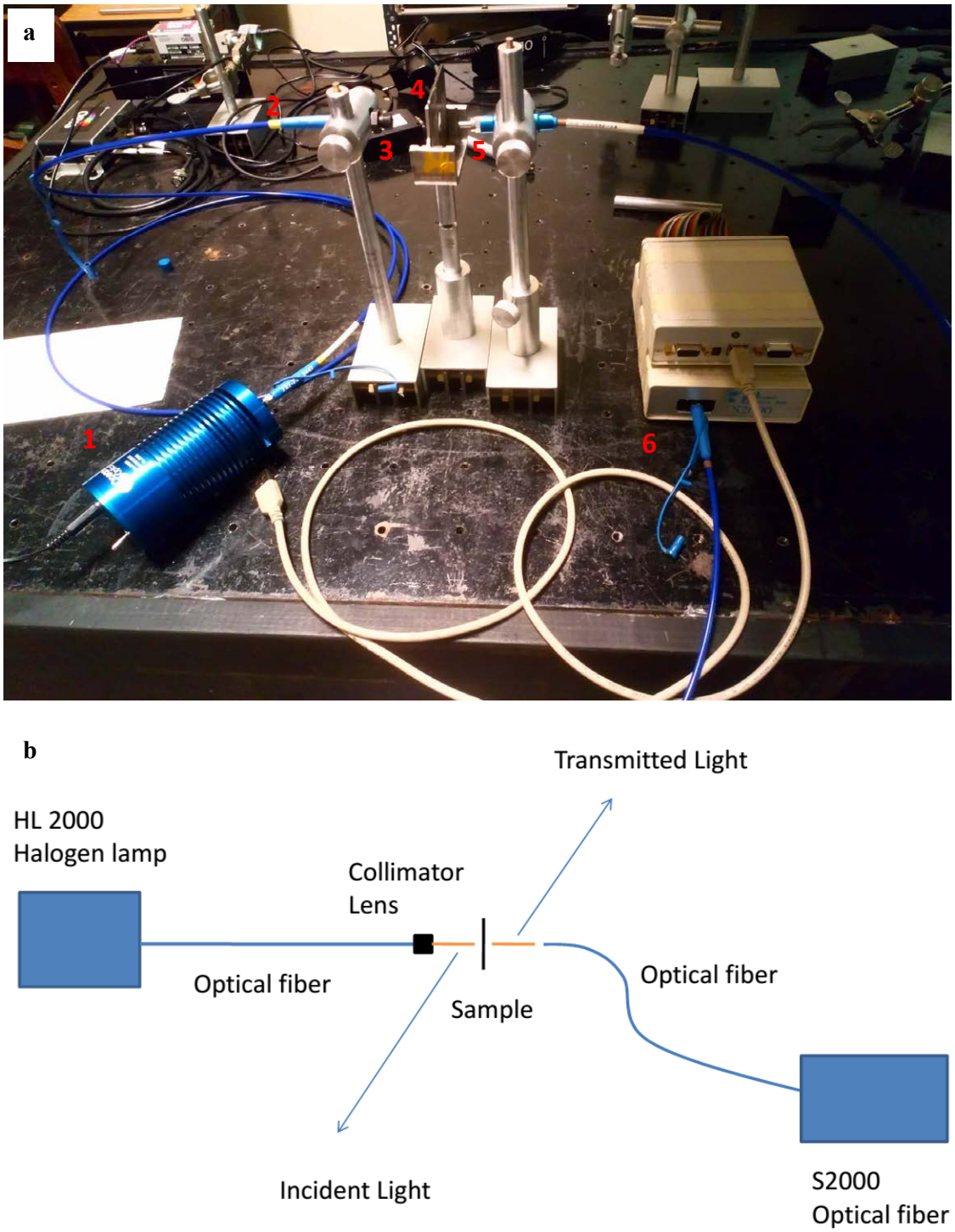


Figure 3.14: a) Image of the experimental setup to measure transmittance 1) halogen lamp Ocean Optics (OO) HL 2000, 2) 600 μm optical fiber, 3) OO 74 VIS collimating lens, 4) sample holder 5) 100 μm optical fiber, 6) OO S2000 spectrometer b) schematic diagram of the experimental setup.

Figure 3.15 present two plots: the first one is the Ocean Optics (OO) HL 2000 halogen lamp spectrum, the second is the transmittance of the glass which was used as substrate to prepare silver NPs onto them. It can be seen that the transmittance is nearly constant, in the spectral region of interest. Thus, it allows us to employ the lamp spectrum as a reference.

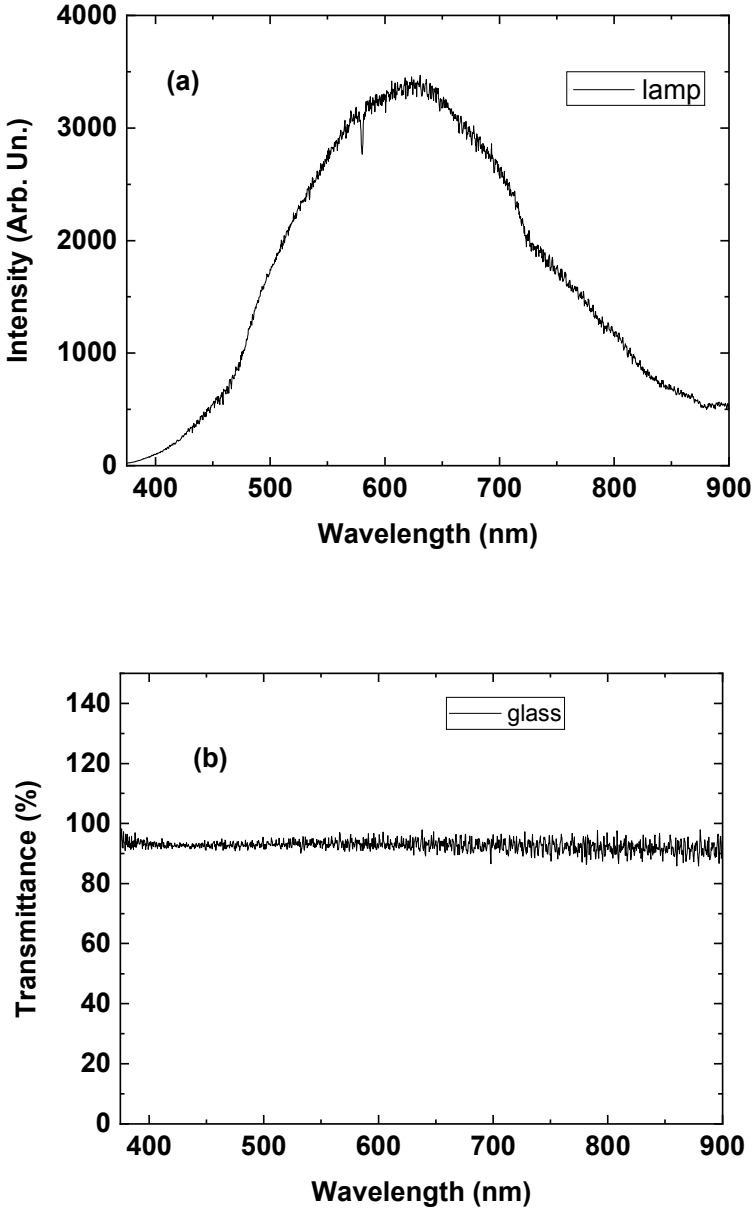


Figure 3.15: a) Ocean Optics (OO) HL 2000 b) Transmittance of glass which was used as substrate to prepare silver nanoparticles by SSD process.

3.2.5.2. Photoluminescence

Luminescent materials convert an incident energy into emissions in the ultraviolet (UV), visible and infrared regions of the spectrum. Luminescence can be stimulated by different sources. When the stimulation is generated by UV or visible light is called photoluminescence. It has been recognized as a useful tool for characterizing the quality of semiconductor materials as well as analyzing the physics behind the radiative recombination. In the case of semiconductors, they are characterized via spectroscopic techniques. Measuring the energy distribution of emitted photons, after optical excitation, we can determine properties of the material.

In semiconductors, excitation of a non-equilibrium density of electrons and holes will lead to the recombination. If it involves emission of photons, the recombination is called radiative. If it proceeds through the emissions of phonons instead of photons, is called non radiative [11]. Optical transitions provide direct access to the energy levels of the material. There are many possible radiative recombination mechanisms. One of them is the band-band recombination which is a transition across the bandgap of a free electron in the conduction band with a free hole in the valence band. As a result, this emission occurs only at energies equal or greater than the band-gap energy. The last one corresponds to recombination of "hot carriers" which have not been totally relaxed to the bottom (top) of conduction (valence) band, prior to the recombination. Other transitions are due to excitons which are free electrons and holes bound by Coulomb interaction. Free to bound transitions involve the radiative recombinations of a free carrier with a carrier bound to an impurity. They come in two varieties: donor-to-valence band and conduction band-to-acceptor [11]. Native lattice defects are also involved in the photoluminescence and they are very important in ZnO [12]. These emissions primarily occur at energies less than the band-gap.

Photoluminescence spectra were measured using the lab setup depicted in **Figure 3.16**. Mainly, it consists in two parts: laser setup (red rectangle) and sample setup (green rectangle). Views of both parts and a schematic diagram are shown in **Figures 3.17** and **3.18** respectively. The photoluminescence of the sample was collected by an optical fiber coupled to an OO S2000 spectrometer. The optical fiber was placed very near the sample, forming an angle with the normal of the sample which is bigger than 45°. Between the sample and the optical fiber, a high pass filter was arranged. The two last actions were made to diminish the peak at 375 nm from laser in the spectra. By this way, the integration time can be increased, without saturation of the spectrometer, which allows us to obtain a better signal. Another correction corresponds to the transfer function of the OO S2000 spectrometer. The measured photoluminescence spectra were divided by this function

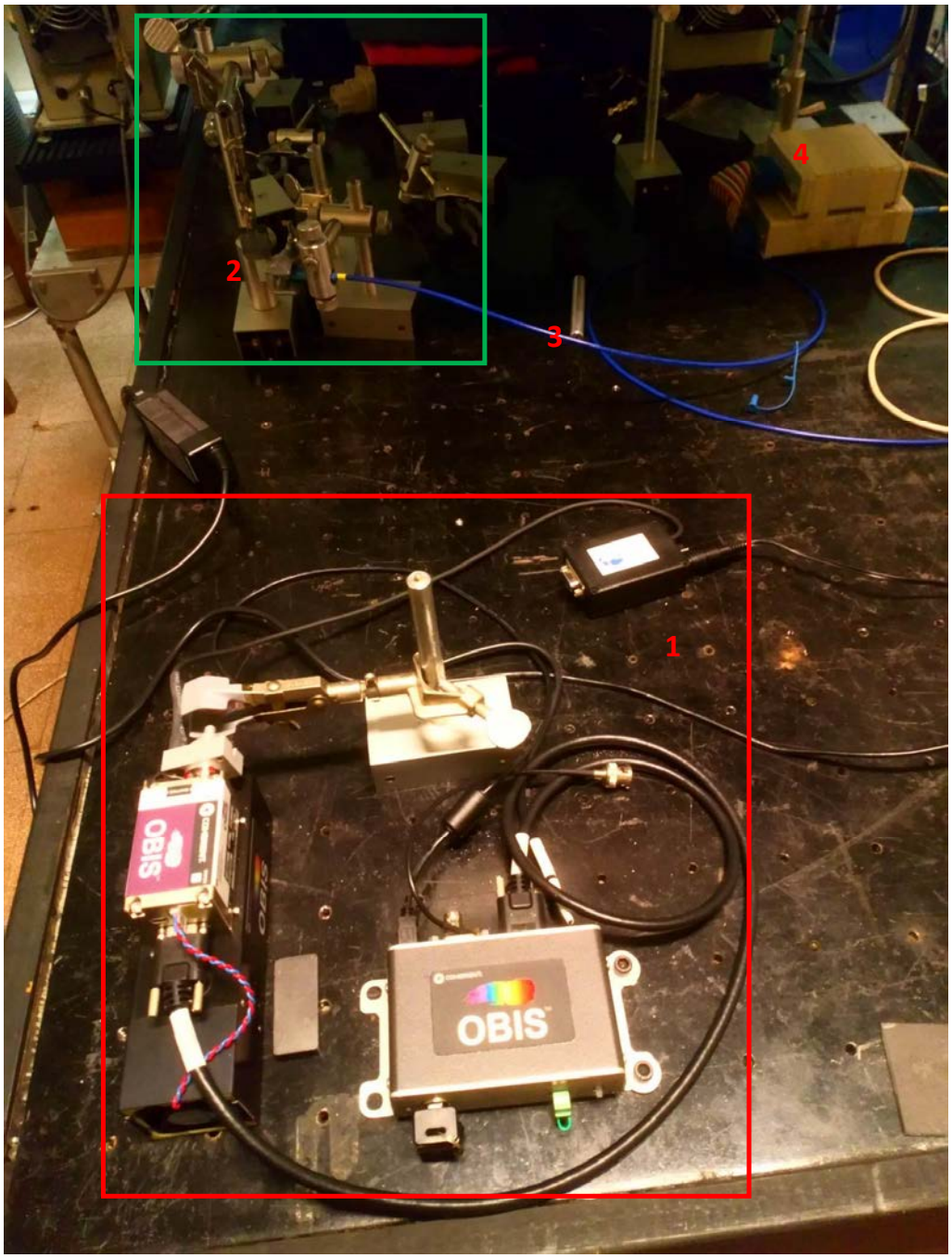


Figure 3.16: Experimental setup for photoluminescence: 1) laser setup, 2) sample setup, 3) optical fiber, 4) OO S2000 spectrometer.

.

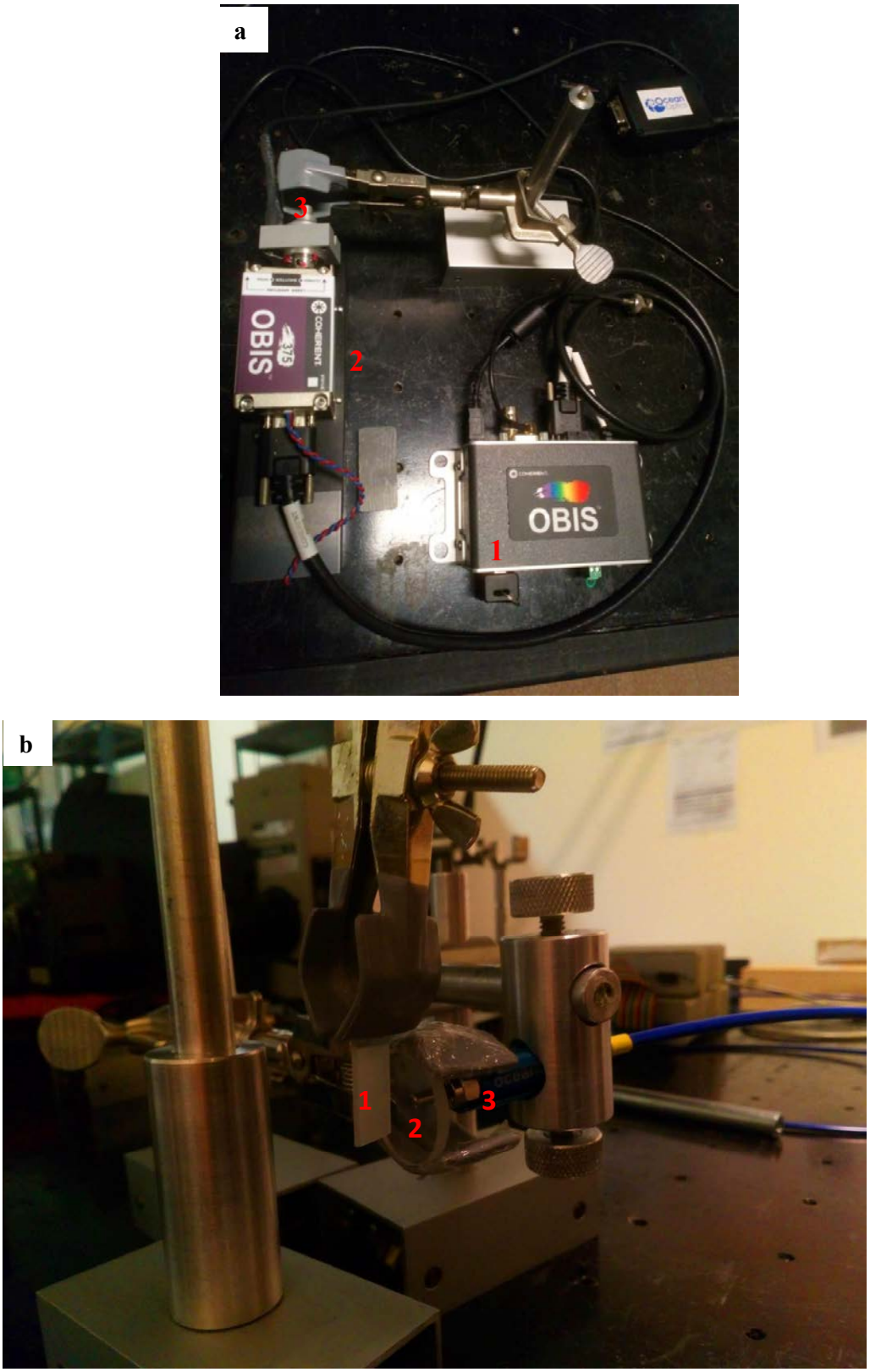


Figure 3.17: a) Laser setup: 1) Power supply, 2) Laser, 3) low pass filter (400 nm) b) Sample setup: 1) Sample 2) Long Pass Filter (UV filter) 3) Optical fiber

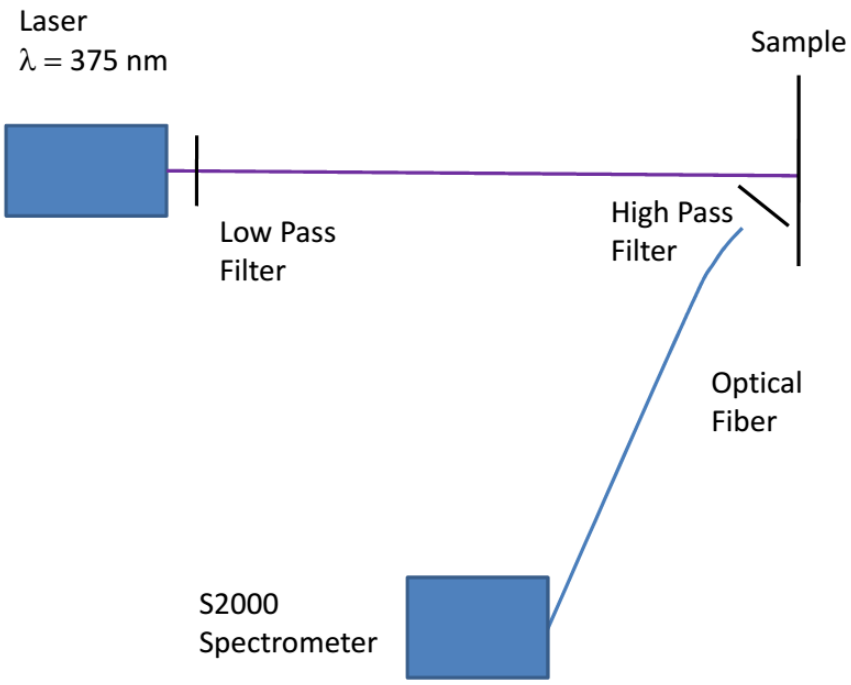


Figure 3.18: Schematic diagram of the experimental sample setup.

3.3. References

[1] Ohring, M. The Materials Science of Thin Films. Academic Press: 2002.

[2] Behrndt, K. H. and Love, R. W. Automatic Control of Film-deposition Rate with the Crystal Oscillator for Preparation of Alloy Films. *Vacuum* **1962**, 12, 1–9.

[3] Solís, D. , Martín Jiménez, F. de P. , Schrebler, R. S. , Navarrete Astorga, E. , López Escalante, M. C. , Peinado Pérez, J. J. , Ramos Barrado, J. R. , and Dalchiele, E. A. Electrochemical growth of ZnO nanorod arrays onto transparent conductive IZO:Ga substrates. *Journal of the Electrochemical Society* **2020**

[4] Campo, L. , Navarrete-Astorga, E. , Pereyra, C. J. , Cuevas, A. , Romero, R. , Ariosa, D. , Henríquez, R. , Muñoz, E. , Marotti, R. E. , Martín, F. , Ramos-Barrado, J. R. , and Dalchiele, E. A. The Effect of a Sputtered Al-Doped ZnO Seed Layer on the Morphological, Structural and Optical Properties of Electrochemically Grown ZnO Nanorod Arrays. *Journal of The Electrochemical Society* **2016**, 163, D392–D400.

[5] Castillo-Rodriguez, J. , Pereyra, C. J. , Valente, P. , Seré, A. , Marotti, R. E. , Hevia, S. A. , Dalchiele, E. A. , and Rio Quero, R. del Seed layer effect on morphological, structural, and optical properties of electrochemically grown ZnO nanowires over different SnO2:F/glass substrates. *Journal of Solid State Electrochemistry* **2020**, 24, 797–808.

[6] Ying, A. J. , Murray, C. E. , and Noyan, I. C. A rigorous comparison of X-ray diffraction thickness measurement techniques using silicon-on-insulator thin films. *Journal of Applied Crystallography* **2009**, 42, 401–410.

[7] Cullity, B. D. Elements of x-ray diffraction. Addison-Wesley Pub. Co: Reading, Mass 1978.

[8] Birnbaum, A. J. , Thompson, C. V. , Steuben, J. C. , Iliopoulos, A. P. , and Michopoulos, J. G. Oxygen-induced giant grain growth in Ag films. *Applied Physics Letters* **2017**, 111, 163107.

[9] Hüfner, S. Photoelectron spectroscopy: principles and applications. Springer: Berlin; New York 1996.

[10] Reimer, L. Scanning electron microscopy: physics of image formation and microanalysis. 2010.

[11] Gilliland, G. D. Photoluminescence spectroscopy of crystalline semiconductors. *Material Science and Engineering* **1997**, R18, 99–400.

[12] Galdámez-Martinez, A. , Santana, G. , Güell, F. , Martínez-Alanis, P. R. , and Dutt, A. Photoluminescence of ZnO Nanowires: A Review. *Nanomaterials* **2020**, 10, 857.

4 Preliminary studies

This chapter consists in a description of the preliminaries studies, which were made to understand how the vacuum evaporator works. Moreover, they were useful for the practice of methods and techniques. We use aluminum as the material to evaporate. The reason of this choice was that it is a relatively cheaper metal compared for example with silver.

4.1 Oblique angle deposition (OAD)

Oblique angle deposition refers to a configuration in which the material flux arrives at the surface of substrate at oblique angle. In this geometry, the main factor that controls the nano-structural evolution of the films is the shadowing effect [2] [3] [4] as shown in **Figure 4.1**. A random growth fluctuation on the substrate produces small islands of deposited materials and shadowed regions behind them are formed. Under these conditions, the absence of diffusion of ad particles means that vapor particles are incorporated at the point of impact. Subsequent vapor deposition occurs preferentially on the non-shadowed regions. The incident vapor flux cannot reach these regions, creating an oriented, rod like structure with high porosity.

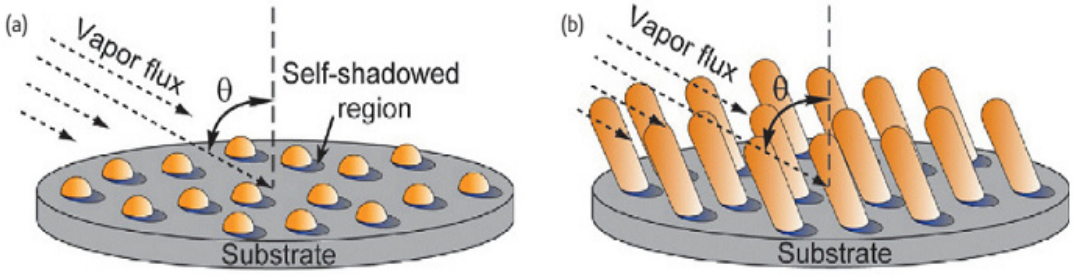


Figure 4.1: Schematic diagrams of the oblique angle deposition. a) small islands and shadowed regions behind them b) rod like structure with high porosity. $\boldsymbol{\theta}$ is the angle between the direction of the vapor flux and the normal to the substrate.

As the vapor incidence angle approaches 90°, the shadowed area increases and a more porous film is produced. In our case, an oblique evaporation of aluminum was made.

4.1.1 Oblique evaporation on an Al film substrate

First, aluminum was deposited on glass at a normal evaporation ($\theta = 0$). FE-SEM micrograph of aluminum film is shown in **Figure 4.2**. Grains are observed in it, and terraces associated with aluminum crystallographic planes are recognized.



Figure 4.2: FE-SEM micrograph of a thermal evaporated Al film at a normal condition (0°). The tilt angle of the micrographs are a) 0° and b) 52°. The white scale bars are 500 nm.

XRD diffractogram of the film of Al which was deposited on glass at a normal evaporation ($\theta = 0$) is shown in **Figure 4.3**. The film is very textured because only (111) and (222) peaks are observed.

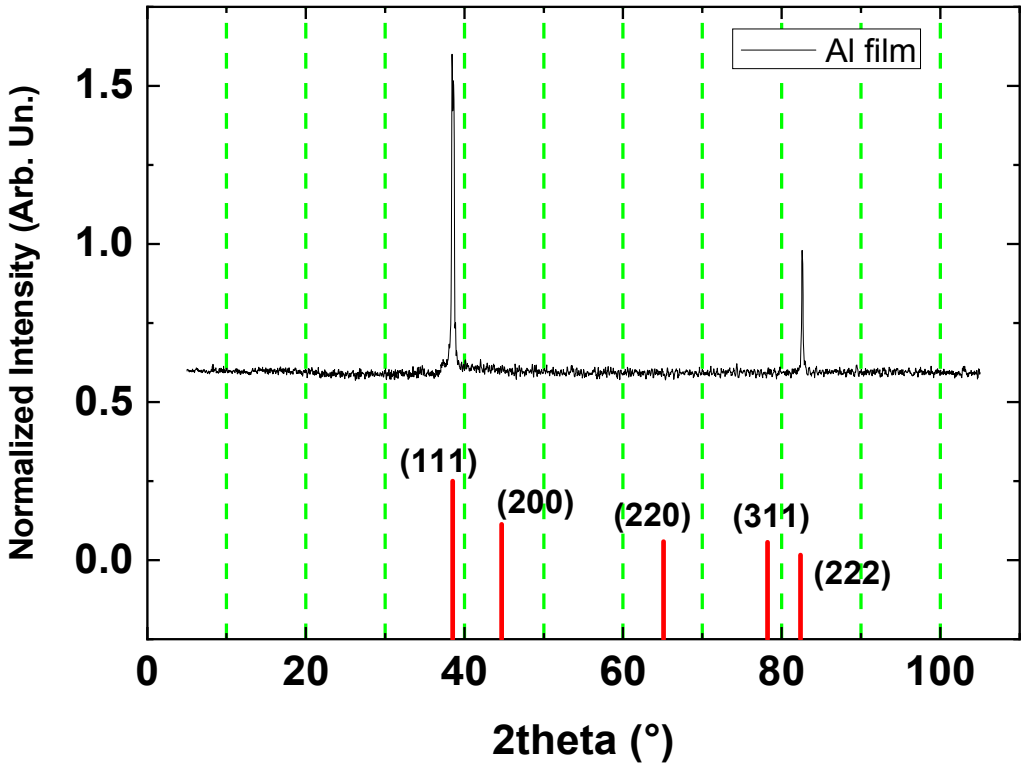


Figure 4.3: X-ray diffractogram of Al thin film obtained under normal evaporation (θ=0). JCPDS pattern was added for comparison (red lines).

In the first evaporation, which was made at an angle of $\theta = 0$, a source with a basket shape was used. Instead, for the oblique evaporation, we used a longer basket source with larger h_d/s ratio, where s is the area and h_d the depth. As this ratio is higher, the evaporation solid angle is smaller and the vapor is more concentrated. The angle between substrate normal and vertical was varied. In this study, we analyze three angles: 65°, 75° and 85°. The FE-SEM images are presented from **Figures 4.4** to **4.8.**

At 65°, there is not oblique evaporation indicators. Nor island, neither rods are recognized in **Figure 4.4**. The topography is smoother than the Al film, because terraces are not observed. Therefore, at this angle, the initial Al film is covered with the evaporated material without shadow effect. **Figure 4.5** and **4.6** present FE-SEM micrograph of a sample prepared with an oblique deposition at 75°. At this angle, contrary to 65°, more important roughness is recognized, specifically there are very small nanoparticles. Therefore, shadow effects already exist at this angle.

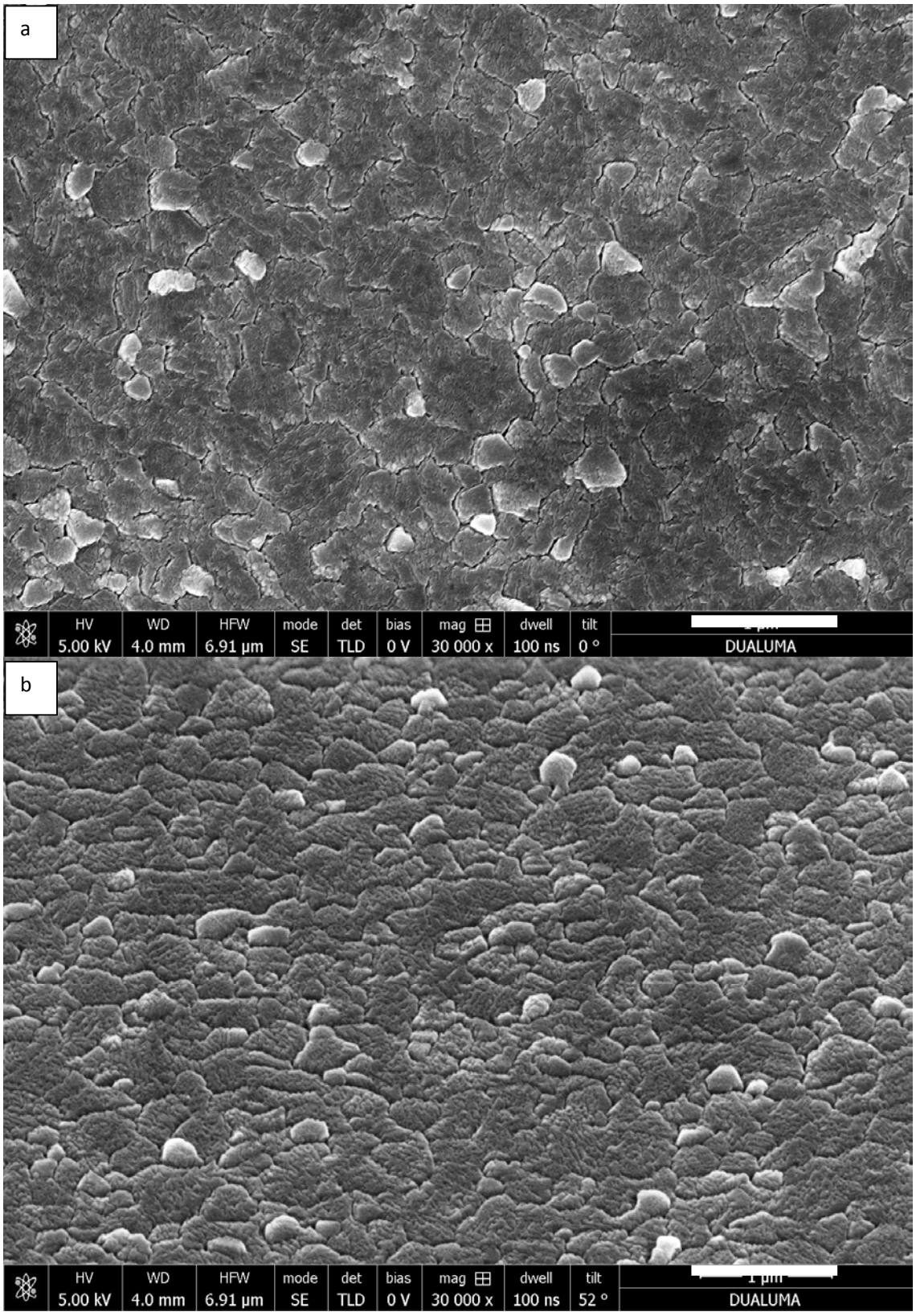


Figure 4.4: FE-SEM micrograph of an oblique angle deposited Al at an angle of 65° on Al thin film.The tilt angles of the micrographs are a) 0° b) 52°. The white scale bar is 1 µm.

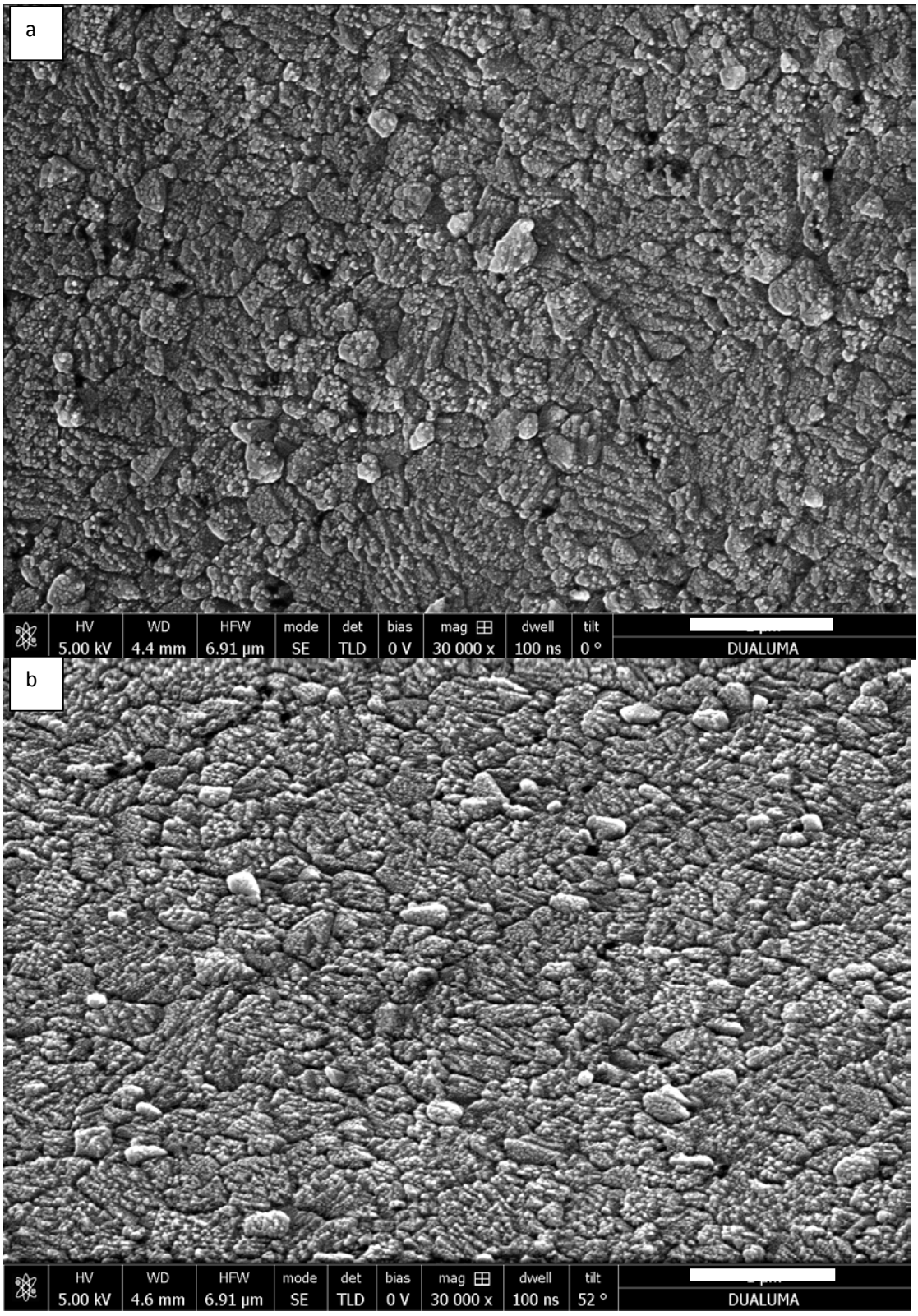


Figure 4.5: FE-SEM micrograph of an oblique angle deposited Al at an angle of 75° on Al thin film.The tilt angles of the micrographs are a) 0° b) 52° **.** The white scale bar is 1 µm.

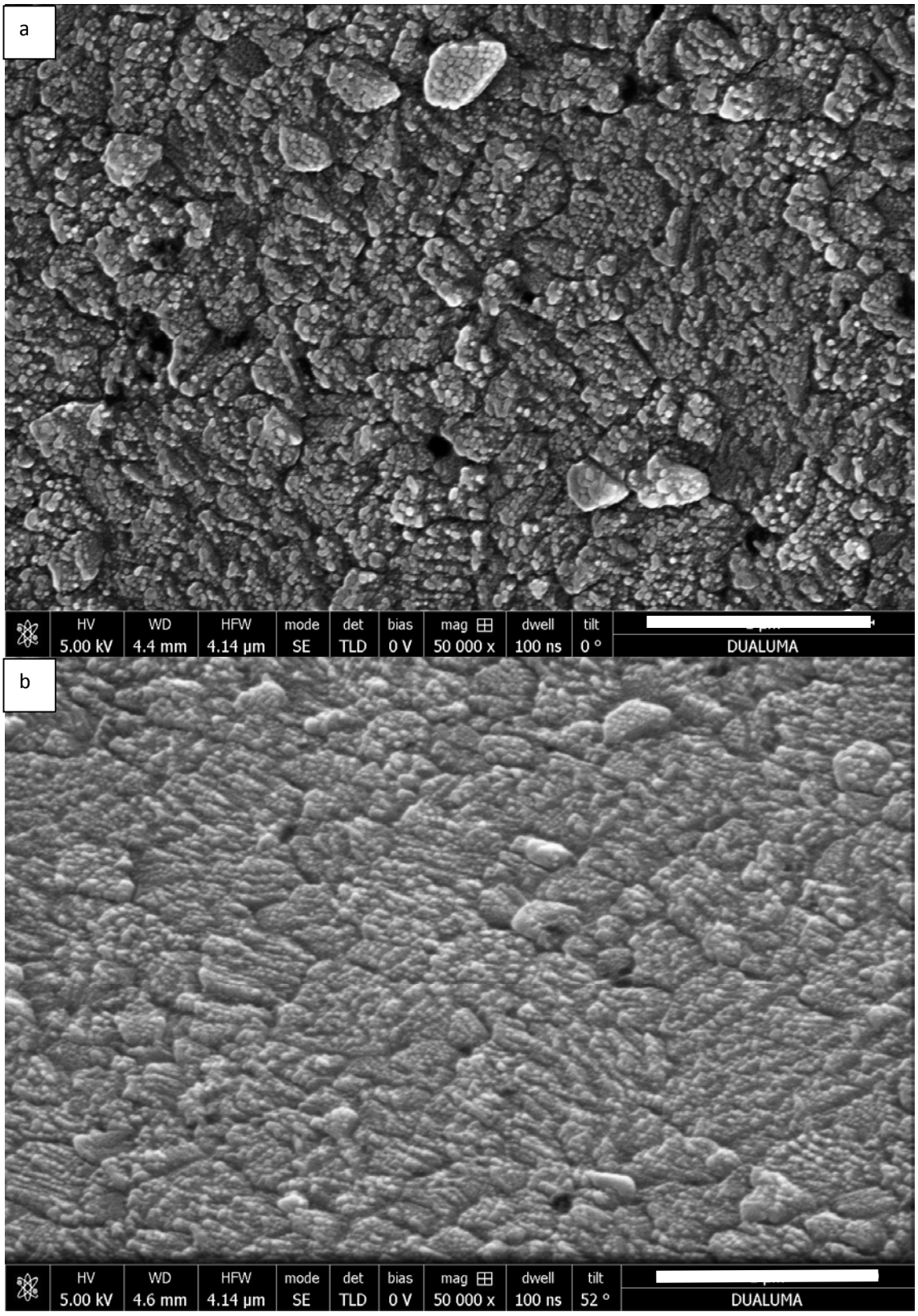


Figure 4.6: FE-SEM micrograph of an oblique angle deposited Al at an angle of 75° on Al thin film. The tilt angle of the micrographs are a) 0° b) 52°. The white scale bar is 1 µm.

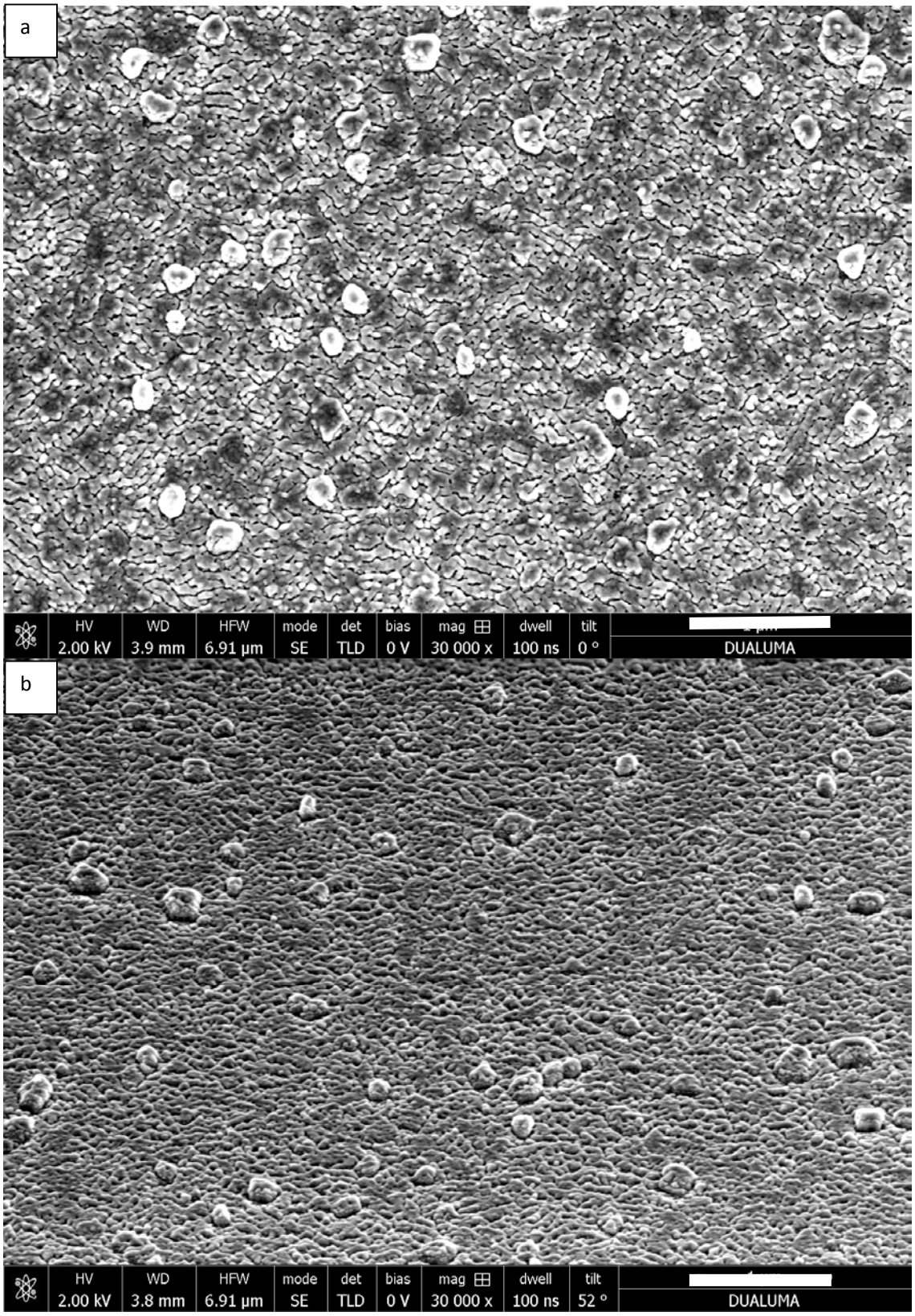


Figure 4.7: FE-SEM micrograph of an oblique angle deposited Al at an angle of 85° on Al thin film. The tilt angle of the micrographs are a) 0° b) 52°. The white scale bar is 1 µm.

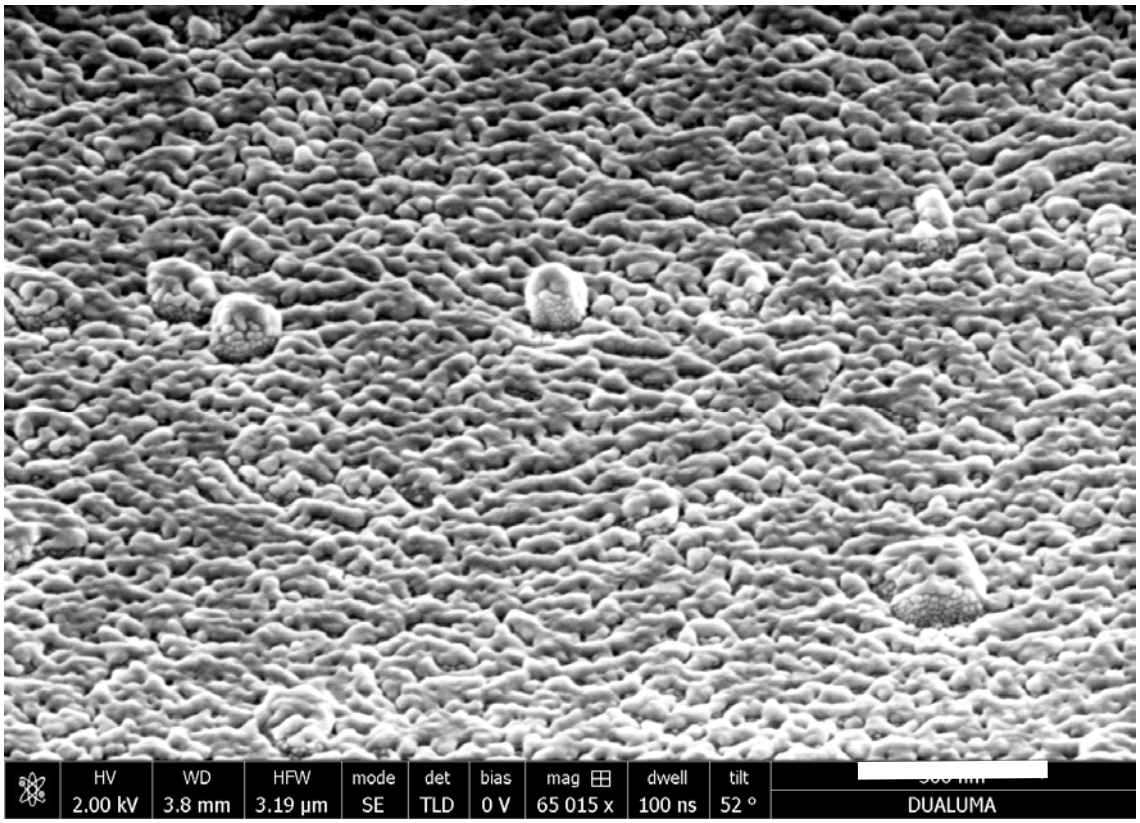


Figure 4.8: FE-SEM micrograph of an oblique angle deposited Al at an angle of 85° on Al thin film.. The white scale bar corresponds to 500 nm**.**

The FE-SEM images of **Figure 4.7** and **4.8**, which correspond to an angle of 85°, show longer structures compared with the sample prepared at an angle of 75°. Also, they are connected between them and porosity can be observed. Here, a shadow effect is clearly developed.

4.1.2 ZnO nanorods decorated with Al nanoparticles

In a second step, we deposit aluminum nanoparticles onto ZnO nanorods (NRs). As ZnO NRs are in many directions, the condition of oblique evaporation is always met**. Figure 4.9** shows FE-SEM images of ZnO nanorods. The thickness of Al measured by the quartz crystal monitor are 15 nm and 43 nm. For the first thickness, tiny nanoparticles are hardly observed in the ZnO surface. Whereas, for 43 nm, the nanoparticles are bigger and generate a more uniform coating without pores.

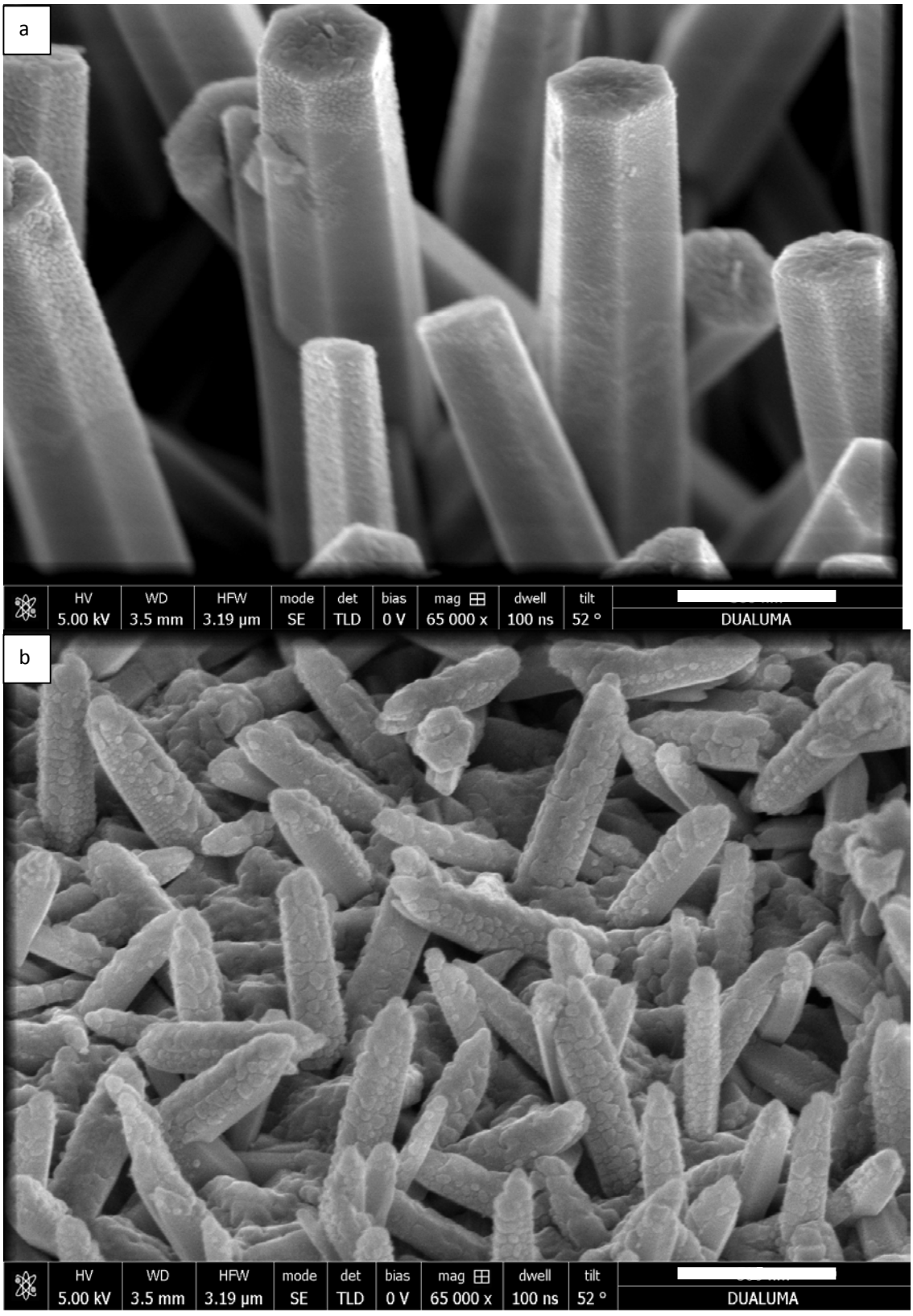


Figure 4.9: ZnO nanowires covered with a layer of Al with a thickness of a) 15 nm b) 43 nm. The white bar corresponds to 500 nm.

4.2 Conclusions

Aluminum films were obtained using the evaporation system depicted in chapter 3. X ray diffractograms show only (111) and (222) denoting a strong texture. FE-SEM micrograph show grains and their frontiers. Crystalline planes were also observed.

Oblique angle deposition was performed. First, a crystalline film was prepared. The oblique deposition was then performed on this layer . At an angle of 65°, the evaporated material only covers the substrate without forming structures. From 75°, shadow effect is observed. At this angle, the substrate surface is covered with small particles. At 85°, these structures are longer and connected between them. They constitutes a porous structure.

Using this idea, ZnO NRs were decorated with Al. As nanorods axis are in many directions, an OAD was achieving on the rod surface. The thickness of the coating, measured by the quartz crystal monitor, were 15 nm and 43 nm. In the first case, tiny NPs were obtained, while in the second case, the NPs are bigger and the NRs are better coated .

Training and adjusting the growth parameters for thermal evaporation was an important part of this thesis work. The oblique evaporation and coating of ZnO NRs were also investigated. The three methods presented here have been used in the following parts.

4.3 References

[1] Ohring, M. The Materials Science of Thin Films. Academic Press: 2002.

[2] Kwon, H. , Lee, S. H. , and Kim, J. K. Three-Dimensional Metal-Oxide Nanohelix Arrays Fabricated by Oblique Angle Deposition: Fabrication, Properties, and Applications. *Nanoscale Research Letters* **2015**, 10, 369.

[3] He, Y. , Fu, J. , and Zhao, Y. Oblique angle deposition and its applications in plasmonics. *Frontiers of Physics* **2014**, 9, 47–59.

[4] Barranco, A. , Borras, A. , Gonzalez-Elipe, A. R. , and Palmero, A. Perspectives on oblique angle deposition of thin films: From fundamentals to devices. *Progress in Materials Science* **2016**, 76, 59–153.

5 Silver nanoparticles grown by Solid State Dewetting process onto glass substrates

One of the most frequent methods to prepare micro-nano particles, controlling geometry and inter-particle distance, is lithography. However, this method has disadvantages such as high patterning time and elevated costs [1]. Solid State Dewetting is a process which morphologically transform a continuous thin film in islands or droplets. The energy which makes this process possible, can be supplied by a thermal treatment. Dewetting can occur at temperatures well below the melting point of a material. Films with thickness of a few nanometers are generally meta-stable in the as deposited state and they will spontaneously de-wet when heated to temperatures at which the mobility of the atoms is sufficiently high to provide effective mass transport. The temperature at which dewetting is observed decreases with film thickness and with the material melting point temperature.

The purpose of this part of the work is to study the Solid State Dewetting (SSD), in order to control the shape, average size and density of arrays of micro-nano particles. These characteristics depend on the desired application. For light trapping in solar cells, we are interested in forming large (>100 nm) and uniformly shaped Ag nanoparticles. The surface plasmon resonance (SPR) wavelength depends on many factors. Some of them are the size and shape of particles, the spill out and the distance between them in an array. In our case, the dependence of size and density upon initial thin film thickness, working temperature and annealing plateau time was studied.

Silver films of different thickness were deposited on glass substrates by thermal evaporation using the system which appears in Figure 3.1. The focus is on the dynamics of SSD. Hence, the substrate was chosen to prevent the performance of the film to be dictated by the crystalline orientation of the substrate. The evaporation material was Ag (99.99%) and the source was a tungsten boat. The substrate was fixed at a distance of 15 cm from the boat. The thickness and the evaporation rate were measured in situ by a quartz monitor. The deposition rate was approximately 1nm/s. **Table 5.1** presents thickness values measured by the quartz monitor compared with ones obtained by profilometer measurements.

Table 5.1: Film thickness given by the quartz monitor (nominal) compared to the thickness measured with the profilometer.

Nominal thickness (nm)	**Profilometer thickness (nm)**
20	32 ± 5
40	53 ± 8
60	74 ± 5
80	94 ± 8

The difference between the nominal thickness and the profilometer thickness is between 12-14 nm for the all cases. The reason of the difference could be an experimental set of the measurements of the profilometer. Hence, I am going to consider the nominal thickness as the most suitable in the rest of the chapter.

Subsequently, the films were annealed in air, in a tube furnace. As depicted in **Figure 5.1**, the annealing consisted in a temperature ramp, until the working temperature, followed by a annealing plateau. The rate of the ramp was 10°C/min and the time of the annealing plateau was varied. At the end, the samples were cooled down naturally.

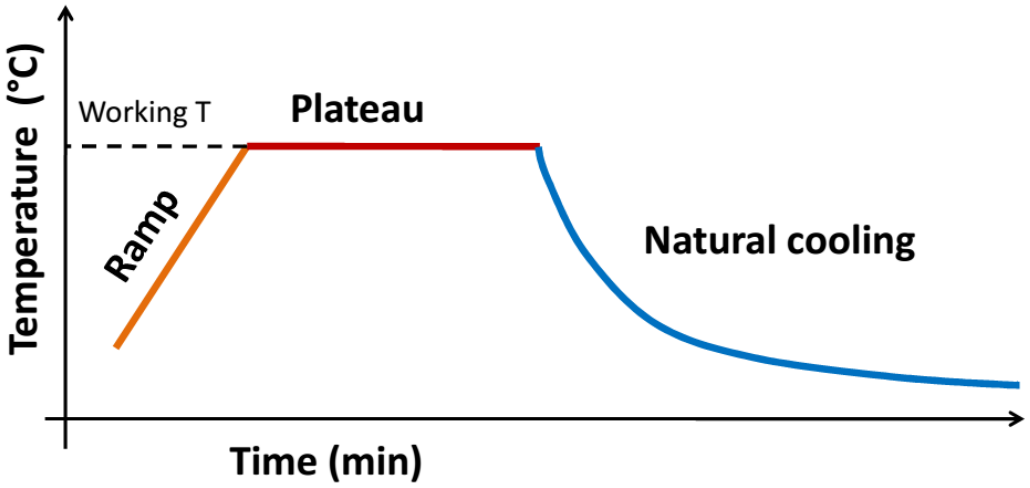


Figure 5.1: Schematic diagram of the thermal treatment (annealing) profile showing the ramp (10°C/min), the annealing plateau at the working temperature and the natural cooling**.** The annealing plateau time is the one between the beginning and the end of the plateau.

The study of the dewetting process consisted of two parts:

- study of the effect of initial film thickness and working temperature
- study of the effect of annealing time

5.1 Morphological studies

5.1.1 Effect of the initial film thickness and of the working temperature

In the first part of this study, samples with initial film nominal thickness of 20 nm, 40 nm, 60 nm, 80 nm, were made by annealing. The annealing plateau time was one hour at different working temperatures (300°C, 350°C, 400°C, 450°C and 500°C). SEM micrographs of silver nanoparticles (NPs), obtained at a working temperature of 400°C, are shown in **Figure 5.2**.

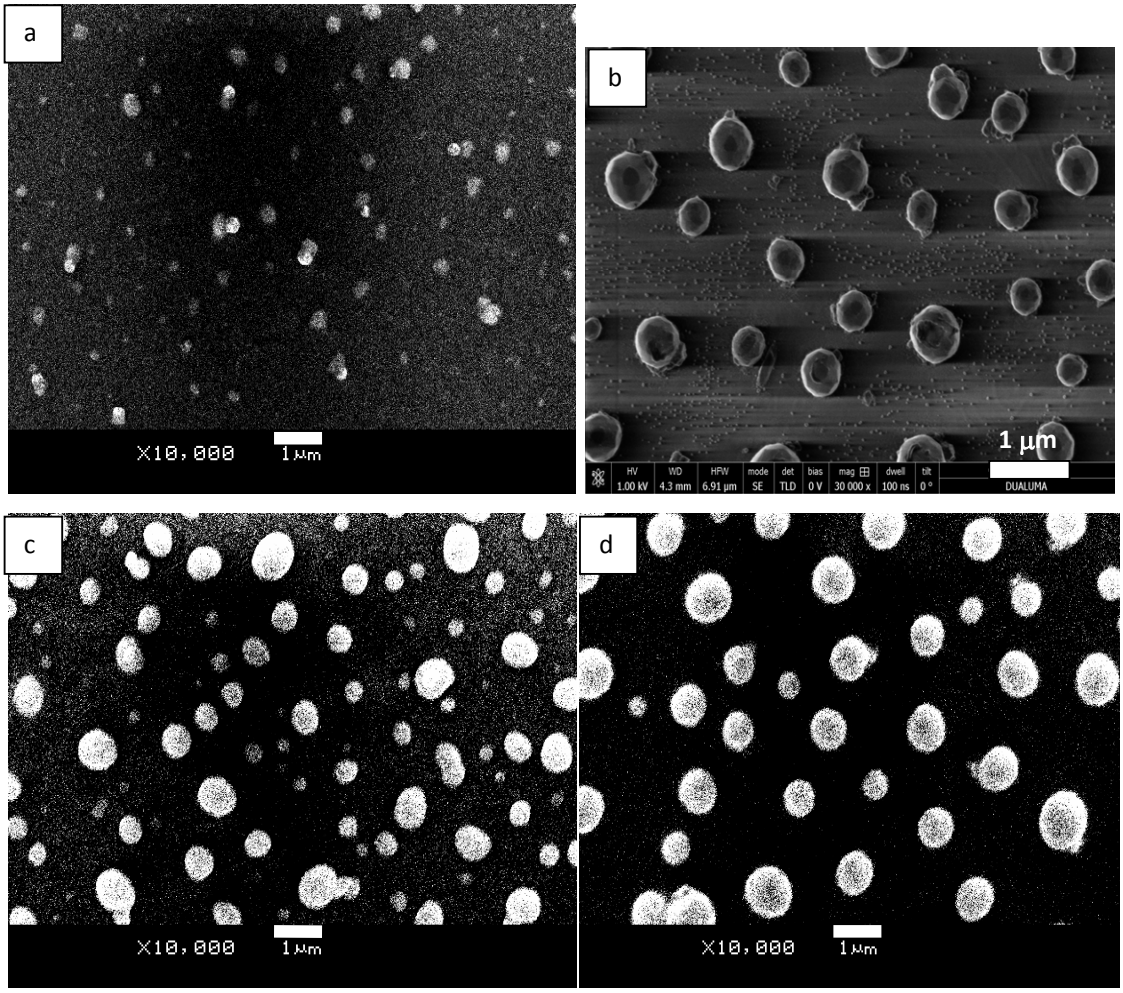


Figure 5.2: SEM micrograph of samples prepared with different initial thin film nominal thickness a) 20 nm, b) 40 nm, c) 60 nm, d) 80 nm. The working temperature was 400°C and the annealing plateau time was one hour. The white scale bar represents 1 µm.

The shapes of nanoparticles were adjusted by using ImageJ software which allows to fit nanoparticles with ellipses. With this fitting, the major axis length and the minor axis length were obtained. The size is defined as the major axis length. Histograms of the size of these nanoparticles were plotted for samples with different initial film thickness and different working temperatures. The time of the annealing plateau was 1 hour. The average values and the standard deviations were obtained. Densities were estimated by counting the number of nanoparticles which appears in certain areas of the micrographs. The mean NPs size values, standard deviations and NPs densities are reported in **Tables 5.2 to 5.5**. The error column corresponds to standard error $\varepsilon_{error} = \frac{\sigma_{desv}}{\sqrt{N}}$, where σ_{desv} is the standard deviation and N is the number of measurements.

Table 5.2: Mean lateral size and density of silver nanoparticles, for samples whose initial thin film nominal thickness was 20 nm.

Working temperature (°C)	NPs mean lateral Size (nm)	Error (nm)	Density (Particles/μm^2)
300	230	8	0.656
350	180	5	0.797
400	250	9	0.328

Table 5.3: Mean lateral size and density of silver nanoparticles for samples whose initial thin film nominal thickness was 40 nm.

Working temperature (°C)	NPs mean lateral size (nm)	Error (nm)	Density (Particles/μm^2)
300	498	10	1.046
350	586	17	0.900
400	496	12	0.750
450	555	12	0.359
500	519	13	0.172

Table 5.4: Mean lateral size and density of silver nanoparticles for samples whose initial thin film nominal thickness was 60 nm.

Working temperature (°C)	NPs mean lateral size (nm)	Error (nm)	Density (Particles/μm^2)
300	worm shape		
350	632	14	0.813
400	710	15	0.766
450	645	11	0.484
500	692	20	0.189

Table 5.5: Mean lateral size and density of silver nanoparticles of samples whose initial thin film thickness was 80 nm

Working temperature (°C)	NPs mean lateral Size (nm)	Error (nm)	NP Density (Particles/μm^2)
300	1000	38	0.469
350	960	29	0.390
400	828	18	0.375
450	839	18	0.406
500	673	19	0.250

As an example, some histograms with their fits are shown in **Figure 5.3**. They correspond to samples, whose SEM micrographs were presented in **Figure 5.2**. The initial film nominal thickness were 20 nm, 40 nm, 60 nm, 80 nm. The working temperature was 400°C. In this figure, a shift to larger mean sizes is observed with the initial thin film thickness. Also the standard deviation increases with the initial thin film thickness.

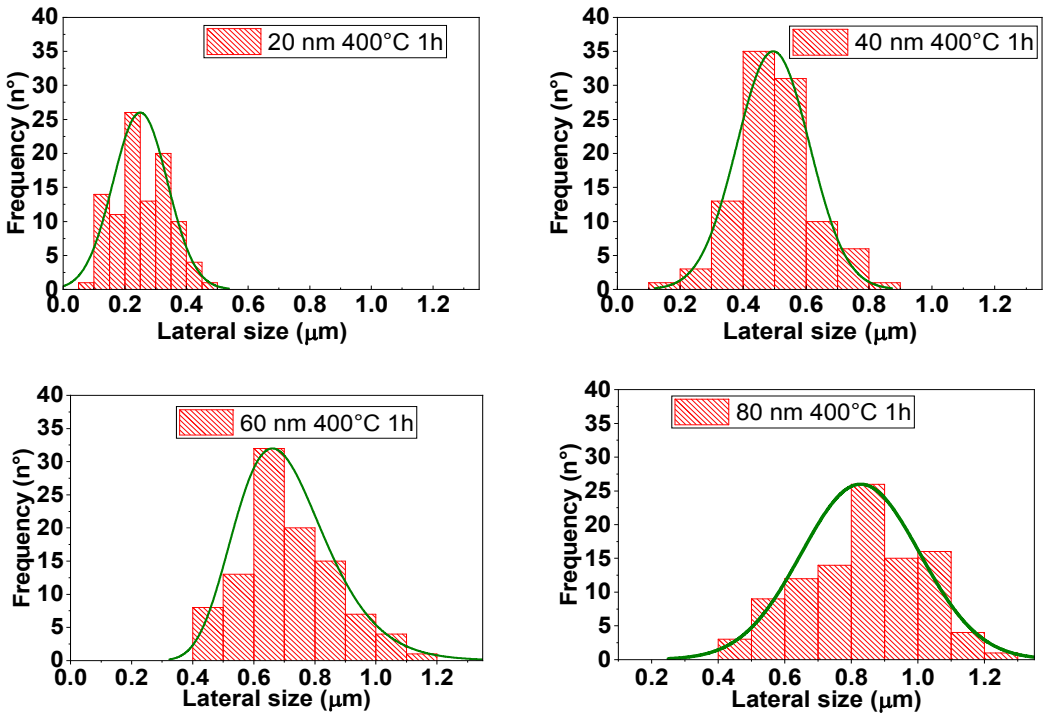


Figure 5.3: Histograms of NP lateral size of samples whose initial thin film nominal thickness were 20 nm, 40 nm, 60 nm, 80 nm. The working temperature was 400°C and the annealing plateau time was 1 hour. The green fitting curves correspond to the distribution with smaller Kolmogorov-Smirnov statistic. The lateral size corresponds to the major axis length of the NP in the plane of the substrate.

Two fits were made for each histogram. One is a normal distribution and the second is a log-normal. The results of the Kolmogorov-Smirnov test for the different distributions are

summarized in **Table 5.6**. When the statistic is smaller, the fitting is better and the curve which is superimposed to the histogram is the better distribution.

Table 5.6: Kolmogorov-Smirnov test for two distribution: normal and log-normal.

ICL Nominal Thickness	Norm Statistics	Norm p	Log norm Statistics	Log norm p
20 nm	0.070	0.72	0.091	0.363
40 nm	0.071	0.70	0.100	0.255
60 nm	0.082	0.50	0.054	1
80 nm	0.058	0.98	0.104	0.218

Based on these tables, plots of NP mean lateral size vs. working temperatures and plots of NP density vs. working temperature are depicted in **Figure 5.4** and **Figure 5.5.**

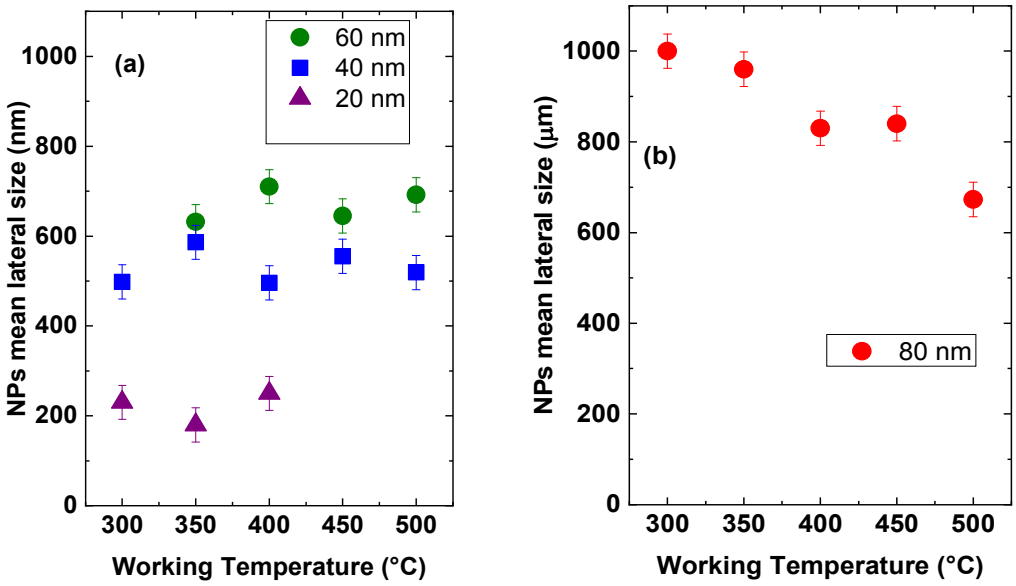


Figure 5.4: Plots of mean NPs lateral size vs. working temperature for an initial thin film nominal thickness of a) 20 nm, 40 nm, 60 nm b) 80 nm. The annealing plateau time was 1 hour and the mean NPs lateral size corresponds to mean major axis length of the NP in the plane of the substrate.

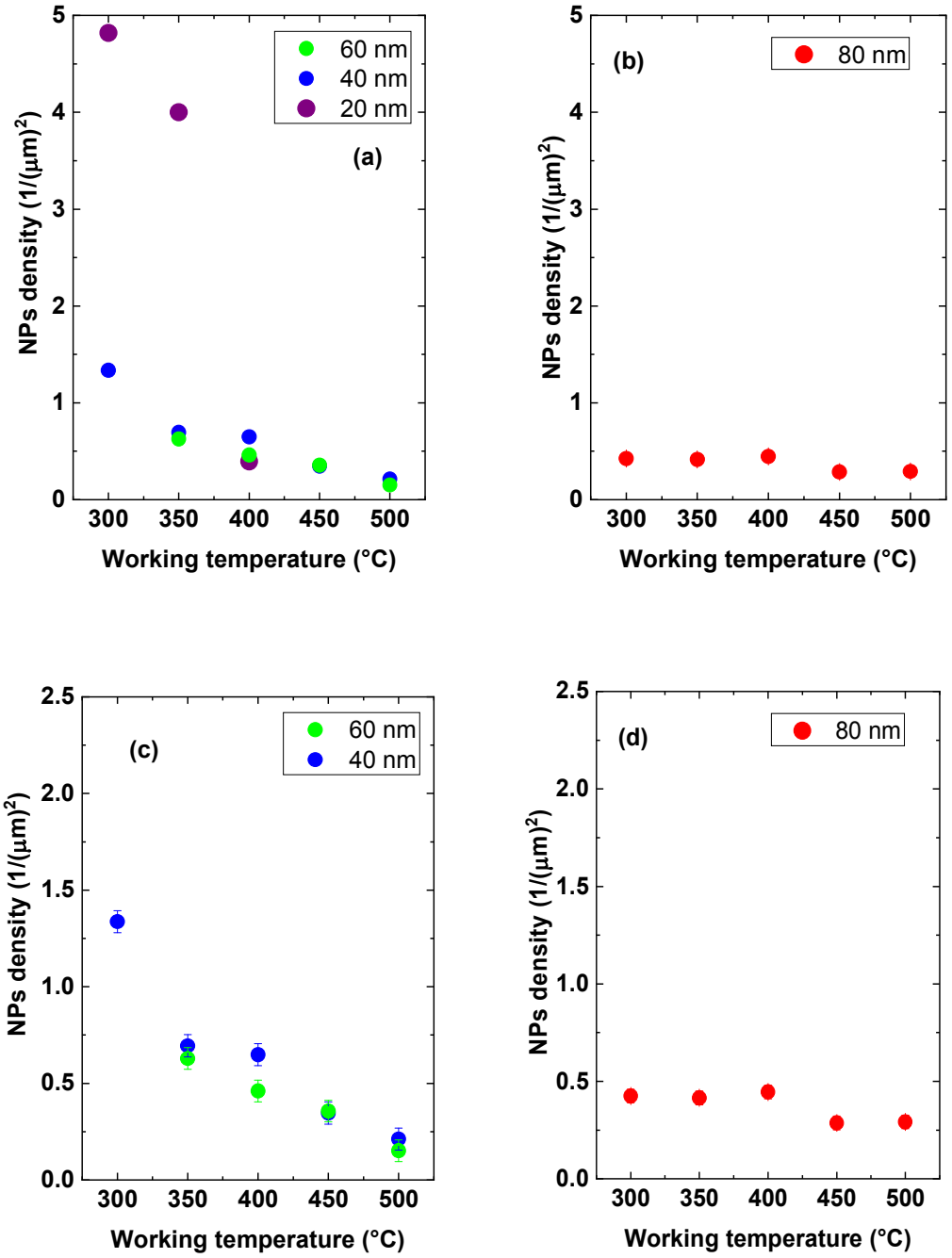


Figure 5.5: Plots of NPs density vs. working temperature for initial film nominal thickness of a) 20 nm, 40 nm and 60 nm, b) 80 nm, c), d) zoom of the previous plots. The density is the number of particles per unit area.

After analyzing, two trends are recognized. The first one corresponds to samples whose initial thin film nominal thickness were 20 nm, 40 nm and 60 nm. In this case, NPs

mean lateral size is almost constant with some dispersion and NPs density drops with working temperature. The second one corresponds to samples whose initial film nominal thickness was 80 nm. NPs lateral size drops and density decreases with working temperature, but much slowly than in the first case.

Since the volume of silver is conserved during the process of dewetting; density, mean size and height of nanoparticles have to change accordingly, when the working temperature is varied.

A consensus in the description of solid state dewetting has not been reached. The mechanism of solid state dewetting is more difficult than the mechanism of dewetting in liquid state. Many concurrent processes and their interplay must be taken into account, when studying the solid state dewetting: grain growth, texture evolution, anisotropic diffusion, particle coarsening and evaporation.

Historically, the first model was based on capillarity approaches, inspired by liquid dewetting, which neglect the crystalline nature of the film. The surface is considered as homogenous and isotropic. The local curvature and the associated gradient of chemical potential is suggested to be the driving force of the material transport.

Ruffino et al. [2] observed that size grows with temperature in a dewetting process of Au on SiO_2 nanowires in dry N_2 environment. They attributed it to the hole formation, which is due to film retreating. The net result of the holes coalescence process is the formation of metal nano-filaments, that they subsequently decay into isolated islands through a Rayleigh instability. They said that the effect of the temperature on the dewetting process, in particular the radius r of the formed NP, is expected to depend on T by an Arrhenius law.

$$r = r_0 \exp\left(-\frac{E_A}{kT}\right) \qquad \textbf{5.1}$$

k, T and E_A are the Boltzmann constant, the absolute temperature and the characteristic activation energy for the dewetting process (depending on the specific driving process, surface diffusion for example), respectively. This fact was also observed by Quan et al. [3]

Our results do not follow this trend. Thus, they cannot be explained by capillarity approaches. Presland et al. [4] observed that in atmospheres containing oxygen, surface agglomeration occurred rapidly on annealing. There is a development of isolated surface hillocks. Transfer of material to hillocks results in denuding the surrounding areas, and eventually this remaining material begins to withdraw from the substrate, forming holes.

On annealing, differential thermal expansion will produce a compressive stress in the film. Removal of material to hillocks above the film surface will reduce this stress. The compressive driving force, however, is present in any atmosphere, and also in gold films which showed no hillock growth. However, quick hillock growth was only observed for silver in the presence of oxygen. The surface energy γ is considerably reduced from hydrogen to oxygen. So, the effect of oxygen in allowing hillock growth is explained by reduction of critical nucleus size, as well as by the rise of D_S (surface diffusivity) (see chapter 2). γ is considerably reduced from 1.2 N/m in hydrogen to 0.2 N/m in oxygen. Thus for $\sigma = 10^9$ N/m^2, $\gamma = 0.2$ N/m gives $R_C \geq 4$Å which is a nucleus size that could form as a

result of thermal activation, while $\gamma = 1.2$ N/m gives the much larger value of $R_C \geq 24$Å . Also the induction favours deep grooves in this atmosphere, so the higher number of holes compared to other atmospheres [5].

Serrano et al. [6] observed the solid state dewetting of gold on glass substrates. Annealing was performed in air. The island size grows with working temperature. Whereas, Serrano et al. [7] also study the dewetting of silver films on glass substrate. They reported that size decreases, height goes up and covered area drops with temperature. The initial film thickness of their samples were 10 nm, 30 nm and 50 nm.

Jacquet et al. [5] studied the dewetting of silver thin films on amorphous silica in two atmospheres: vacuum and oxygen. They reported that in oxygen there are three steps: induction, hole propagation and sintering. During induction some grains grow more than their neighbours and became the particles which are observed at the end of dewetting. Extraordinary grain growth is another dominant feature of hole propagation. It occurs close the holes, but also far away. A growing grain accumulates material from the initial layer contained in an area of influence which can extend up to 1 μm. In contrast to capillarity models, no rim was observed during the propagation, because the material was agglomerated into the growing grains. The dewetting front propagates in the directions where no material has agglomerated and it does not propagate along grain boundaries, but whole grains are shrinking. The front takes then a finger shape and bypasses the grains where agglomeration has already taken place. Surface diffusion governs grain growth and thus it could be a possible transport path, instead interface diffusion, grain boundary sliding or grain boundary diffusion. So, in this case, dewetting involves neither the propagation of a rim, nor a succession of growth and shrinkage of touching grains. Whereas, dewetting results from the propagation of holes, disappearance of small entities and abnormal growth of a limited number of grains [8].

Serrano et al. [7] also observed an increase of catchment area and height with working temperature. This fact can explain the trends observed by us.

As depicted in **Figure 5.6**, at constant working temperature, the mean NPs lateral size grows with the initial thin film thickness. This fact was observed by Farzinpour et al. [9]. The agglomeration occurs on increasingly larger length scales as silver layer thickness enlarges. Jacquet et al.[10], observed experimentally that the average diameter D of the final particles, obtained after dewetting, is proportional to the initial thickness of the silver layer.

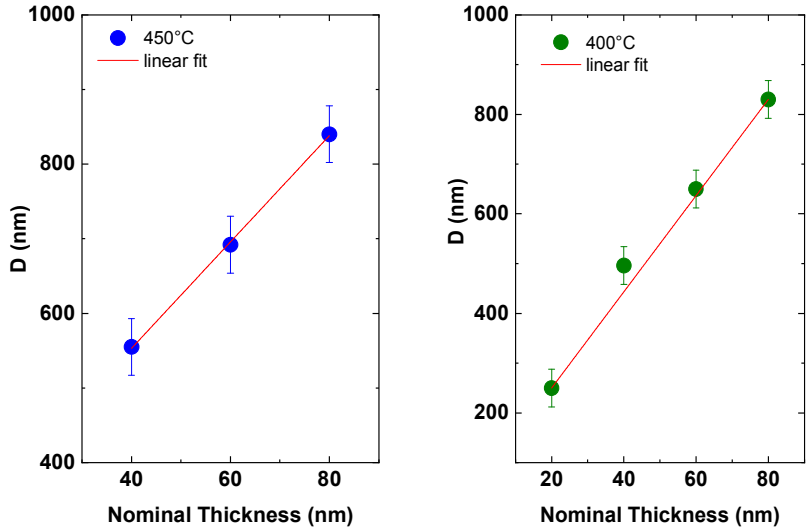
A linear fit was made to the graphs in **Figure 5.6**. This fit allows us to conclude that lateral size has a linear behaviour, with profilometer thickness. It is in accordance with Leroy et al. [11], who affirm that whatever the experimental conditions are, the island size varies linearly with the thickness of the film d. Although the dewetting state is limited by kinetics, it is possible to use a simple thermodynamic model to understand this scaling. The thermodynamic limit only gives a lower limit.

The free energy change, ΔF, due to the transformation of a volume V of film (thickness d and initial area before dewetting S) into a spherical shaped particle forming a

contact angle θ with the substrate, is described in Chapter 2. The minimum radius associated to the formation of a nanoparticle is obtained from the condition $\Delta F < 0$:

$$r_{min} = \frac{3}{2} Kd \qquad \textbf{5.2}$$

The deduction of the last equation is shown in Chapter 2. Leroy et al. suggested that the numerical discrepancy between estimated and experimental values originates from material data uncertainties, simplified equations (the true island shape and the generation mechanism are not considered) and especially from the thermodynamics approach that misses all the kinetic effects.



.

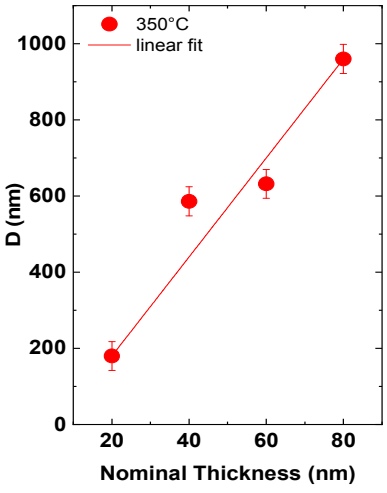


Figure 5.6: Plots of mean NP lateral size (D=2r) (in the plane of the substrate) vs nominal thickness of the initial film, for different working temperatures. The annealing plateau time was 1 hour.

Thus, the thermodynamic approach only gives the minimum size of the islands formed by dewetting, close to equilibrium conditions. Even, if the temperature is implicitly

contained in the previous equations (through the surface free energy values), the temperature effect on the dewetting cannot be fulfil by this simple approach because i) far from equilibrium kinetic effects have to be considered ii) a long annealing of the islands may results in an island size increase due to Ostwald ripening or coalescence.

Table 5.7 : Slope for different working temperatures.

Working Temperature (°C)	**350**	**400**	**450**
Slope	13.0	9.7	7.1

Clearly, there is a lineal relation between size and the initial thickness of the thin film. But the slope of this linear fit depends on temperature: when the temperature increases, the slope goes down.

5.1.2 Effect of the final ramp temperature and of the annealing plateau time.

In the second part of this study, the thermal treatment was interrupted at different temperatures on the ramp or at different times in the annealing plateau. The interrupted annealing method, also was employed by Malyi et al. [12]. Cooling the sample generates thermal stresses, due to the mismatch of thermal expansion coefficients of glass and silver, but it may relax, for example by dislocation plasticity in the interior of the particles. In the present experiment, thickness was kept constant. Initial thin films with nominal thickness of 40 nm and 80 nm were used. The annealing processes which ends on the ramp, at certain temperature, are shown in the diagram of **Figure 5.7**. A collection of SEM images of samples is displayed, as a function of the final temperature of the ramp, in **Figure 5.8**. The nominal thickness of the initial film was 80 nm. After that, the sample was cooled naturally.

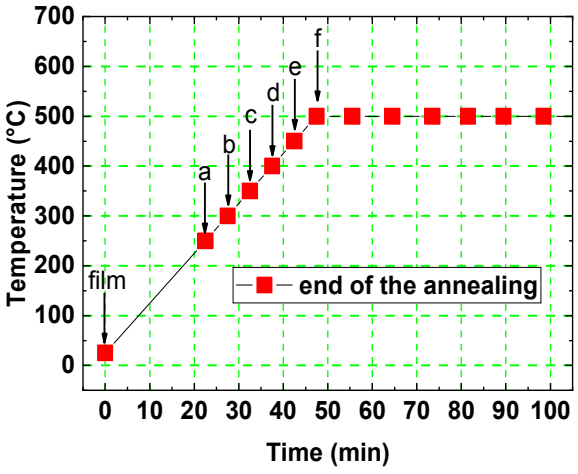


Figure 5.7: Diagram of the annealing profile indicating the points where the annealing processes end. In the present case, it ends on the ramp. Labels are associated with micrographs of **Figure 5.8** and **Figure 5.9**.

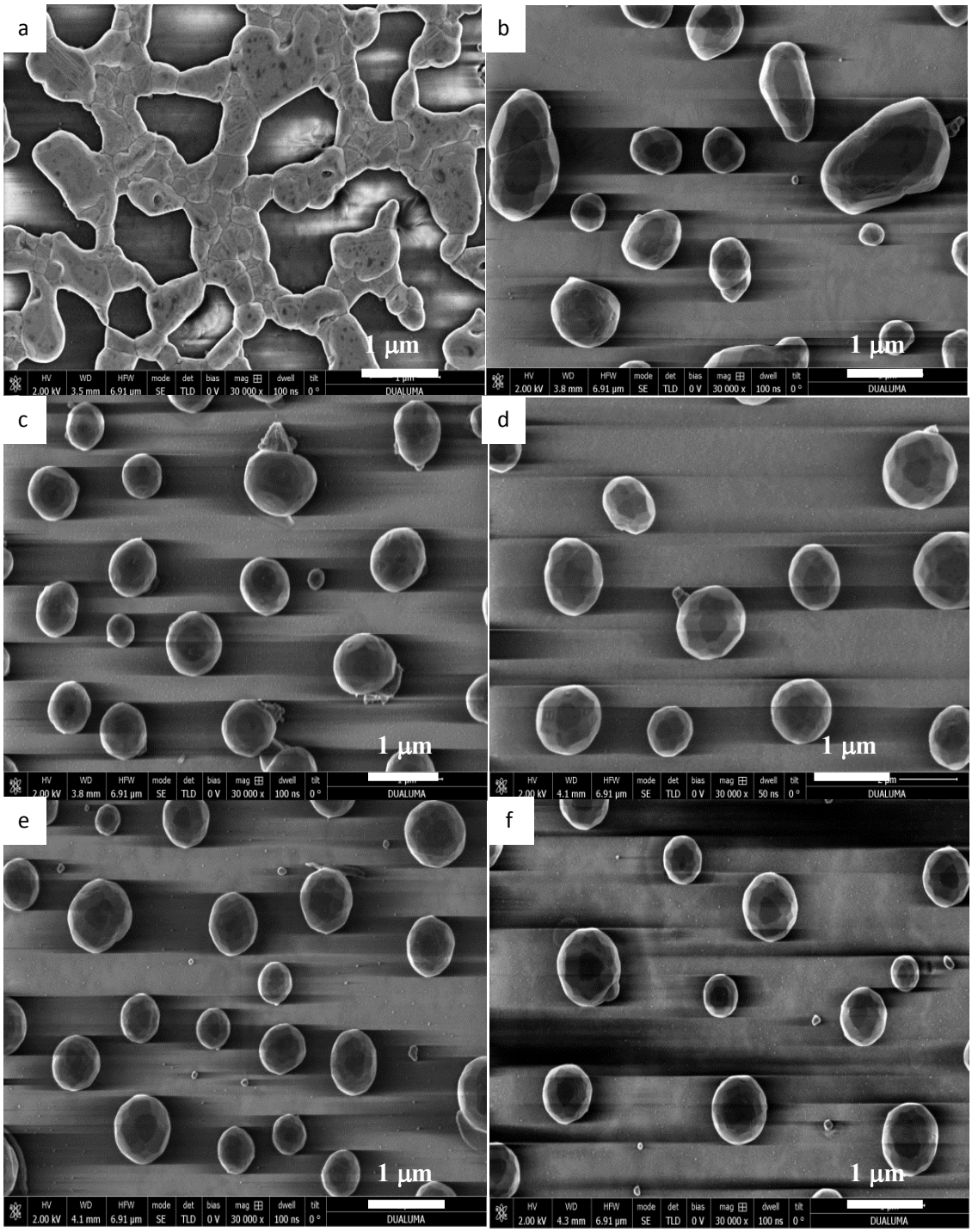


Figure 5.8: FE-SEM images of samples with initial film nominal thickness of 80 nm. The annealing ended at ramp temperatures of: a) 250°C b) 300°C c) 350°C d) 400°C, e) 450°C f) 500°C. The white scale bar represents 1 µm.

The collection of FE-SEM images of **Figure 5.9**, corresponds to the same samples, but were taken at a tilt angle of 52°.

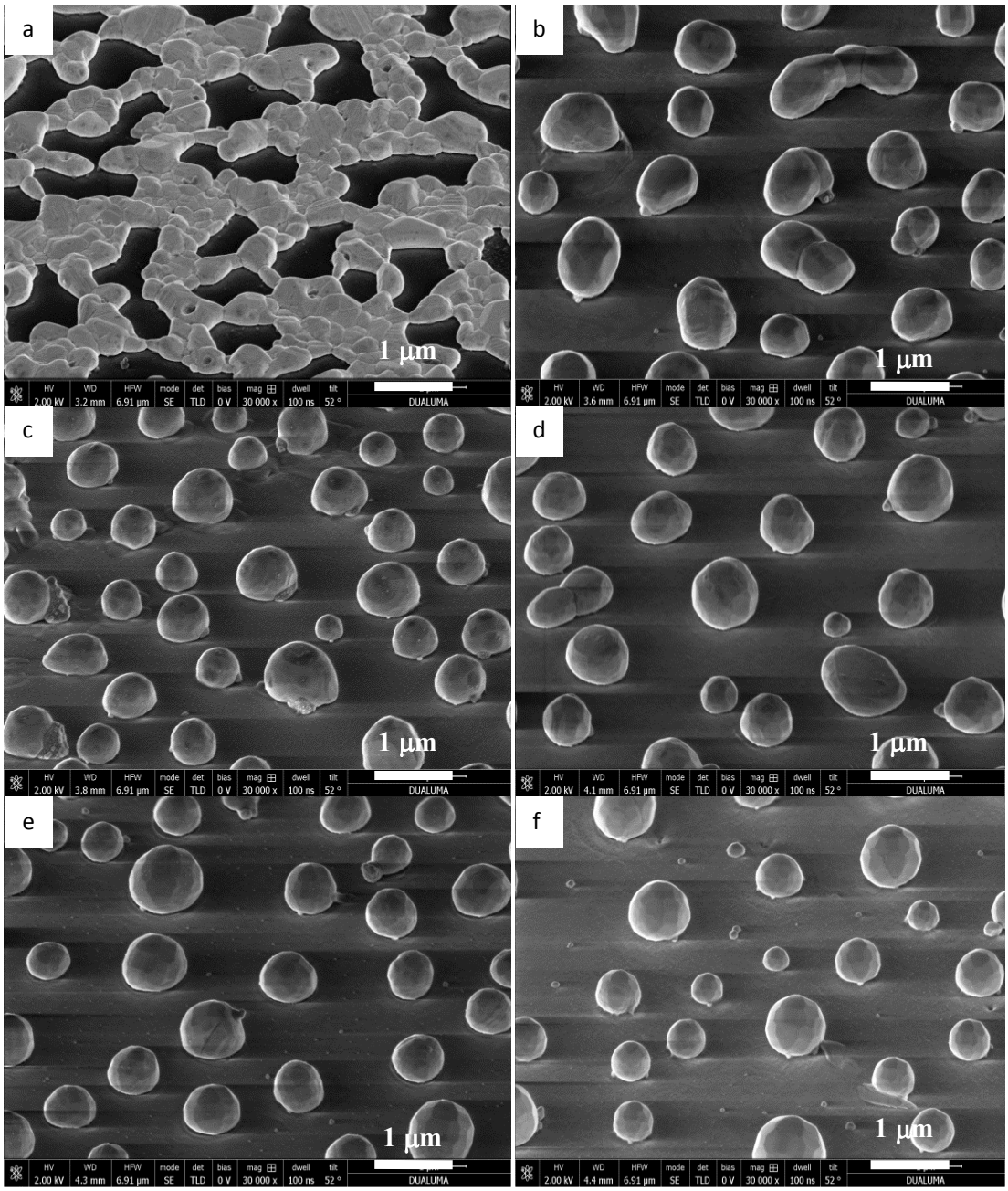


Figure 5.9: FE-SEM of samples with an initial film thickness of 80 nm. The tilt angle is 52°.The annealing ended at a ramp temperature of a) 250°C, b) 300°C, c) 350°C, d) 400°C, e) 450°C, f) 500°C. The white scale bar represents 1 µm.

In **Figure 5.9 a,** silver domains become tortuous and worm like. Disconnected objects are observed in **Figure 5.9 b,** but they have not a defined shape. Also, some of them are still attached, with a line as a frontier. From **Figure 5.9 c** to **Figure 5.9 f,** the islands acquire a defined geometrical aspect. At 400°C, a rounded triangle shape appears on their top and it is more notorious for higher temperatures.

Jacquet et al. [13], suggested that, independently of the silver diffusion path, the successive reorganization of grains is the main source of grooving. The main cause of this process is the reduction of the total energy of the system and, after it, new contact angles appear. The grain size of metallic films increases when films are annealed at temperatures that are high enough to activate boundary migration. It leads to configurations closer to the equilibrium state at the triple line. But this equilibrium depends on the atmosphere as shown in **Figure 5.10**. Induction favours deep grooves in this oxygen atmosphere.

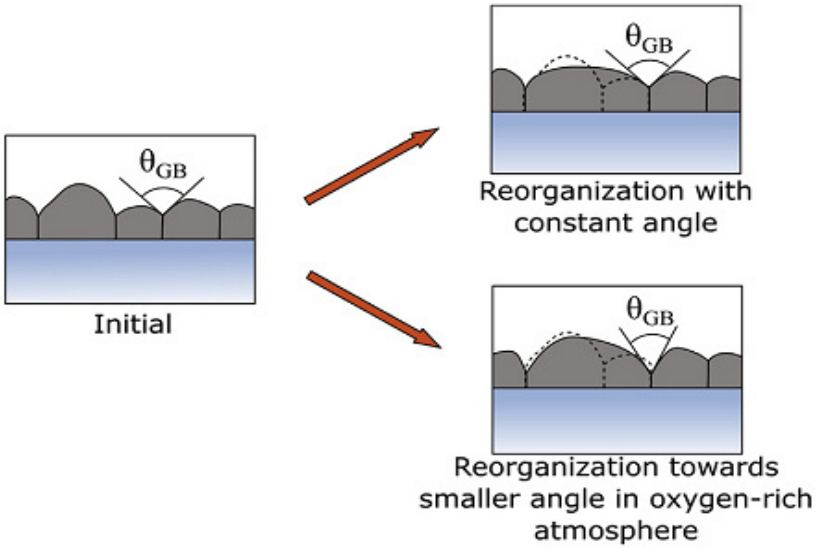


Figure 5.10: Schematic representation of grain reorganization in different atmospheres.

The reduction of the grain boundary area is made by the growth of specific grains at the expense of their neighbours. Smallest grains are eliminated and a change in texture to reduce the surface energy occurs. Muller et al. [14] observed that grains at the edge of holes are more textured than grains in the remaining film. Voids which grow along grain boundaries can be a consequence of total energy minimization or a kinetic phenomenon.

Derkach et al. [15] suggested that dewetting holes tend to develop and preserve elongated morphologies along the grain boundaries in the film. Grain boundaries energies in polycrystalline metals exhibit a wide range of energies, hanging from coherent twin boundaries with energies of few mJ/m^2 in some face center cubic metal (8 mJ/m^2 for silver [16]) to the energies comparable with the surface energy of respective metals (1543 mJ/m^2 for silver [17]). Dewetting holes developed in polycrystalline thin films should reflect the network of grain boundaries with the most energetic grain boundaries pulling the growing hole in their direction. This effect can be appreciated in **Figure 5.9 a**.

Schaffir et al. [18] attributed the kinetic phenomenon to the fact that the grain boundary acts as a fast diffusion path for vacancies and metal atoms.

The overall kinetics of dewetting, after the breakup of polycrystalline film into a set of islands by pinhole growth and percolation, is controlled by GB migration and Ostwald

ripening. In **Figure 5.8 a** and **5.8 b**, grain boundaries are observed. From **Figure 5.8 c** to **Figure 5.8 f**, particles acquire spherical shape and GB are not observed anymore.

SEM micrographs of samples, whose thermal treatment ended at a certain time of the annealing plateau, as shown in **Figure 5.11**, are displayed in **Figure 5.12** and **Figure 5.13**. The micrographs, which were taken at a tilting angle of 52°, allow us to observe the morphology of particles. From 8 min to 17 min, particles get a defined shape. At 26 min, particles lost their spherical shape. In this sample, a very thin layer of silver appears on the substrate among NPs and it is an indicator of Ostwald ripening. From 42 min to 51 min, this layer is not visible in the FE-SEM micrographs.

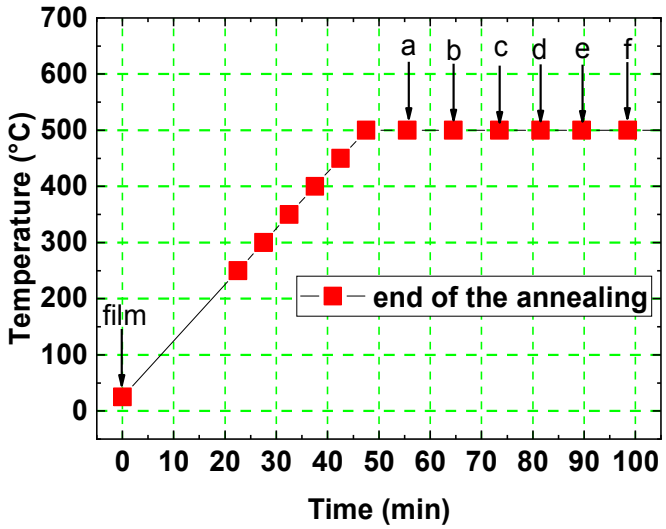


Figure 5.11: Diagram of the annealing profile. Red squares indicate the end of the annealing. Labels are associated with micrographs of **Figure 5.12 and Figure 5.13.**

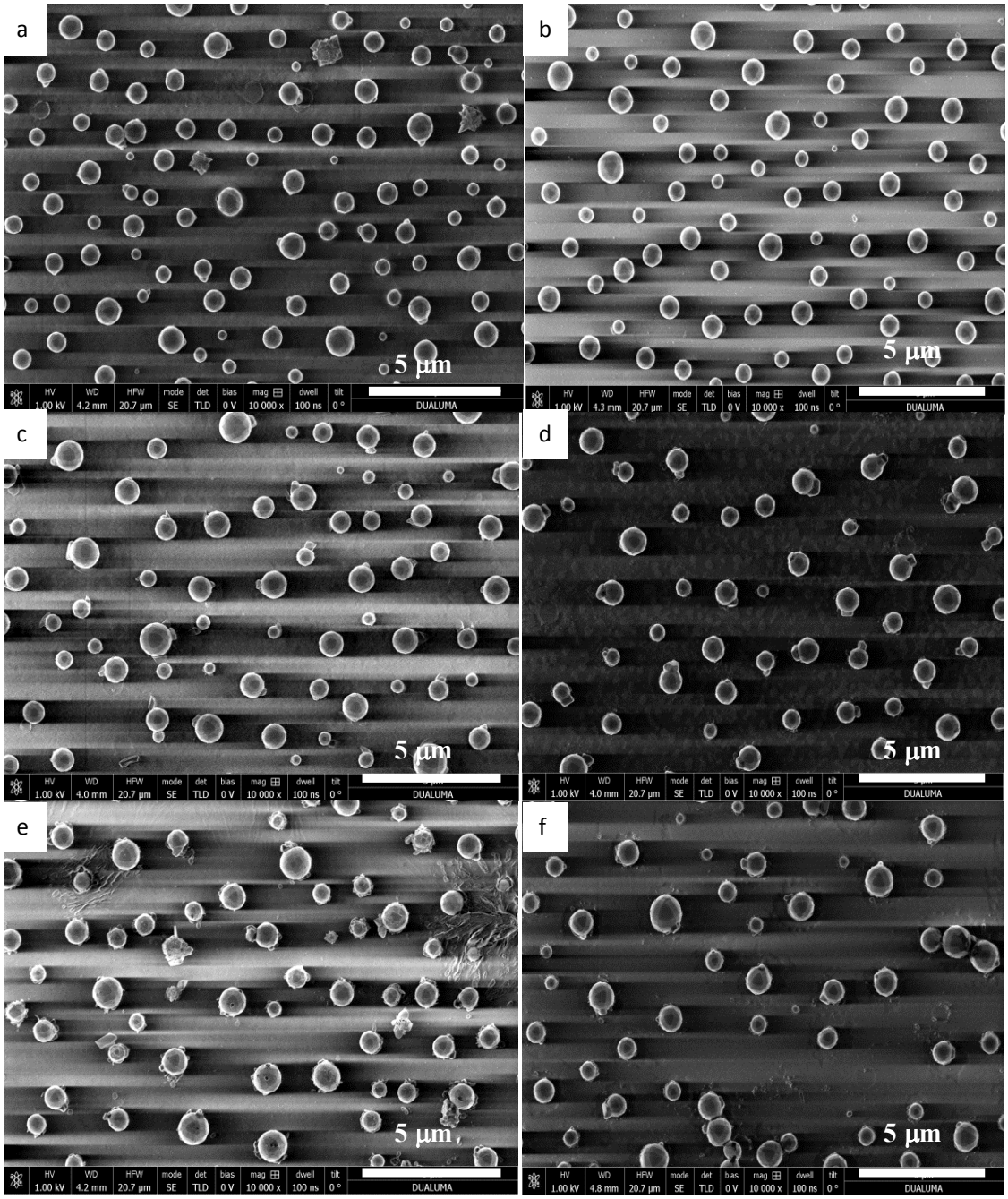


Figure 5.12: FE-SEM image of samples with an initial film nominal thickness of 80 nm and a working temperature of 500°C. The annealing plateau time was varied: a) 8min, b) 17 min, c) 26 min, d) 34 min, e) 42 min, f) 51 min. The white scale bar represents 5 µm.

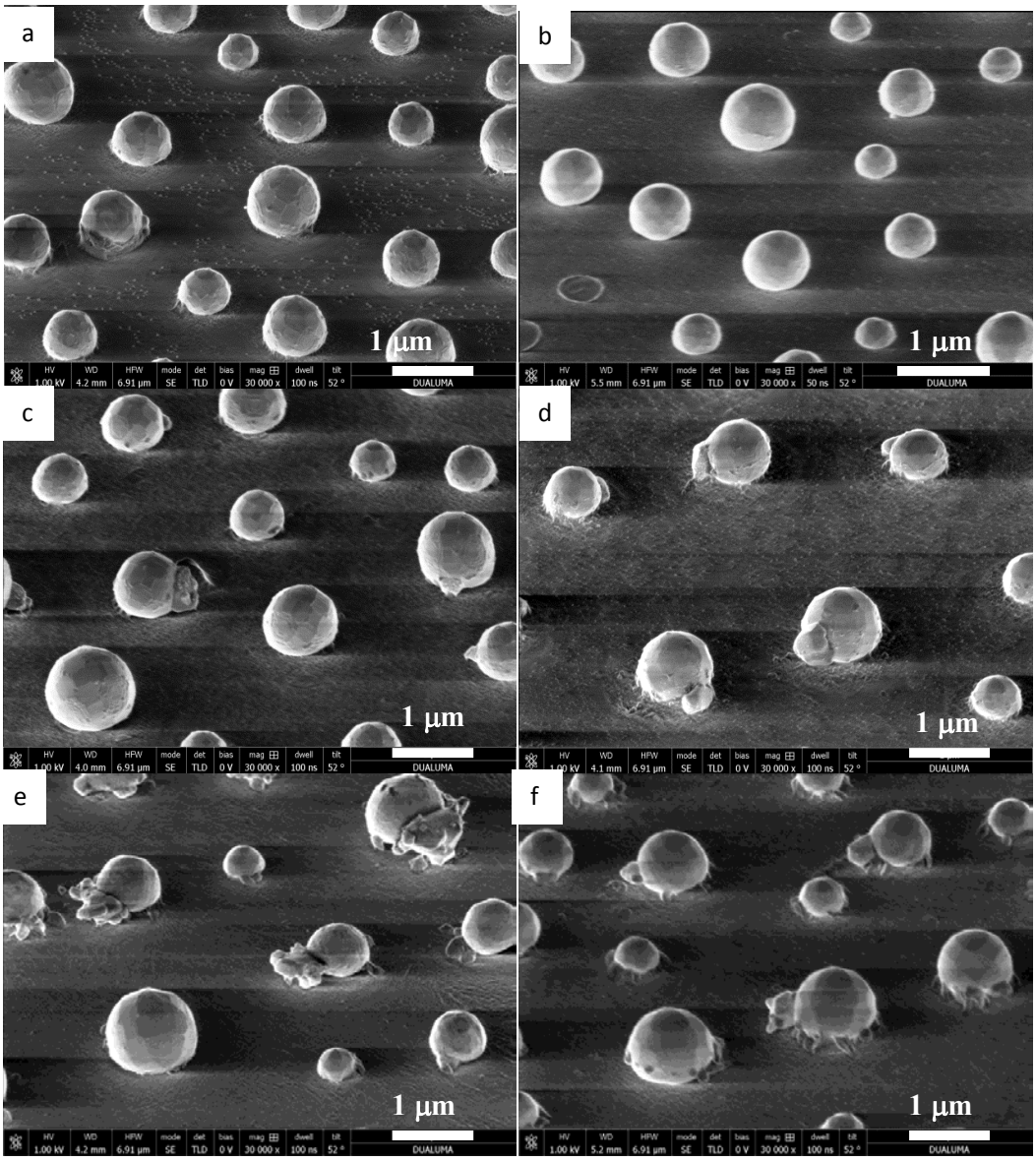


Figure 5.13: SEM image at a tilting of 52° of samples with an initial film thickness of 80 nm and a working temperature of 500°C. The annealing plateau time was varied: a) 8min, b) 17 min, c) 26 min, d) 34 min, e) 42 min, f) 51 min. The white scale bar represent 1 µm.

Plots of NP lateral size vs. final ramp temperature and NPs lateral size vs. time of the annealing plateau are presented in **Figure 5.14 a** and **Figure 5.14 b,** respectively. During the annealing plateau, NPs mean lateral size grows, reaches a maximum at 51 min and then drops abruptly. The additional thermal energy provided to Ag particles during annealing leads to re-crystallization. Also, if the annealing plateau time is bigger, residual stress relaxation takes place. New grain formation during re-crystallization process is usually accompanied by a decrease of the mean NPs size, as annealing plateau time increases [12] [19] . Density is also plotted as a function of both ramp temperature and of annealing plateau time in **Figure 5.14 c** and **Figure 5.14 d** respectively. Density is mainly constant for the ramp and in the case of the plateau, it drops between 0 min to 51 min.

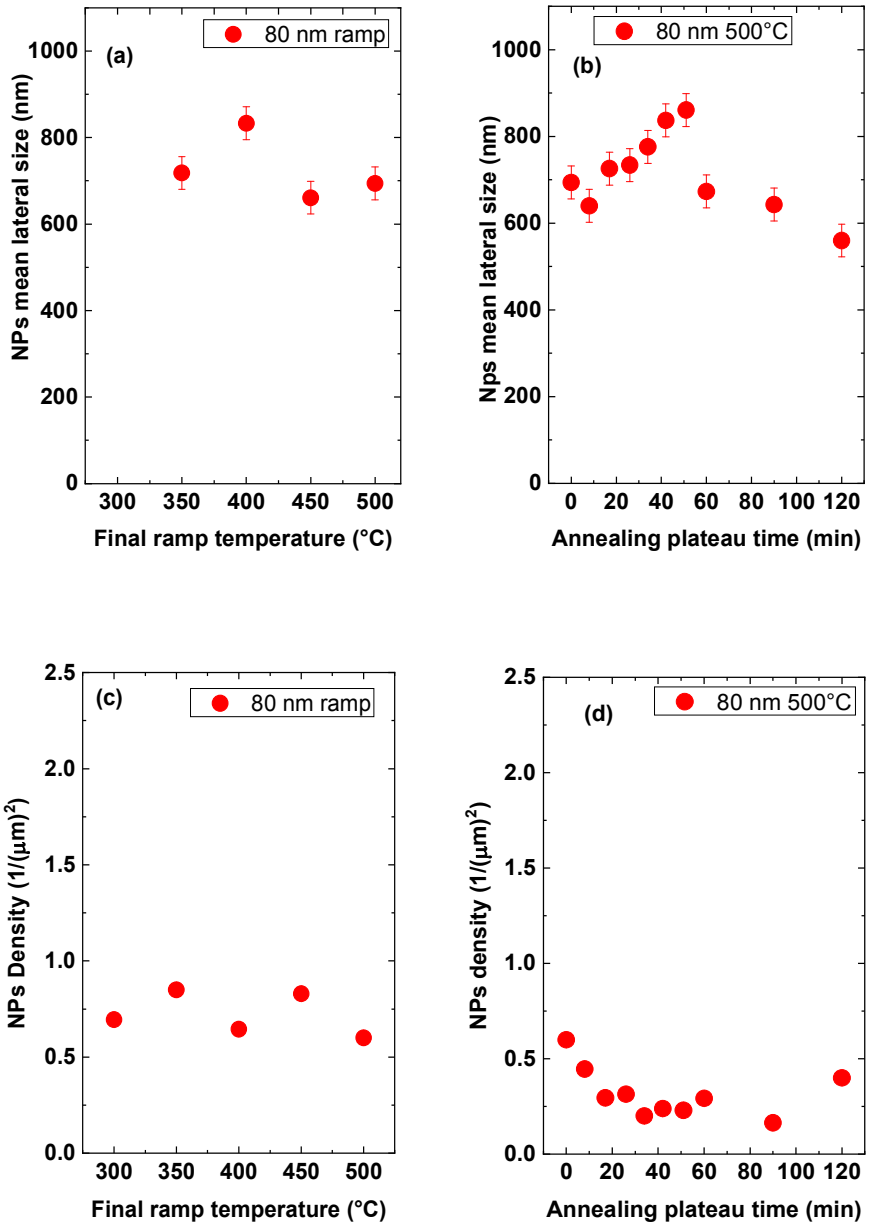


Figure 5.14: a) Plot of mean NP lateral size (in the plane of the substrate) and c) density (number of particles per unit area) vs. final ramp temperature for samples whose TT ends on the ramp. b) Plot of mean NP lateral size (in the plane of the substrate) and d) density (number of particles per unit area) vs. annealing plateau time for samples whose TT ends in the plateau. The initial film thickness was 80 nm for all cases and for b) and d) the working temperature was 500°C.

A detailed study of lateral size (D) dependence with annealing plateau time was made. A theoretical analysis of Ostwald ripening made by Thiel et al. [19] indicates that in the attachment-detachment limit, the average in plane particle size as a function of time, verifies $D \sim t^{\frac{1}{2}}$. A D^2 vs. t plot was made, and a linear fit was superimposed as shown in **Figure 5.15**. We conclude that the evolution in the plateau follows the Ostwald ripening.

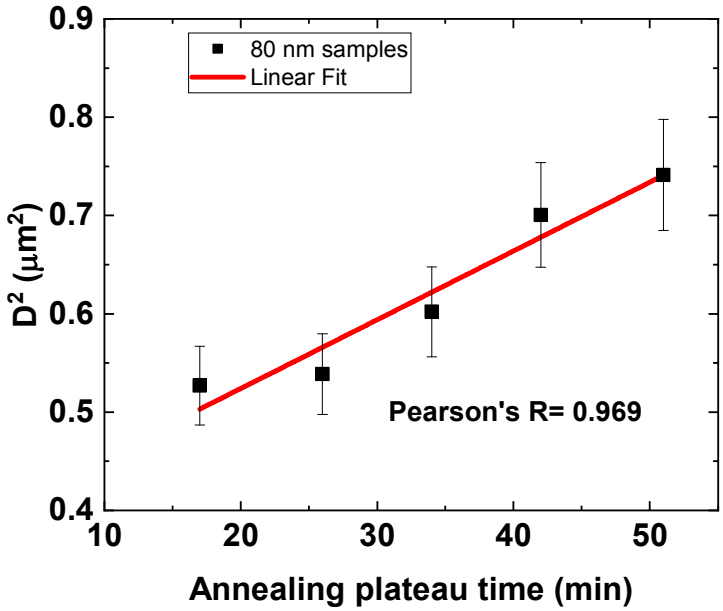


Figure 5.15: Graph of D^2 vs. annealing plateau time. A linear fit is superimposed. The working temperature was 500°C. D is the mean lateral size (in the plane of the substrate) The initial thin film thickness was 80 nm and the working temperature was 500°C.

AFM images were acquired and they are shown in **Figure 5.16.** The volume of the particles was modelled by a spherical skullcap volume. There is a minimum at 34 min. It is an indicator, that there is a very thin layer of silver, between nanoparticles. To bigger times, silver agglomerates again in particles. But the shape of nanoparticles is less spherical than particles at 17 min. A plot of volume vs. annealing plateau time is shown in **Figure 5.17**.

Using the AFM images, the mean height was calculated for each sample. Using this quantity, the mean size in the plane of the substrate, and the density, a total volume of silver of the array was calculated. The plot of the calculated volume in function of annealing plateau time is shown in **Figure 5.17**.

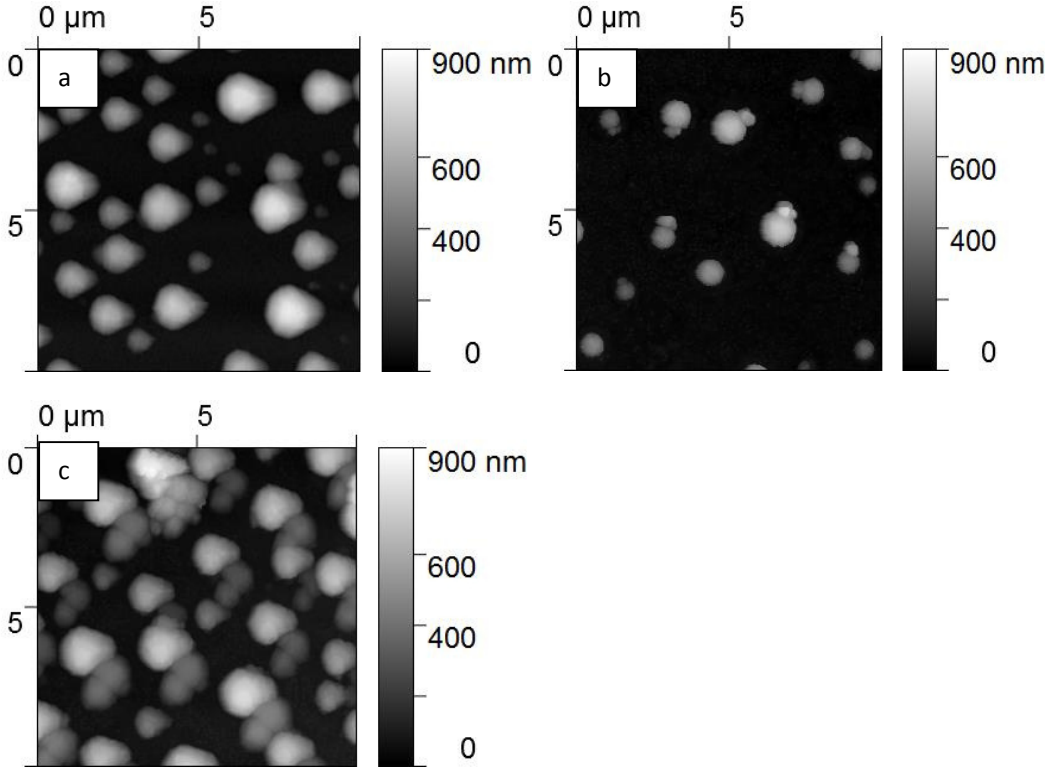


Figure 5.16: AFM image of samples whose thermal treatment ended at a) 17 min, b) 34 min, c) 51 min on the plateau. The initial thin film nominal thickness was 80 nm and the working temperature was 500°C

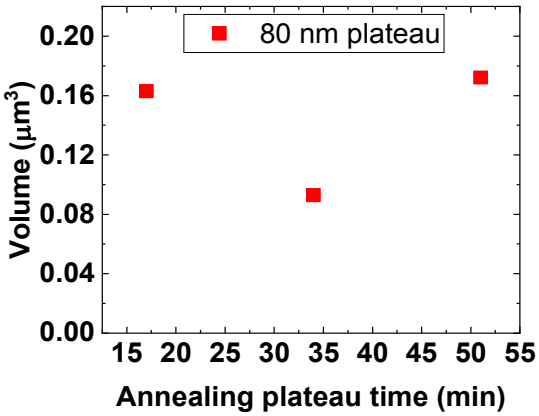
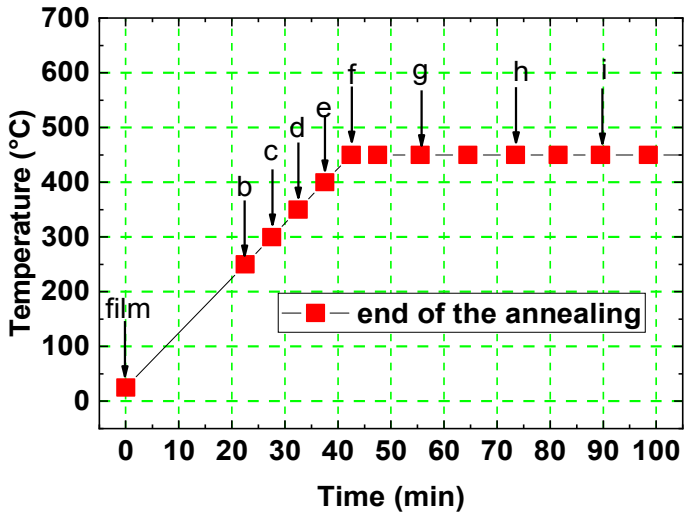


Figure 5.17: Calculated volume of the silver nanoparticle array vs. annealing plateau time for the samples whose AFM images are shown in Figure 5.16. To calculate it, the volume of the particles was modelled as spherical skullcap volume, the mean height of NPs obtained from AFM images of Figure 5.16, the mean lateral size and the density were used.

The volume decreases from 17 min to 34 min. This is due to Ostwald ripening. Atoms detach from a particle and diffuse, through the substrate, to another particle and attach to it. So, at a

certain time of the annealing plateau, there are many single atoms of silver on the substrate and the volume of the NPs is smaller. Also, in **Figure 5.16 c**, it is observed that NPs are constituted by agglomeration of smaller parts. This is important, because we are going to see that the in plane stress is compressive at 51 min of the plateau, thus there are many grain boundaries. At 60 min, in plane stress became tensile and the mean lateral size of NPs decreases. This is associated with the elimination of grain boundaries and re-crystallization.

The same procedure was implemented for samples whose initial film thickness was 40 nm. A diagram of the annealing process is shown in **Figure 5.18**.



..

Figure 5.18: Diagram of the annealing profile. Red squares indicate the end of the annealing. Labels are associated with FE-SEM micrographs of **Figure 5.19** and **Figure 5.20.**

A collection of micrographs of samples with initial thin film nominal thickness of 40 nm is shown in **Figure 5.19**. They are displayed as a function of the final temperature of the ramp. The time of the annealing plateau was 0 min. For 250°C, the film is broken, but particles have not a regular shape. At 300°C, particles have more rounded appearance, but there are some of them which are still connected. From 350°C to 450°C, particles acquire a more spherical shape and a triangular facet is observed on their top.

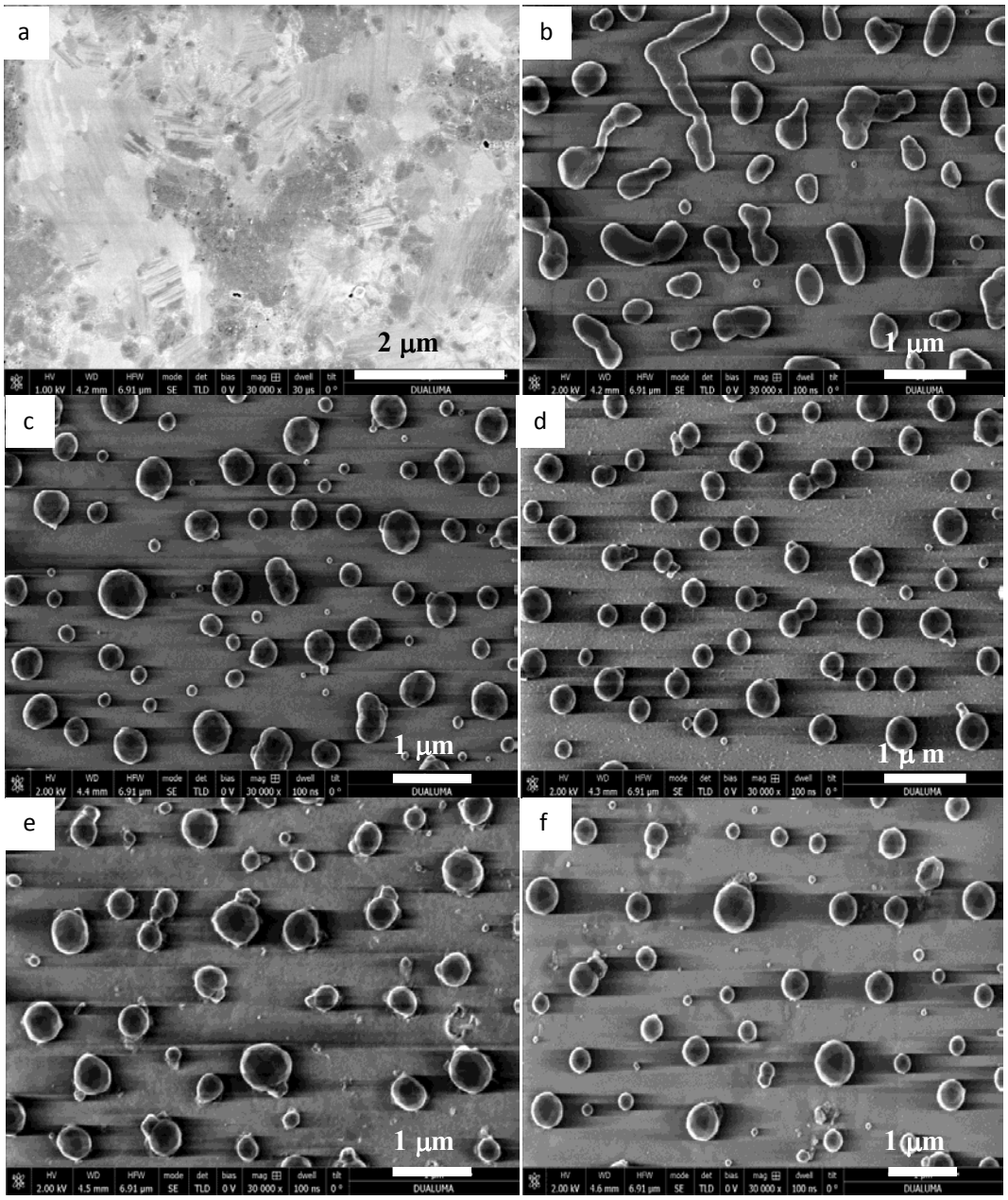


Figure 5.19: SEM images of samples with an initial film nominal thickness of 40 nm a) Untreated film. Samples where the annealing ended on the ramp temperature of: b) 250°C, c) 300°C, d) 350°C, e) 400°C, f) 450°C. The white bar scale is 1 μm, except a) which is 2 μm.

Another collection of micrographs is shown in **Figure 5.20**. They are displayed as a function of annealing plateau time. The working temperature was 450°C.

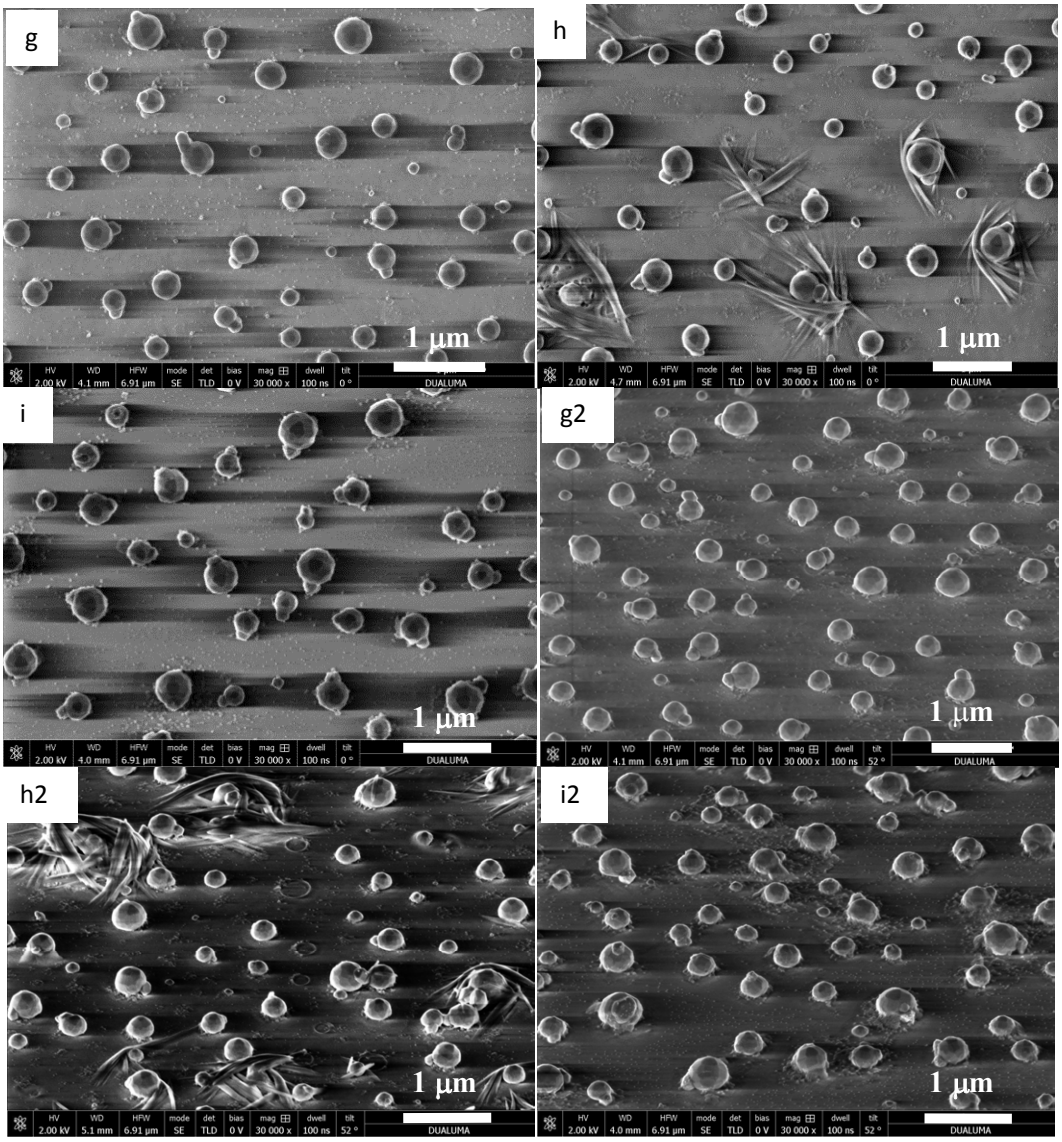


Figure 5.20: SEM images of samples with an initial film nominal thickness of 40 nm and a working temperature of 450°C. The annealing plateau time was varied: g) 17 min, h) 34 min, i) 51 min. Image obtained at a tilt angle of 52° of g2)17 min h2)34 min i2) 51 min. The white scale bar is 1 µm.

Plots of NPs mean lateral size and density are shown in **Figure 5.21**. **Figure 5.21 a** and **Figure 5.21 c** correspond to different final ramp temperatures**. Figure 5.21 b and Figure 5.21 d** correspond to different annealing plateau times. NPs mean lateral sizes (D) decrease with final ramp temperature, while density is almost constant. This can be explained by the NPs growth along the normal to the substrate direction. The triangular shaped structure appearing on top of NPs become more visible as the temperature is increased. In the case of different annealing plateau times, NPs mean lateral size grows with time and density has a trend of decrease. The SEM micrograph of the sample, whose annealing plateau time was 42 min, shows many areas of the substrate which are not covered with nanoparticles. This fact can explain the small value of density.

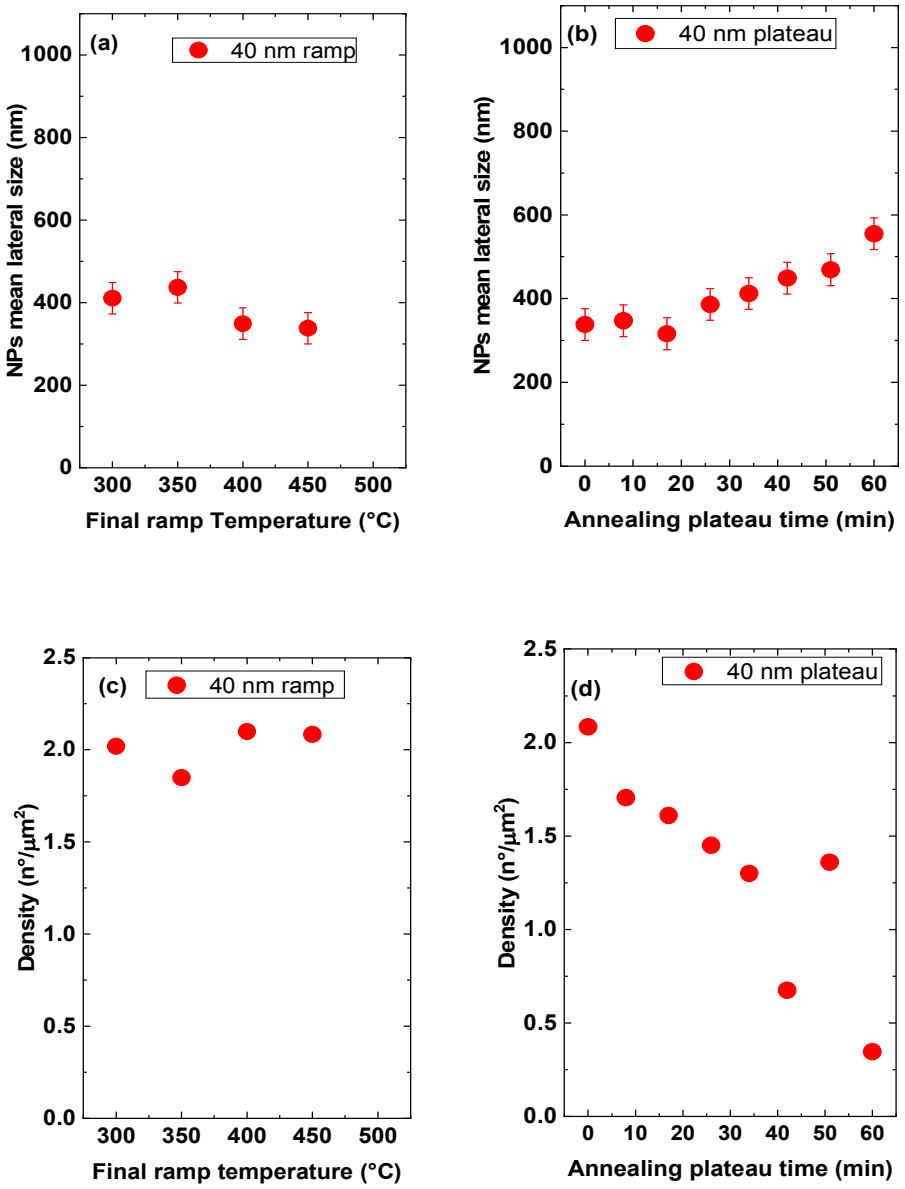


Figure 5.21: a) Plot of mean NP lateral size (in the plane of the substrate) and c) density (number of particles per unit area) vs. final ramp temperature for samples whose TT ends on the ramp. b) Plot of mean NP lateral size (in the plane of the substrate) and d) density (number of particles per unit area) vs. annealing plateau time for samples whose TT ends in the plateau. The initial film nominal thickness was 40 nm for all cases and for b) and d) the working temperature was 450°C.

The same study of Ostwald ripening made for the 80 nm samples was repeated with the 40 nm samples. In Figure 5.22, a linear fit of D^2 vs annealing plateau time t was superimposed and again, the evolution with time follows this theory.

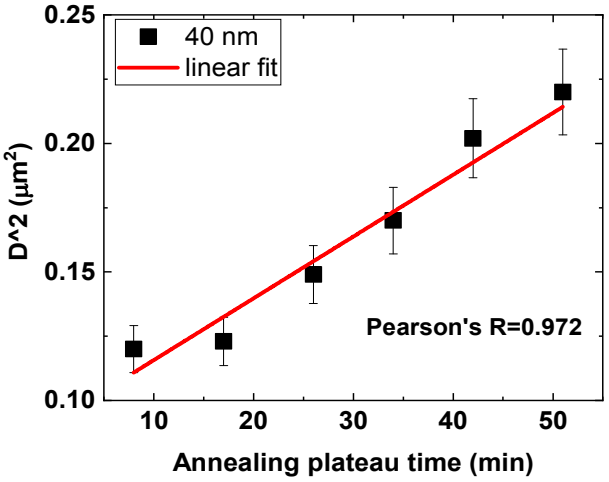


Figure 5.22: Graph of D^2 vs. annealing plateau time for samples whose initial thin film thickness was 40 nm. A linear fit is superimposed. The working temperature was 450°C. D is the mean lateral size (in the plane of the substrate)

The same AFM study, as for the 80 nm film nominal thickness, was made for the 40 nm film. In **Figure 5.23**, AFM images are shown for samples whose thermal treatment ended at 17 min, 34 min and 51 min of the plateau.

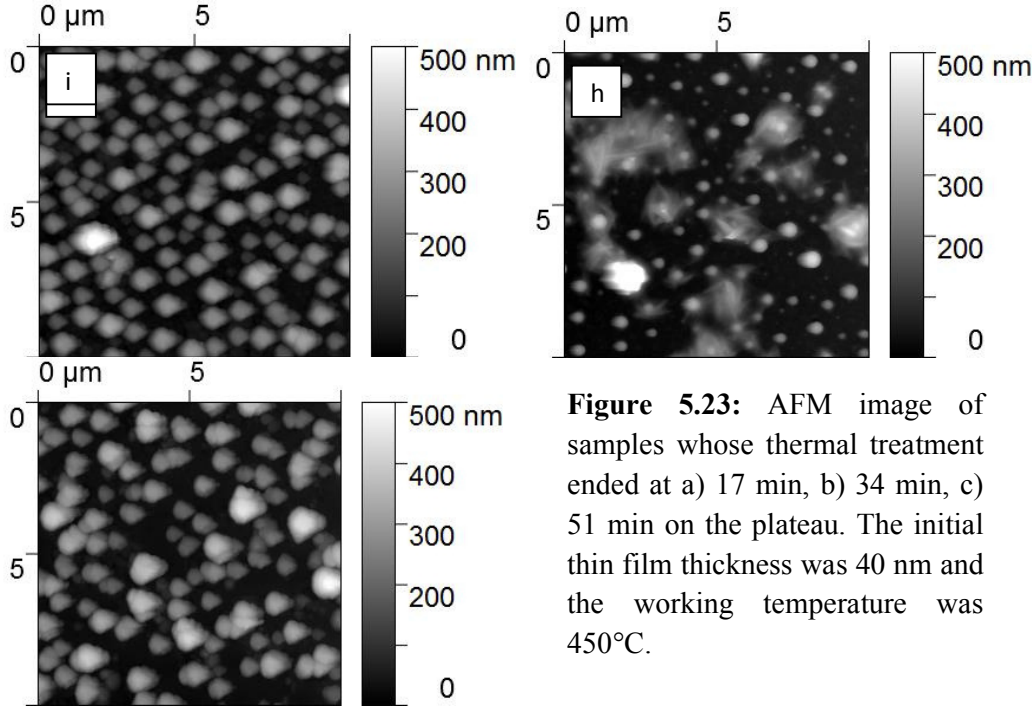


Figure 5.23: AFM image of samples whose thermal treatment ended at a) 17 min, b) 34 min, c) 51 min on the plateau. The initial thin film thickness was 40 nm and the working temperature was 450°C.

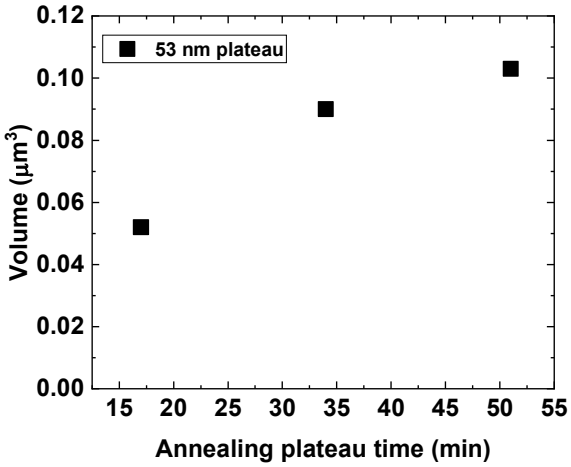


Figure 5.24: Calculated volume of the silver nanoparticle array vs. annealing plateau time for the samples whose AFM images are shown in Figure 5.23. To calculate it, the volume of the particles was modelled as spherical skullcap volume, the mean height of NPs obtained from AFM images of Figure 5.23, the mean lateral size and the density were used.

In **Figure 5.25,** the morphology of nanoparticles prepared from an initial film whose nominal thickness was 40 nm, is shown. The working temperature was 350°C and the time was 0 min. Rounded triangles are observed in the upper part of nanoparticles, but it has not a defined shape.

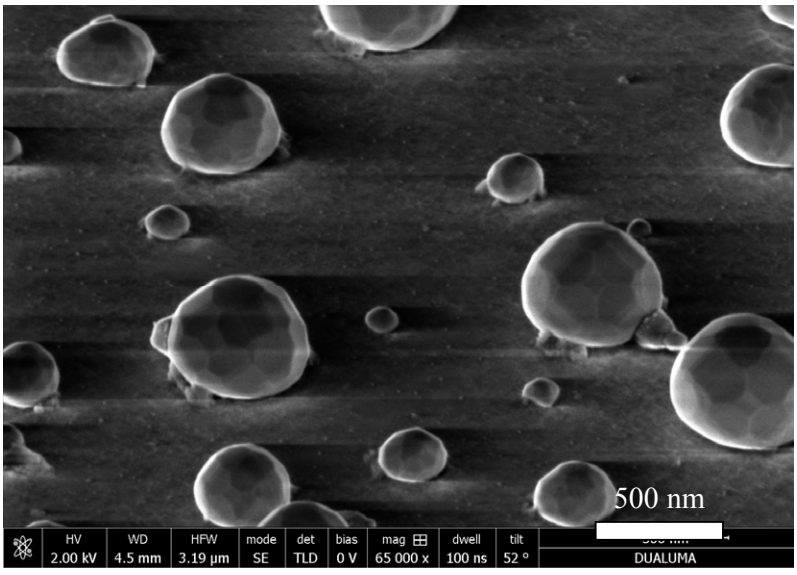


Figure 5.25: FE-SEM micrograph of a sample prepared with an initial thin film whose thickness was 40 nm. The annealing ended on the ramp at 350°C.

Figure 5.26 shows the evolution of nanoparticles morphology with annealing plateau time. The working temperature was 450°C. It is observed that nanoparticles became more faceted with time. The upper part of a nanoparticle is observed in **Figure 5.26 d**. The shape

corresponds to a rhombi-cuboctahedron. But it is combined with spherical shape, which minimizes the surface area.

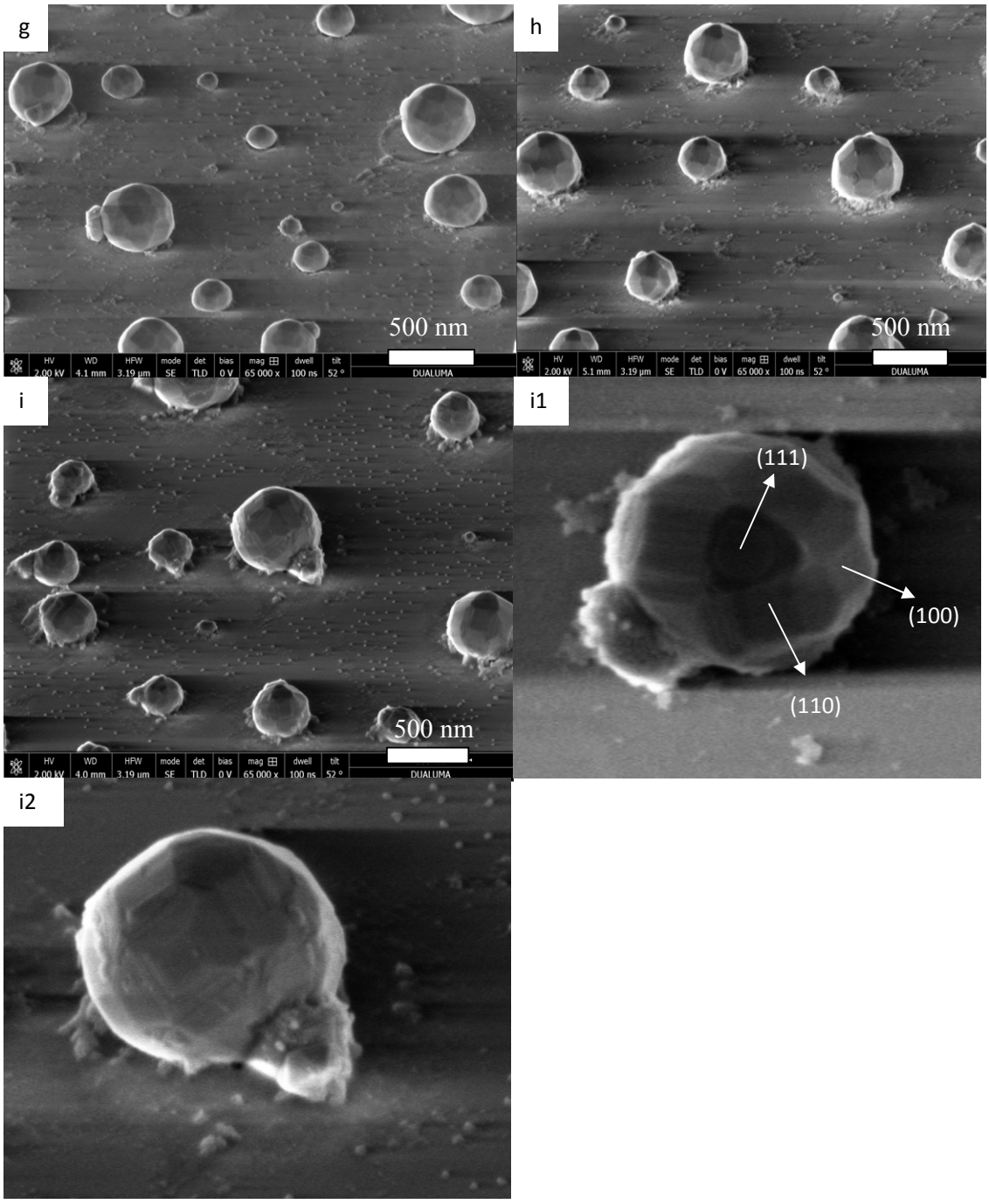


Figure 5.26: FE SEM micrograph of samples whose thermal treatment ended at g) 17 min h) 34 min i) 51 min of the plateau i1-i2) nanoparticle morphology. The initial thin film had a nominal thickness of 40 nm and the working temperature was 450°C.

In **Figure 5.27**, FE-SEM micrographs show the detailed morphology of nanoparticles obtained from an initial thin film whose nominal thickness was 60 nm, for 1 hour and 500°C.

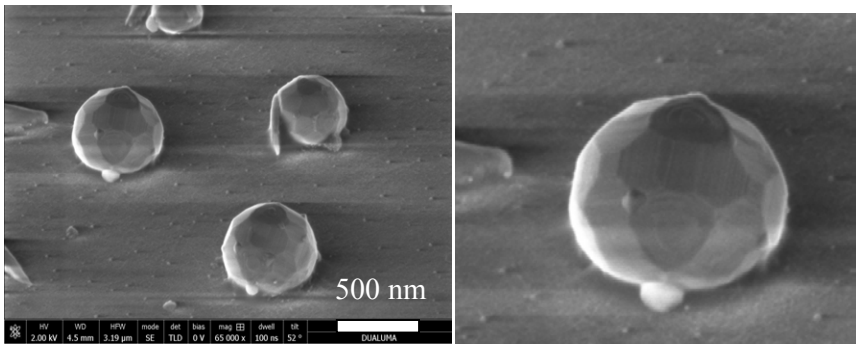


Figure 5.27: FE-SEM micrographs of a sample prepared with an initial thin film nominal thickness of 60 nm. The annealing temperature was 500°C and the annealing plateau time was 1 hour.

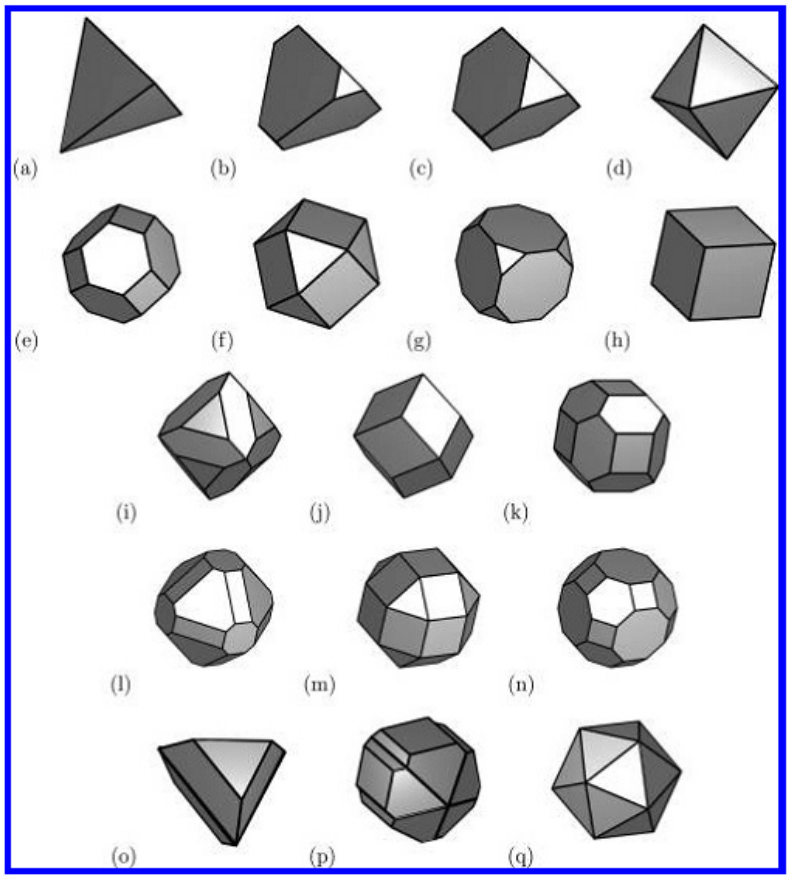


Figure 5.28:.List of geometric bodies a) tetrahedron b) minimally truncated tetrahedron c) truncated tetrahedron d) octahedron e) truncated octahedron f) cuboctahedron g) truncated cube h) cube i) truncated rhombic dodecahedron j) rhombic dodecahedron k) cubo rhombic dodecahedron l) doubly truncated octahedron m) small rhombi-cuboctahedron n) great rhombi-cuboctahedron o) triangular prism, p) marks decahedron q) regular icosahedron [20].

If the shape is compared with the list of geometric bodies which appears in **Figure 5.28**, it is a rounded rhombi-cuboctahedron. Rounded triangles are observed in the upper part and in the lateral surface. Triangles corresponds to (111) surfaces. Small squares are also observed and

they corresponds to (100) and (110) ones [21]. (111) surface has the smaller energy γ and (100) has small stress. Hence, the shape corresponds to a Wulff construction and it contributes to the energy minimization.

A practical summary of the above detailed study is contained in **tables 5.8 and 5.9**. They show the main dependences of NPs mean lateral size and density with working temperature, time and initial thin film thickness. To select a range of size, an initial thin film thickness has to be chosen. The temperature where the SSD is possible, depends on thickness. To fine tune the NPs mean lateral size and NPs density, the most important parameter is the time of the plateau. Hence, first you have to choose the working temperature and then the annealing plateau time.

Table 5.8: Table of size and density dependence on working temperature and annealing plateau time. For initial film nominal thickness of 20 nm, 40 nm, 60 nm and 80 nm.

80 nm	**Temperature**	**Time**	**(20, 40, 60) nm**	**Temperature**	**Time**
Size	Yes	Yes	Size	No	Yes
Density	No	Yes	Density	Yes	Yes

Table 5.9: Table of size and density dependence on initial thin film thickness

	Thickness
Size	Yes
Density	No

5.2 Structural studies: X ray diffraction analysis

5.2.1 Effects of the initial thin film thickness and of the working temperature.

The texture of a polycrystalline film influences the energy of the system by changing the surface energy and interface film/substrate energy. Surface energy is defined as the excess surface free energy per unit area for a specific plane. It is an important factor that influences various surface phenomena including faceting, roughening and crystal growth. The value of the surface energy for a specific crystal plane can be obtained by theoretical calculations. The surface energy of Ag is different for different crystal planes and their values for the {111}, {100} and {110} planes obey the following relation $\gamma(111) < \gamma(100) < \gamma(110)$ [22]. Therefore, Ag polycrystalline films would tend to adopt a texture which decreases the energy of the system. This adaptation becomes possible if sufficient thermal energy is supplied to the system to overcome the activation energy barrier for atomic motion or grain boundary motion. The enhancement of the (111) peak in comparison with others is a sign of the reduction of total energy of the system by grain re-organization. Some residual oxide peaks may appear below (111) peak.

Agglomeration lets preferential reduction of the surface area of non ⟨111⟩ textured grains, which have bigger surface energy. ⟨111⟩ textured grains are not very much affected by this process. Also, reduction of the interfacial energy is likely to be a key driving force for agglomeration, because the interfacial energy between Ag and SiO_2 is higher than any of the other energy components that determine the total free energy of the system. In **Figure 5.29** and **Figure 5.30** a collection of X-ray diffractograms are shown. Diffractograms of initial thin films appear on the left, while diffractograms after thermal treatment are on the right.

In the case of precursor films, four peaks corresponding to crystalline Ag, are recognized. They are (111), (200), (311), (222). After the thermal treatment, (111) and (222) peaks enhance in comparison with other peaks, mainly in samples whose initial thin film nominal thickness were 40 nm and 80 nm. After subtraction of the $K\alpha_2$ contribution, the position of the (111) peaks and their full width at half maximum (FWHM) were extracted using a gaussian fit. Intrinsic width B, corrected from instrumental contribution, is:

$$B = \sqrt{B_m^2 - B_{ins}^2} \qquad \textbf{5.3}$$

and the crystallite size obtained by Scherrer equation is:

$$\boldsymbol{D_C = \frac{k\lambda}{B\cos\theta}} \qquad \textbf{5.4}$$

K=0.9, $\lambda = 1.54$ Å and B_{ins}, which is the instrumental broadening, was obtained from a diffractogram of a silicon monocrystal. In this case, B_{ins} is 0.14°

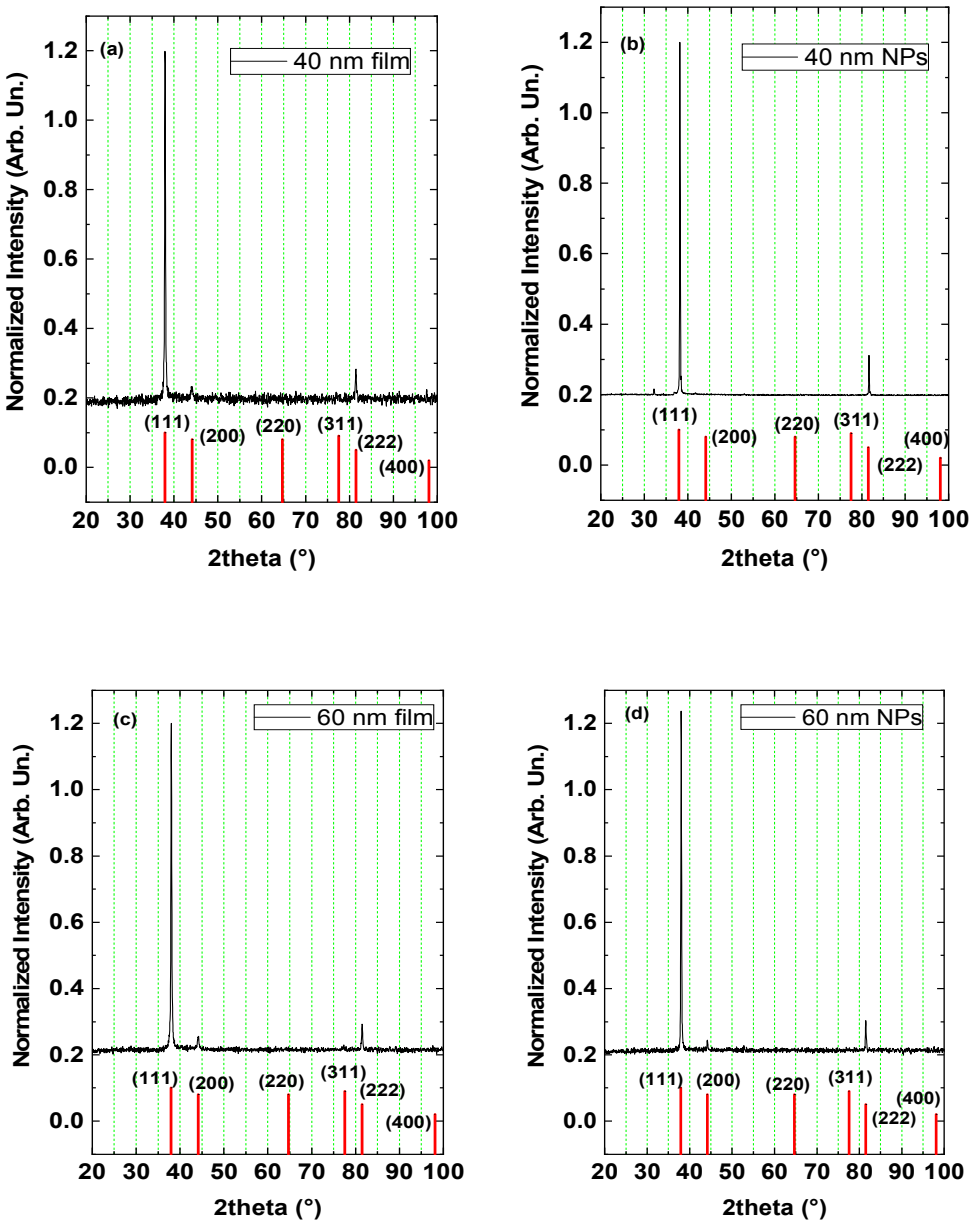


Figure 5.29: X-ray diffractogram of a silver initial thin film on glass whose nominal thickness was a) 40 nm and c) 60 nm. X-ray diffractogram of samples of silver NPs on glass prepared by a SSD activated by a thermal treatment of 450°C 1 h. The initial thin film nominal thickness were b) 40 nm and d) 60 nm. JCPDS pattern of Ag was added for comparison (red lines).

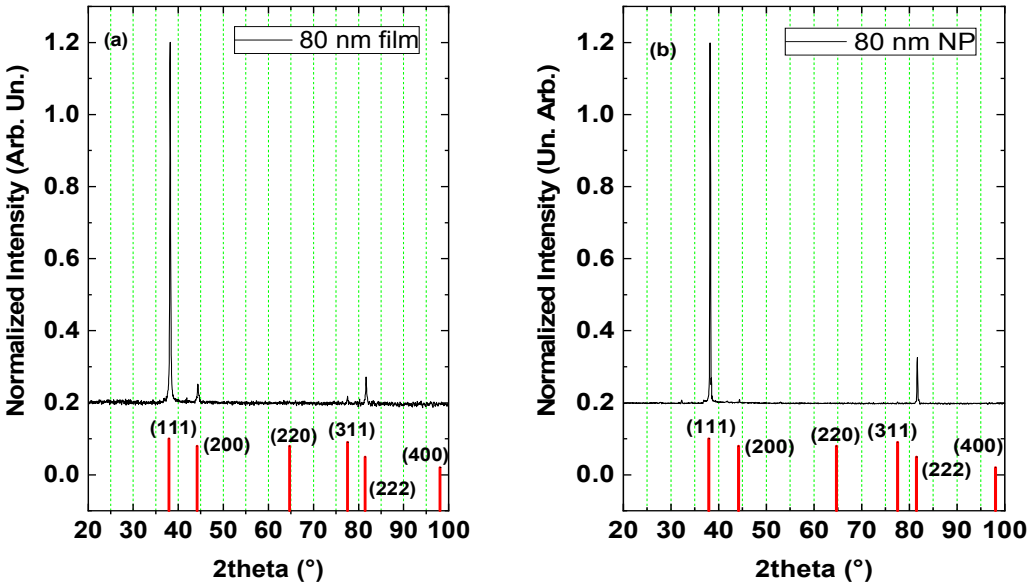


Figure 5.30: a) X-ray diffractogram of a silver initial thin film on glass whose nominal thickness was 80 nm. b) X-ray diffractogram of samples of silver NPs on glass prepared by a SSD activated by a thermal treatment of 450°C 1 h. The initial thin film nominal thickness was 80 nm. JCPDS pattern of Ag was added for comparison (red lines).

A statistical study of the out of plane crystallite (OPC) size and (111) peak positions of initial thin films was made. The results are shown in **Figure 5.31.** The mean size grows with thickness and the (111) peak positions are at higher angles than for the bulk. Thus, grains are compressed in the out of plane direction.

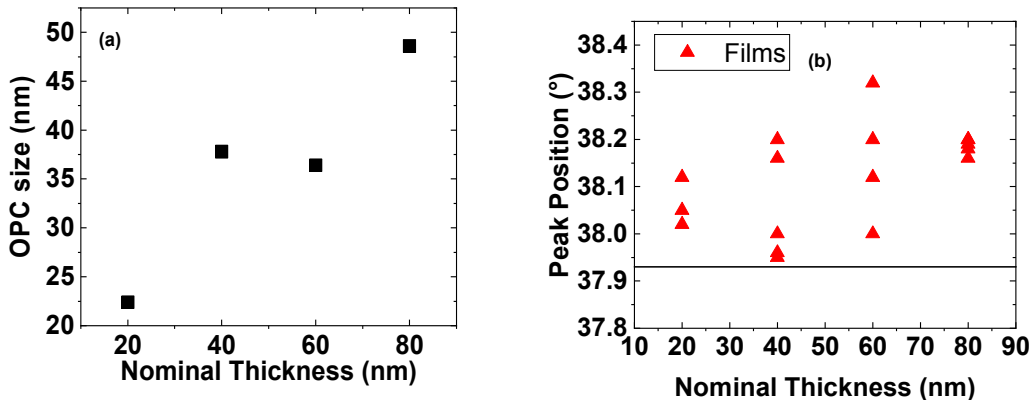


Figure 5.31: a) Mean out of plane crystallite (OPC) size calculated by Scherrer equation of films vs. nominal thickness b) Peak positions of (111) peak for films vs. nominal thickness. The horizontal line corresponds to the bulk value.

In **Figure 5.32**, positions of the (111) peaks vs. working temperature are presented. In general, the positions are at higher angles than for the bulk. But the trend presents a minimum at a certain temperature. For an annealing plateau time of one hour, this minimum is in the 400°C-450°C region.

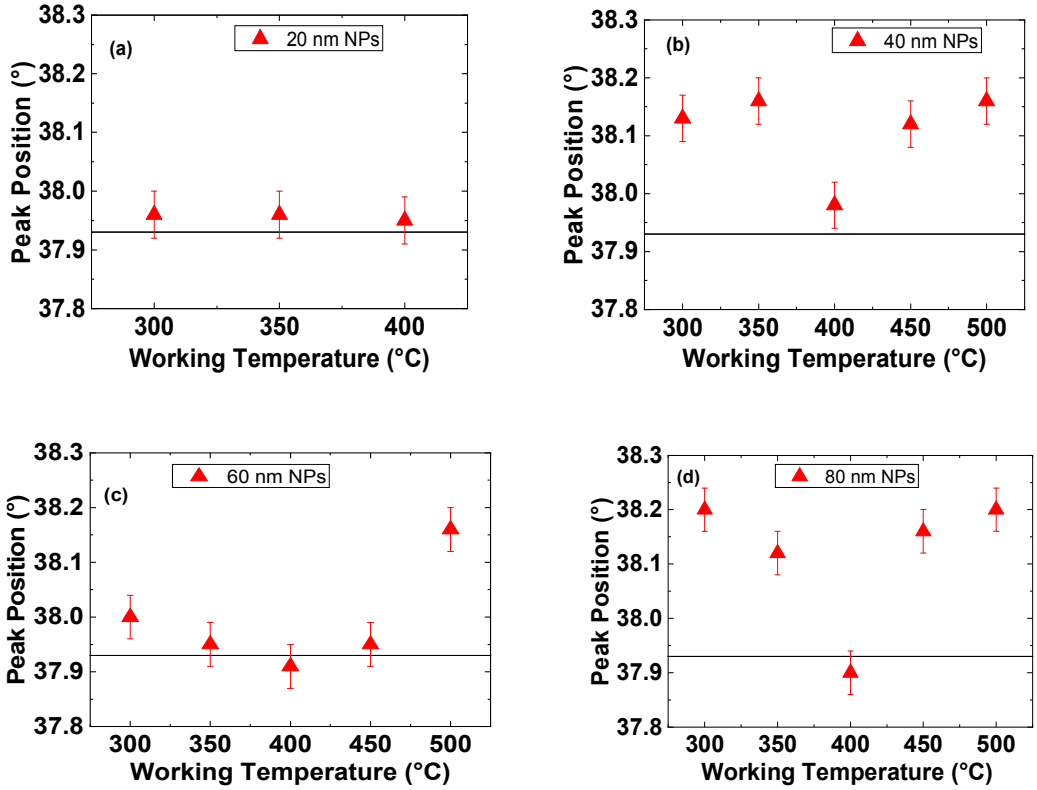


Figure 5.32: Position of the (111) peak vs. working temperature for samples whose initial thin film nominal thickness was a) 20 nm, b) 40 nm, c) 60 nm, d) 80 nm. The annealing plateau time was 1 hour. The line indicates the (111) peak position for the bulk.

The out of plane strain was calculated using the equation:

$$\varepsilon_z = -\frac{\Delta\theta}{tg\theta} \qquad \textbf{5.5}$$

where θ is the position of the peak and $\Delta\theta$ is the shift compared with the bulk peak position. Using linear elastic theory and considering the normal to the samples as a stress-free direction, the in plane strain ε_x can be calculated as a function of the measured out of plane strain ε_z and Poisson ratio ν:

$$\varepsilon_x = -\frac{(1-\upsilon)\varepsilon_z}{2\upsilon} \qquad \textbf{5.6}$$

The in-plane stress can be calculated as follows:

$$\sigma_x = M_{hkl}\varepsilon_x \qquad \textbf{5.7}$$

where M_{hkl} is the biaxial modulus for the considered crystallographic orientation. The biaxial modulus for Ag [111] orientation grains is $M_{[111]} = 175$ GPa [23].

Figure 5.33 shows plots of OPC size and stress vs. working temperature for different silver initial thin film nominal thickness.

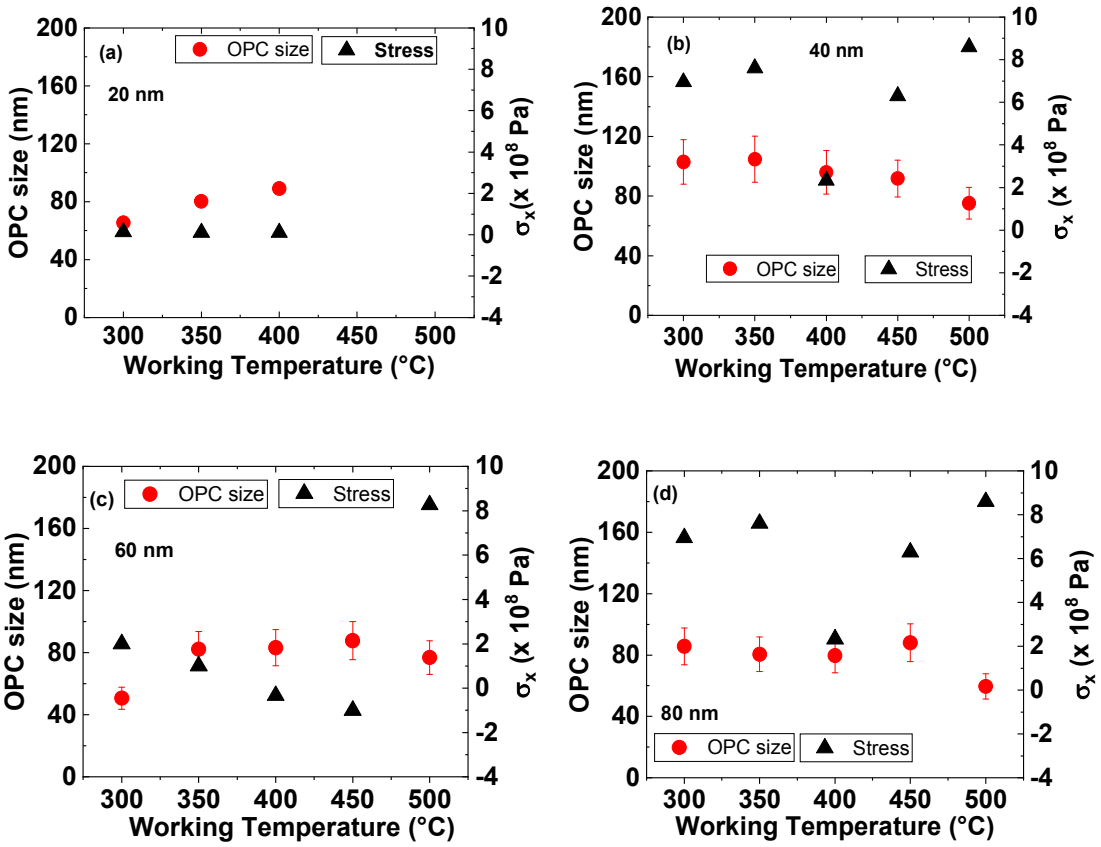


Figure 5.33: Plots of the out of plane crystallite (OPC) size calculated by Scherrer equation, using (111) X-ray diffraction peak, and in plane stress calculated by **equation 5.7** vs. working temperature. The nominal thickness of the initial thin film was a) 20 nm, b) 40 nm, c) 60 nm and d) 80 nm. The annealing plateau time was 1 hour for all cases.

It is observed that OPC sizes of samples are larger than those of initial thin films. A general trend is that OPC remains constant, except for 500°C. The in-plane stress shows a minimum between 400°C and 450°C. It is important to say that at 550°C, there are only peaks of silver oxide in the X-ray diffractogram. In the case of samples prepared with an initial thin film of 20 nm, this temperature is 450°C.

With only these results, it is difficult to conclude. For this reason, we made a study varying the final ramp temperature and annealing plateau time. Two initial thin film thicknesses were used: 40 nm and 80 nm. Also, two working temperatures were studied: 450°C and 500°C.

5.2.2 Effects of the final ramp temperature and of the annealing plateau time

Figure 5.34 is a diagram of the temperature profile of the annealing process. The red squares indicate the end of the annealing. In this plot, a plateau at 500°C is shown, but the profile is valid for other working temperatures.

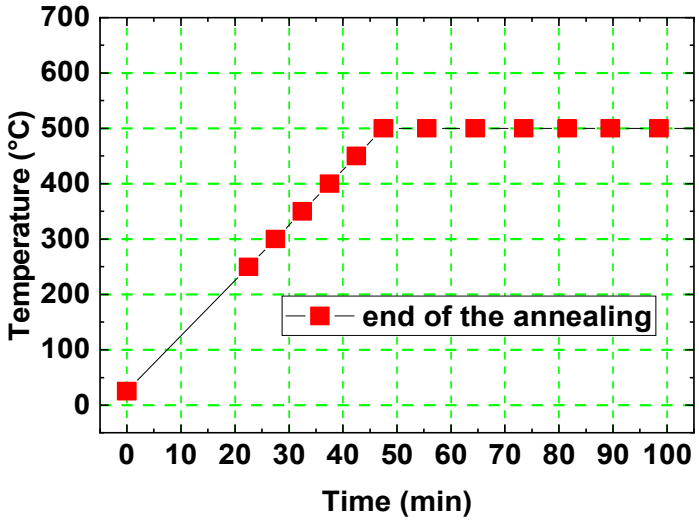


Figure 5.34: Diagram of the annealing profile. Red squares indicate the end of the annealing.

Figure 5.35 a shows graphs of OPC size and in-plane stress vs. final ramp temperature (0 min annealing plateau time). **Figure 5.35 b** and **Figure 5.35 c** display plots of OPC size and stress vs. annealing plateau time. The working temperatures were 450°C and 500°C respectively. In **Figure 5.35 a**, a minimum of OPC size and a maximum of the in plane stress are recognized at 350°C. For this temperature, spherical disconnected objects are observed in FE-SEM micrographs for the first time. An abrupt change of stress occurs from 350°C to 400°C and OPC grows again. So, re-organization of grains occurs to diminish the in-plane stress. In **Figure 5.35 b**, OPC size and in-plane stress are plotted as a function of annealing plateau time. The working temperature was 450°C. At 0 min, the in-plane stress is compressive, then there is an abrupt increment towards high tensile stress after 8 min. For later times, both in-plane stress and OPC size remain constant.

In **Figure 5.35 c**, the working temperature was 500°C. OPC size reaches a maximum at 8 min. From 17 min to 120 min, it decreases. An explanation for the difference with **Figure 5.35 b** (plateau at 450°C) could be the dependence of viscosity of glass with time. Indeed, in the transformation region of glass, the measured viscosity at each temperature is time dependent. But, for example, Bouras et al. [24] mention that the transition temperature of borosilicate glass is 565°C. Another, borosilicate glass called Borofloat33 has a transformation temperature of 525°C [25]. Both temperatures are above 500°C. AFM images show that average height of NPs decreases from 17 min of the plateau due to Ostwald

ripening. It is followed by a decrease in the OPC size. Silver agglomerates in some particles, but the OPC size does not grow. Stress has a compressive minimum at 51 min, jumps abruptly to a huge tensile stress and then decreases slowly to lower stress values. A re-crystallization occurs. This time coincides with an abrupt increase in density and an abrupt decrease in the average lateral size of particles.

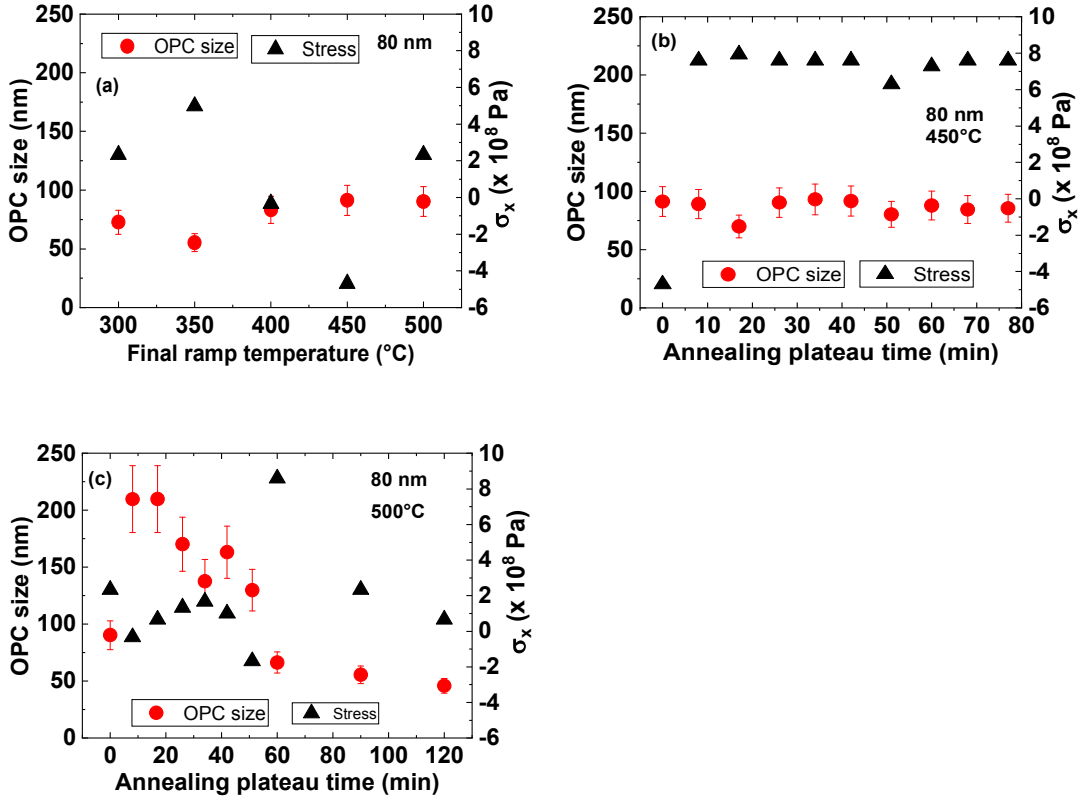


Figure 5.35: a) Out of plane crystallite (OPC) size calculated by Scherrer equation, using (111) X-ray diffraction peak, and in plane stress calculated by **equation 5.7** vs. final ramp temperature (see **Figure 5.34**). OPC size and in plane stress vs. annealing plateau time for working temperature b) 500°C, c) 450°C. The initial film nominal thickness was 80 nm and the annealing ends on the ramp (a) or in the plateau (b,c).

Figure 5.36 a and **Figure 5.36 b** are plots of OPC size and in plane stress vs. temperature reached at a certain final ramp temperature and at a certain annealing plateau time respectively. The initial thin film nominal thickness was 40 nm. A minimum of OPC size and maximum of tensile stress occur at 300°C. At this ramp temperature, FE-SEM image of **Figure 5.19 c** shows disconnected objects with spherical shape, compared with the worm like shape (observed at 250°C). At 350°C, the stress has become compressive and the OPC size is larger than at 300°C. Again, there is an abrupt change in the stress by grain re-organization. For different annealing plateau times, OPC size remains constant. In this case, AFM images of **Figure 5.23** show an increase of NPs height. Ostwald ripening is observed in these samples, but some particles disappear and the mass agglomerates on others. Stress is

constant until 60 min, where there is a sharp increase. During Ostwald ripening, atoms of silver detach particles and attach to others. The remaining particles after this process are far from the Winterbottom shape. Therefore, this step could represent a re-crystallization, where several grains transform into single one.

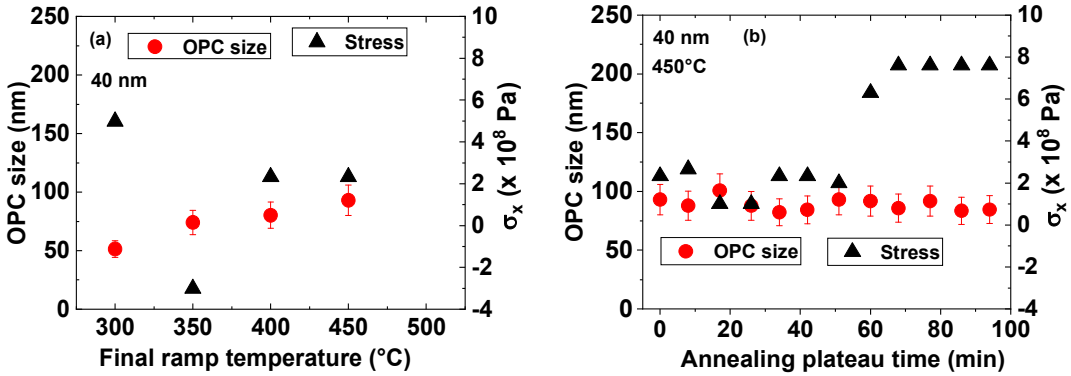


Figure 5.36: a): Graphs of out of plane crystallite (OPC) size calculated by Scherrer equation, using (111) X-ray diffraction peak, and in plane stress calculated by **equation 5.7** vs. final ramp temperature (see **Figure 5.34**). The initial thin film nominal thickness was 40 nm. b) OPC size and in plane stress vs. annealing plateau time. The working temperature was 450°C and the initial film nominal thickness was 40 nm.

Jacquet et al. [8] observed that silver atoms move from the smallest grains, the particle grows on specific facets and its center of mass has a slight displacement. Malyi et al. [12] observed the transformation of a bi-crystal of gold into a single crystal due to GB migration. After that, a shape change occurs due to curvature driven surface diffusion along the non-singular surfaces. At the end of this process it acquires the final shape of single crystal particle, with singular facets. It is shown in Figure 5.37.

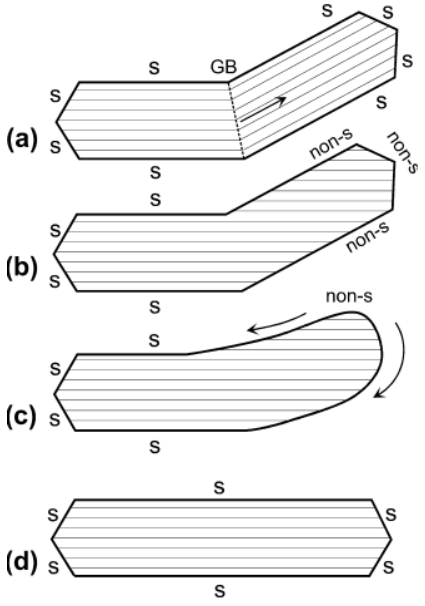


Figure 5.37: Schematic illustration of the mechanism of apparent grain rotation in the bi-crystal particle: (a) the initial configuration of a faceted bi-crystal with singular surface and a GB (b) the transformation of the bi-crystal into a single crystal due to GB migration (c) the shape change of the particle due to surface diffusion (d) the final shape of a single crystal particle with singular facets [11]

Figure 5.38 shows the comparison between samples whose annealing ended on the ramp (0 min) and after 1 hour of annealing plateau. First, OPC sizes for samples prepared with 1 hour of plateau, are equal or larger than for samples whose TT ended on the ramp, except for the working temperature of 500°C. Concerning stress, after one hour of annealing plateau, samples exhibit larger stress values for all working temperatures. Second, the difference in OPC size is bigger for low temperatures (below 400°C). Thus, the grains increase in all directions (out of plane and in plane) for working temperatures below 400°C. While at 400°C and 450°C, grains grow mainly in the in-plane directions. If we observe the FE-SEM micrographs of samples with working temperatures below 400°C and 0 min of annealing plateau (**Figure 5.8** and **Figure 5.19**), the triangle on the top of NP's is not yet well defined. Thus, they need to continue the process on the annealing plateau. Third, the stress for samples after 1 hour on the annealing plateau depends on initial stress at the end of the ramp. In the case of initial compressive stress, there is huge change toward tensile stress after 1 hour annealing. Compressive stress implies high density of grain boundaries. Thus, there is a tendency to increase the in-plane grain size, which favours the decrease in energy. This is observed for 450°C and 80 nm and for 350°C and 40 nm.

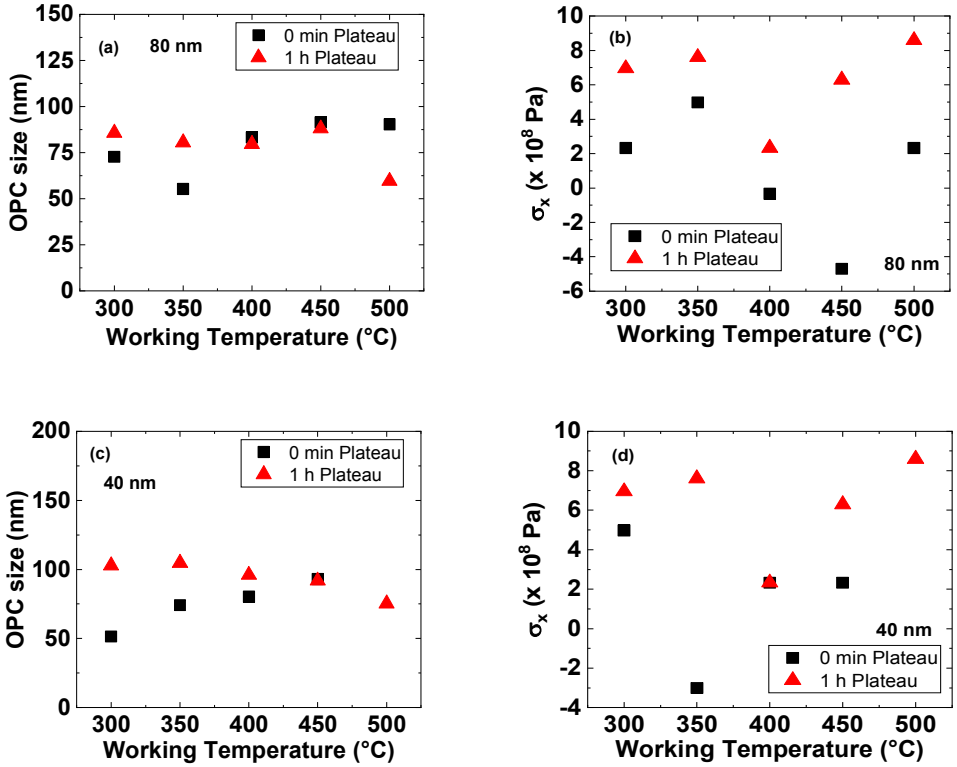


Figure 5.38: Plots of out of plane crystallite (OPC) size calculated by Scherrer equation, using (111) X-ray diffraction peak (a and c), and in plane stress calculated by **equation 5.7** (b and d) vs working temperature. The black squares correspond to samples whose annealing plateau time is 0 min. The red triangles correspond to samples with an annealing plateau time of 1 hour. The nominal thickness of the initial film was 80 nm (a,b) and 40 nm (c,d).

5.3 Optical Properties (Transmittance)

5.3.1 Effects of the initial film thickness and of the working temperature

UV-Vis optical transmittance spectra of different samples were measured. Spectra which correspond to different thickness of the initial thin film and different working temperature are shown in **Figure 5.39**.

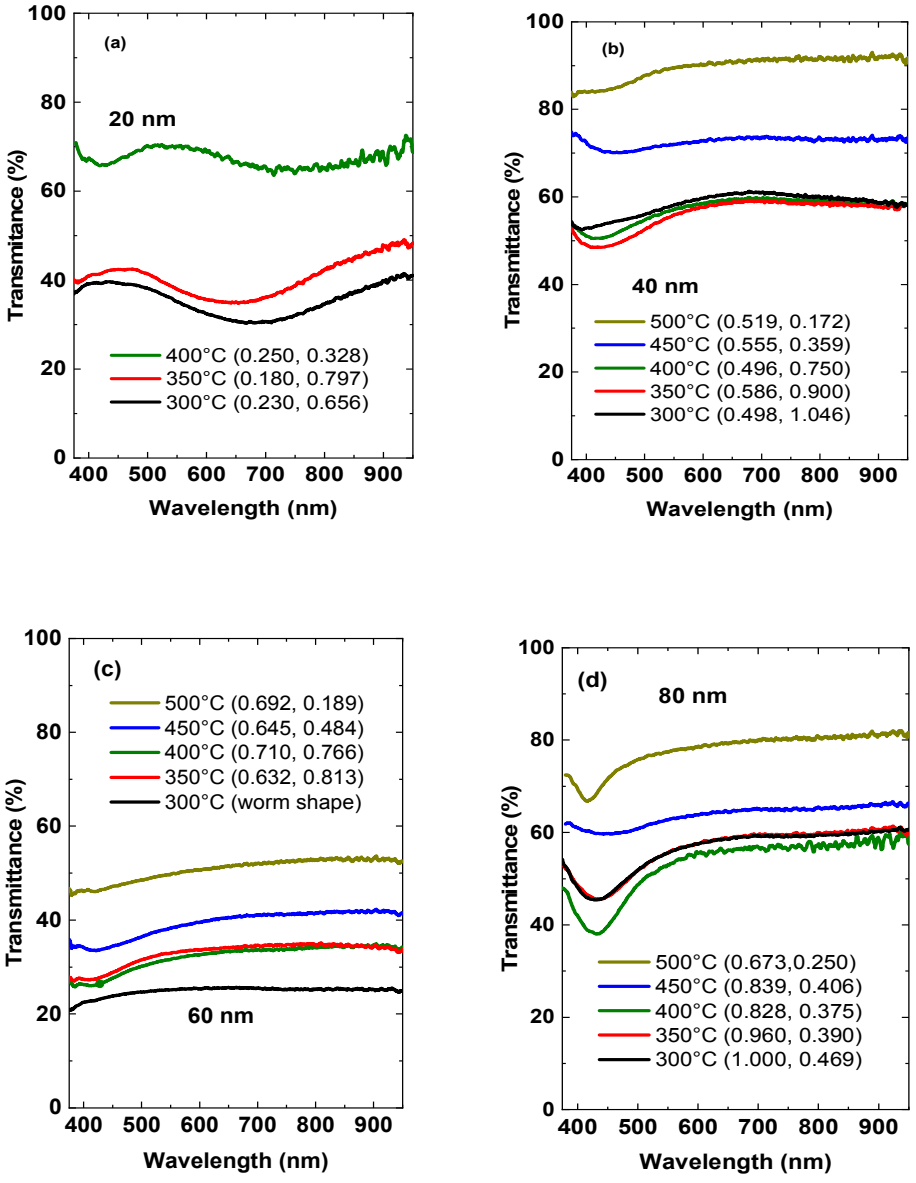


Figure 5.39: Optical transmittance for samples obtained at different working temperatures. The annealing plateau time was 1 hour. The nominal thickness of the initial thin films were a)

20 nm b) 40 nm c) 60 nm and d) 80 nm. The quantities, which are in the parenthesis, are the mean lateral size (μm) and density (particles/μm^2)

For an initial thin film nominal thickness of 40 nm, 60 nm and 80 nm, the transmittance of samples prepared with a thermal treatment whose working temperatures were 450°C and 500°C are larger than the transmittance of samples prepared with a thermal treatment whose working temperature were 400°C, 350°C and 300°C. Also, a separation between the two groups of spectra is recognized. One reason of this behaviour is that the presence of oxide in the surface of NPs is more important for 450°C and 500°C. The presence of silver oxide is presented in **Figure 5.52** and **Figure 5.53**.

For most of the curves, there is a dip in the transmittance spectra. This dip corresponds to a surface plasmon resonance (SPR).

Plots of SPR wavelengths vs working temperature are shown in **Figure 5.40**. The annealing plateau time was 1 hour. Different colors correspond to different initial thin film thicknesses. All SPR wavelengths, falls below 450 nm and are largely influenced by the interaction between NPs.

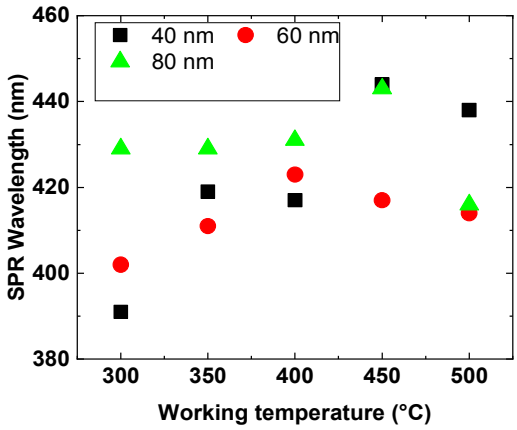


Figure 5.40: SPR wavelengths for different working temperatures. The annealing plateau time was 1 hour. Each symbol corresponds to different nominal thickness of the initial film.

For samples prepared with a film with a nominal thickness of 40 nm, SPR wavelength increases with working temperature. These samples exhibit the clearest trend. In the case of 60 nm samples, there is a red shift from 300°C to 400°C and a blue shift from 400°C to 500°C. For 80 nm samples, SPR wavelength has a red shift until 450°C. From 450°C to 500°C, there is a blue shift.

In the case of hemispherical particle on a substrate whose dielectric constant ε_{sub} fulfill $(\varepsilon_{sub}/\varepsilon_m = 2.25)$, the polarizability of the hemispherical particle is:

$$\alpha(\omega) = 0.52R_H^3 \frac{\frac{\varepsilon(\omega)}{\varepsilon_m} - 1}{\frac{\varepsilon(\omega)}{\varepsilon_m} + 6.61} \quad \textbf{5.8}$$

Now $Re[\alpha]$ and $Im[\alpha]$ will be calculated, both in function of wavelength (λ). For that, I consider ε_{out} =1 and $\varepsilon(\lambda) = (n + ik)^2$. n and k are the real part and imaginary part of the complex refractive index. Both were obtained from [27], in function of wavelength. The plots of $Re[\alpha]/R_H^3$ and $Im[\alpha]/R_H^3$ are shown in **Figure 5.41.**

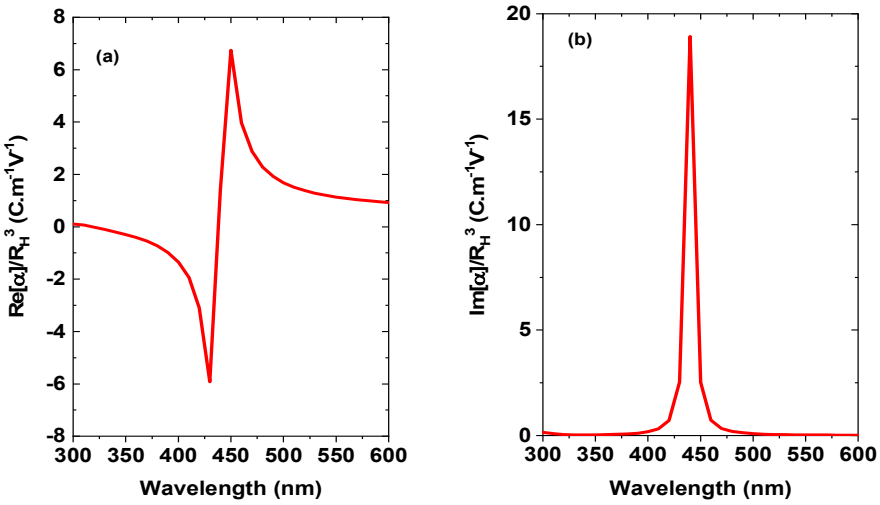


Figure 5.41:a) $\boldsymbol{Re[\alpha]/R_H^3}$ and b) $\boldsymbol{Im[\alpha]/R_H^3}$ for a hemispheroid supported on glass. The maximum of $\boldsymbol{Im[\alpha]/R_H^3}$ is at 440 nm. $\boldsymbol{\alpha}$ is the polarizability and $\boldsymbol{R_H}$ is the radius of the hemispheroid in the plane of the substrate.

The correlation between SPR wavelength of **Figure 5.40** with NPs mean lateral size and/or NPs density are shown in **Figure 5.42**. Two trends are observed in these plots. The first is between SPR wavelength and mean lateral size, for samples whose initial thin film nominal thickness is 80 nm. There is a blue shift with mean lateral size. The second is between SPR wavelength and density for an initial thin film nominal thickness of 40 nm. Again, it corresponds to a blue shift. Malynich et al. [28], Haynes et al. [29], Zou et al. [30] and Félidj et al. [31] also noted a blue shift of SPR wavelength with density. However Gunnarson et al. [32], Tabor et al. [33] and Jain et al. [34] noted a red shift, The red shift was observed for NPs, whose diameters were smaller than 100 nm. Gong et al. and Kinnan et al. observed that for arrays of particles larger than 128 nm there is a blue shift [35] [36]. Thus it is in accordance with the sizes of NPs of the samples prepared in this work. In spite of that, it is very important to mention that the mean lateral size and the density are not varied independently.

But these correlations, are not enough to explain the shifts of surface plasmon resonance because the mean lateral size an density are not varied independently. After that, the dependence of SPR wavelength on $\left(\frac{d_{CC}}{D}\right)$ was studied. d_{CC} is the average distance

between particles (with their nearest neighbours) and D is the average diameter of the particles.

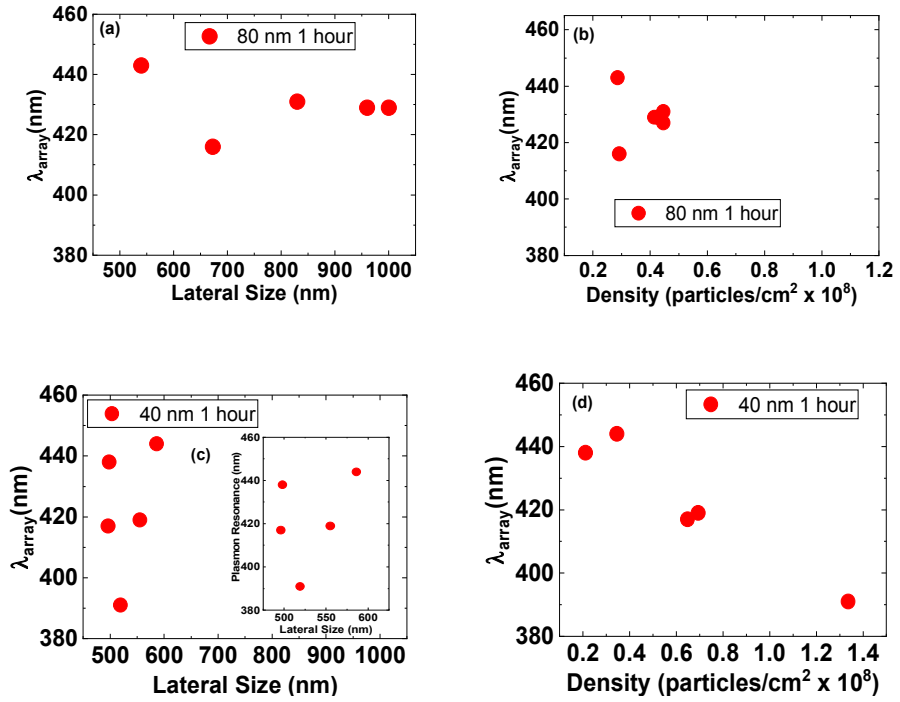


Figure 5.42: $\boldsymbol{\lambda_{array}}$ (wavelength of the surface plasmon resonance of the array) vs D (mean lateral size) and vs density of nanoparticles for samples whose initial thin film nominal thickness was 80 nm a) b) and 40 nm c) d). The annealing plateau time was 1 hour in all cases. It is very important to mention that the mean lateral size and the density are not varied independently.

Jenkins et al. observed a blue shift of SPR from dipole coupling in gold NPs random arrays. The theoretical extinction spectra of this array on glass are independent of the incident polarization (in plane) of the electric field [37]. Markel et al. [38] and Zou et al. [30] proposed a model for infinite chains and arrays. In this approach, the retarded dipole sum S of **equation 2.24**, consist of electrostatic $\left(\sim\frac{1}{r^3}\right)$, radiative $\left(\frac{1}{r}\right)$ and retardation $\left(e^{i\vec{k}.\vec{r}}\right)$ contributions, where $\vec{k}$ and $\vec{r}$ are the wave and coordinate vectors of the incoming radiation. The real part of S determines the plasmon resonance wavelength, while the imaginary part determines the plasmon bandwidth. In the near field, electrostatic contribution dominates, while for far fields, the radiative one is more important. The fractional plasmon shift is $\left(\frac{\Delta\lambda}{\lambda_{isol}}\right)$, where

$$\Delta\lambda = \left|\lambda_{array} - \lambda_{isol}\right| \qquad \textbf{5.9}$$

λ_{array} is the SPR wavelength of the array, while λ_{isol} is the SPR of the isolated particle. The change in the SPR wavelength is mainly due to interactions from neighbours NPs. A collective constructive interference of the re radiated electromagnetic wave does not occur

because the randomness. Hence, the far field interaction becomes negligible and the SPR wavelength is dependent on the average particle size and distance between NPs. There are many theoretical studies which debate the SPR dependence on size, shape and distance between NPs. The inter-particle dipolar coupling decay with centre to centre distance as d_{CC}^{-3} (electrostatic coupling) or d_{CC}^{-1} (radiative coupling) (see chapter 2) [39]. While, the intra-particle restoring potential (inverse of the dipole polarizability) is inversely proportional to D^3 [34]. If only the d_{CC}^{-3} term is considered, the fractional shift $\left(\frac{\Delta\lambda}{\lambda_{isol}}\right)$ is a function of $\left(\frac{d_{CC}}{D}\right)^{-3}$. Jain et al. [34] considered an universal scaling behaviour with an exponential function. But it has been a matter of great discussion. Kadkhodazadeh et al. [40] found a relation of $\left(\frac{D}{d_{CC}}\right)^{n}$ for dimmers and n=3 is for classical dipolar coupling. From **Table 5.10** to **5.12,** we summarize the values of SPR wavelength and the relation d/D for different working temperatures. Each table corresponds to different initial thin film thickness.

Table 5.10: Table of d_{CC}/D and λ_{array} (nm) for different working temperatures. The annealing plateau time was 1 hour, and the initial film nominal thickness was 40 nm. The asterisks correspond to points plotted in **Figure 5.43**

Temperature (°C)	d_{CC} (µm)	D (µm)	d_{CC}/D	λ_{array} (nm)
300 (*)	1.212	0.498	2.434	391
350	1.344	0.586	2.294	419
400 (*)	1.393	0.496	2.808	417
450 (*)	1.950	0.555	3.514	444
500 (*)	2.046	0.519	3.942	438

Table 5.11: The description of the table is the same as Table 5.10, except the initial film nominal thickness which is 60 nm.

Temperature (°C)	d_{CC} (µm)	D (µm)	d_{CC}/D	λ_{array} (nm)
350 (*)	1.128	0.632	1.785	409
400 (*)	1.414	0.710	1.991	413
450 (*)	1.634	0.645	2.533	420
500	2.944	0.692	4.254	417

Table 5.12: description of the table is the same as Table 5.10, except the initial film nominal thickness which is 80 nm.

Temperature (°C)	d_{CC} (µm)	D (µm)	d_{CC}/D	λ_{array} (nm)
300 (*)	1.818	1.000	1.818	429
350 (*)	1.807	0.960	1.882	429
400 (*)	1.916	0.828	2.314	431
450	2.642	0.839	3.148	443
500	2.078	0.673	3.088	416

Figure 5.43 shows plots of SPR wavelength vs $\left(\frac{d_{CC}}{D}\right)^{-3}$. The plotted points correspond to the asterisks of the **tables 5.10** to **5.12**. Using $\Delta\lambda = \lambda_0 - \lambda$, the two following equations were obtained:

$$\Delta\lambda = k\lambda_{isol}\left(\frac{d_{CC}}{D}\right)^{-3} \quad \textbf{5.10}$$

$$\lambda = \lambda_0 - k\lambda_{isol}\left(\frac{d_{CC}}{D}\right)^{-3} \quad \textbf{5.11}$$

k is a proportional constant. Plots of **Figure 5.43** shows, corresponding to samples prepared by an annealing of one hour. Linear fits were made and different values of λ_0 were obtained.

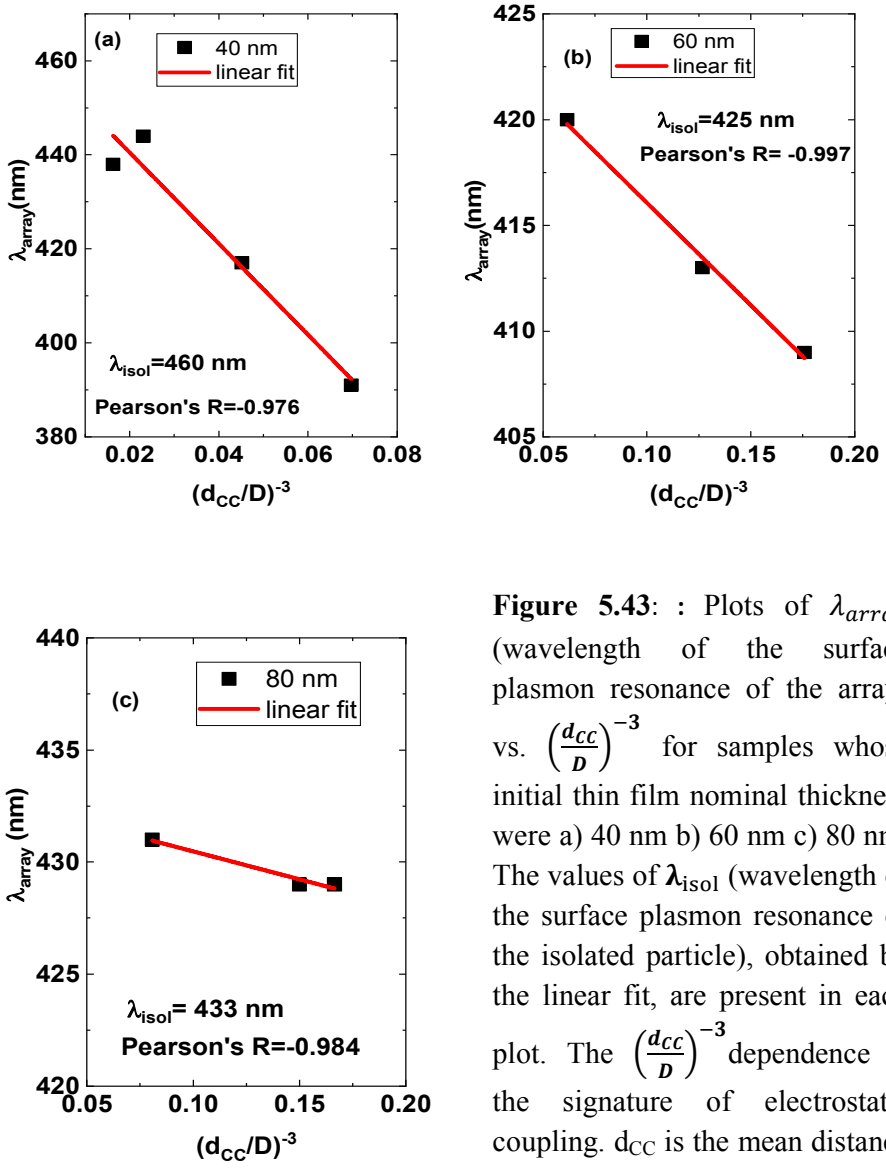


Figure 5.43: **:** Plots of λ_{array} (wavelength of the surface plasmon resonance of the array) vs. $\left(\frac{d_{CC}}{D}\right)^{-3}$ for samples whose initial thin film nominal thickness were a) 40 nm b) 60 nm c) 80 nm. The values of $\boldsymbol{\lambda}_{\text{isol}}$ (wavelength of the surface plasmon resonance of the isolated particle), obtained by the linear fit, are present in each plot. The $\left(\frac{d_{CC}}{D}\right)^{-3}$ dependence is the signature of electrostatic coupling. d_{CC} is the mean distance between nearest neighbours and D is the mean lateral size.

The linear dependence with $\left(\frac{d_{CC}}{D}\right)^{-3}$ leads to electrostatic coupling. This behaviour was observed by Kadkhodazadeh et al. [40] for silver dimers. These explanations consider collective modes by coupling dipoles of the different NPs, but there are other factors which generate red-shift or blue-shift of surface plasmon resonance of individual nanoparticles (for example: shape, spill out)

5.3.2 Effect of the final ramp temperature and of the annealing plateau time.

UV Vis optical transmittance spectra of samples, whose thermal treatment ended at certain temperature on the ramp, are shown in **Figure 5.44 a**. The spectra of samples, whose process ended at different annealing plateau times, are shown in **Figure 5.44 b**. In both cases the initial film nominal thickness was 80 nm**.** A transmittance dip, corresponding to Surface Plasmon Resonance (SPR), is recognized between 400 nm and 500 nm. In the case of the annealing plateau, at a time of 90 min, it is difficult to recognize the dip. Also, lateral size and density obtained by SEM micrographs are minimal for these annealing plateau times.

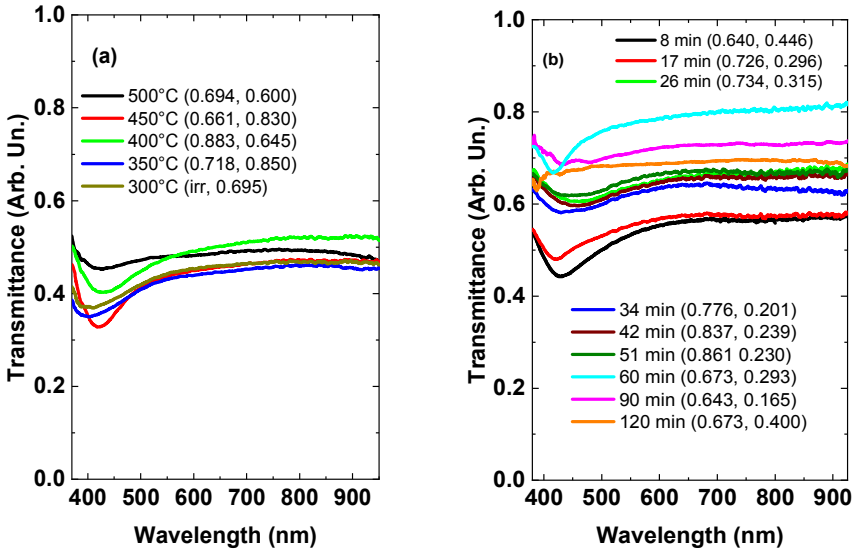


Figure 5.44: Transmittance spectra of samples whose thermal treatment finished a) at different temperatures on the ramp and b) at different times on the annealing plateau. The initial thin film thickness was 80 nm. The quantities, which are in the parenthesis, are the mean lateral size (μm) and density (particles/μm^2). Irr means irregular shape

For spectra depicted in **Figure 5.44,** the wavelength of transmittance dip was obtained and plotted as a function of time (see **Figure 5.45**). A big increase of the transmittance is recognized when the time of the annealing plateau pass from 17 min to 26 min. It coincides with the beginning of the decrease of the OPC size, after reaching a maximum at 8-17 min, as shown in **Figure 5.35 c**. The formation of silver oxide could be generating this big increase. SPR wavelength exhibits a red-shift trend with final ramp temperature. It can be caused by different factor such as the increasing of the size of NPs, the decreasing of NPs density and

the increment of the silver oxide in particles. Kuzma et al. [41] and Serrano et al. [7] concluded that the content of oxygen in nanoparticles grows with working temperature.

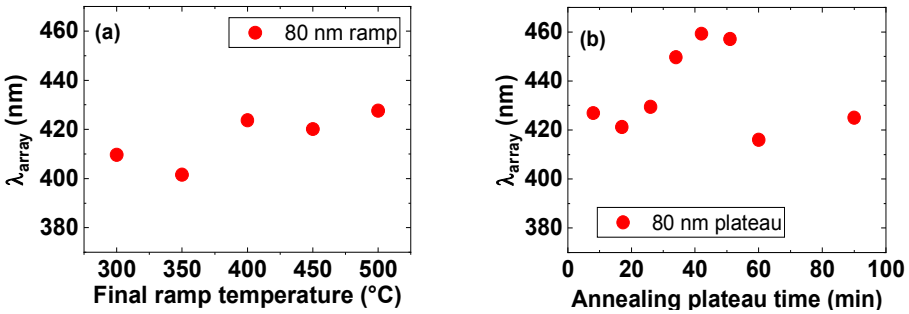


Figure 5.45: $\boldsymbol{\lambda_{array}}$ (wavelength of the surface plasmon resonance of the array) of samples with an initial thin film nominal thickness of 80 nm. The annealing ends on the a) ramp and on the b) annealing plateau. The working temperature was 500°C.

Plots of SPR wavelength vs lateral size and vs density, for the ramp are shown in **Figure 5.46**.

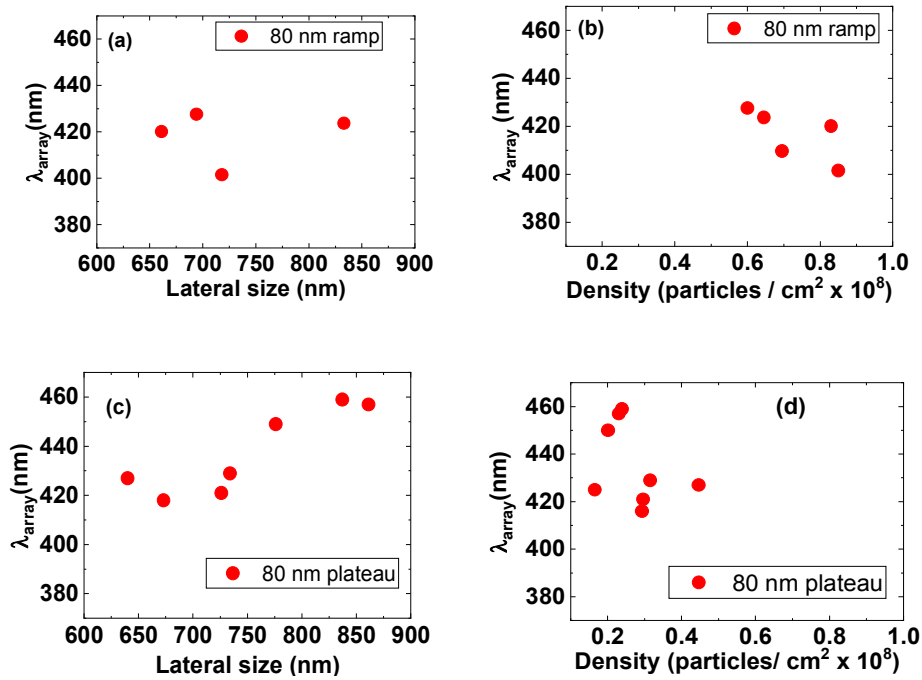


Figure 5.46: $\boldsymbol{\lambda_{array}}$ (wavelength of the surface plasmon resonance of the array) vs mean lateral size and $\boldsymbol{\lambda_{array}}$ vs density for an initial thin film nominal thickness of 80 nm. a) and b) are for ramp and c) and d) are for annealing plateau. The working temperature was 500°C. The mean lateral size and density are not varied independently.

Past studies show that SPR wavelength exhibits a red shift when lateral size enlarged and blue shift when density increases [28]. For the ramp, there is not a clear trend of SPR with NPs mean lateral size. Conversely, a tendency is recognized for density: there is a blue

shift. The case of the plateau is different. Indeed, if the SPR wavelength is plotted against lateral size, there is a red shift, but there is not a clear trend for density. It is important to mention that the mean lateral size and density are not varied independently and these plots do not provide us with a quantitative study of SPR wavelength with lateral size and density. Hence, the mean distance between nanoparticles (with their near neighbours) $\boldsymbol{d_{CC}}$ is calculated statistically, as well as the average lateral size D. The values of $\boldsymbol{d_{CC}}$, D, $\left(\frac{d_{CC}}{D}\right)$ and SPR wavelength are summarized in **Table 5.13** and **Table 5.14**.

Table 5.13: Table of d_{CC}/D and SPR wavelength for samples whose annealing ends on the ramp. d_{CC} is the mean distance between nearest neighbour NPs, D is the NPs mean lateral size. The initial thin film nominal thickness was 80 nm.

Final Ramp Temperature (°C)	d_{CC} (μm)	D (μm)	d_{CC}/D	SPR wavelength (nm)
350 (*)	1.281	0.718	1.794	402
400 (*)	1.885	0.883	2.263	424
450 (*)	1.419	0.661	2.147	420
500 (*)	1.792	0.694	2.582	428

Table 5.14: Table of d_{CC}/D and SPR wavelength for samples whose annealing finished on the annealing plateau. d_{CC} is the mean distance between nearest neighbour NPs, D is the NPs mean lateral size. The initial thin film nominal thickness was 80 nm and the working temperature was 500°C.

Annealing plateau time(min)	d_{CC} (μm)	D (μm)	d_{CC}/D	SPR wavelength (nm)
8 (*)	1.604	0.640	2.506	429
17 (#)	2.040	0.726	2.810	421
26 (#)	2.096	0.734	2.856	429
34 (#)	2.371	0.776	3.055	449
42 (#)	2.739	0.837	3.272	459
51 (#)	2.741	0.861	3.184	457
60	2.067	0.673	2.93	416
90	1.989	0.643	3.11	425
120	1.511	0.673	2.24	388

Plots of SPR wavelength vs $\left(\frac{d_{CC}}{D}\right)^{-3}$ are shown in **Figure 5.47** and linear fits were made. The Pearson's correlation coefficients are -0.976 and -0.981. It is an evidence of strong negative linear relation between these quantities. Kadkhodazadeh et al. [40] observed this behaviour in

silver dimmers, and attributed it to the classical dipolar interaction (electrostatic coupling: see chapter 2), found also in NPs chains. Until the annealing plateau time of 8 min, $\boldsymbol{\lambda_0}$ is 443 nm, while from 17 min to 51 min, $\boldsymbol{\lambda_0}$ is 527 nm. It is an indicative that the relation (h/R) is smaller for the second case.

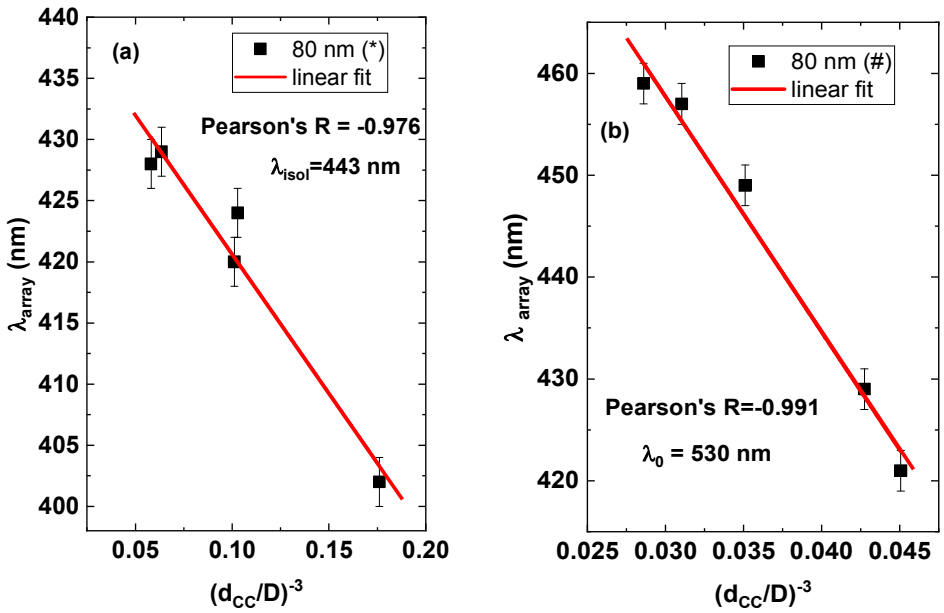


Figure 5.47: a) Plot of $\boldsymbol{\lambda_{array}}$ (wavelength of the surface plasmon resonance of the array) vs. $\left(\frac{d_{CC}}{D}\right)^{-3}$ for data identified with (*) b) Plot of $\boldsymbol{\lambda_{array}}$ vs. $\left(\frac{d_{CC}}{D}\right)^{-3}$ for data identified with (#). The values of $\boldsymbol{\lambda_{isol}}$ (wavelength of the surface plasmon resonance of the isolated particle), obtained by the linear fit, are 460 nm and 527 nm for a) and b) respectively. The dependence in $\left(\frac{d_{CC}}{D}\right)^{-3}$ represents electrostatic coupling. d_{CC} is the mean distance between nearest neighbours and D is the mean lateral size (in the plane of substrate). The initial thin film nominal thickness was 80 nm.

Kuwata et al. [42] studied the dependence of SPR with the morphology of prolate spheroids. They consider $\boldsymbol{a}$ as major axis length and $\boldsymbol{b}$ is the minor axis length. They obtained that if the aspect ratio $\boldsymbol{a/b}$ is bigger, the SPR wavelength has a red shift. Sherbak et al. [43], used the surface integral equations approach to find polarizability spectra and the SPR wavelengths of axisymmetric hemispheroids differing in aspect ratio. They concluded that if $\boldsymbol{h_H/R_H} < 1$, SPR wavelengths have a red shift in comparison with $\frac{\boldsymbol{h_H}}{\boldsymbol{R_H}} = \boldsymbol{1}$. h is the height of the nanoparticle from the substrate, while R is the radius in the plane of the substrate. Therefore, samples whose annealing plateau time is bigger than 8 min, NPs shape become more hemispheroidal because $\boldsymbol{\lambda_{isol}}$ is 527 nm.

Transmittance spectra of samples whose initial thin film nominal thickness was 40 nm are shown in **Figure 5.48**. Spectra of samples whose annealing processes end at 250°C and 300°C, do not show the transmittance dip. This is a sign that particles have not acquired a

defined shape after these annealing processes. However, the dip is present for samples, whose TT ends at 350°C, 400°C and 450°C. Transmittance spectra of samples whose thermal treatment finished at a certain time on the annealing plateau, show a dip, although it is not easy to recognize.

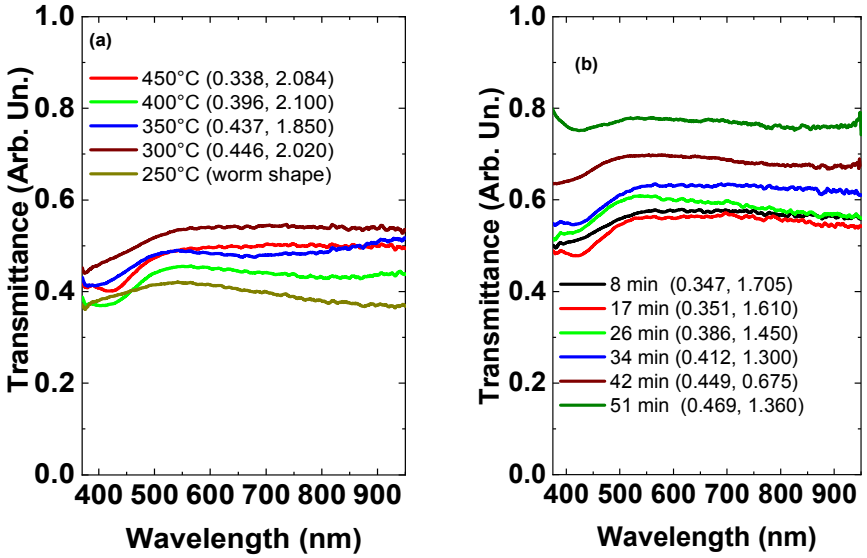


Figure 5.48: Transmittance spectra of samples whose thermal treatment finished a) at different temperatures on the ramp and b) at different times on the annealing plateau. The initial thin film thickness was 40 nm. The quantities, which are in the parenthesis, are the mean lateral size (mm) and density (particles/mm^2)

The SPR wavelengths are plotted vs. ramp temperature and vs. annealing plateau time. They are displayed in **Figure 5.49 a** and **Figure 5.49 b**.

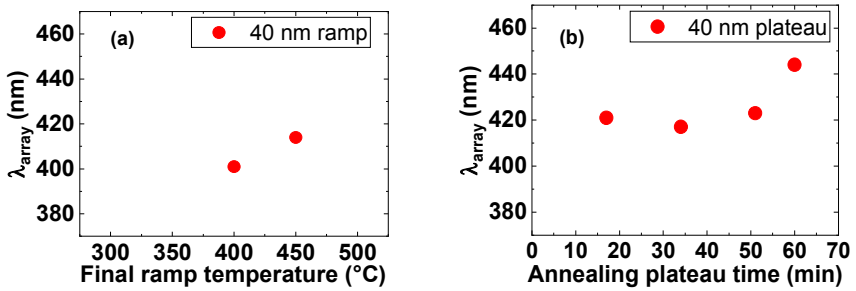


Figure 5.49: a) Surface plasmon resonance (SPR) wavelength vs. final temperature of the ramp for samples whose thermal treatment ends on the ramp b) SPR wavelength vs. annealing plateau time for samples whose thermal treatment ends in the plateau. .

The analysis of SPR with lateral size or density is more difficult than for 80 nm samples. The related plots are shown in **Figure 5.50**. When the annealing ends on the ramp, SPR wavelength exhibits a blue shift for increasing density. Whereas, there is a red shift with

lateral size. If it ends on the annealing plateau, SPR wavelength has a red shift with lateral size. But it is not a clear tendency for density.

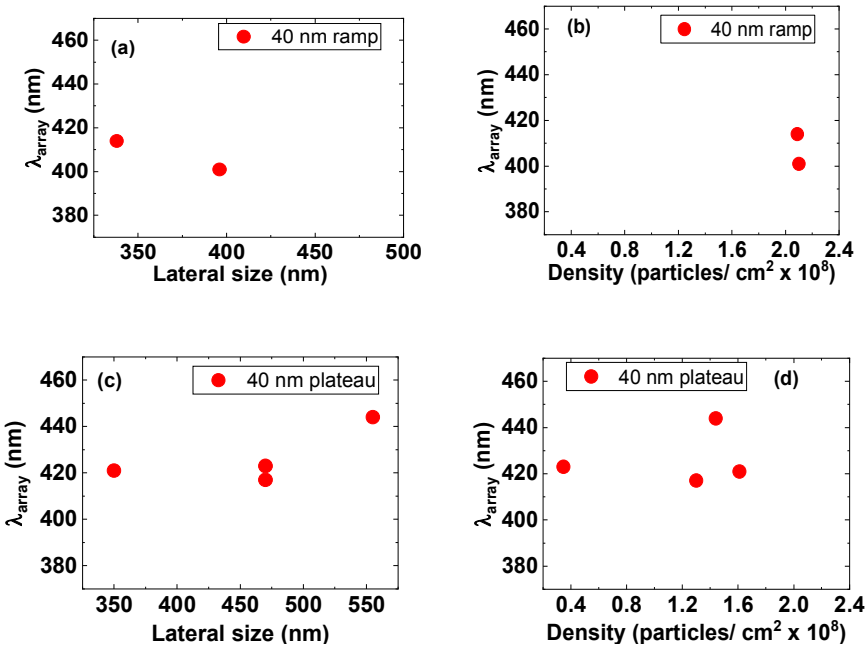


Figure 5.50: a) c) $\boldsymbol{\lambda_{array}}$ (surface plasmon resonance wavelength of the array) vs mean lateral size of NPs, b) d) $\boldsymbol{\lambda_{array}}$ vs density. The nominal thickness of the initial thin film was 40 nm. The mean lateral size and density are not varied independently.

Again, plots of $\boldsymbol{\lambda_{array}}$ with density and size do not let us to conclude. Hence, the mean distance between nearest neighbour particles was calculated statistically as well as the average lateral size (see Tables **5.15** and **5.16**).

Table 5.15: Table of d_{CC}/D and λ_{array} for samples whose annealing finished on the ramp. d_{CC} is the mean distance between particles and D is the particle diameter. The nominal thickness of the initial thin film was 40 nm.

Temperature (°C)	d_{CC} (μm)	D (μm)	d_{CC}/D	λ_{array} (nm)
400	0.814	0.396	2.056	401
450	0.750	0.338	2.219	414

Table 5.16: Table of d_{CC}/D and λ_{array} for samples whose annealing finished on the annealing plateau. d is the mean distance between particles and D is the particle diameter. The initial thin film nominal thickness was 40 nm.

Annealing plateau time (min)	d_{CC} (μm)	D (μm)	d_{CC}/D	λ_{array} (nm)
17	0.850	0.351	2.421	421
34	0.925	0.412	2.245	417
51	1.060	0.469	2.260	423
60	1.630	0.555	2.937	444

In this case, only a linear dependence with $\left(\frac{d_{CC}}{D}\right)^{-3}$ was obtained, as shown in **Figure 5.51**, which corresponds with electrostatic coupling. The λ_{isol} obtained was 464 nm.

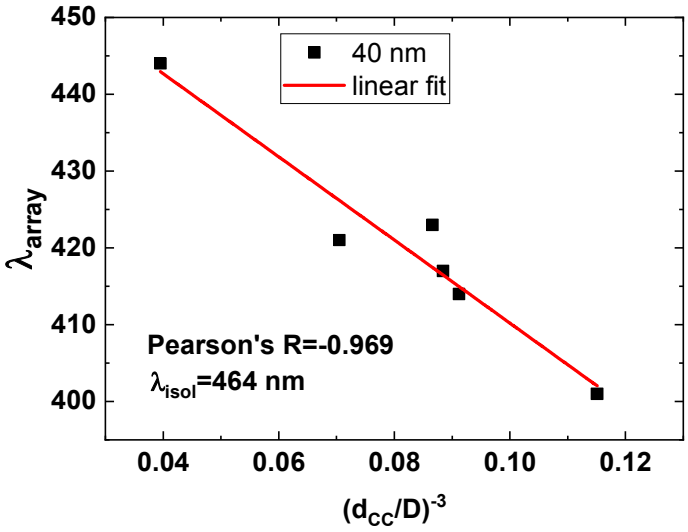


Figure 5.51: Plot of $\boldsymbol{\lambda_{array}}$ (surface plasmon resonance wavelenght of the array) vs. $\left(\frac{d_{CC}}{D}\right)^{-3}$ with a linear fit. The obtained value of $\boldsymbol{\lambda_{isol}}$ (surface plasmon resonance of an isolated particle) is 464 nm. The dependence in $\left(\frac{d_{CC}}{D}\right)^{-3}$ represents electrostatic coupling. d_{CC} is the mean distance between nearest neighbours and D is the mean lateral size.

The evolution of oxygen content in the samples is revealed in **Figure 5.52**. **Figure 5.52 a** corresponds to surface XPS spectra for different final temperatures of the ramp. The black curve corresponds to XPS spectra of the sample. The pink one corresponds to Ag contribution and the blue one corresponds to Ag oxide one. The red one is the cumulative fit.

XPS spectra after 1 min Ar etching are shown in **Figure 5.52 b** for the same samples as in **Figure 5.52 a**. The spectra of the initial film without TT can be adjusted by pure Ag peaks. The peak at approximately 368.5 eV corresponds to Ag $3d_{5/2}$ and the peak at approximately 374.5 eV correspond to Ag $3d_{3/2}$ [44]. The same is observed for the sample whose TT finished at 300°C. But, for temperatures of 400°C and 500°C, the spectra have to be adjusted by peaks of both Ag and Ag oxide.

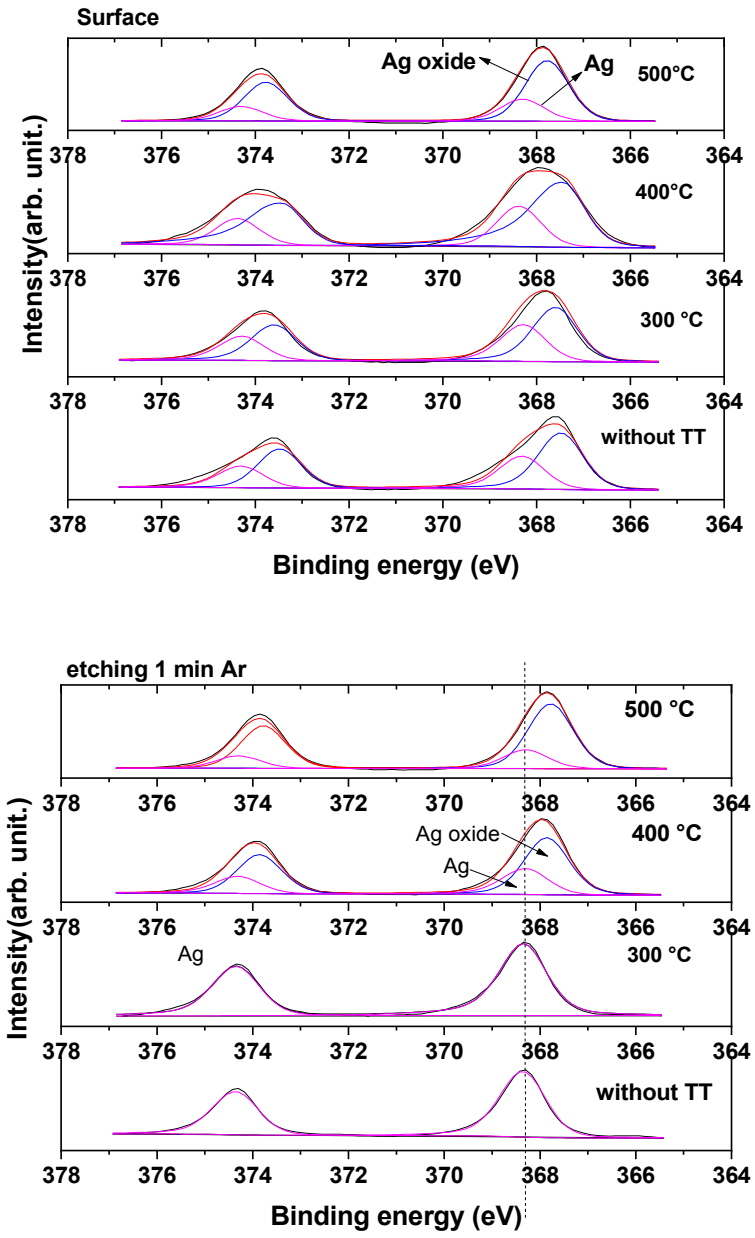


Figure 5.52: a) Surface XPS spectra of samples, whose thermal treatment finished on the ramp, at a certain temperature b) XPS spectra after 1 min Ar etching for the same samples. The nominal thickness of the initial thin film was 80 nm

The amount of Ag oxide increases when the temperature grows from 300°C to 500°C, as shown in **Figure 5.53**. In the case of XPS measurements, which were made at surface level, atomic percentage of Ag oxide grows with final temperature of the ramp. The sample without TT has a 62% of silver oxide on the surface. The analysis after etching shows a clear difference between temperatures below 400°C and ones which are higher than 400°C. As explained before, it could generate the abrupt changes in the transmittance and variations of the SPR wavelength. When nanoparticles are covered by a layer of Ag oxide, plasmon resonance undergoes a red shift.

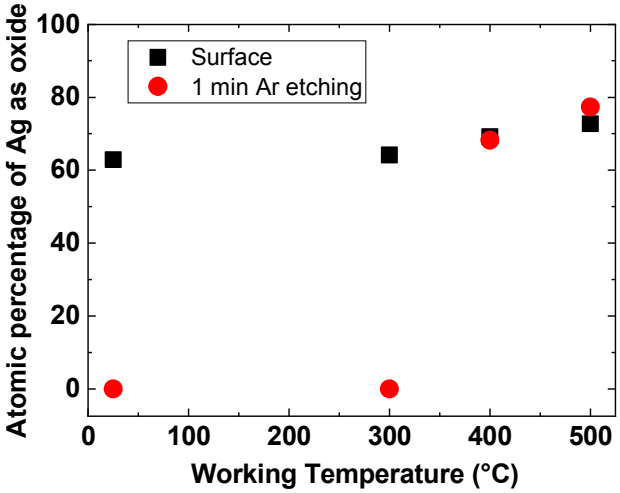


Figure 5.53: Atomic percentage of Ag as oxide vs final temperature of the ramp. The nominal thickness of the initial film was 80 nm.

5.4 Conclusions:

A study of the solid state dewetting (SSD) of Ag films was performed in order to control the size and density of arrays of nanoparticles. Silver nanoparticles were synthesized through Solid State Dewetting of a meta-stable thin film. The annealing consisted in a ramp from room temperature to a required one. It can be followed by an annealing plateau whose duration time can be chosen. After the thermal treatment, sample was naturally cooled.

The dewetting was made in air atmosphere. For samples whose initial thin film nominal thickness were 20 nm, 40 nm and 60 nm, density decreases with working temperature and mean lateral size is mainly constant. In the case of samples prepared with an initial thin film whose nominal thickness was 80 nm, density remains constant. Whereas NPs lateral size decreases. These trends cannot be explained by capillarity approaches. In atmospheres containing oxygen there is an abnormal growth of some grains which will become the final nanoparticles. These grains grab the mass which is in their area of influence. The holes propagate until disconnected objects appear on the surface. At this time, NPs are made up of many grains. Later they will evolve to adopt the Winterbottom equilibrium shape.

For 1 hour of the annealing plateau, average size of particles increases with the thickness of the initial film. It exhibits a linear trend and the slope depends on the working temperature. For higher temperatures, the slope is smaller.

For samples whose thermal treatment ends on the ramp, NPs mean lateral size decrease with final temperature for an initial thin film nominal thickness of 40 nm. Whereas density is almost constant. This fact leads to an increase of the size in the normal to the substrate direction. For samples prepared with an initial thin film with nominal thickness of

80 nm, there is not a clear trend. Although, both quantities looks like constant. In the case of samples whose thermal treatment ends in the plateau, NP mean lateral size increases and density decreases. For 80 nm, there is an abrupt change in the size at 60 min. This is also observed for stress, which is compressive at 51 min and positive at 60 min. This can be attributed to the re-crystallization and removal of high energy grain boundaries. So, when the time of the plateau is varied, the mean lateral size of NPs and density can be modified, but not independently.

The presence of silver oxide on the surface of nanoparticles has an important influence in the structural and optical characteristics. A big increase in the transmittance occurs for samples whose annealing was 1 hour and the working temperature were 450°C and 500°C. It is explained by the formation of silver oxide at these temperatures, which is shown by XPS studies. The same change occurs when the OPC size begins to decrease, after reaching a maximum at 8-17 min of the annealing plateau time for a working temperature of 500°C and initial film nominal thickness of 80 nm. Thus, it can be an alternative explanation to the experimental observations attributed to Ostwald ripening.

Plasmon resonance wavelength resonance can be varied from 390 to 460 nm. The position depends on the relation between d (distance between nanoparticles) and D (size). A linear dependence of SPR wavelength with $\left(\frac{d}{D}\right)^{-3}$ was observed, this fact leads to an electrostatic coupling. The λ_0 values, which represent the SPR wavelength of isolated NP, are 464 nm for an initial film nominal thickness of 40 nm, 443 nm and 527 nm for 80 nm. The last two values for the same initial film thickness denotes a change in the aspect ratio (h/R) of the NPs. Particularly, λ_0 is larger when h/R is smaller.

The solar spectrum has a maximum at $\lambda_{max} = 500\, nm.$ So, metal nanoparticles which absorb and scatter in this range of the spectrum are important to plasmonics solar cells. Far field scattering increases the absorption efficiency by increasing the length of the optical paths of the incident photons in the absorbing mediums. Confining the electromagnetic waves at the metal semiconductor interfaces produces high intensity near fields, resulting in an increase in the number of absorption events compared to their bare counterparts. Plasmons which occur in metal nanostructures can decay non radiatively and generate hot carriers.

The Surface Plasmon Resonance wavelength depends on many factors: i.e. shape, size and density of NPs and spill out. To obtain NPs, with the wanted average size and the average density, three important factors have to be taken into account. The first one is the thickness of the initial film. The second one is the working temperature, and the third one is the time of the annealing plateau. The ideal working temperatures depend on the substrate and on the deposited metal. In our case, the ideal range is from 350°C to 500°C. If it is necessary to prepare an array which absorbs and scatters light in the interesting region of the solar spectrum, the initial film nominal thickness has to be at less 80 nm. For smaller thickness, arrays present less scattering. The density of NPs is selected by the time of the annealing plateau. The maximum suitable time is 1 hour. After that, the observed general trends collapse and it becomes difficult to control them.

5.5 References

[1] Ye, J. , Zuev, D. , and Makarov, S. Dewetting mechanisms and their exploitation for the large-scale fabrication of advanced nanophotonic systems. *International Materials Reviews* **2019**, 64, 439–477.

[2] Ruffino, F. and Grimaldi, M. G. Dewetting process of Au films on SiO2 nanowires: Activation energy evaluation. *Physica E: Low-dimensional Systems and Nanostructures* **2015**, 69, 121–126.

[3] Quan, J. , Zhang, J. , Xueqiang, Q. , Junying, L. , Ning, W. , and Yong, Z. A study on the correlation between the dewetting temperature of Ag flm and SERS intensity. *Scientific Reports* **2017**, 7, 14771.

[4] Presland, A. E. B. , Price, G. L. , and Trimm, D. L. Hillock formation by surface diffusion on thin silver films. *Surface Science* **1972**, 29, 424–434.

[5] Jacquet, P. , Podor, R. , Ravaux, J. , Lautru, J. , Teisseire, J. , Gozhyk, I. , Jupille, J. , and Lazzari, R. On the solid-state dewetting of polycrystalline thin films: Capillary versus grain growth approach. *Acta Materialia* **2018**, 143, 281–290.

[6] Serrano, A. , Rodriguez de la Fuente, O. , and García, M. A. Extended and localized surface plasmons in annealed Au films on glass substrates. *Journal of Applied Physics* **2010**, 108, 074303.

[7] Serrano, A. , Llorca-Hernando, O. , Campo, A. Del , Rubio-Marcos, F. , Rodríguez de La Fuente, O. , Fernández, J. F. , and García, M. A. Ag-AgO nanostructures on glass substrates by solid-state dewetting: From extended to localized surface plasmons. *Journal of Applied Physics* **2018**, 124, 133103.

[8] Jacquet, P. , Podor, R. , Ravaux, J. , Teisseire, J. , Gozhyk, I. , Jupille, J. , and Lazzari, R. Grain growth: The key to understand solid-state dewetting of silver thin films. *Scripta Materialia* **2016**, 115, 128–132.

[9] Farzinpour, P. , Sundar, A. , Gilroy, K. D. , Eskin, Z. E. , Hughes, R. A. , and Neretina, S. Altering the dewetting characteristics of ultrathin gold and silver films using a sacrificial antimony layer. *Nanotechnology* **2012**, 23, 495604.

[10] Jacquet, P. , Bouteille, B. , Dezert, R. , Lautru, J. , Podor, R. , Baron, A. , Teisseire, J. , Jupille, J. , Lazzari, R. , and Gozhyk, I. Periodic Arrays of Diamond□Shaped Silver Nanoparticles: From Scalable Fabrication by Template□Assisted Solid□State Dewetting to Tunable Optical Properties. *Advanced Functional Materials* **2019**, 1901119.

[11] Leroy, F. , Borowik, Ł. , Cheynis, F. , Almadori, Y. , Curiotto, S. , Trautmann, M. , Barbé, J. C. , and Müller, P. How to control solid state dewetting: A short review. *Surface Science Reports* **2016**, 71, 391–409.

[12] Malyi, O. , Klinger, L. , Srolovitz, D. J. , and Rabkin, E. Size and shape evolution of faceted bicrystal nanoparticles of gold on sapphire. *Acta Materialia* **2011**, 59, 2872–2881.

[13] Jacquet, P. , Podor, R. , Ravaux, J. , Lautru, J. , Teisseire, J. , Gozhyk, I. , Jupille, J. , and Lazzari, R. On the solid-state dewetting of polycrystalline thin films: Capillary versus grain growth approach. *Acta Materialia* **2018**, 143, 281–290.

[14] Müller, C. M. and Spolenak, R. Microstructure evolution during dewetting in thin Au films. *Acta Materialia* **2010**, 58, 6035–6045.

[15] Derkach, V. , Novick-Cohen, A. , and Rabkin, E. Grain boundaries effects on hole morphology and growth during solid state dewetting of thin films. *Scripta Materialia* **2017**, 134, 115–118.

[16] Porter, D. E.; Easterling, K. E.; and Sherif, M. Y. Phase transformation in metal and alloys. CRC Press: 2014.

[17] Wang, S. G. , Tian, E. K. , and Lung, C. W. Surface energy of arbitrary crystal plane of bcc and fcc metals. *Journal of Physics and Chemistry of Solids* **2000**, 61, 1295–1300.

[18] Shaffir, E. , Riess, I. , and Kaplan, W. D. The mechanism of initial de-wetting and detachment of thin Au films on YSZ. *Acta Materialia* **2009**, 57, 248–256.

[19] Thiel, P. A. , Shen, M. , Liu, D.-J. , and Evans, J. W. Coarsening of Two-Dimensional Nanoclusters on Metal Surfaces. *The Journal of Physical Chemistry C* **2009**, 113, 5047–5067.

[20] González, A. L. , Noguez, C. , Beránek, J. , and Barnard, A. S. Size, Shape, Stability, and Color of Plasmonic Silver Nanoparticles. *The Journal of Physical Chemistry C* **2014**, 118, 9128–9136.

[21] Kim, D. Y. , Im, S. H. , Park, O. O. , and Lim, Y. T. Evolution of gold nanoparticles through Catalan, Archimedean, and Platonic solids. *CrystEngComm* **2010**, 12, 116–121.

[22] Kim, H. C. , Theodore, N. D. , and Alford, T. L. Comparison of texture evolution in Ag and Ag(Al) alloy thin films on amorphous SiO2. *Journal of Applied Physics* **2004**, 95, 5180–5188.

[23] Birnbaum, A. J. , Thompson, C. V. , Steuben, J. C. , Iliopoulos, A. P. , and Michopoulos, J. G. Oxygen-induced giant grain growth in Ag films. *Applied Physics Letters* **2017**, 111, 163107.

[24] Bouras, N. , Madjoubi, M. A. , Kolli, M. , Benterki, S. , and Hamidouche, M. Thermal and mechanical characterization of borosilicate glass. *Physics Procedia* **2009**, 2, 1135–1140.

[25] BOROFLOAT 33-Thermal properties.

[26] Napolitano, A. , Simmons, J. H. , Blackburn, D. H. , and Chidester, R. E. Analysis of Low Temperature Viscosity Data for Three NBS Standard Glasses. *Journal of Research of the National Bureau of Standards - A. Physics and Chemistry* **1974**, 78A

[27] McPeak, K. M. , Jayanti, S. V. , Kress, S. J. P. , Meyer, S. , Iotti, S. , Rossinelli, A. , and Norris, D. J. Plasmonic Films Can Easily Be Better: Rules and Recipes. *ACS Photonics* **2015**, 2, 326–333.

[28] Malynych, S. and Chumanov, G. Light-Induced Coherent Interactions between Silver Nanoparticles in Two-Dimensional Arrays. *Journal of the American Chemical Society* **2003**, 125, 2896–2898.

[29] Haynes, C. L. , McFarland, A. D. , Zhao, L. , Van Duyne, R. P. , Schatz, G. C. , Gunnarsson, L. , Prikulis, J. , Kasemo, B. , and Käll, M. Nanoparticle Optics: The Importance of Radiative Dipole Coupling in Two-Dimensional Nanoparticle Arrays †. *The Journal of Physical Chemistry B* **2003**, 107, 7337–7342.

[30] Zou, S. and Schatz, G. C. Narrow plasmonic/photonic extinction and scattering line shapes for one and two dimensional silver nanoparticle arrays. *The Journal of Chemical Physics* **2004**, 121, 12606.

[31] Félidj, N. , Aubard, J. , Lévi, G. , Krenn, J. R. , Salerno, M. , Schider, G. , Lamprecht, B. , Leitner, A. , and Aussenegg, F. R. Controlling the optical response of regular arrays of gold particles for surface-enhanced Raman scattering. *Physical Review B* **2002**, 65, 075419.

[32] Gunnarson, L. , Rindzevicius, T. , Prikulis, J. , Kasemo, B. , Käll, M. , Zou, S. , and Schatz, G. C. Confined Plasmons in Nanofabricated Single Silver Particle Pairs: Experimental Observations of Strong Interparticle Interactions. *Journal of Physical Chemistry B* **2005**, 109, 1079–1087.

[33] Tabor, C. , Murali, R. , Mahmoud, M. , and El-Sayed, M. A. On the Use of Plasmonic Nanoparticle Pairs As a Plasmon Ruler: The Dependence of the Near-Field Dipole Plasmon Coupling on Nanoparticle Size and Shape †. *The Journal of Physical Chemistry A* **2009**, 113, 1946–1953.

[34] Jain, P. K. , Huang, W. , and El-Sayed, M. A. On the Universal Scaling Behavior of the Distance Decay of Plasmon Coupling in Metal Nanoparticle Pairs: A Plasmon Ruler Equation. *Nano Letters* **2007**, 7, 2080–2088.

[35] Gong, Y. , Zhou, Y. , He, L. , Xie, B. , Song, F. , Han, M. , and Wang, G. Systemically tuning the surface plasmon resonance of high-density silver nanoparticle films. *The European Physical Journal D* **2013**, 67, 87.

[36] Kinnan, M. K. and Chumanov, G. Plasmon Coupling in Two-Dimensional Arrays of Silver Nanoparticles: II. Effect of the Particle Size and Interparticle Distance. *The Journal of Physical Chemistry C* **2010**, 114, 7496–7501.

[37] Jenkins, J. A. , Zhou, Y. , Thota, S. , Tian, X. , Zhao, X. , Zou, S. , and Zhao, J. Blue-Shifted Narrow Localized Surface Plasmon Resonance from Dipole Coupling in Gold Nanoparticle Random Arrays. *The Journal of Physical Chemistry C* **2014**, 118, 26276–26283.

[38] Markel, V. A. Coupled-dipole Approach to Scattering of Light from a One-dimensional Periodic Dipole Structure. *Journal of Modern Optics* **1993**, 40, 2281–2291.

[39] Geddes, C. D. Reviews in Plasmonics 2017. Springer International Publishing: Cham 2019.

[40] Kadkhodazadeh, S. , Lasson, J. R. de , Beleggia, M. , Kneipp, H. , Wagner, J. B. , and Kneipp, K. Scaling of the Surface Plasmon Resonance in Gold and Silver Dimers Probed by EELS. *The Journal of Physical Chemistry C* **2014**, 118, 5478–5485.

[41] Kuzma, A. , Weis, M. , Flickyngerova, S. , Jakabovic, J. , Satka, A. , Dobrocka, E. , Chlpik, J. , Cirak, J. , Donoval, M. , Telek, P. , Uherek, F. , and Donoval, D. Influence of surface oxidation on plasmon resonance in monolayer of gold and silver nanoparticles. *Journal of Applied Physics* **2012**, 112, 103531.

[42] Kuwata, H. , Tamaru, H. , Esumi, K. , and Miyano, K. Resonant light scattering from metal nanoparticles: Practical analysis beyond Rayleigh approximation. *Applied Physics Letters* **2003**, 83, 4625–4627.

[43] Scherbak, S. A. and Lipovskii, A. A. Plasmonic properties of metal nanoislands: surface integral equations approach. *Journal of Physics: Conference Series* **2016**, 741, 012120.

[44] Wagstaffe, M. , Hussain, H. , Acres, M. J. , Jones, R. , Syres, K. L. , and Thomas, A. G. Structure and Reactivity of a Model Oxide Supported Silver Nanocluster Catalyst Studied by Near Ambient Pressure X-ray Photoelectron Spectroscopy. *The Journal of Physical Chemistry C* **2017**, 121, 21383–21389.

6 ZnO nanowires decorated with silver nanoparticles through the Solid State Dewetting process.

Zinc oxide, as a semiconductor metal oxide, offers attractive optical capacities such as a wide band gap (3.37 eV) with large exciton binding energy (60 meV), high dielectric constant and high carrier saturation velocity [1]. Also, it can be easily synthesized into large scale array: 1D ZnO structures. 1D nanostructures are generally used to describe large aspect ratio shapes: rods wires, tubes. When the radial diameter of the 1D nanostructure is lower than some characteristic lengths (Bohr exciton radius, phonon mean free path, light of the wavelength), the effects of the quantum mechanics will be crucial. In addition, if the aspect ratio is extremely large, quantum particles can be easily driven and makes nanowires the ideal candidate for charge or energy transport materials.

The attractive characteristic of ZnO is the superior mobility of electrons, which exceeds that of the anatase titanium oxide by more than an order of magnitude [2]. Thus, NWs have strong light absorption and rapid carrier collection [3]. Compared to planar solar cells, NWs photovoltaic devices have enhanced optical absorption due to some effects: ZnO NRs can reduce reflectivity and the incoming light is captured and confined into guided modes which lead to concentration of the electromagnetic field inside the absorbing material. Also nanowires, support the light along a diffusive path leading to multiple scattering between the wires [3].

Near band edge (NBE) photoluminescence efficiency of naked ZnO NWs is usually low. To enhance the NBE emission and suppress the defect related emission, several methods have been considered to increase the visible light response of wide band gap semiconductors. One of them consists in forming hetero-structures or integrating semiconductors with plasmonic metals such as Cu, Pd, Pt, Ag, Au. In our case, using suitable materials as metal NPs, the optical properties of ZnO NRs can be modified.

The metal/semiconductor (M/SC) integration links the semiconducting properties with surface plasmon resonances, creating new behaviors of the combined system. The band gap structures of the semiconductors will be affected after the combination with noble metals [4]. Similarly, the plasmonic properties of the metal will be also modified by the semiconductor component [5].

In metal/semiconductor coupling nanosystems, three quantities are important: i) the work functions of the components, ii) their electron affinity and iii) the Fermi level of each material. When metals are coupled to semiconductors, two distinct types of junctions could be observed: the Schottky barrier or the Ohmic contact.

The majority of the plasmonics layers using metal nanoparticles, usually form a two dimensional (2D) plasmonic domains. The biggest limitation is that optical active layers (photoactive layers) with thickness greater than 100 nm, are not sufficiently enhanced. The

reason is that the effect occurs in the closeness of the plasmonic probes as it can be observed in **Figure 6.1,** which presents simulation results for electric field intensity. To overcome it, three dimensional (3D) plasmonic nanostructures have been suggested, in order to deliver plasmonic effects to a wider range of optical active layers. However, 3D dispersion of plasmonics nanoparticles in optical devices is not easy due to random distribution and aggregation of nanoparticles. Therefore, it is essential to develop a strategy for creating tunable 3D plasmonics nanostructures via an efficient fabrication process.

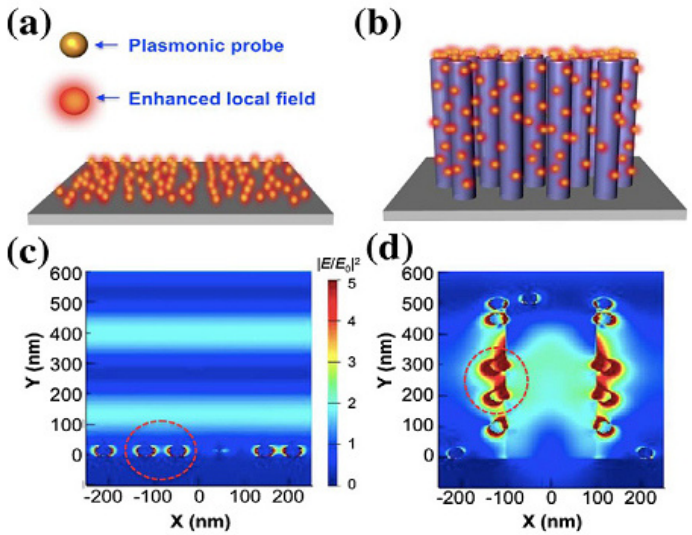


Figure 6.1: a) 2D plasmonic nanostructure b) 3D plasmonic nanostructure. Simulation results for electric field intensity distribution on c) 2-D dispersed nanoparticles and on d) 3D dispersed nanoparticles on a ZnOnanorod [6].

An optical measurement technique to study the charge carrier transference is Photoluminescence (PL). PL quenching or PL enhancement were often observed in semiconductor-metal nanostructures coupling systems. However the involved mechanisms are not clear and they are still under hot debate due to the complicated coupling process, between excitons and surface plasmons (SPs). Understanding the coupling process and mechanisms is extremely important for the application of SPs phenomenon. There are mainly three mechanism that account for the PL enhancement and quench

- Surface plasmon resonance scattering of metal may enhance the emission while SPR absorption quenches the emission [7] .
- the local field enhancement increases excitation rate and radiative recombination rate, whereas non-radiative energy transfer from semiconductor to metal nanostructures generate PL quenching [8][9].
- the PL can be enhanced due to the electron transfer from metal NP's to semiconductors, conversely, the electron transfer from semiconductors to metal NP's results in PL quenching [10].

In this work, to create a 3D plasmonic nanostructure without conventional nanolithography methods, vertically ZnO nanowires (NWs) were prepared by electrodeposition. The initial coating layer (ICL) of silver was deposited on them by vacuum thermal deposition. Dewetted Ag nanoparticles are finally self-assembled onto the ZnO NWs via an annealing process, creating large area 3D dispersed Ag nanoparticles on ZnO NWs. The diameter of the dewetted Ag nanoparticles was tuned by modulating the thickness of the initial Ag thin film, which lead to a shift in the localized surface plasmon resonance (LSPR) wavelength.

ICL thickness has been measured through the quartz monitor, which was placed very close to the sample. **Table 6.1** summarizes the characteristic parameters of different samples: silver ICL thickness, working temperature and duration of the annealing plateau (see Figure 5.1). The last two correspond to the thermal treatment (TT).

Table 6.1: Samples of ZnO nanowires and their decoration with silver

Sample	ICL Thickness (nm)	Temperature (°C)	Annealing Plateau Time (min)
Z24	100	300	60
C94	50	400	60
C19	50	300	60
C101	40	400	60
C93	30	400	60
Z48	30	300	60
Z28	20	300	60
C91	15	300	60
Z31	10	300	60
C88	5	without TT	
G18	6	300	17
G16	12	300	17
G17	12	300	34
G11	12	300	51

6.1 Morphological studies

The morphology of the silver nanostructures as obtained through a Solid State Dewetting process depends on the thickness of the ICL and on the thermal treatment parameters: annealing plateau time and working temperature. SEM micrograph of a sample with an as deposited silver ICL of 50 nm, is shown in **Figure 6.2 a**. It can be observed that NWs are covered by silver. Whereas, after the annealing process, some broken NWs and large silver NPs among NWs can be observed in **Figure 6.2 b**. The evaporation process with a rate of 2.5 Å/s or less is not the cause of breaking NWs. Therefore, the break of NWs occurs during the thermal treatment. It could be related with the movements of silver atoms or with the size of NPs, which are too big to be supported by NWs.

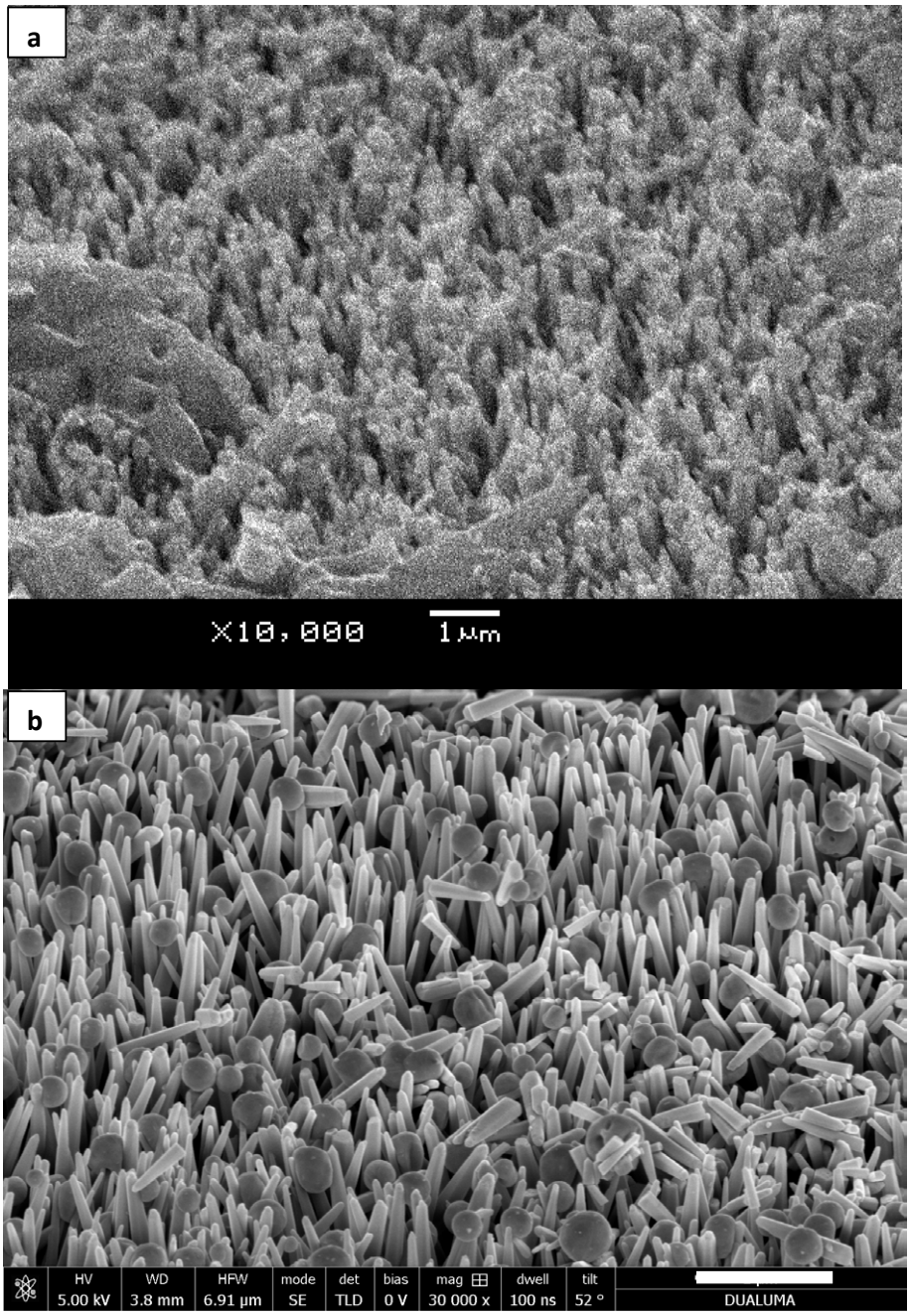


Figure 6.2: ZnO NWs with an Ag ICL of 50 nm before a) and after b) the TT. The working temperature was 300°C and the annealing plateau time was 1 hour. The white scale bar corresponds to 1 µm.

In **Figure 6.3**, two SEM micrographs of different samples after the TT are shown. The initial ICL thickness values were 30 nm and 15 nm. The thermal treatment parameters were 300°C and 1 hour for both ICL thickness values.

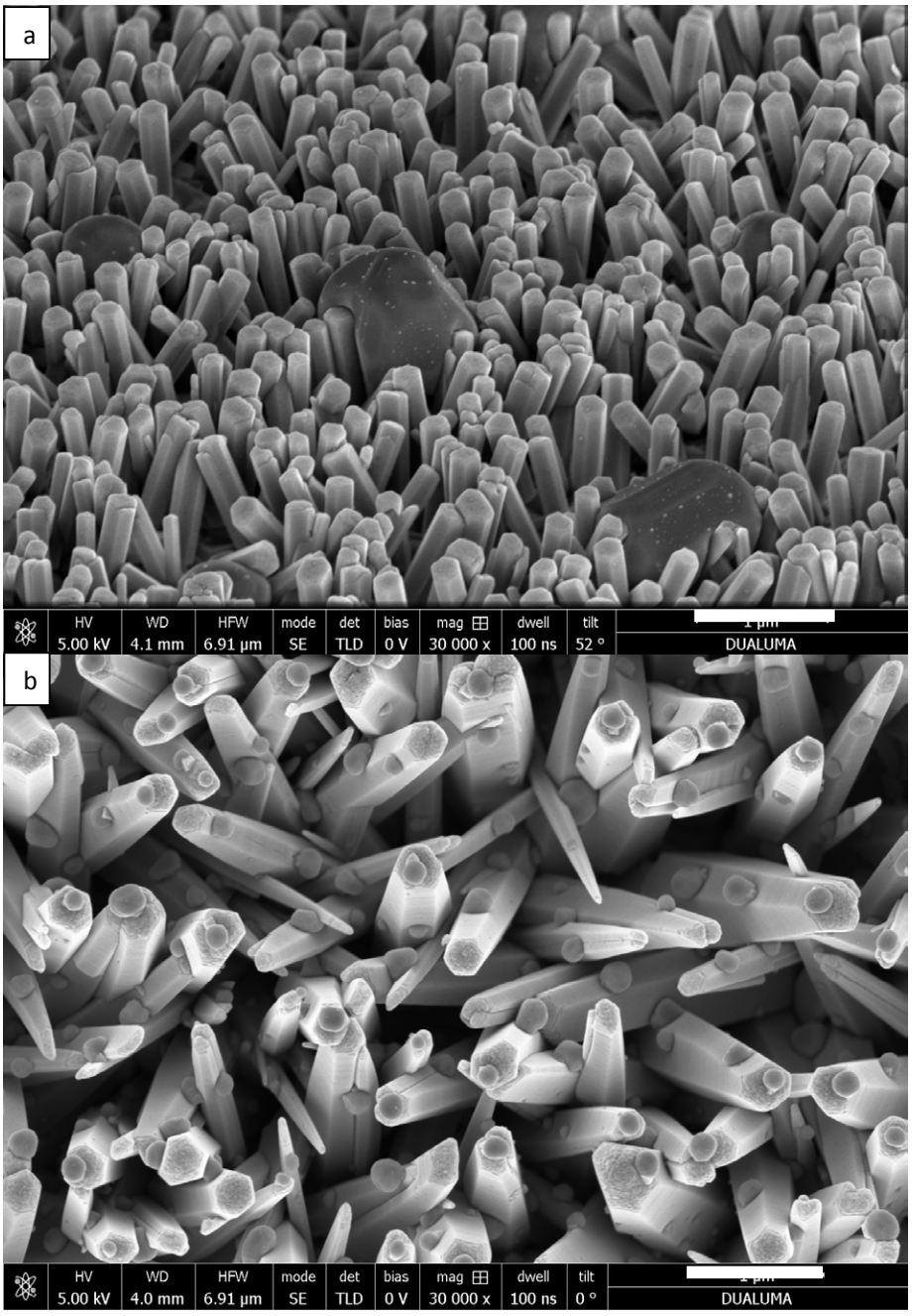


Figure 6.3: FE-SEM micrographs of samples with an initial coating layer of :a) 30 nm, b) 15 nm. The working temperature and the annealing plateau time were 300°C and 1 hour, respectively. The white scale bar corresponds to 1 µm.

For the case of an ICL of 30 nm (**Figure 6.3a**), there are big Ag NPs filling the space among ZnO NWs. Whereas, for an ICL of 15 nm (**Figure 6.3b**), most of Ag NPs have a size that can be supported by ZnO NWs. Although the NWs of the two samples are different (size and shape), we can conclude that, for a specific working temperature and annealing plateau time, we have to find the suitable ICL thickness. **Figure 6.4** shows FE-SEM micrographs of

ZnO nanowires covered with a silver ICL of 5 nm (measured by the quartz monitor) before annealing.

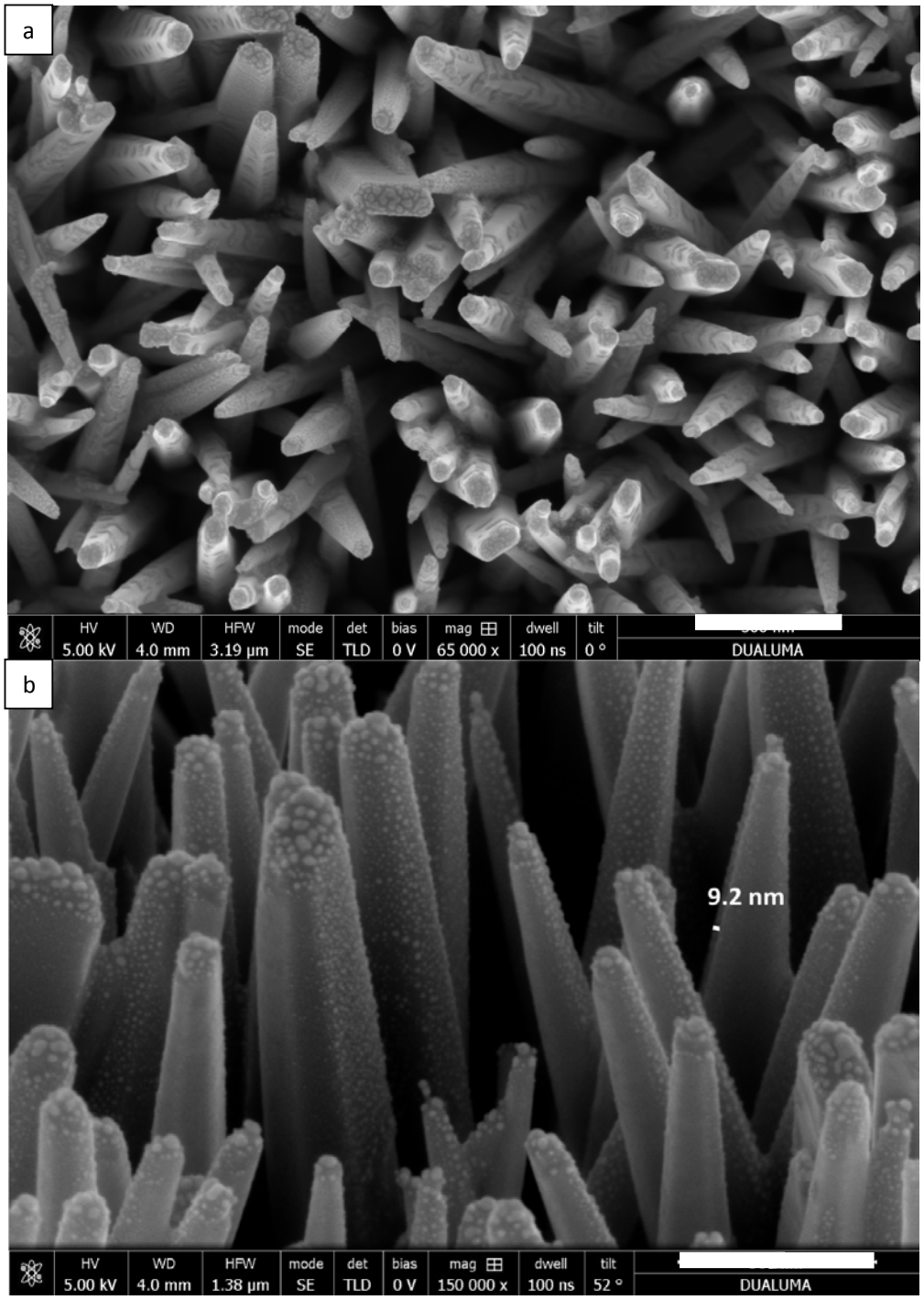


Figure 6.4:FE-SEM micrographs of sample C88 with a coating layer of silver of 5 nm without TT. The white scale bar corresponds to 300nm**.** The tilt angle and the white scale bar are a) 0°, 500 nm and b) 52°, 300 nm.

It can be observed that the ZnO NWs covered by this silver layer exhibit a surface roughness. As indicated in **Figure 6.4b**, the effective thickness of this layer is about 9.2 nm.

In the following parts of this chapter, the samples which will be decorated with Ag, have ZnO NWs with similar shape and size. An ICL of Ag with a thickness of 15 nm (or lower) is adequate for the SSD process onto the ZnO NWs arrays, with a thermal treatment at 300°C and an annealing plateau time of 1 hour. Thus, the dependence on the annealing plateau time will be further studied. To this end, the ICL silver thickness will be kept constant at a value of 12 nm. **Figure 6.5** shows a micrograph of naked ZnO NWs array, which will be further decorated by Ag NPs.

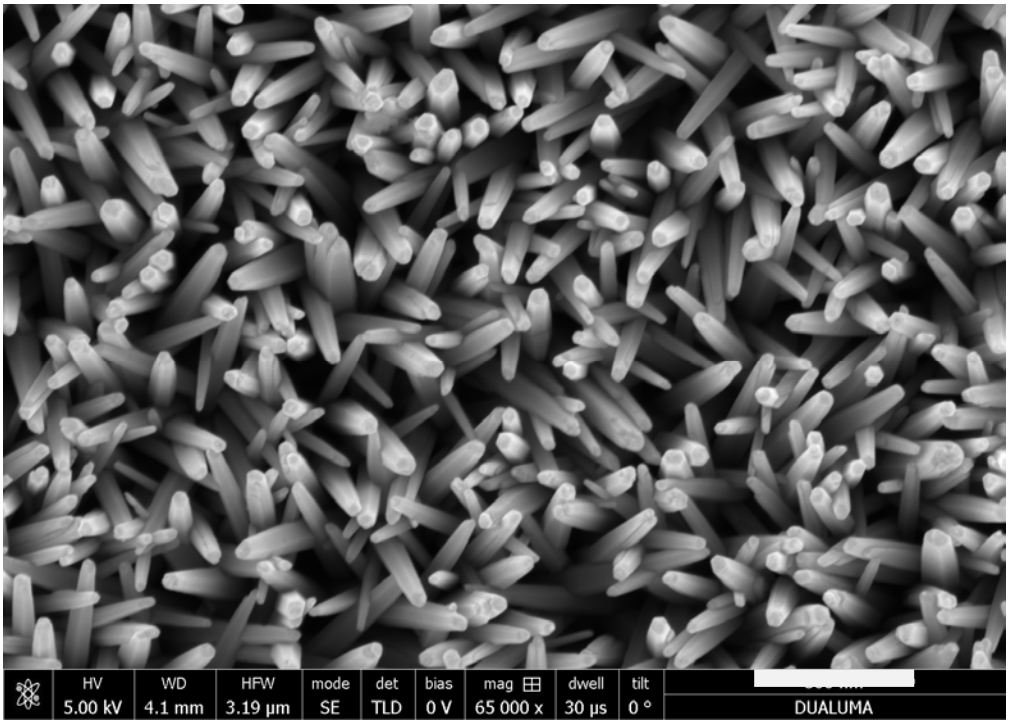


Figure 6.5: FE-SEM micrograph of a sample of naked ZnO nanowires. The white scale bar corresponds to 500 nm.

FE-SEM micrographs of different samples of ZnO nanowires, decorated with Ag nanoparticles, are presented in **Figure 6.6** to **Figure 6.8 (**ICL thickness 12 nm and working temperature 300°C). The studied annealing plateau times were 17 min, 34 min and 51 min, respectively. The naked ZnO NWs arrays are very similar in each sample and they are not broken after the thermal treatment. Silver nanoparticles are observed in micrographs of **Figure 6.6**, which correspond to a sample with initial thin film of 12 nm, working temperature of 300°C and an annealing plateau time of 17 min. They are decorating the ZnO nanowires both on their top and on their lateral faces. Micrographs of **Figure 6.7** correspond to a sample submitted to an annealing process with a working temperature of 300°C and plateau time of 34 min. Tiny nanoparticles, decorating lateral faces of the ZnO NWs, are observed. But there are larger NPs on the top of the NWs and among them. The existence of the tiny NPs and the smaller number of NPs with measurable size than for 17 min, is an evidence that during thermal treatment, atoms could move by Ostwald ripening [11][12].

Also, for an annealing plateau time of 51 min, tiny NPs disappear and the number of NPs with measurable size increases. This is observed in **Figures 6.7, 6.8 and 6.10**.

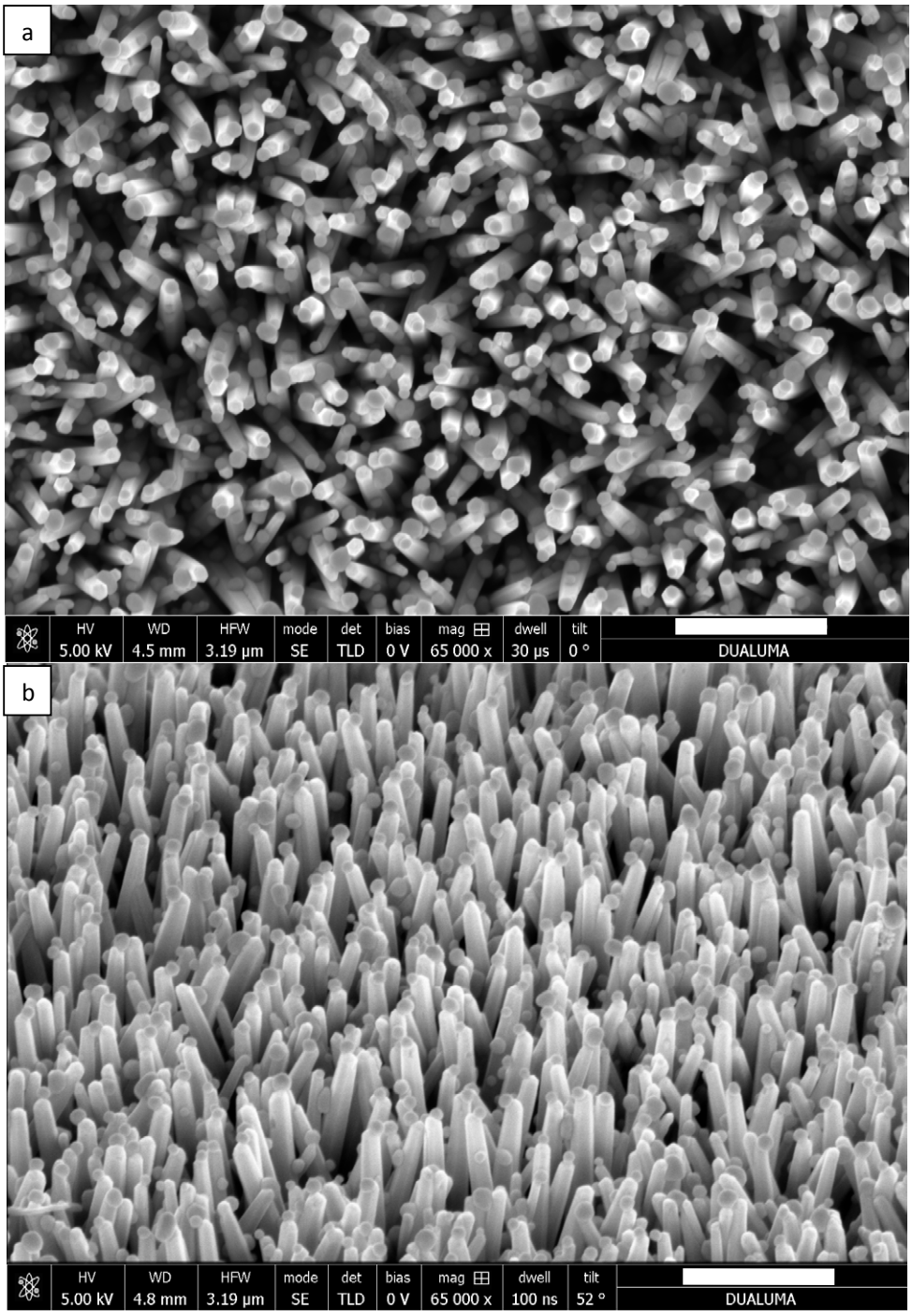


Figure 6.6: FE-SEM micrographs of a sample whose working temperature was 300°C and the annealing plateau time was 17 min. The silver ICL thickness was 12 nm. The white scale bar corresponds to 500 nm. The tilt angle is a) 0° and b) 52°.

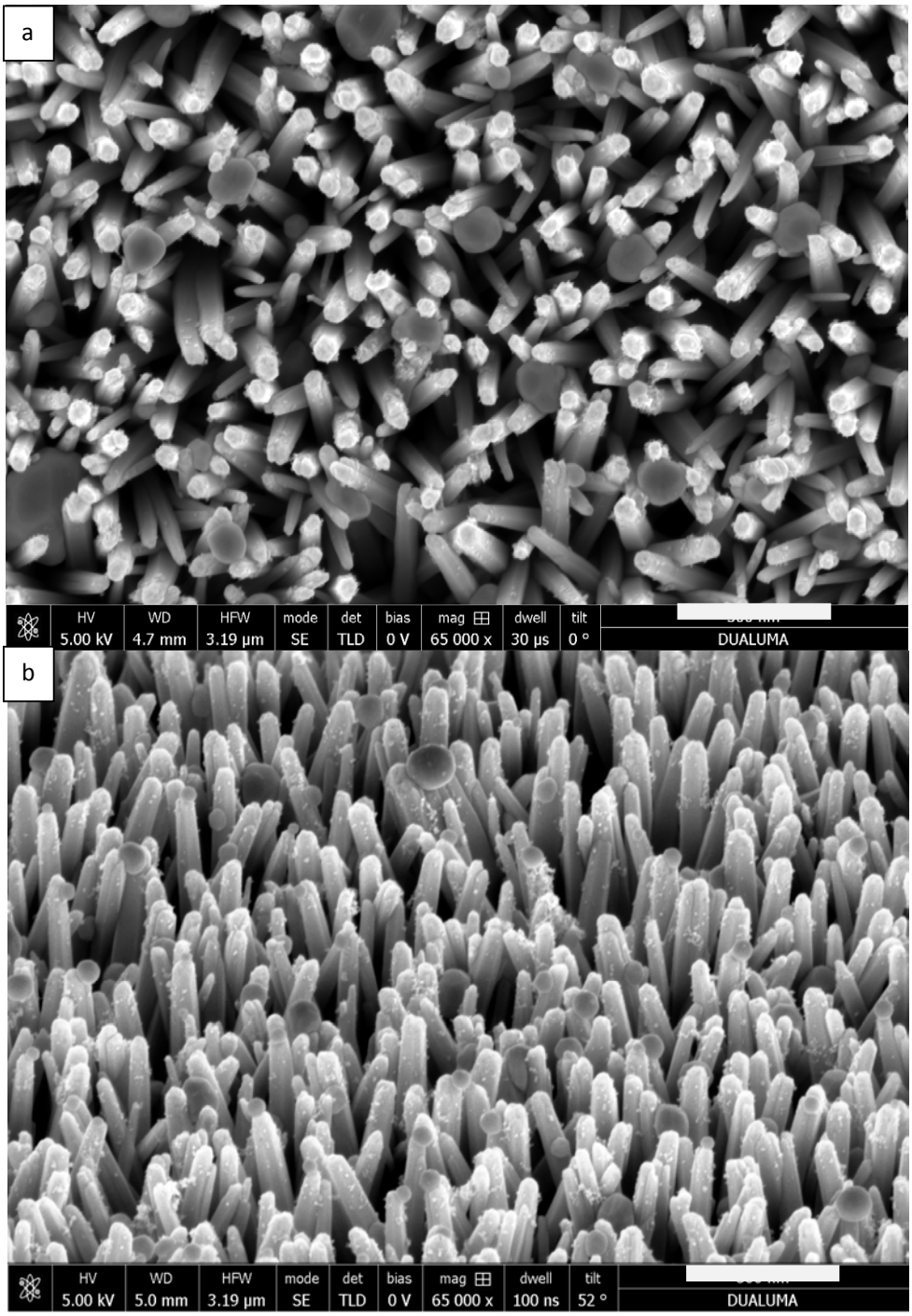


Figure 6.7: FE-SEM micrographs of sample whose working temperature was 300°C and the annealing plateau time was 34 min. The silver ICL thickness was 12 nm. The white scale bar corresponds to 500 nm. The tilt angle is a) 0° and b) 52°.

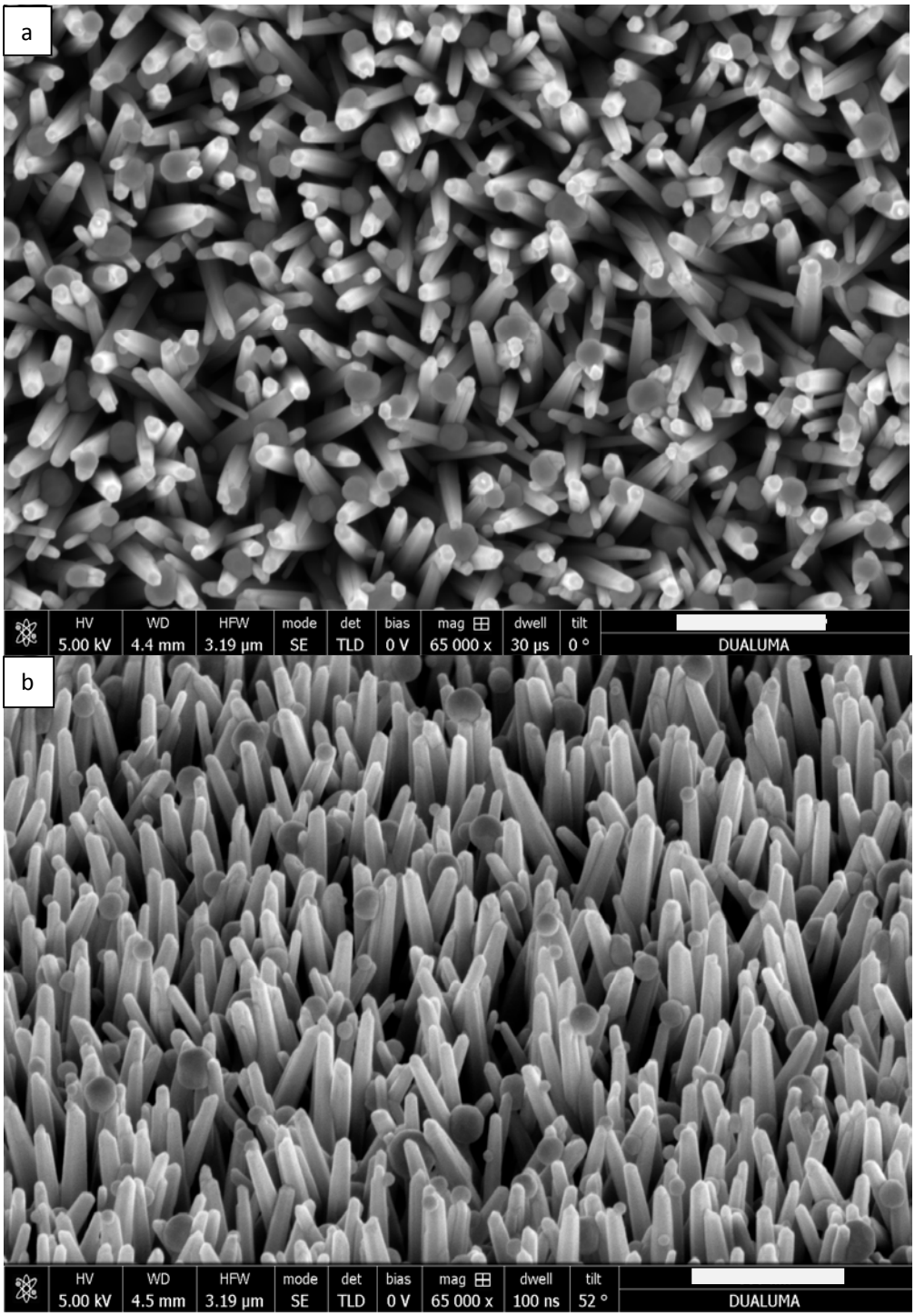


Figure 6.8: FE-SEM micrographs of a sample whose working temperature was 300°C and the annealing plateau time was 51 min. The silver ICL thickness was 12 nm. The white scale bar corresponds to 500 nm. The tilt angle is a) 0° and b) 52°.

Now, the thickness of the layer was varied to 6 nm, while the working temperature was kept at 300°C and the annealing plateau time was 17 min. The micrographs of this sample are displayed in **Figure 6.9**. Its characteristics are similar to the one with an ICL of 12 nm, working temperature of 300°C and annealing plateau time of 17 min, but Ag NPs appear smaller.

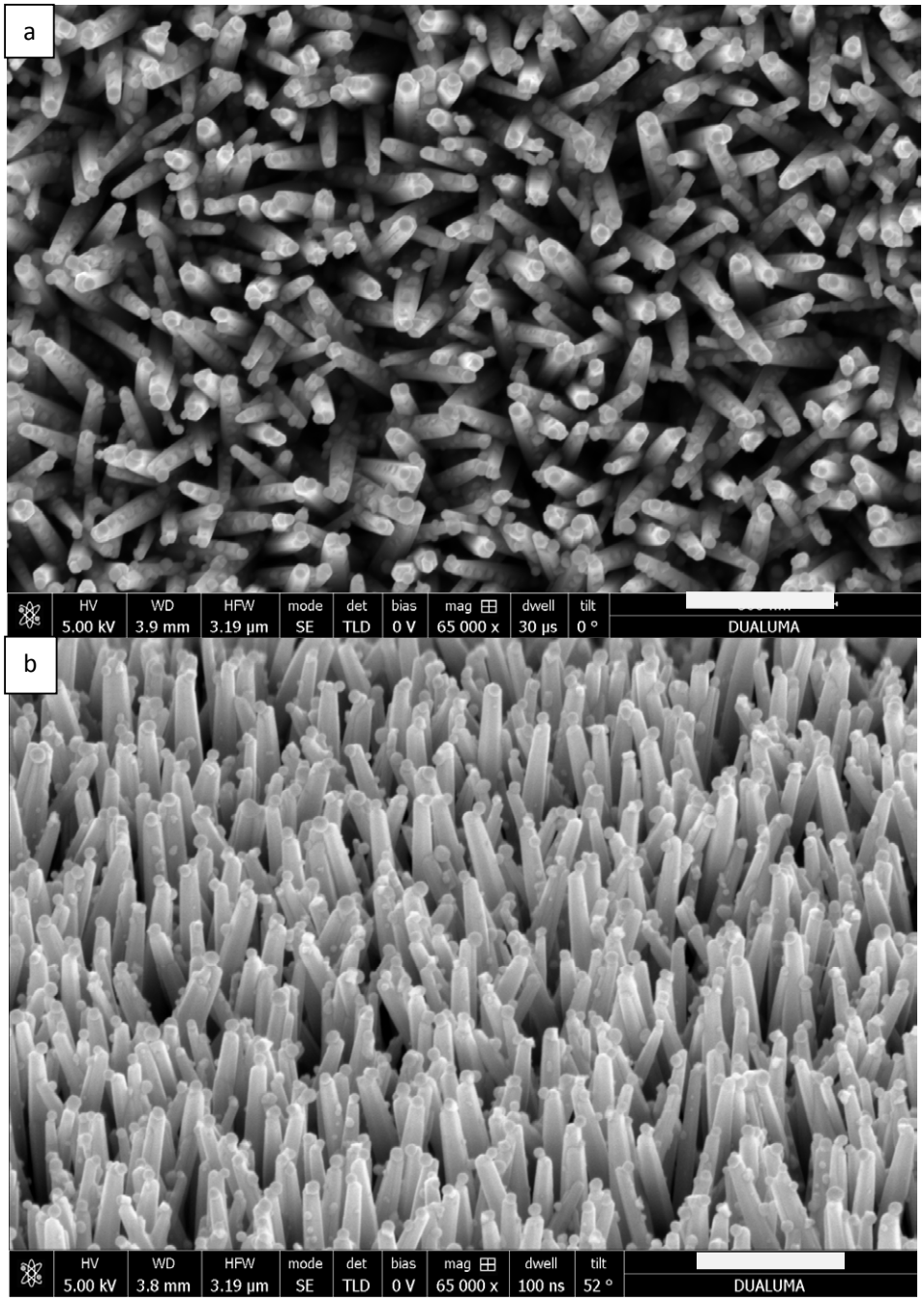


Figure 6.9: FE SEM micrographs of a sample whose working temperature was 300°C and the plateu time was 17 min. The silver ICL thickness was 6 nm. The white scale bar corresponds to 500 nm. The tilt angle is a) 0° and b) 52°.

6.1.1 Silver NPs size distribution

Histograms of Ag NPs size are shown in **Figure 6.10.** All the samples were prepared at a working temperature of 300°C, while the ICL thickness and the annealing plateau time were varied. For a constant ICL thickness of 12 nm, the annealing plateau times were 17 min, 34 min and 51min. For an annealing plateau time of 17 min, the ICL thickness were 6 nm and 12 nm.

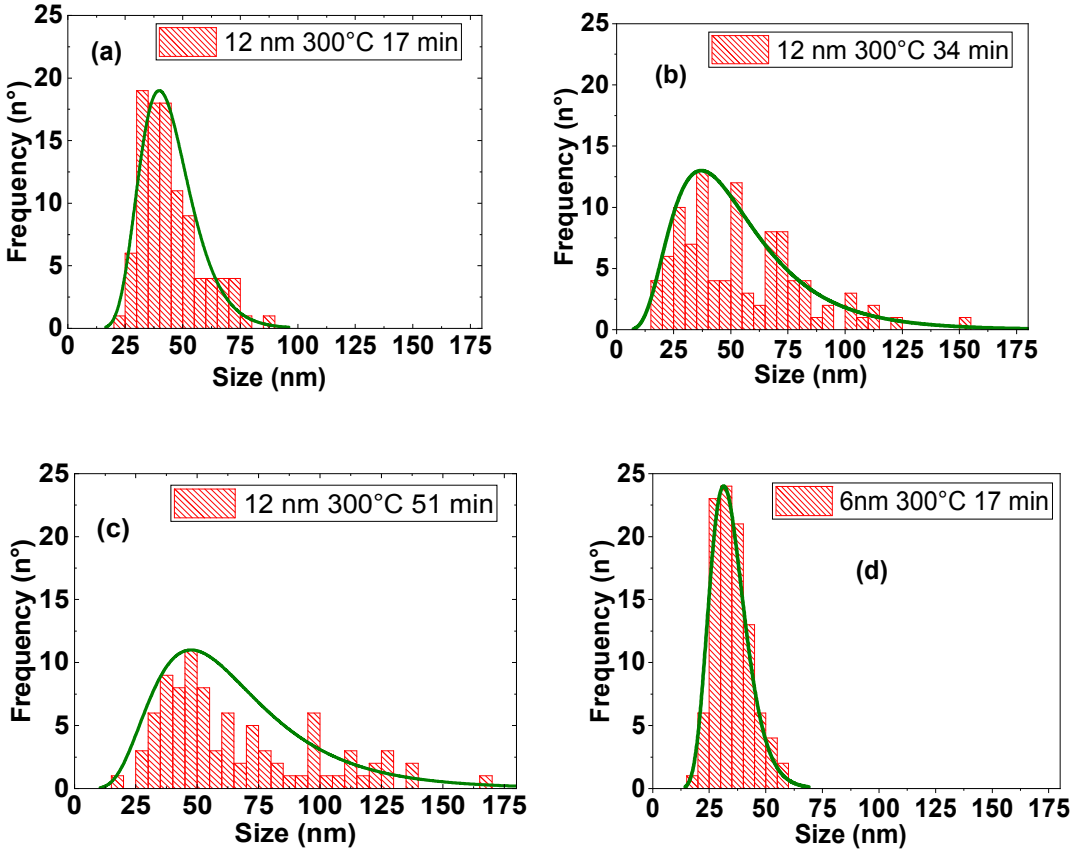


Figure 6.10: Histograms of Ag NPs sizes for different samples. The ICL thickness and the annealing plateau times were a) 12nm, 17 min; b)12nm, 34 min; c) 12 nm, 51 min; d) 6 nm, 17 min.

All histograms were fitted with a log-normal distribution. This distribution was observed in many different works. Thøgersen et al. [13] studied the effect of solar irradiation on Ag nanocrystals on a carbon film and they investigated the growth rate and particle distribution with solar irradiation time. They observed a log-norm size distribution for different times. Simonsen et al. [14] studied the sintering mechanism of Pt NPs dispersed on a planar amorphous Al_2O_3. A statistical analysis of an ensemble of Pt NPs showed that the particle size distributions change their shape from an initial Gaussian distribution via a log normal distribution to a Lifshitz Slyozov Wagner distribution. In our case, for a sample with

an ICL thickness of 12 nm, the width of the histogram for 17 min is smaller than those for 34 min and 51 min, which means a narrow size distribution. Bigger nanoparticles grow in detriment of smaller ones, hence the width of the histogram increase with time. This can be explained by Ostwald ripening. The second comparison corresponds to the same annealing plateau time, and different ICL thickness. The mean size and the width of the histogram of a sample with an ICL of 6nm are smaller than for a sample with an ICL of 12 nm, both submitted to the same SSD process. Thus, I can conclude that reducing annealing times and initial thicknesses, the homogeneity of NPs is improved. The mean sizes of the obtained Ag NPs are summarized in **Table 6.2**. Also, they are plotted as a function of the annealing time in **Figure 6.11,** for the case of an ICL of 12 nm**.**

Table 6.2: Dependence of the mean size of the Ag nanoparticles for different ICL values and annealing plateau times.

ICL Thickness (nm)	Working temperature (°C)	Annealing plateau time (min)	Size (nm)
6	300	17	34
12	300	17	44
12	300	34	54
12	300	51	66

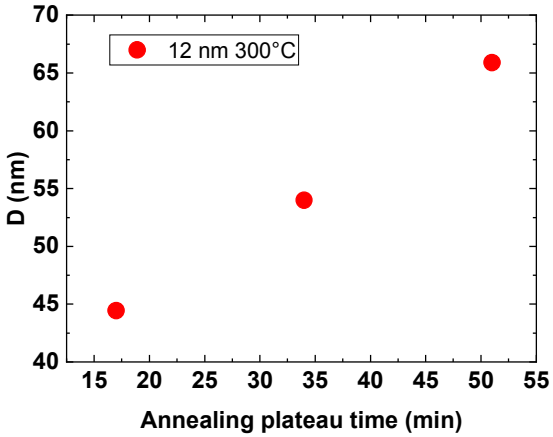


Figure 6.11: Mean size (D) of nanoparticles vs. annealing plateau time. The ICL thickness and the working temperature were 12 nm and 300°C, respectively.

6.2 Structural studies

A TEM micrograph of a ZnO NW decorated with silver NPs, is shown in **Figure 6.12 a.** The Ag NPs were prepared with an ICL of 6 nm. The working temperature was 300°C and the annealing plateau time was 17 min. An EDX mapping of the same NW decorated with NPs is shown in **Figure 6.12 b**. Silver is mapped in red and zinc in green. The presence of zinc is

mainly due to the ZnO NW. Silver is only forming nanoparticles and no coating layer of silver is observed.

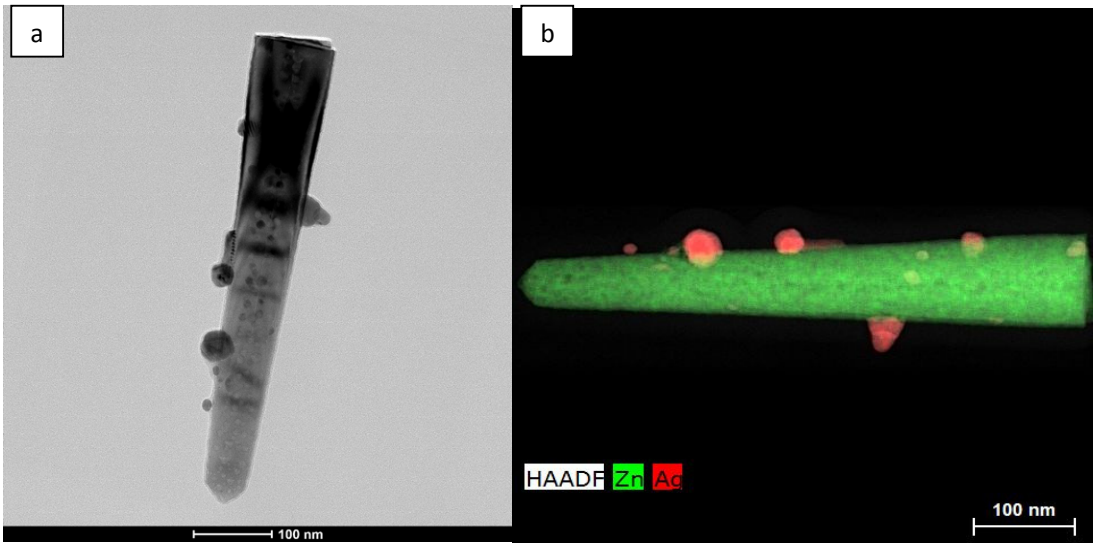


Figure 6.12: a) TEM micrograph of a single ZnO nanowire with particles of silver decorating it. The ZnO nanowire was detached from a sample prepared with a coating layer of 6 nm. The working temperature was 300°C and the annealing plateau time was 17 min. **b)** EDX mapping of the ZnO nanowire with Ag particles, which appears in **a).** Green colour correspond to Zn and red colour to Ag.

A high resolution TEM micrograph of a nanoparticle supported by a ZnO nanowire is displayed in **Figure 6.13 a**. Crystallographic planes of silver are observed. One method to obtain the average distance between planes, consists in the length of a line, divided by the number of black lines perpendicular to it. Another method, which is smoother, is the analysis of the 2D FFT. It is presented in **Figure 6.13 c**. The distance of a given spot to the centre of the reciprocal map is the inverse of the distance between the corresponding planes in direct space.

In **Figure 6.13 c,** the distance between the central point and one marked with arrow is 4.29 nm^{-1}. Thus, it represents a distance between consecutive planes of 2.3Å and corresponds to (111) crystallographic orientation of silver, (d= 2.32 Å) as tabulated in JCPDS 03-0931.

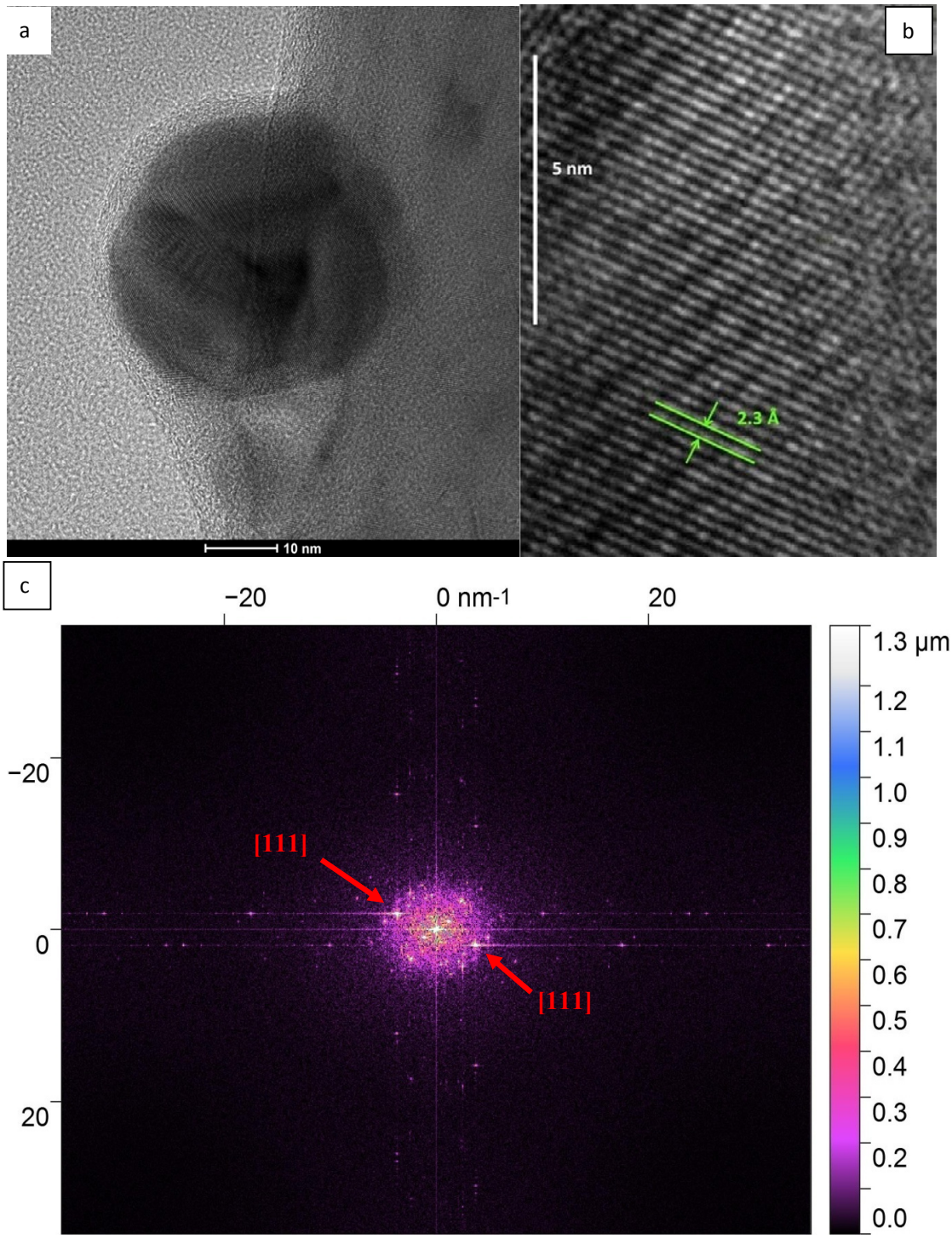


Figure 6.13: HR-TEM micrograph of a silver nanoparticle attached to the ZnO nanowire of **Figure 6.12**. b) Zoom of **Figure 6.13 a**, showing crystallographic planes. The white bar represents 5 nm and 2.3A corresponds to the distance between planes. c) 2D FFT (Fast Fourier Transform) of **Figure 6.13b.** The bright points indicated by arrows correspond to (111) oriented planes.

6.2.1 X-rays diffraction analysis

X-ray diffractograms of naked ZnO NWs (**Figure 6.14**) and of ZnO NWs with silver, are displayed in the following figures. Two different samples were prepared from naked ZnO NWs arrays. In one case, the thickness of the ICL was 50 nm (sample C19) and in the other one, it was 12 nm (sample G17). The TT was the same for both samples, which consisted in one hour of annealing plateau at a working temperature of 300°C. An additional X-ray diffractogram is presented, corresponding to the intermediate step, which consists of ZnO NWs covered with silver ICL of 50 nm without TT.

Peaks of ZnO are recognized in all diffractograms. In particular, they correspond to (002), (101), (102), (103) and (200) family of planes. They are present, still after the addition of the silver ICL and after the TT. The most intense diffraction peak corresponds to the (002) crystallographic plane and the second most intense to the (103).

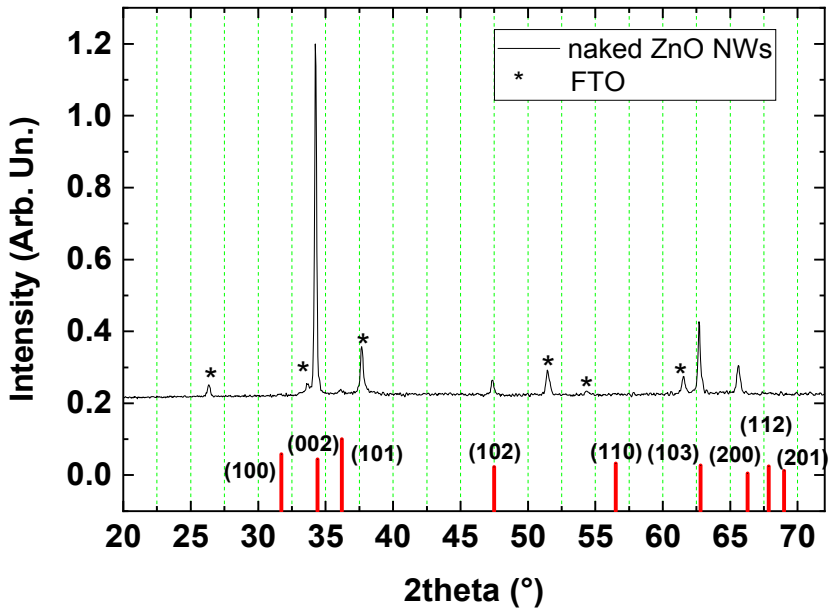


Figure 6.14: X-ray diffractogram of naked ZnO nanowires. The peaks indicated with asterisks are attributed to FTO and a JCPDS pattern of ZnO was added for comparison (red vertical lines).

The X- ray diffractogram of **Figure 6.15 a** corresponds to ZnO NWs covered by a silver ICL of 50 nm but without TT. In this case, Ag peaks are not detected. As observed in **Figure 6.2 a**, the silver layer covers the nanowires and they do not break. Whereas, after a thermal treatment of 300°C for 60 min, peaks of silver appear, as observed in **Figure 6.15 b**. Specifically, the peaks correspond to (111) planes, which is the most intense, and to (200) Ag planes. Thus, there are a significant number of (111) and (200) planes parallel to the

substrate. This is in good agreement with the FE-SEM of this sample which can be found in **Figure 6.2 b**. The NPs are formed on the broken NWs or among NWs without damage.

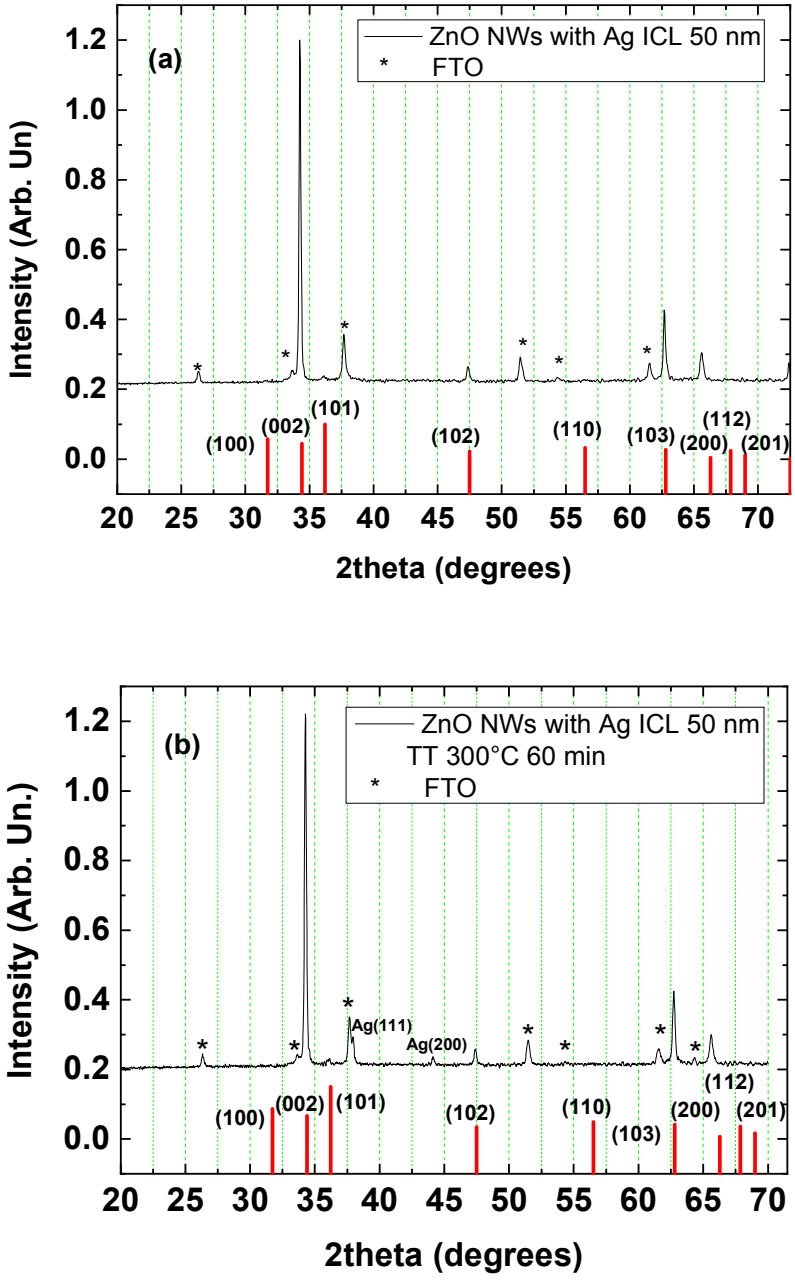


Figure 6.15: X ray diffractogram of ZnO nanowires with a silver ICL of 50 nm a) without TT and b) after a TT, whose working temperature was 300°C and the annealing plateau time was 1 hour. The peaks indicated with asterisks are attributed to FTO and a JCPDS pattern of ZnO was added for comparison (red vertical lines).

A Gaussian fit of the Ag (111) peak was made, resulting that the position of the peak is 37.9° and its FWHM (full width at half maximum) is 0.22°. It is shown in **Figure 6.16**. Using the Scherrer equation and knowing the instrumental width correction, which is 0.14°, a ca. 59 nm crystallite size value has been obtained.

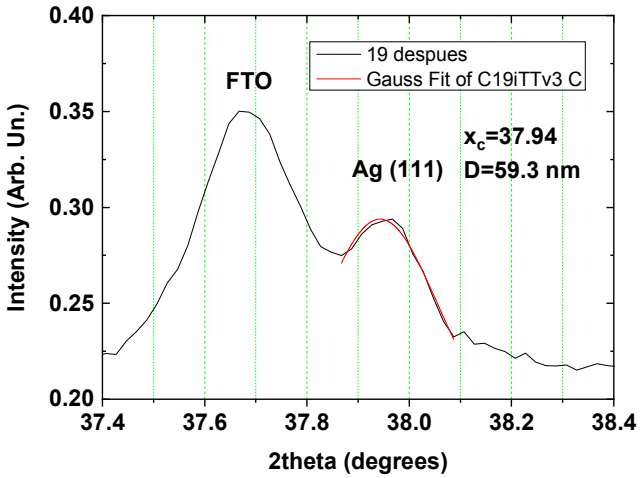


Figure 6.16: Zoom of **Figure 6.16** showing the FTO and the Ag(111) diffraction peaks in detail. In red: the gaussian fit of Ag peak

It is approximately four times smaller than the mean size of NPs, which is 238 nm. This mean size was obtained using **Figure 6.2 b**. Thus, NPs are constituted by many crystallite domains. The histogram is presented in **Figure 6.17** and corresponds to NPs of **Figure 6.2b .**

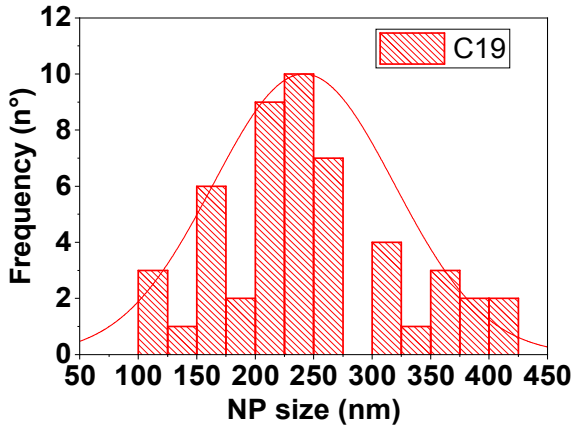
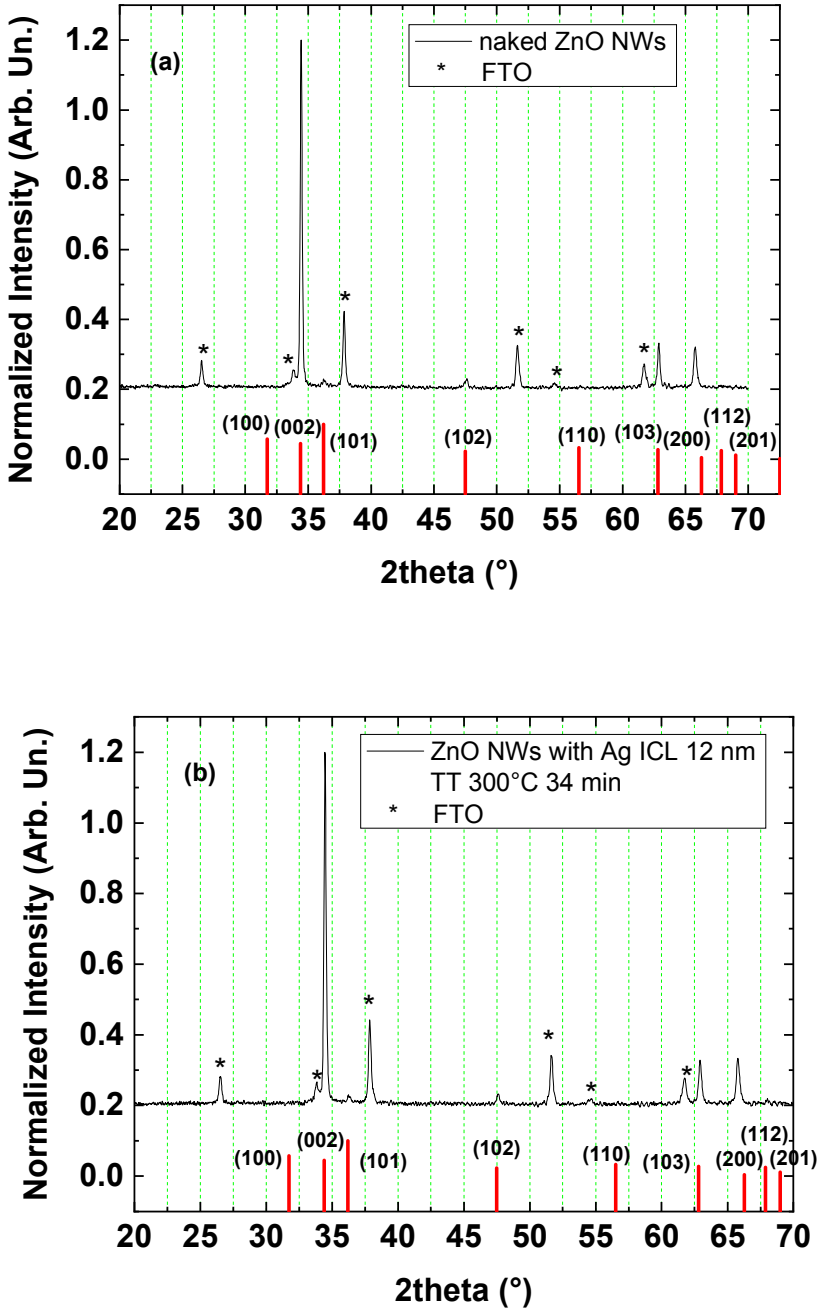


Figure 6.17: Histogram of the Ag NPs size distribution of sample C19. The Ag ICL thickness was 50 nm, the working temperature and the plateau time were 300°C and 60 min, respectively.

The X-ray diffractograms from samples of naked ZnO NWs and ZnO NWs decorated with Ag NPs are shown in **Figure 6.18.** The thickness of the ICL was 12 nm and the TT consisted in 34 min of annealing plateau at a working temperature of 300°C.



.

Figure 6.18: X-ray diffractogram of a) naked ZnO NWs b) ZnO NWs after a coating of Ag ICL whose thickness was 12 nm, the working temperature and the plateau time were 300°C and 34 min, respectively. The peaks indicated with asterisks are attributed to FTO and a JCPDS pattern of ZnO was added for comparison (red vertical lines).

The ZnO peaks, which are observed, are (002), (101), (102), (103) and (200). The most intense is the (002) peak and the second is the (200). Also, the intensity of the (200) is very similar to the (103) one. However, peaks of silver are not present after TT. One reason of the difference with sample C19 is the following: nanowires of sample C19 are broken and silver particles are formed on and between them. For this NPs, the ZnO nanowire array looks like a layer. Thus, there are many planes parallel to substrate. Whereas, in sample G17, particles are formed on the faces of nanowires, which are not broken. Thus, there are many small nanoparticles in all directions which do not generate a defined peak.

6.3 Optical properties

6.3.1 UV-Vis optical transmittance

Optical properties of the Ag NPs/ZnO nanostructures were studied by transmittance and photoluminescence. Transmittance spectra are presented in **Figure 6.19**. The black curves correspond to naked ZnO NWs. There is an absorption edge, which corresponds to the intrinsic transition. In the case of samples with silver nanoparticles, transmittance grows more smoothly with wavelength and it decreases, compared to the transmittance of naked ZnO NWs. It can be appreciated at shorter wavelengths with a dip between 400 nm and 500 nm which corresponds to surface plasmon resonance of silver nanoparticles. Transmittance spectra of samples whose ICL thickness was 12 nm, but with different annealing plateau times, are shown in **Figure 6.19 a**. From 400 nm to 500 nm, the transmittance for the 17 min sample is smaller than for the 34 min and for the 51 min ones. For the sample prepared with an ICL of 6 nm and an annealing plateau time of 17 min, the same trend is observed but in a narrow wavelength range (400-450 nm). As presented in chapter 2 and 5, this can be explained in terms of the relation (d_{CC}/D), where d_{CC} is the mean distance between the centres of nearest neighbours and D is the NP mean size. When this value is smaller, a strong interaction between NPs occurs. Therefore, the resonance has a blue shift and it is narrower.

Figure 6.19 b shows the absorbance of naked NWs and some samples of ZnO NWs with silver. The parameter α_{exp} is the experimental absorption coefficient which is $\alpha_{abs}d^*$. α_{abs} and d^* are the absorption coefficient and the thickness of the sample, respectively.

The optical absorbance of samples with silver is larger than one for naked ZnO NWs. Moreover, there are also difference in their profiles. The absorbance spectra of the samples present a peak corresponding to the absorption edge of the ZnO and in some case a peak or shoulder between 400 nm and 500 nm, corresponding to SPR of silver nanoparticles. The last is recognized for (6 nm 300°C 17 min), (12nm 300°C 17 min), (12 nm 300°C 34) min and (12 nm 300°C 51 min) samples. In the last two cases, the ZnO NWs show more uncovered surface, making the absorbance in the 400 nm-500 nm spectral region smaller.

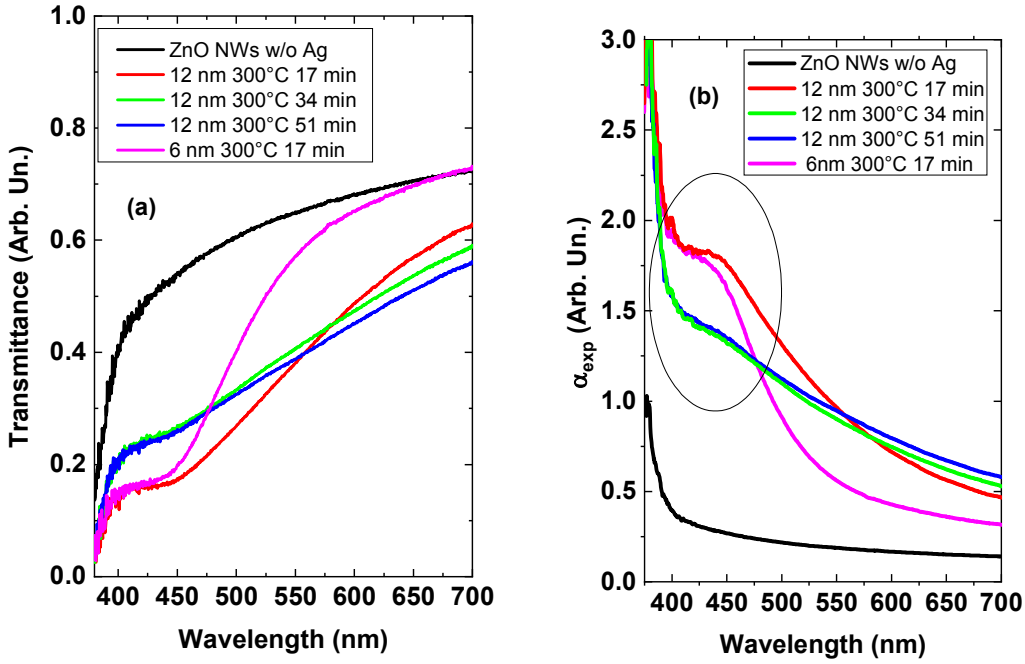


Figure 6.19: a) UV-Vis transmittance and b) experimental absorption coefficient of naked ZnO NWs arrays (black) and samples of ZnO NWs of the same type, decorated with silver NPs. Fabrication characteristics for each sample are specified in the legend by the thickness of the ICL, the working temperature and the annealing plateau time. The oval which appears in **Figure 6.19 b** is indicating the peaks or shoulders which correspond to SPR.

Tauc plots were made to obtain the band gap of ZnO in a typical sample with naked ZnO NWs. The experimental absorption coefficient $\alpha_{exp}$was obtained through equation 6.2:

$$\alpha_{exp} = -\ln(T_{exp}) \qquad \textbf{6.1}$$

where T_{exp} is the experimental measured transmittance. A linear fit was made to calculate the band gap energy, as shown in **Figure 6.20 a**. Its value is 3.20 eV. Another Tauc plot is shown in **Figure 6.20 b**. In this case, a proper background for any residual below bandgap energy absorption was subtracted and it generates a new α_{exp} [15]. An indirect band gap ($\alpha_{exp} \propto \left(h\nu - E_g\right)^2$) was considered as a background

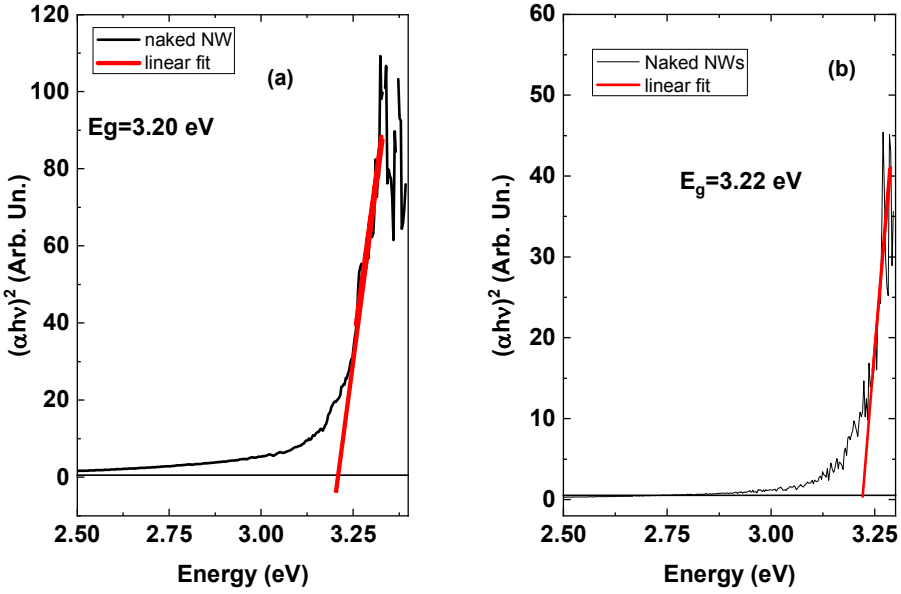


Figure 6.20: Tauc plots of naked NWs a) before and b) after substracting indirect absorption. Linear fits were made and their intersections with the horizontal axis correspond to the optical bandgap energy (E_g)

6.3.2 Room temperature photoluminescence studies

Spectroscopic photoluminescence is a technique which allows determining properties of the material such as defects species or defect concentrations. Their characteristics and the experimental set up used in this work, are described in chapter 3.

6.3.2.1 Evolution of the different emission bands

Figure 6.21 shows plots of the room temperature photoluminescence (PL) for different samples and different conditions: naked ZnO NWs, ZnO NWs with a silver ICL and ZnO NWs decorated with Ag NPs through the SSD process. The typical photoluminescence of a ZnO NWs array sample shows a band towards UV, which is denominated near band edge NBE or exciton emission. It is most probably that this PL band is due to direct transitions of electrons from the conduction band tails to valence band ones. Different bands can also be observed in the visible region of the spectrum and they correspond to defects in the lattice of ZnO [16] [17] [18] [19].

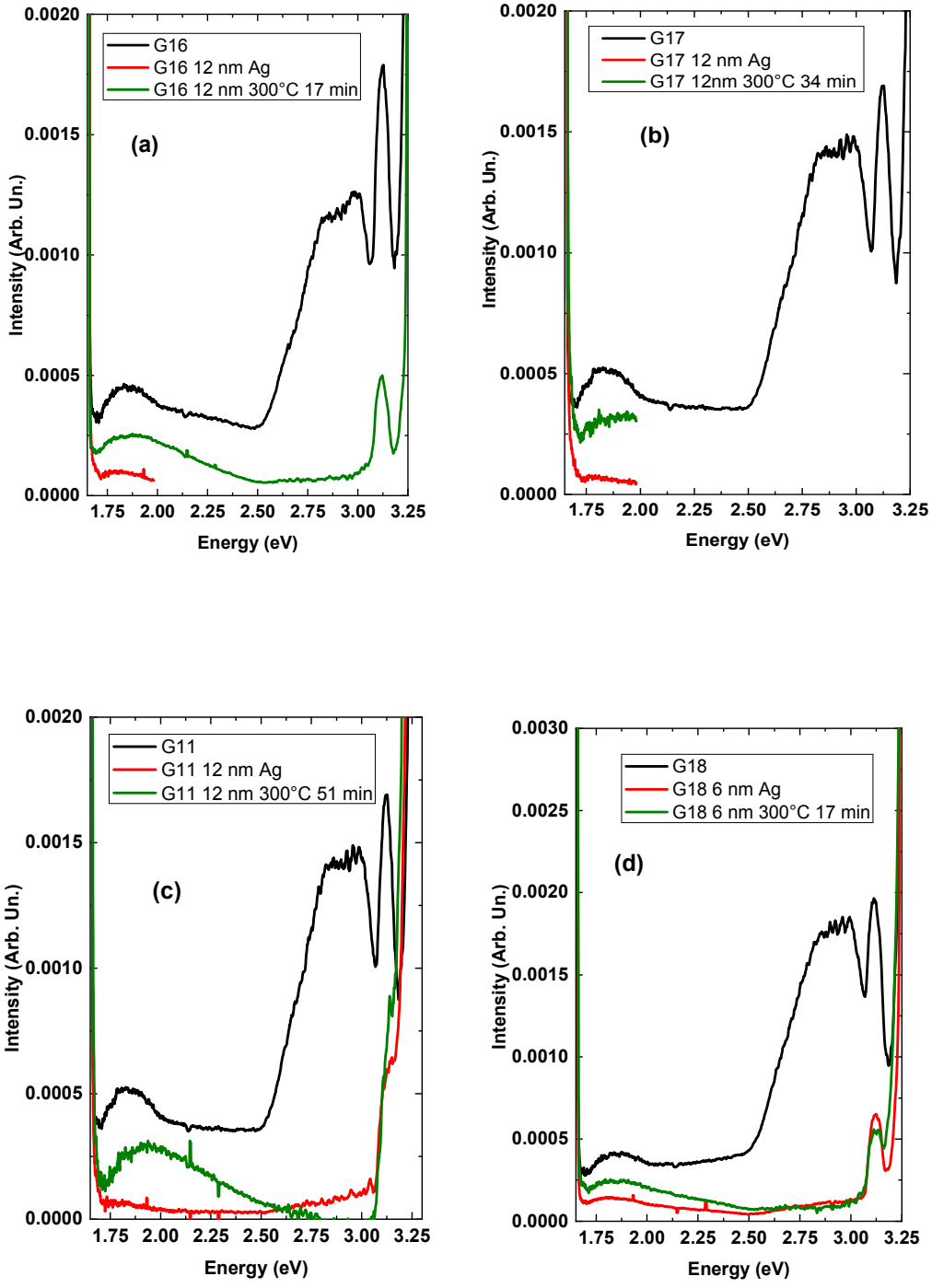


Figure 6.21:Room temperature photoluminescence of different samples: naked ZnO NWs (black curves), ZnO NWs with a silver ICL (red curves) defined by the ICL thickness, ZnO NWs decorated with silver NPs through the SSD process (olive curves) defined by the ICL thickness and the values of the annealing: working temperature and annealing plateau time.

For all the samples, the photoluminescence of naked ZnO NWs presents a narrow band corresponding to NBE, and a broad band due to defects. The first one appears in all cases. Although it is attenuated, photoluminescence spectra of NWs with a silver ICL presents two bands in the visible region: one in the violet region and the other in the red one. The lack of the blue emission can be due to SPR generated by the roughness of the ICL film. For the case of ZnO NWs decorated with NPs, the violet and blue emission are absent. It can be explained by the SPR absorption generated by the silver NPs or by the inherent thermal treatment suffered by the ZnO during the SSD process. As the bands in the violet-blue region are present in the photoluminescence spectra of naked ZnONWs after annealing (see discussion below), the lack of this band can be attributed to the SPR optical absorption.

In the following, a detailed study of the photoluminescence will be presented. Each spectrum, corresponding to different samples and conditions, will be fitted with different Gaussian functions. The PL emissions will be attributed to the corresponding energy transitions. Energy bands diagrams will be displayed to support the interpretation.

The photoluminescence spectra for different naked ZnO nanowires samples are shown in **Figures 6.22** and **6.23**. They were fitted with four or five Gaussian functions. The first one corresponds to the near band edge (NBE) emission and it is located at 3.12 eV-3.13 eV. The second one, is located at 3.0 eV. Venkatesh et al. [20] mention that this emission is due to a transition from the minimum of the conduction band to a Zn vacancy level (V_{Zn}) (0.3 e V above the maximum of the valence band). This transition is a clear evidence for the presence of zinc vacancies in the nanostructure. A wide band in the blue region, whose centre is at 2.90 eV, is observed. Zheng et al. attributed this band to transitions from extended Zn interstitial states (Z_{ni}) defects to the valence band. Electrons can first undergo transitions to the conduction band or Z_{ni} states. Then, they relax to extended Z_{ni} states and finally they fall into the valence band with blue emissions. The fourth peak is placed at 1.83 eV, Manzano et al. showed that corresponds to transitions from conduction band to substitutional oxygen at Zn sites (O_{Zn}) [16]. In some cases a fifth band appears at 2.20 eV which is attributed to a transition from the ZnO conduction band to oxygen vacancies [17], [21].

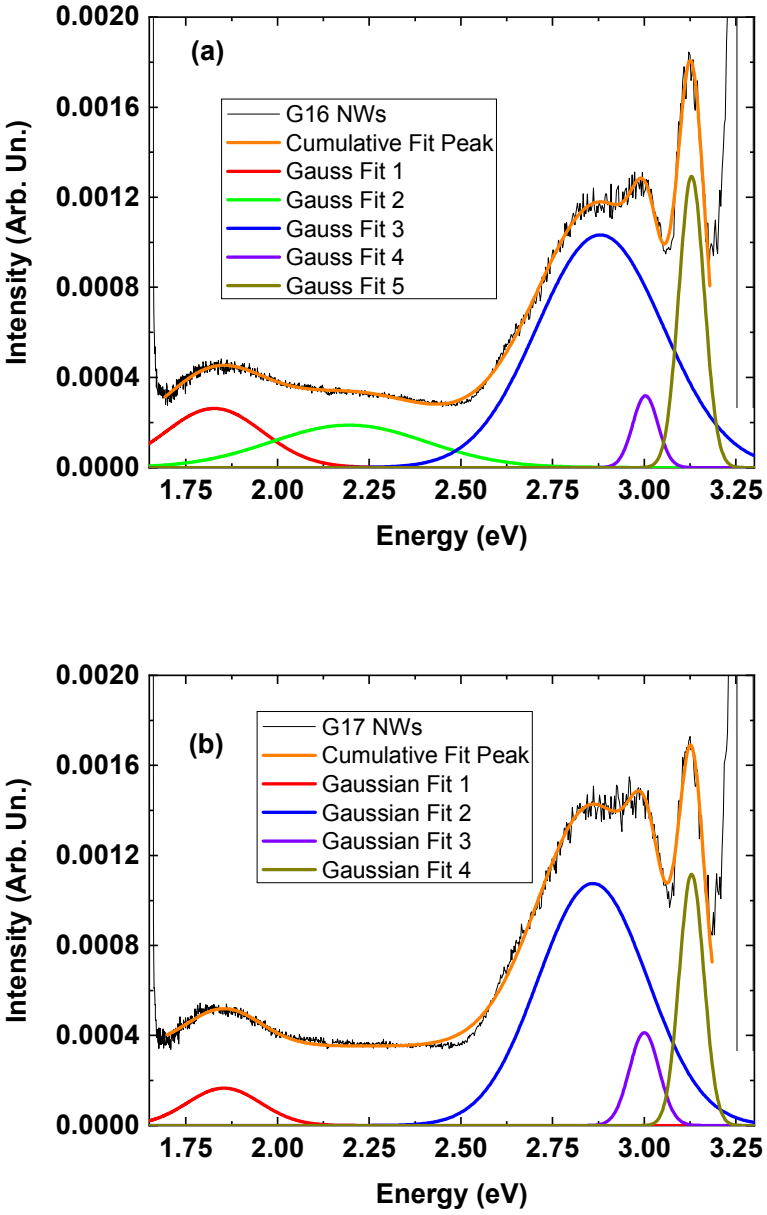


Figure 6.22: Photoluminescence of naked ZnO NWs samples: a) G16 and b) G17), with their respective Gaussian fits. The black curve corresponds to the experimental photoluminescence while the orange one is the cumulative sum of the different contributions with the addition of a constant k. The dark yellow Gaussian fit is attributed to the NBE emission. The violet, blue, green and red Gaussian fits are emissions due to defects.

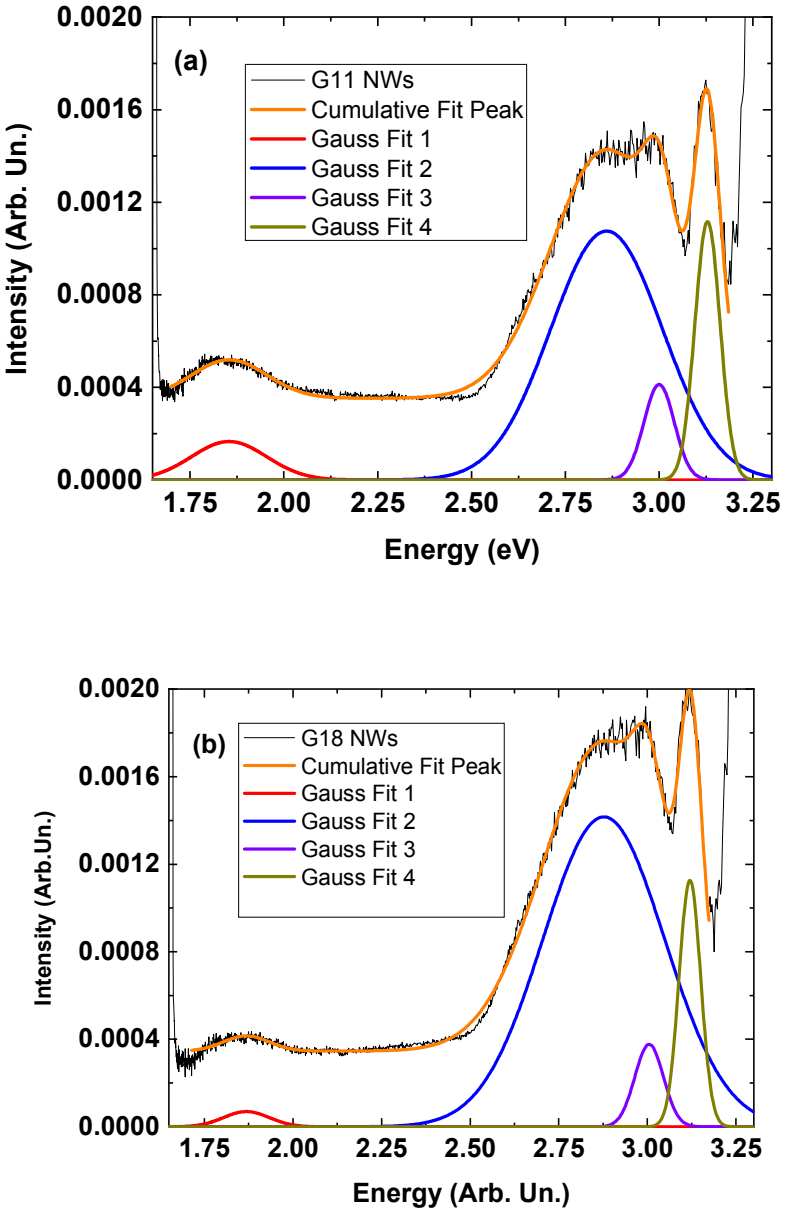


Figure 6.23: Photoluminescence of naked ZnO NWs samples: a) G11 and b) G18, with their respective Gaussian fits. The black curve corresponds to the experimental photoluminescence while the orange one is the cumulative sum of the different contributions with the addition of a constant k. The dark yellow Gaussian fit is attributed to the NBE emission. The violet, blue and red Gaussian fits are emissions due to defects.

In the first step, ZnO nanowires were coated with a silver ICL 12 nm thick (samples G16, G17 and G11) and 6 nm thick (sample G18). Photoluminescence spectra of those silver coated ZnO NWs are shown in **Figures 6.24** and **6.25**.

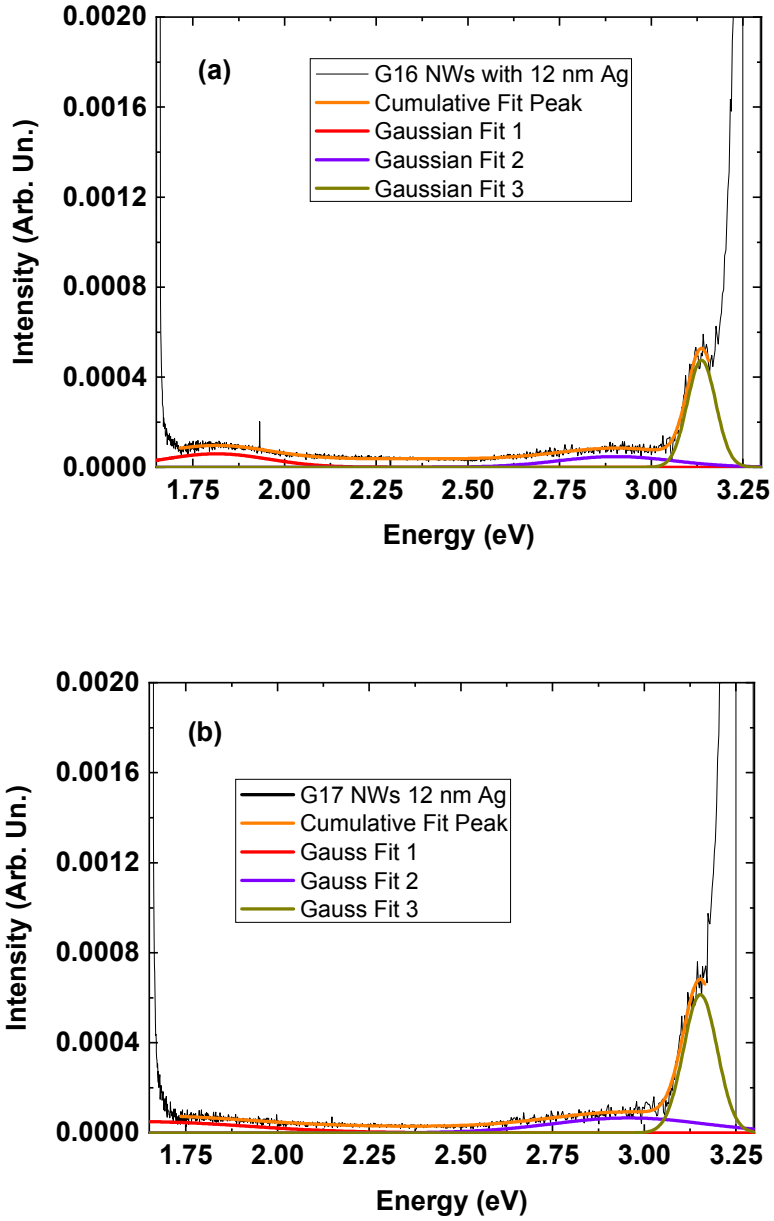


Figure 6.24: Photoluminescence of ZnO NWs samples a) G16 and b) G17) with a silver ICL whose thickness was 12 nm. Gaussian fits were made. The black curve corresponds to the experimental photoluminescence spectrum while the orange one is the cumulative sum of the different contributions with the addition of a constant. The dark yellow Gaussian fit is attributed to the NBE emission. The violet and red Gaussian fits are emissions due to defects

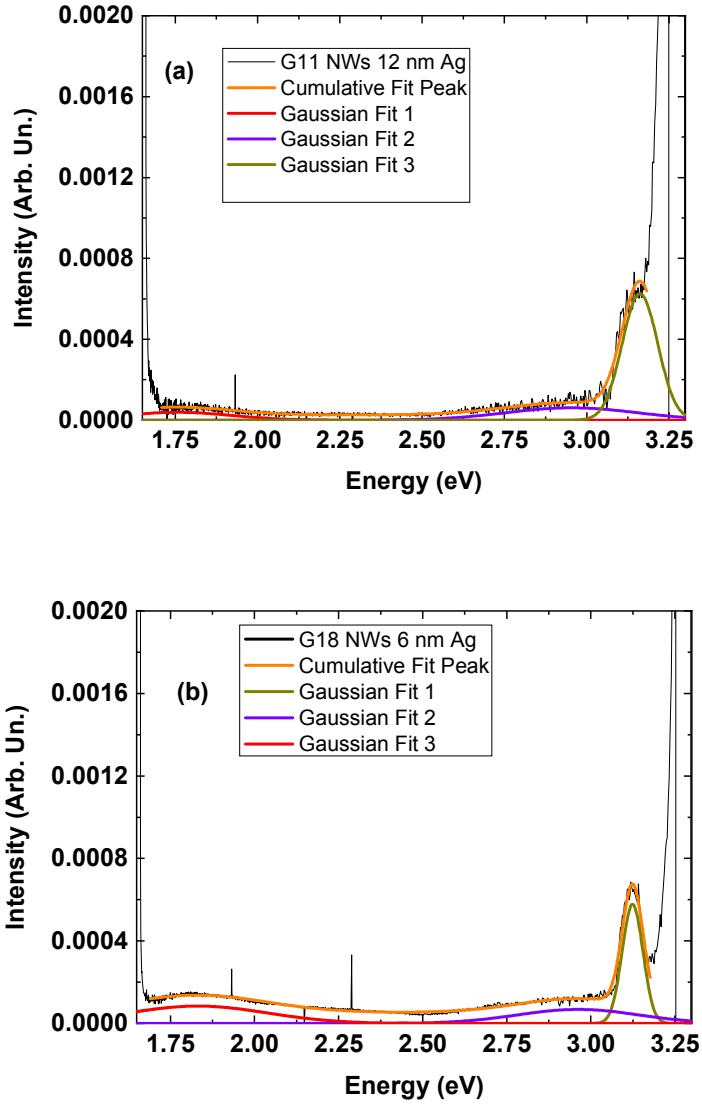


Figure 6.25: Photoluminescence of ZnO NWs samples a) G11 and b) G18) with a silver ICL whose thickness were 12 nm and 6 nm respectively. Gaussian fits were made. The black curve corresponds to the experimental photoluminescence spectrum while the orange one is the cumulative sum of the different contributions with the addition of a constant. The dark yellow Gaussian fit is attributed to the NBE emission. The violet and red Gaussian fits are emissions due to defects

The spectra depicted in **Figures 6.24** and **6.25** were fitted with three Gaussian functions. The first one, which corresponds to the NBE emission band, is placed at 3.14 eV, 3.15 eV, 3.16 eV and 3.12 eV for samples (G16: 12 nm 300°C 17 min), (G17: 12 nm 300°C 34 min), (G11: 12 nm 300°C 51 min) and (G18: 6 nm 300°C 17 min), respectively. The second one in the violet region, which corresponds to transitions from the minimum of the conduction band to a V_{Zn} is between 2.90 and 2.96 eV. The third one which is centred at ca. 1.80 eV, is attributed

to transitions from the conduction band to the O_{Zn}. For sample G17, this band is centred at 1.63 eV. In this case, the emission can be assigned to transitions from the oxygen vacancies to the valence band.

In **Figures 6.26** and **6.27,** we present the photoluminescence spectra of the silver coated ZnO NWs after the solid state dewetting process. They are composed of ZnO NWs decorated with Ag NPs. The working temperature was 300°C and the annealing plateau times were 17 min, 34 min and 51 min.

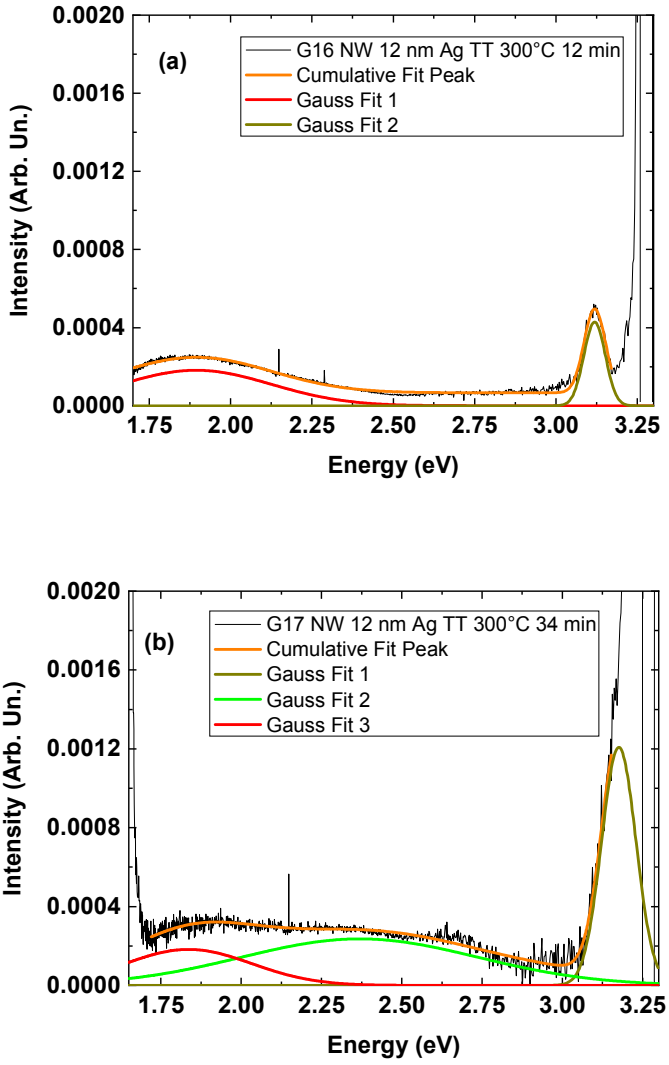


Figure 6.26: Photoluminescence of ZnO NWs samples a) G16 and b) G17 decorated with Ag NPs. The ICL thickness was 12 nm, the working temperature was 300°C and the annealing plateau times were a) 17 min and b) 34 min. Gaussian fits were made. The black curve corresponds to the experimental photoluminescence spectrum while the orange one is the cumulative sum of the different contributions with the addition of a constant. The dark yellow Gaussian fit is attributed to the NBE emission. The green and red Gaussian fits are emissions due to defects.

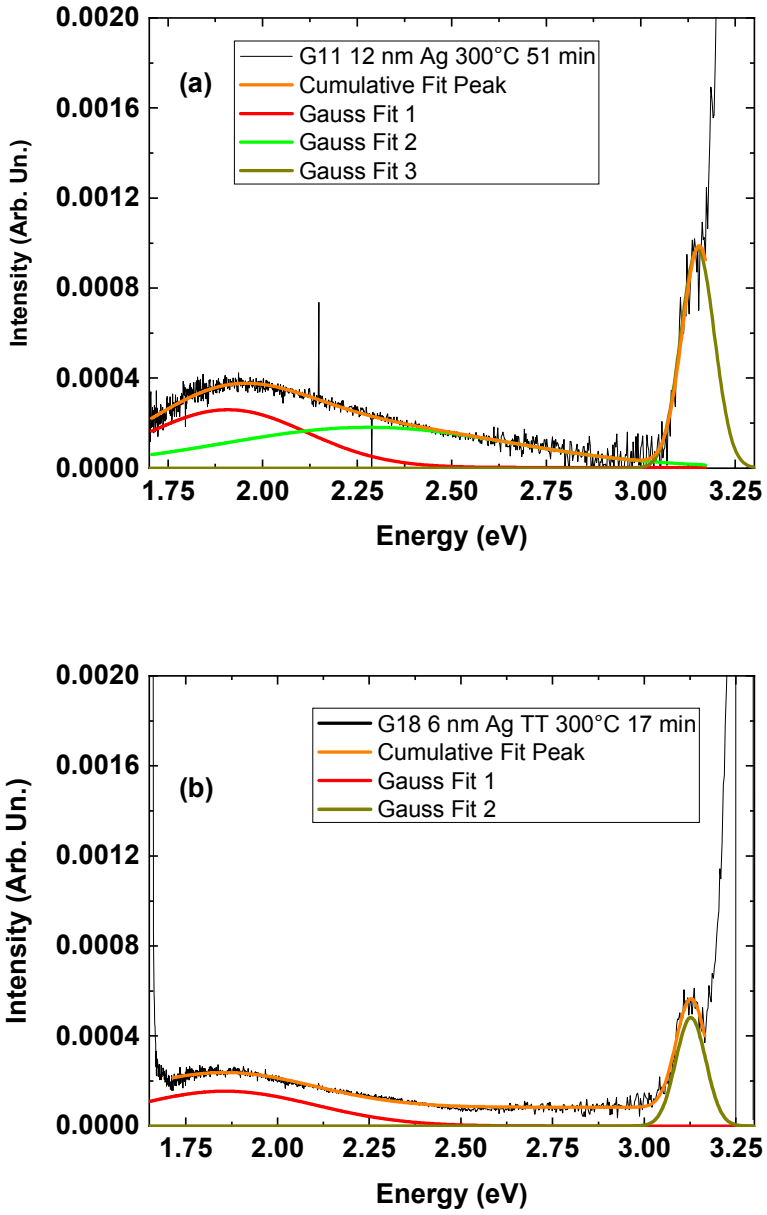


Figure 6.27: Photoluminescence of ZnO NWs samples a) G11 and b) G18 decorated with Ag NPs. The ICL thickness were a) 12 nm and b) 6 nm, the working temperature was 300°C and the annealing plateau times were a) 51 min and b) 17 min, respectively. Gaussian fits were made. The black curve corresponds to the experimental photoluminescence spectrum while the orange one is the cumulative sum of the different contributions with the addition of a constant. The dark yellow Gaussian fit is attributed to the NBE emission. The green and red Gaussian fits are emissions due to defects.

The energy values for the centre of the Gaussian fits are summarized in **Table 6.3.** The energy level diagrams, showing some of the principal defects levels in ZnO and the related photoluminescence emissions transitions observed in the studied samples are shown in **Figures 6.28** and **6.29**.

Table 6.3: Energy values of the different photoluminescence emission peaks observed in the samples under study.

Sample	NBE Peak (eV)	Peaks in violet - blue region (eV)	Peak in green region (eV)	Peak in red region (eV)
G16	3.13	3.00, 2.88	2.20	1.83
G16 12 nm Ag	3.14	2.91	-	1.81
G16 12 nm 300°C 17 min	3.12	-	-	1.89
G17	3.13	3.00, 2.86	-	1.85
G17 12 nm Ag	3.15	2.96	-	1.63
G17 12 nm 300°C 34 min	3.18		2.37	1.84
G11	3.13	3.00, 2.86	-	1.85
G11 12 nm	3.16	2.95		1.76
G11 12 nm 300°C 51 min	3.15	-	2.27	1.91
G18	3.12	3.01, 2.88		1.86
G18 6nm	3.12	2.96		1.83
G18 6 nm 300°C 17 min	3.13	-	-	1.87

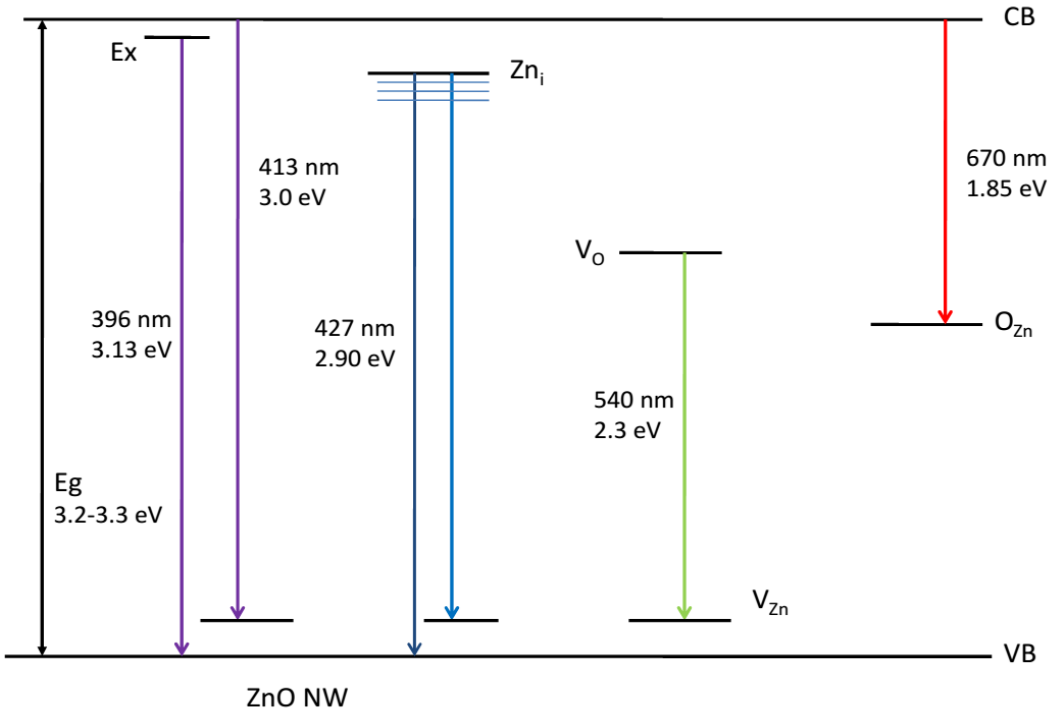


Figure 6.28: Diagram of energy levels and emissions (wavelength and energy) observed in the photoluminescence spectra of naked ZnO NWs. CB (conduction band), VB (valence band), Ex (exiton), V_{Zn}(zinc vacancies), Vo (oxygen vacancies), O_{Zn} (substitutional oxygen).

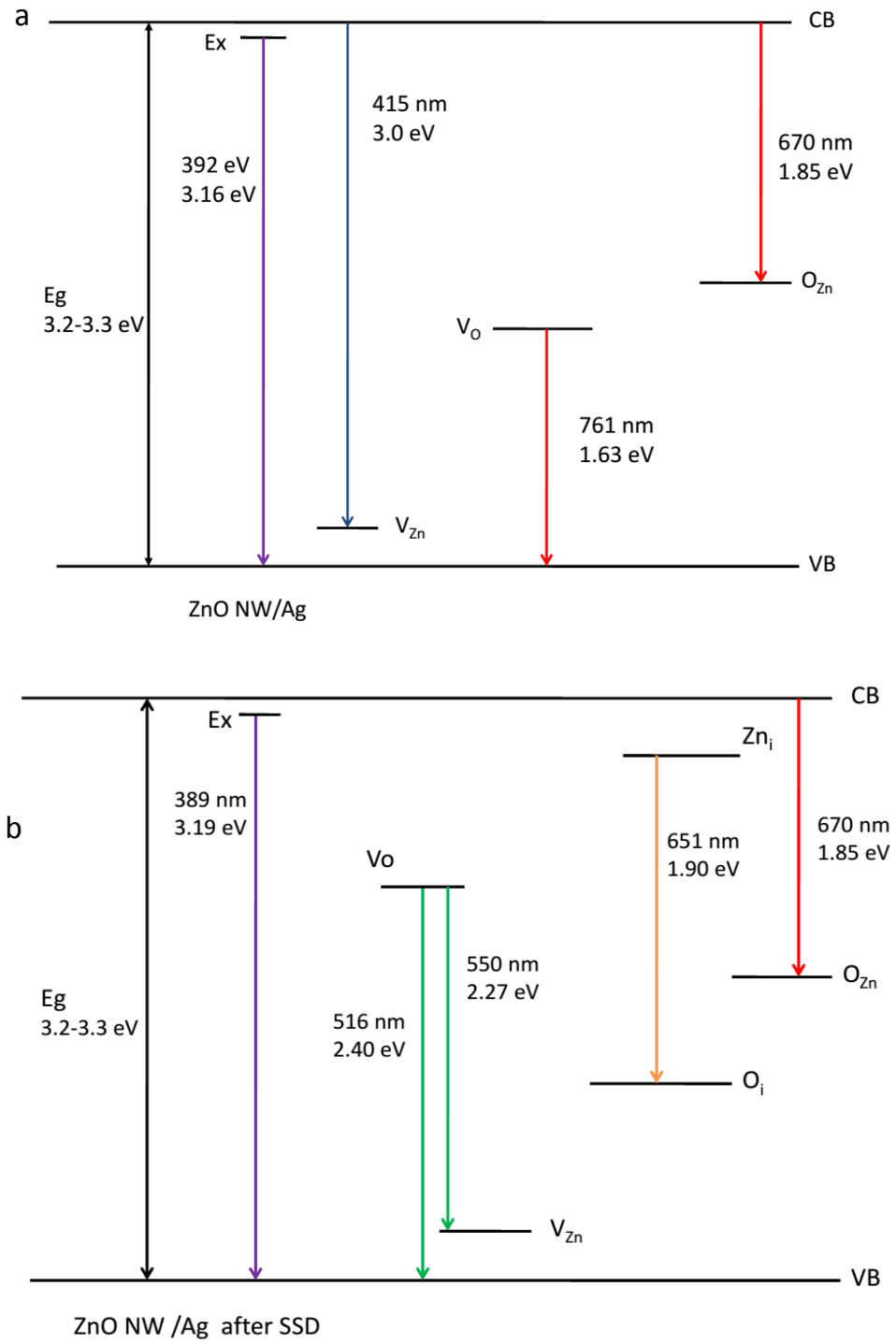


Figure 6.29: Diagram of energy levels and emissions (wavelength and energy) observed in the photoluminescence spectra of a) ZnO NWs with an Ag ICL, b) ZnO NWs decorated with Ag NPs. CB (conduction band), VB (valence band), Ex (exiton), V_{Zn}(zinc vacancies), Vo (oxygen vacancies), O_{Zn} (substitutional oxygen).

Each Gaussian fitting function is characterized by two main parameters of interest: centre position, and the area below the curve I_{band_i} (it is considered as the integrated PL intensity [27-29]). As it has been said above, five PL bands can be observed: NBE, violet, blue, green and orange-red. The integrated PL intensity of the different Gaussian functions are summarized in **Table 6.4**.

Table 6.4: Integrated intensity of the different Gaussian functions employed in the PL spectra de-convolution process.

Sample	NBE Int. (Arb. Unit)	Violet Int. (Arb. Un.)	Blue Int. (Arb. Un.)	Green Int. (Arb. Un.)	Red Int. (Arb. Un.)
G16	$1.12x10^{-4}$	$2.74x10^{-5}$	$4.45x10^{-4}$	$9.99x10^{-5}$	$8.69x10^{-5}$
12 nm Ag	4.62×10^{-5}		$1.86x10^{-5}$		$2.12x10^{-5}$
12 nm 300°C 17 min	$3.53x10^{-5}$				$1.05x10^{-4}$
G17	$9.39x\ 10^{-5}$	$4.18x10^{-5}$	$4.02x10^{-4}$	-	$4.16x10^{-4}$
12 nm Ag	$8.46x10^{-5}$	$3.05x10^{-5}$		-	$1.60x10^{-5}$
12 nm 300°C 34 min	$1.62x10^{-4}$			$2.18x10^{-4}$	$9.02x10^{-5}$
G11	$9.39x10^{-5}$	4.18x10-5	$4.02x10^{-4}$		$4.16x10^{-4}$
12 nm Ag	$6.26x10^{-4}$	$6.13x10^{-5}$			$3.9x10^{-5}$
12 nm 300°C 51 min	$1.09x10^{-4}$			$1.71x10^{-4}$	$1.35x10^{-4}$
G18	$8.61x10^{-5}$	$3.8x10^{-5}$	$6.09x10^{-4}$	-	$1.23x10^{-5}$
6 nm Ag	$4.46x10^{-5}$	$3.08x10^{-5}$			$4.32x10^{-5}$
6 nm 300°C 17 min	$4.93x10^{-5}$				$9.52x10^{-5}$

Now, the normalized integrated photoluminescence $I_{band_norm_i}$ will be considered as:

$$I_{band_norm_i} = \frac{I_{band_i}}{\sum_i I_{band_i}} \qquad \textbf{6.2}$$

where I_{band_i} is the integrated intensity of the PL emission band i. Plots of normalized integrated photoluminescence (PL) are shown from **Figure 6.30** to **6.33**. For each sample, bar graphs are presented for each condition: naked ZnO NWs, ZnO NWs/Ag and ZnO NWs/Ag after SSD.

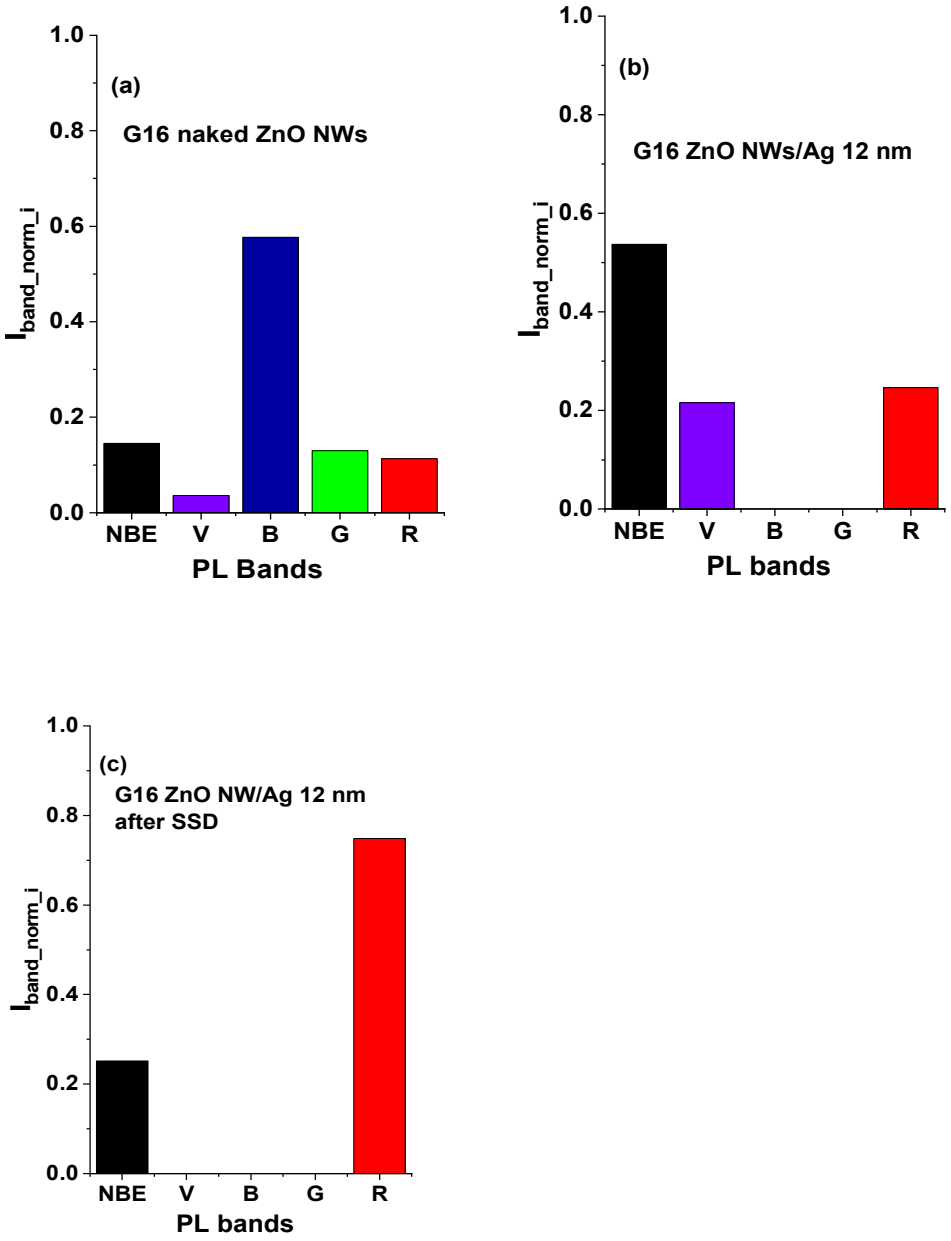


Figure 6.30: Normalized integrated PL for the different bands (NBE (near band edge), V (violet), B (blue), G (green), R (red)) of sample G16 in different conditions a) naked ZnO NWs w/o TT b) ZnO NWs/Ag 12 nm c) ZnO NWs/Ag 12 nm after SSD. The working temperature and the annealing plateau time were 300°C and 17 min, respectively.

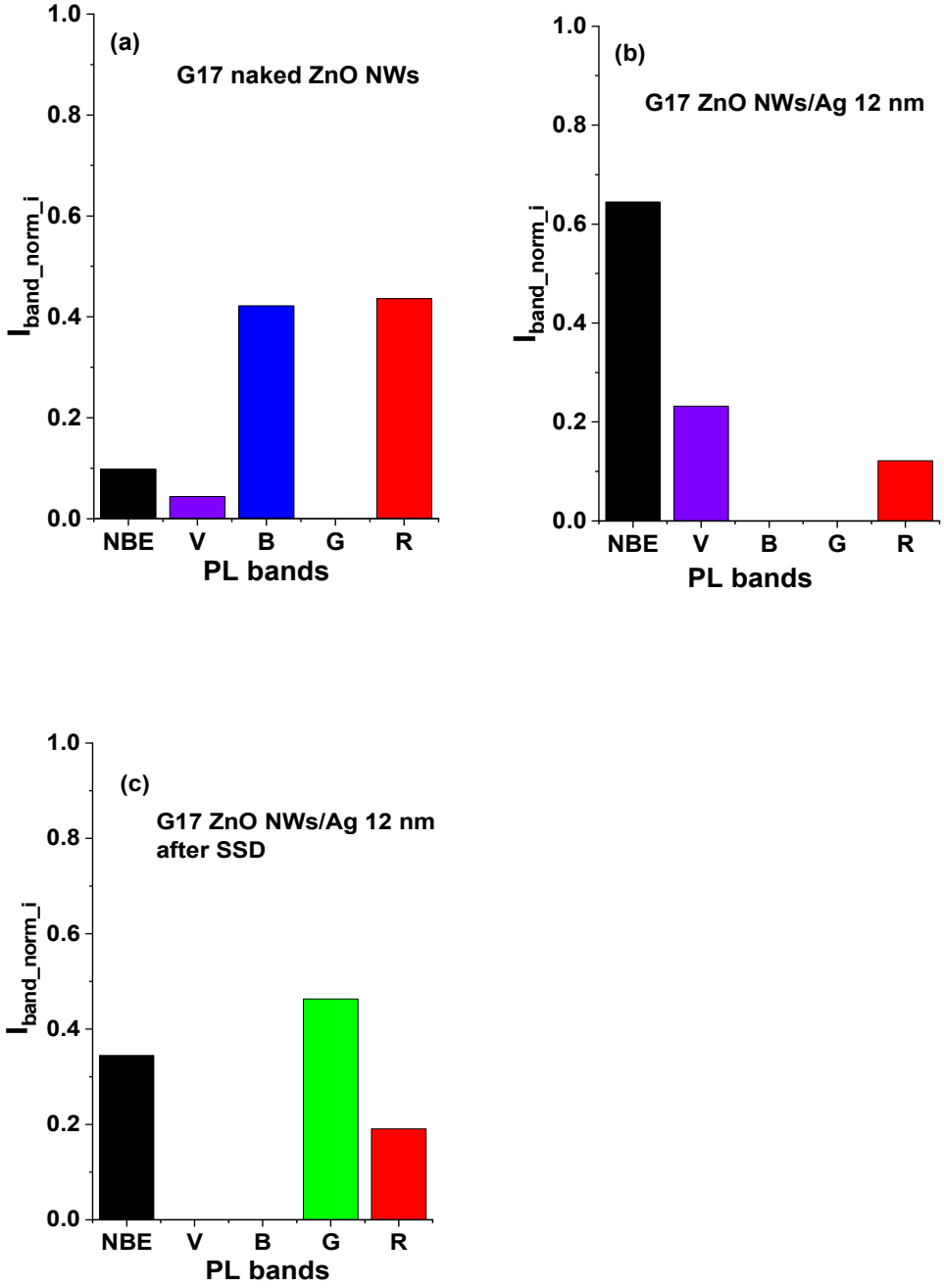


Figure 6.31: Normalized integrated PL for the different bands (NBE (near band edge), V (violet), B (blue), G (green), R (red)) of sample G17 in different conditions a) naked ZnO NWs w/o TT b) ZnO NWs/Ag 12 nm c) ZnO NWs/Ag 12 nm after SSD. The working temperature and the annealing plateau time were 300°C and 34 min, respectively.

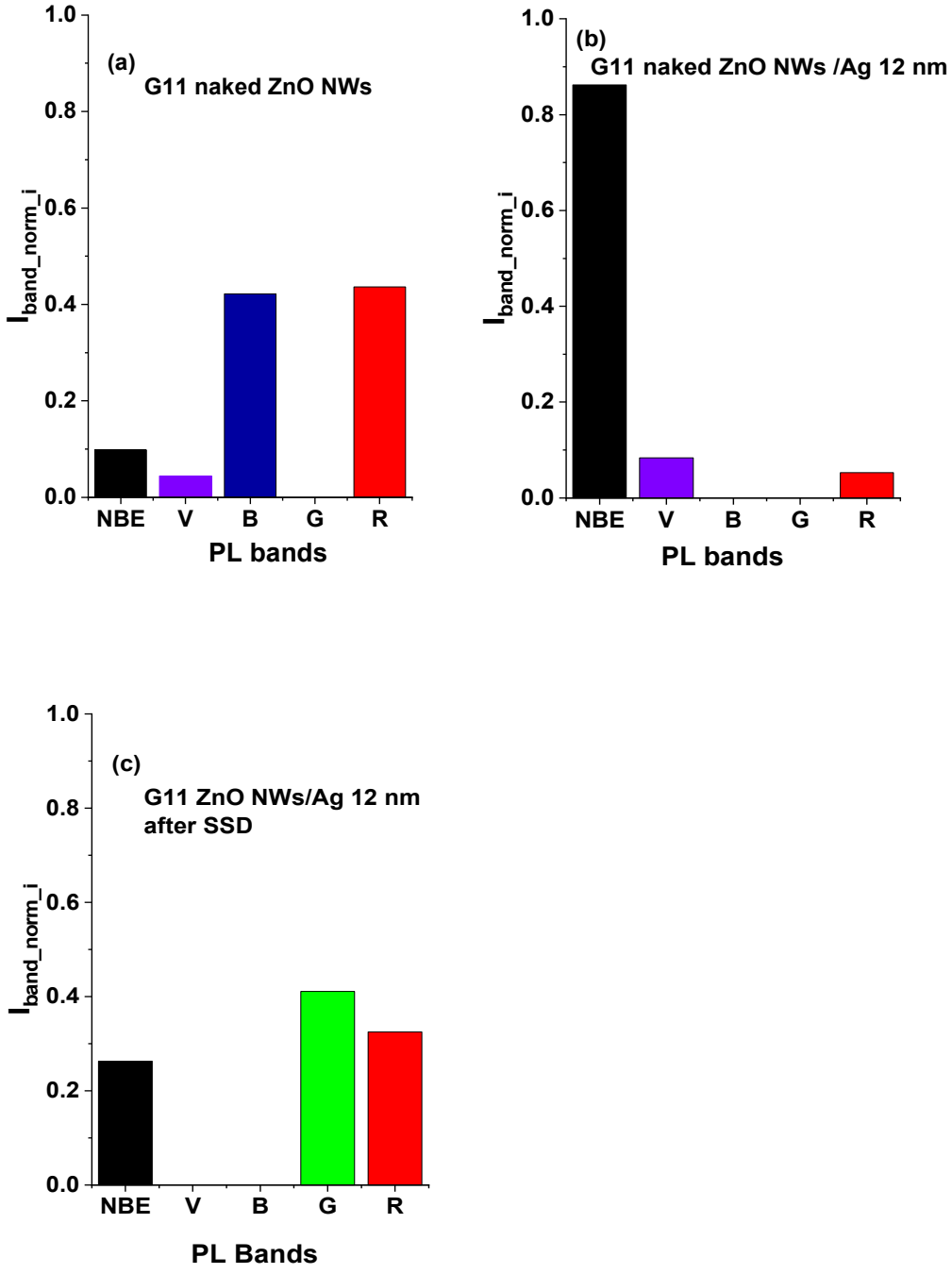


Figure 6.32: Normalized integrated PL for the different bands (NBE (near band edge), V (violet), B (blue), G (green), R (red)) of sample G11 in different conditions a) naked ZnO NWs w/o TT b) ZnO NWs/Ag 12 nm c) ZnO NWs/Ag 12 nm after SSD. The working temperature and the annealing plateau time were 300°C and 51 min, respectively.

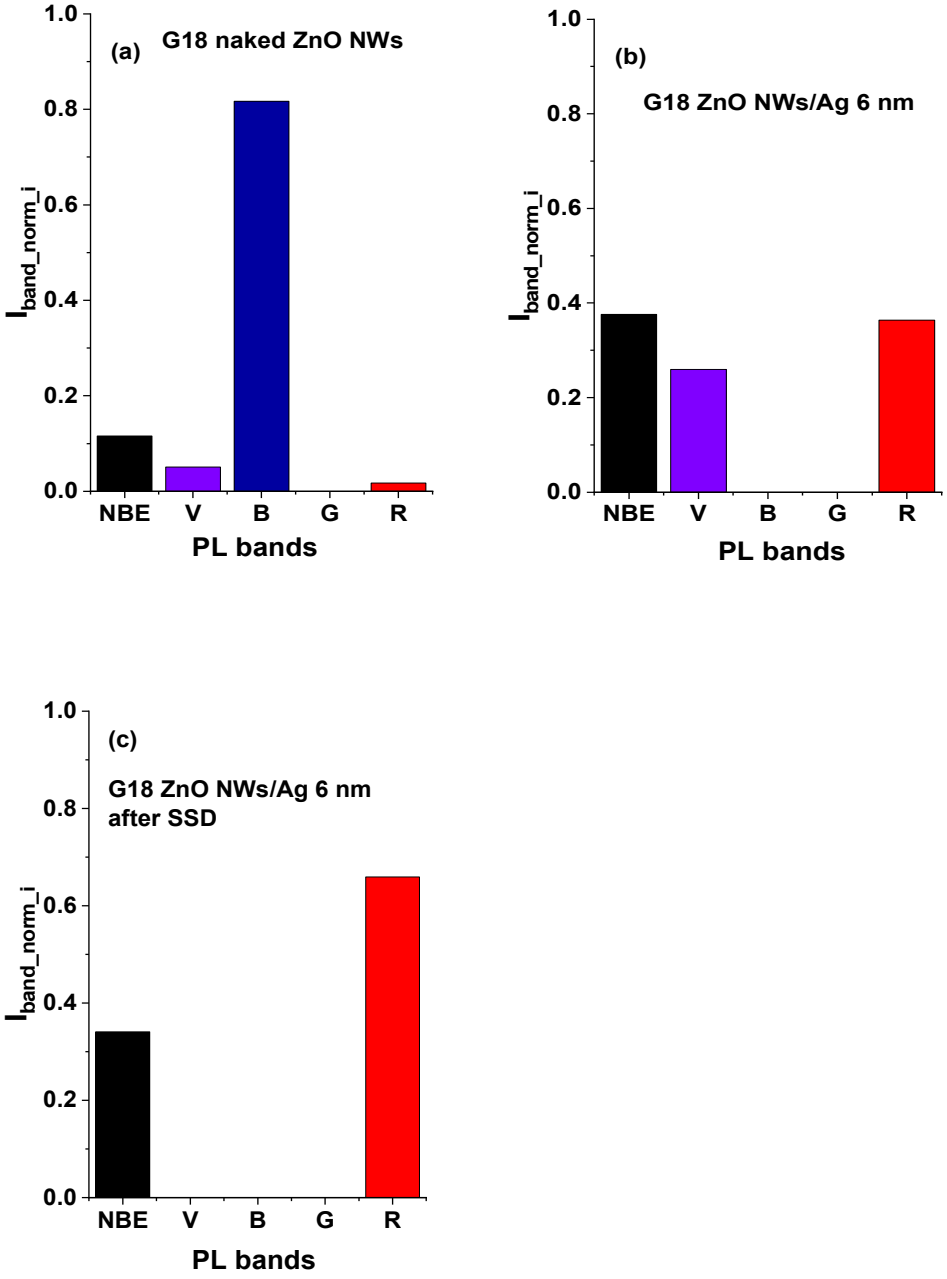


Figure 6.33: Normalized integrated PL for the different bands (NBE (near band edge), V (violet), B (blue), G (green), R (red)) of sample G17 in different conditions a) naked ZnO NWs w/o TT b) ZnO NWs/Ag 6 nm c) ZnO NWs/Ag 6 nm after SSD. The working temperature and the annealing plateau time were 300°C and 17 min, respectively.

For naked ZnO NWs, the PL emissions due to defects are more significant than the NBE one. The band exhibiting the highest intensity is located in the blue region. For ZnO NWs with 12 nm Ag, the NBE enhances and the violet and red bands are present. The violet and blue bands are attenuated or absorbed (mainly the blue band) by the SPR generated by the roughness consisting of metal NPs. Hong et al.[22] observed in silver films prepared by magnetron sputtering, a SPR due to roughness of the film. The red band is also attenuated, but it may be due to silver continuous coating which acts as a filter. For ZnO NWs/Ag after SSD, the bands in the violet and blue disappear. After SSD, NPs are observed in the FE-SEM micrographs, decorating the surface of ZnO NWs. Hence, the lack of this bands can be explained by SPR absorption.

Another important quantity is the ratio $R_{NBE-def} = \frac{I_{NBE}}{I_{def}}$. I_{NBE} and I_{def} are the integrated PL intensity of the NBE peak and the sum of the integrated PL intensities of the different defects bands, respectively. The information which this quantity gives to us, is the enhancement or reduction of the NBE emission with respect to defects ones. Moreover, it provides a measure of the optical quality or defect states of the different nanostructured ZnO samples.

The relation $R_{NBE-def}$ for different samples and different conditions are presented in **Table 6.5**. The different conditions are: naked ZnO NWs, ZnO NWs coated with a silver ICL and ZnO NWs decorated with Ag NPs. The largest values are those corresponding to ZnO NWs with a silver ICL, probably because in this case the ICL acts as an optical filter to the visible part of the spectrum, generating a decrease of the visible PL emission compared with that of the NBE one. $R_{NBE-def}$ for ZnO NWs with Ag NPs, is larger than the one exhibited by naked ZnO NWs. However, this trend may be due either to the presence of the Ag NPs or to the effect of the thermal treatment on ZnO NWs.

Table 6.5: $R_{NBE-def}$ for different ZnO nanostructured samples and different conditions.

Sample	**G16** **12 nm 17 min**	**G17** **12 nm 34 min**	**G11** **12 nm 51 min**	**G18** **6 nm 51 min**
Naked ZnONWs w/o TT	0.170	0.109	0.109	0.131
ZnONWs/Ag	1.163	1.82	6.25	0.602
ZnONWs/Ag after SSD	0.337	0.526	0.356	0.518

To investigate the eventual effects of the annealing on the ZnO NWs during SSD, naked ZnO NWs have been submitted to the same procedure. In this way, it is possible to decouple the effect of the Ag NPs and the merely annealing effect on the PL results. The

working temperature was 300° C and the annealing plateau times were 17 min (sample G71), 34 min (sample G73) and 51 min (sample G70). The spectra are presented in **Figures 6.34** to **6.36**.

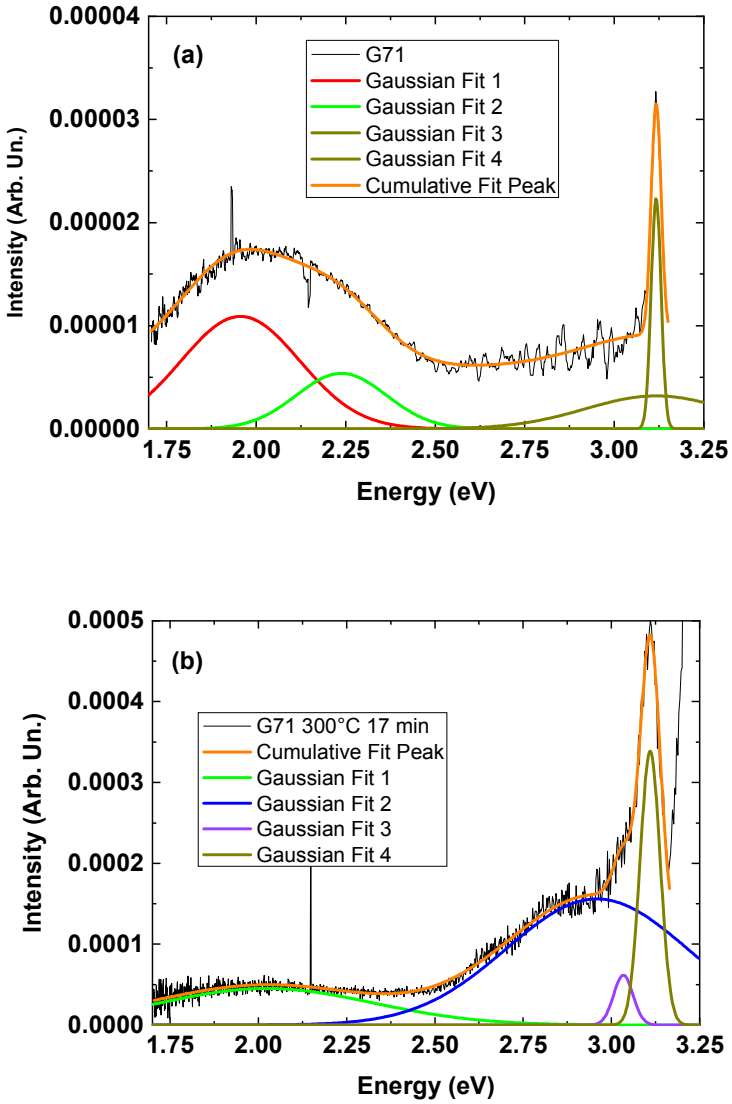


Figure 6.34:Photoluminescence of naked ZnO NWs sample (G71), before a) and after b) thermal treatment. The working temperature and the annealing plateau time were 300°C and 17 min, respectively. The black curve corresponds to the experimental photoluminescence while the orange one is the cumulative sum of the different contributions plus a constant. The dark yellow Gaussian fit is attributed to the NBE emission and the others correspond to emissions due to defects.

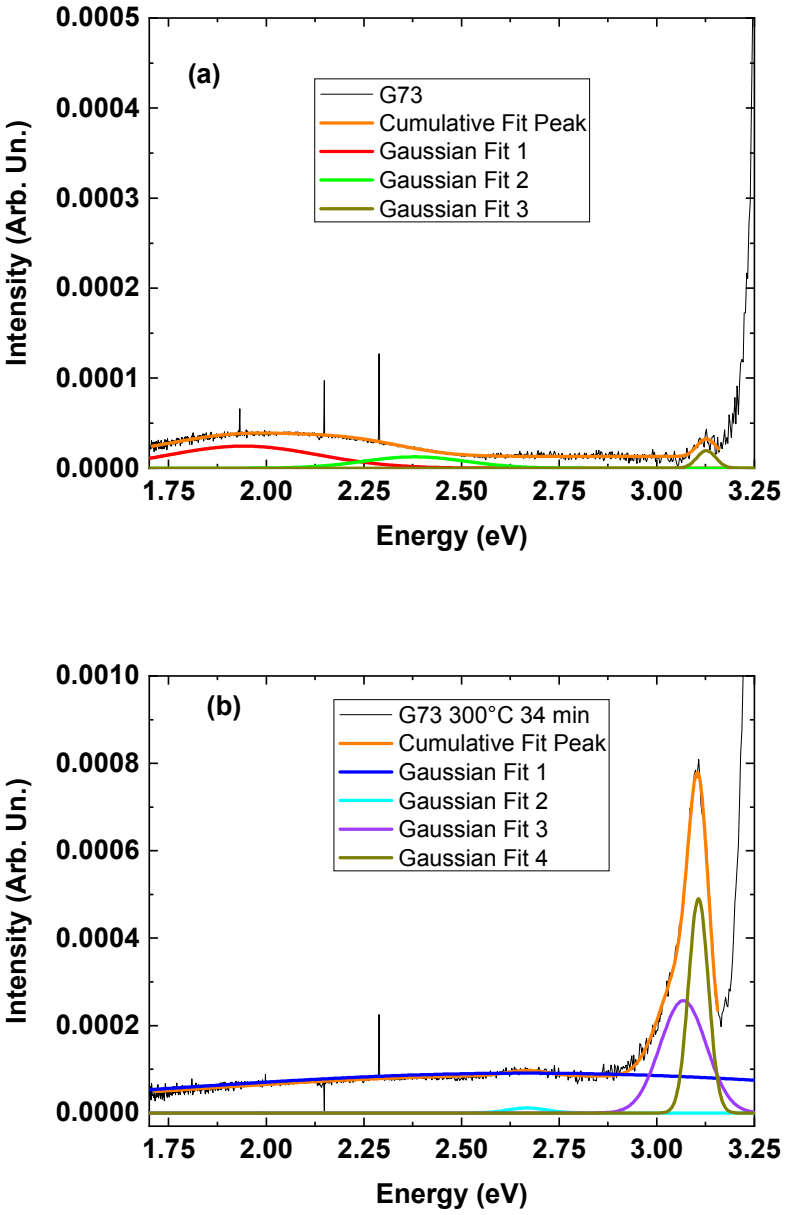


Figure 6.35: Photoluminescence spectra of naked ZnO NWs sample (G73), a) before and b) after annealing. The working temperature and the annealing plateau time were 300°C and 34 min, respectively**.** The black curve corresponds to the experimental photoluminescence while the orange one is the cumulative sum of the different contributions plus a constant. The dark yellow Gaussian fit is attributed to the NBE emission and the others correspond to emissions due to defects.

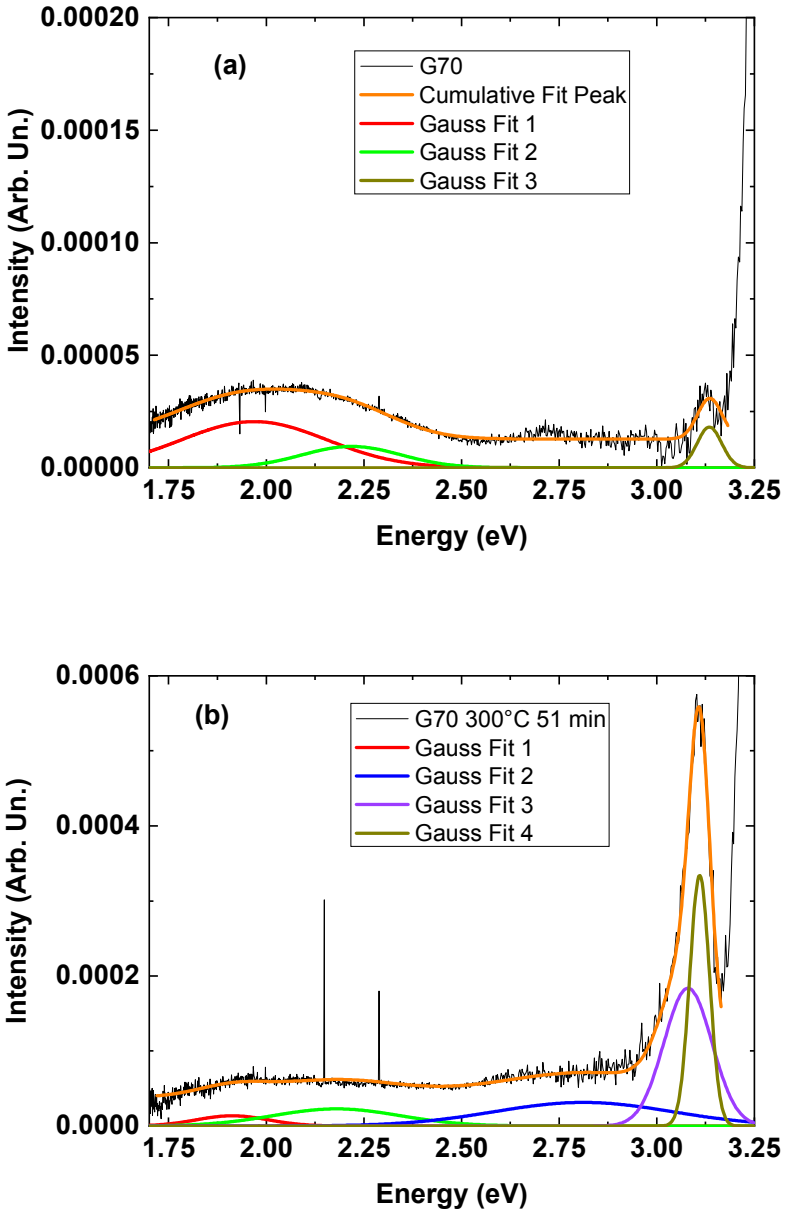


Figure 6.36: Photoluminescence spectra of naked ZnO NWs sample (G73), a) before b) and after annealing. The working temperature and the annealing plateau time were 300°C and 51 min, respectively. The black curve corresponds to the experimental photoluminescence while the orange one is the cumulative sum of the different contributions plus a constant. The dark yellow Gaussian fit is attributed to the NBE emission and the others correspond to emissions due to defects.

.

Tables 6.6 and **6.7** are for naked ZnO NWs before and after the annealing. **Table 6.6** presents the energies of the Gaussian function peaks centres. Four PL bands are recognized: NBE, violet-blue, green and red. **Table 6.7** summarizes the integrated intensity (area) for each band.

Table 6.6: Position of the different PL bands in energy values.

Sample	NBE (eV)	Violet-Blue (eV)	Green (eV)	Red (eV)
w/o TT (G71)	3.12		2.24	1.96
TT 300°C 17 min (G71)	3.11	3.03, 2.96	2.02	
w/o TT (G73)	3.13		2.38	1.94
TT 300°C 34 min (G73)	3.11	3.07,2.67		
w/o TT (G70)	3.14		2.22	1.97
TT 300°C 51 min (G70)	3.11	3.08,2.81	2.18	1.91

Table 6.7: Integrated intensity of the different Gaussian peaks

Sample	NBE (Arb.Un.)	Violet (Arb. Un.)	Blue (Arb. Un.)	Green (Arb. Un.)	Red (Arb. Un.)	$\frac{I_{NBE}}{I_{def}}$
w/o TT (G71)	$7.72x10^{-7}$			$1.69x10^{-6}$	$4.52x10^{-6}$	0.124
300°C 17 min (G71)	$2.4x10^{-5}$	$4.24x10^{-6}$	$1x10^{-4}$	$3.41x10^{-5}$		0.173
w/o TT (G73)	$1.18x10^{-6}$			$4.17x10^{-6}$	$1.17x10^{-5}$	0.074
300°C 34 min (G73)	$3.11x10^{-5}$	$3.80x10^{-5}$	$2.14x10^{-4}$			0.123
w/o TT (G70)	$1.41x10^{-6}$			$3.00x10^{-6}$	$9.56x10^{-6}$	0.112
300°C 51 min (G70)	$2.11x10^{-5}$	$2.83x10^{-5}$	$1.80x10^{-5}$	$9.29x10^{-6}$	$3.13x10^{-6}$	0.359

Figure 6.37 a shows the $\frac{I_{NBE}}{I_{def}}$ relation for samples of naked ZnO NWs before and after a thermal treatment. $\frac{I_{NBE}}{I_{def}}$ is the relation between the integrated intensity of the near band edge (NBE) emission and the sum of the integrated intensity of the different emissions due to defects. The working temperature was 300°C and the plateau times were 17 min, 34 min and 51 min. For each thermal treatment, a different initial sample was used. In all cases $\frac{I_{NBE}}{I_{def}}$ increases when the naked ZnO NWs sample is submitted to a thermal treatment and it can be explained by the improvement in the crystallinity of the lattice of the ZnO. **Figure 6.37 b** presents the $\frac{I_{NBE}}{I_{def}}$ of samples of ZnO NWs with a silver ICL, whose thickness was 12 nm, and $\frac{I_{NBE}}{I_{def}}$ of the initial samples of naked ZnO NWs. $\frac{I_{NBE}}{I_{def}}$ of samples with a silver ICL is bigger than one of naked ZnO NWs. The reason can be that the ICL acts as a filter mainly for the visible PL emissions.

Figure 6.38 a presents the $\frac{I_{NBE}}{I_{def}}$ of samples of ZnO NWs decorated with silver NPs after the SSD process activated by a thermal treatment and $\frac{I_{NBE}}{I_{def}}$ of the initial naked ZnO NWs samples. **Figure 6.38 b** shows $\frac{R_{after}}{R_{before}}$ as a function of the annealing plateau time. The R_{before} in both cases, corresponds to $\frac{I_{NBE}}{I_{def}}$ of the initial naked ZnO NWs without TT. While R_{after} is this ratio for naked ZnO NWs after the TT or for ZnO NWs decorated with Ag NPs (after the SSD process). In the last case, the ICL thickness and the working temperature were 12 nm and 300°C, respectively. As observed in **Figure 6.38 b**, the relation $\frac{R_{after}}{R_{before}}$ is larger for ZnO/Ag with TT (submitted to the SSD process) than for naked NWs with TT. So, this enhancement is mainly due to the presence of the Ag NPs, independently of the effect caused by the TT over ZnO NWs. The largest change occurs for ZnO/Ag after 34 min of annealing plateau.

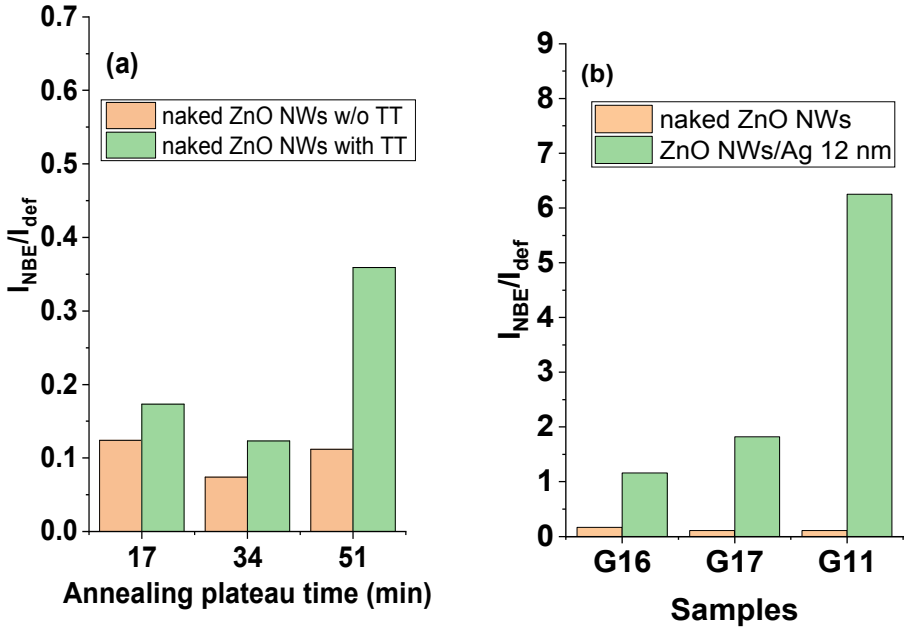


Figure 6.37: a) Relation between the integrated intensity of the NBE emission ($\boldsymbol{I_{NBE}}$) and the integrated intensity of emission due to defects ($\boldsymbol{I_{def}}$) for samples of naked ZnO NWs before (orange) and after (green) the thermal treatment. The working temperature was 300°C and the plateau times were 17 min, 34 min and 51 min. For each thermal treatment a different original sample was used. b) Relation between the integrated intensity of the NBE emission ($\boldsymbol{I_{NBE}}$) and the integrated intensity of emission due to defects ($\boldsymbol{I_{def}}$) for samples of naked ZnO NWs before (orange) and after the deposit of the ICL of silver whose thickness was 12 nm. For each deposit, a different original sample was used, and they are indicated by G16, G17 and G11 in the horizontal axis.

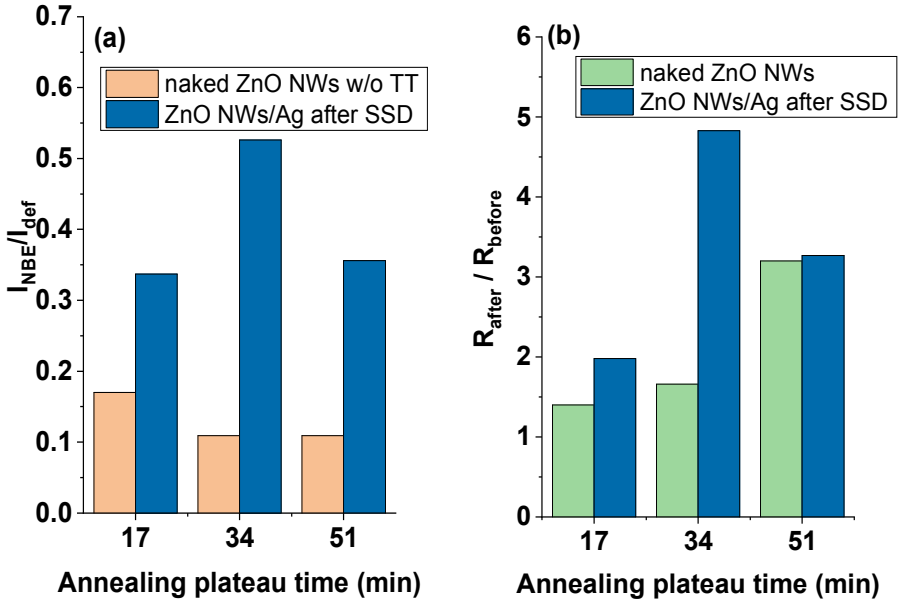


Figure 6.38: a) Relation between the integrated intensity of the NBE emission ($\boldsymbol{I_{NBE}}$) and the integrated intensity of emission due to defects ($\boldsymbol{I_{def}}$) for samples of naked ZnO NWs before (orange) and after (green) the thermal treatment which activated the Solid State Dewetting process. Silver NPs were formed in the surface of the ZnO NWs. The silver ICL thickness was 12 nm, the working temperature was 300°C and the plateau times were 17 min, 34 min and 51 min. For each thermal treatment a different original sample was used. b) Relation between $\boldsymbol{I_{NBE}}/\boldsymbol{I_{def}}$ after and before the thermal treatment for naked ZnO NWs (green) and for ZnO NWs with a silver ICL of 12 nm (blue). The working temperature was 300°C and the plateau times were 17 min, 34 min and 51 min.

The physics of the metal/semiconductor interaction of these hybrid nanostructures still remains unclear and it is under debate. In this work, the laser wavelength is 375 nm**,** hence the SPR of silver NPs is not directly activated by the laser emission. Prajapati et al. [23] and Kuiri et al. [24] suggest that it can be possible that the blue and green emissions from defects of ZnO NWs can be absorbed by the Ag NPs, trapping this energy in the plasmonic near field [23]. Surface plasmons can decay either radiatively via emission of a photon or non radiatively through the generation of excited carriers, typically referred as hot carriers. Understanding the initial distribution of carriers generated by plasmon decay, before inelastic relaxation is the first key step towards exploiting these phenomena. In the past, initial hot carrier distribution generated by plasmon decay has been estimated within a simple electron gas model. But, it does not capture the material dependence and miss inter-band transitions in noble metals. For example, Sundararaman, Atwater et al.[25] combined quantized plasmon

modes from experimental dielectric function with electronic states from first principles density functional theory (DFT), to calculate the initial distribution of hot carriers in real materials

When semiconductors are directly attached to the metal nanostructure, hot electrons can be captured and extracted to the semiconductors before thermalization. Zhou et al. [26] and Wu et al. [27] mention that there are two different plasmon induced hot electrons injection process. One is the plasma induced hot electron transfer mechanism (PHET) which consists in a transfer of hot electrons formed by the plasmon decay of metal nanostructures, into the semiconductor. But, it competes with electron relaxation by rapid electron-electron scattering in the metal conduction band on times scales of hundreds of femtoseconds. Thus, PHET require interfacial charge separation on an even faster time scale. The other is plasmon induced metal to semiconductor interfacial charge transfer transition (PICTT). In this case, the metal plasmon serves as a light absorber, but strong coupling and mixing of the metal and semiconductor levels lead to a new plasmon decay: the direct generation of an electron in the semiconductor and an electron hole in the metal. The PICTT mechanism was first reported to have a highly efficient plasmon induced electron -hole pair separation in Au-CdSe nanorods. CdSe is a narrow band gap semiconductor with a bandgap of 1.76 eV and the Schottky barrier is 0.64. However, there are still few reports of this mechanism in one dimensional (1D) formed by a metal and a wide bandgap semiconductor.

An schematic diagram of the energy and charge transfer mechanism which occur in the Ag nanoparticle-ZnO nanowire is shown in Figure 6.39. It is similar to one proposed by Prajapati et al. [23].

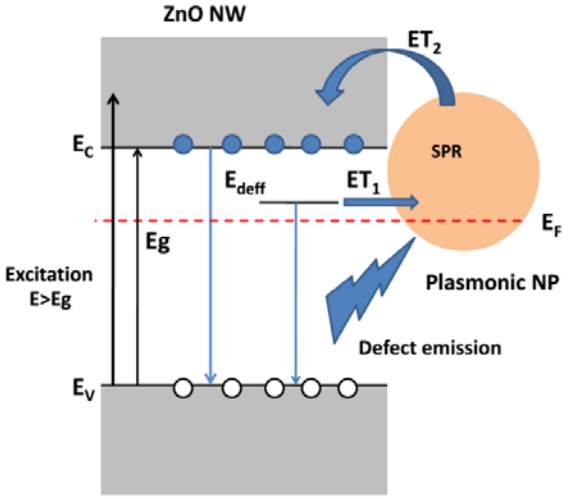


Figure 6.39: Schematic diagram of the energy and charge transfer mechanisms in the Ag nanoparticle coupled with the ZnO NW, similar to one proposed by Prajapati et al. [23]. E_C is the minimum of the conduction band, E_V is the maximum of the valence band, $\boldsymbol{E_g}$ is the bandgap energy, $\boldsymbol{E_{deff}}$ is defect level and $\boldsymbol{E_F}$ is the fermi level. $\boldsymbol{ET_1}$ is the electron transfer from the defect level to the plasmonic NP and $\boldsymbol{ET_2}$ is the electron transfer from the nanoparticle to the conduction band.

Prajapati et al. [23] neglect explicit involvement of the energy states in the metal NP and finer details, for example a fraction of the electron excited in the metal NP may not be transferred to the ZnO CB, but thermalize in the NP itself by non radiative de excitation.

Various sub bandgap defect states in the ZnO can exist in the proximity of the Fermi level of silver. Depending on their alignment, an electron transfer from this defect levels in ZnO to the Ag NPs is possible (ET1 in **Figure 6.39**). It is likely made by tunnelling effect [23] and it generates an increase of the electron density in Ag NPs. The transfer (similar to ET2 in Figure 6.38) is an indirect pathway of two steps including the decay of surface plasmons and the transfer of hot electrons from the interface of metal-ZnO to the CB (conduction band of ZnO). Su et al. [28] also proposed the same processes: a transfer of electrons from defects band of ZnO to the Fermi level of Ag and an absorption of the emission from defects by the silver NP, generating a SPR. Electrons are pumped to higher energy states and then migrate to the conduction band through non radiative decay. The collection efficiency of hot carriers in plasmonics structures depends on both the initial energy distribution and transport of them. Also, Rahman et al. [29] concluded that a higher number of the electrons are transferred from Ag to ZnO in silver/ zinc oxide heterostructures, fabricated by them, when the ratio of silver is increased. Besides, they observed changes in the photoluminiscence properties of ZnO as a result of the strong interaction between the semiconductor and the metalic particles. It points to an efficient electron transfer from Ag to ZnO components.

Electrons with sufficient energy to overcome or tunneling the energy barrier between Ag and ZnO, may be transferred to the conduction band of ZnO (ET_2 process in **Figure 6.38**), which result in an increase of CB electron density. These additional electrons are available for electron-hole recombination in ZnO, enhancing the NBE emission intensity, while partially deteriorating the visible emission [23]. Briefly, this plasmon-assisted electron transfer process results in the visible light suppression and the NBE PL emission enhancement of ZnO nanostructures. These process were observed in ZnO decorated with Ag NPs by many researchers [22, 24, 25, 26] .

6.3.2.2 ZnO NBE PL emission band energy analysis and its relation with the Ag SPR coupling

The bandgap energy value of the naked ZnO NWs without TT, studied in this work, are comprised between 3.20 eV and 3.22 eV, after subtracting the background. The NBE emission band is centred at 3.12-3.14 eV. Thus, it is attributed to the exciton emission.

The energies of the NBE PL emission bands are summarized in **Tables 6.8**, and **6.9**. Each column of **Table 6.8** corresponds to a different sample and each row corresponds to a different condition of the sample: naked ZnO NWs, ZnO NWs/Ag and ZnO NWs/Ag after SSD. **Table 6.9** is for naked ZnO NWs without or with TT. For each sample after SSD, the mean size of NPs and the mean distance between the nearest neighbours were calculated statistically and these values are shown in **Table 6.10**.

Table 6.8: NBE PL emission energy in eV for different samples and different conditions: naked ZnO NWs, ZnO NWs with a layer of Ag and ZnO NWs decorated with Ag NPs. The samples are identified by the Ag ICL thickness and the annealing plateau times.

Samples	**G16 (12 nm 17 min)**	**G17 (12 nm 34 min)**	**G11 (12 nm 51 min)**	**G18 (6 nm 17 min)**
Naked ZnO NWs w/o TT	3.13 eV	3.13 eV	3.13 eV	3.12 eV
ZnO NWs/Ag	3.14 eV	3.15 eV	3.16 eV	3.12 eV
ZnO NWs/Ag after TT	3.12 eV	3.19 eV	3.15 eV	3.13 eV

Table 6.9: NBE PL emission energy values in eV for naked ZnO NWs without TT and with TT.

Sample	**without TT**	**with TT**
G71 (TT: 300°C 17 min)	3.12 eV	3.11 eV
G73 (TT: 300°C 34 min)	3.13 eV	3.11 eV
G70 (TT: 300°C 51 min)	3.14 eV	3.11 eV

Table 6.10: d_{CC} (mean distance between nearest neighbouring AgNPs), D (mean size of Ag NPs), NBE emission energy for different ZnO NWs/Ag after SSD. The working temperature of the annealing was 300°C

Sample	**d_{CC} (nm)**	**D (nm)**	d_{CC}/D	**NBE energy (eV)**
12 nm 17 min (G16)	103	44	2.34	3.12
12 nm 34 min (G17)	205	54	3.79	3.18
12 nm 51 min (G11)	190	66	2.88	3.15
6 nm 17 min (G18)	90	34	2.65	3.13

λ_{SPR} depends on many factors: size and shape of the NPs, density, etc. As presented in chapters 2 and 5, plots of the NBE PL emission energy as a function of d_{CC}/D are presented in **Figure 6.40**. A clear trend is observed and consists in an increase of NBE emission band energy with (d_{CC}/D). It suggests the idea that the defect emission in the blue region of the spectrum overlap better when (d_{CC}/D) is bigger. Electrons are excited by SPR decay and then are transferred to conduction band of ZnO. More states are ocuppied, thus the NBE energy increase can be due to Burstein Moss effect.

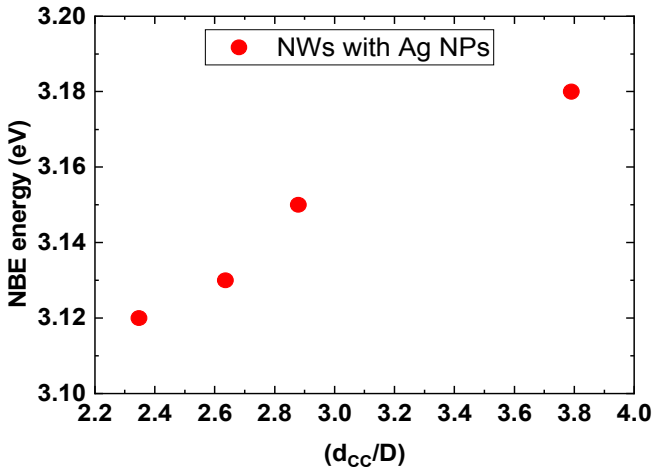


Figure 6.40: Near band edge (NBE) emission band energy vs (d_{CC}/D). d_{CC} is the mean distance between the nearest neighbours and D is mean size, both of silver nanoparticles which are covering the surface of ZnO NWs of four samples: 12 nm 300°C 17 min, 12 nm 300°C 34 min, 12 nm 300°C 51 min, 6 nm 300°C 17 min. The quantities which characterize the sample are: initial coating layer thickness, working temperature and annealing plateau time.

For naked ZnO NWs there is a red shift of the NBE emission band after the TT, as can be observed in **Figure 6.41 a**. Whereas, the NBE energies of ZnO NWs coated with an Ag ICL layer of 12 nm are bigger than the one for naked NWs for the three samples, as observed in **Figure 6.41 b**. After the SSD, NBE energy decreases in two cases (17 min and 51 min) while it increases for 34 min. Also, it is larger than NBE emission energies of the initial naked ZnO NWs without TT for two cases: 34 min and 51 min, whereas it is smaller for 17 min. Therefore, the NBE energy of ZnO NWs decorated with Ag NPs depends on the size and density of the NPs which generate a better or worse coupling with the ZnO defect emissions.

It has been well known that an increase in the carrier density leads to fill states in the conduction band. Therefore a blue shift of the optical bandgap and the NBE emission to higher energies occur. This effect is called Burstein Moss shift (BMS) [32], [33]. Zhu et al. also observed a blue shift of the NBE emission band energy, after the ZnO disks were covered by Au NPs [34] and they attributed this fact to the BMS effect too. A filling of the CB states can occur when the ZnO defect emissions are in resonance with the surface plasmon excitations of Ag NPs [26,27]. Hence varying (d_{CC}/D), λ_{array} can be tuned to be in accordance with ZnO defect emissions.

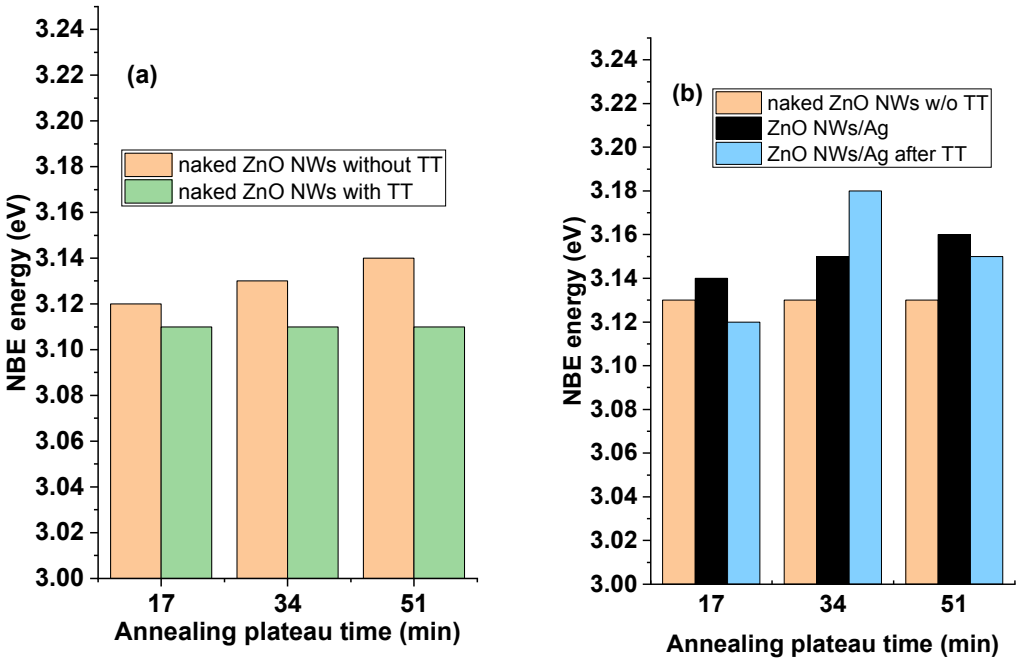


Figure 6.41: a) Near band edge (NBE) photoluminescence (PL) emission energy of naked ZnO NWs after TT (green) as a function of annealing plateau time. The working temperature was 300°C. NBE PL emission energy of the initial naked ZnO NWs without TT (orange) is also presented for each case. b) NBE PL emission energy of ZnO NWs decorated with Ag NPs after the SSD process (blue) as a function of the annealing plateau time. The ICL thickness was 12 nm and the working temperature was 300°C. In this plot, NBE PL emission energy of ZnO NWs coated with an Ag ICL whose thickness is 12 nm (black) and the one of the initial naked ZnO NWs without TT (orange) are also presented for each case.

6.5 Conclusions

3D plasmonic nanostructures were fabricated using ZnO NWs. A layer of Ag was deposited on them by thermal vacuum deposition. An annealing generates a process of dewetting and silver NPs are formed on sides and on tops of ZnO NWs. The size and density of NPs depend on the thickness of the initial layer, working temperature and annealing plateau time.

If the thickness of ICL is too large, for example 50 nm, it is observed that ZnO NWs are broken after the annealing of 300°C for 1 hour. In this case, silver covers the upper part of the array as a film. Thus, during the annealing process, atoms move and agglomerate in some places, breaking NWs. X-ray diffractograms show silver peaks only after the annealing. The

most important is the (111) peak, which is indicating that (111) planes are formed parallel to the substrate.

For an ICL thickness of 12 nm or less and a working temperature of 300°C, NPs are decorating ZnO NWs and they are not broken. X-ray diffractograms do not show silver peaks, before and after annealing. But the analysis of HR TEM micrographs concludes that NPs have mainly (111) planes.

When the annealing plateau time is varied, keeping ICL thickness and working temperature constant, Ostwald ripening process is observed. The histograms present a log-normal distribution and the mean size of NPs increases with the annealing plateau time. This last trend is also observed in chapter 5.

Optical properties were studied by transmittance and photoluminescence. Absorbance spectra of naked ZnO NWs with TT show a band edge due to the band gap. The band gap energy of naked ZnO NWs were calculated by Tauc plots. Their values were 3.20 eV and 3.22 eV. The last one was obtained after subtracting a background which includes absorption for energies below the band gap. Whereas, for samples with ZnO NWs/Ag after SSD, a shoulder due to SPR between 400 nm and 500 nm is observed.

Photoluminescence spectra present different bands. There is one, called near band edge (NBE) emission, usually attributed to exciton. The others, which are at the visible regions, correspond to defects. The relation between NBE integrated PL emission and the sum of defects integrated PL emissions $\frac{I_{NBE}}{I_{def}}$ enlarges when the naked ZnO NWs are submitted to a TT. This increase can be caused by the better crystallinity after TT. But, it is stronger for ZnO NWs/Ag and ZnO NWs/Ag after TT. The reason is that Ag NPs harvest electron and energy from defects. SPR in the silver nanoparticles can decay non radiatively, generating excited carriers, which can be injected in the ZnO conduction band. Thus, they become available to NBE transition.

Another related quantity is the NBE emission band energy. For naked ZnO NWs, it exhibits a red shift after TT. However if it is covered by Ag (ZnO/Ag), it presents a blue shift. If the ZnO/Ag is submitted to a TT and the Solid State Dewetting occurs, increase and decrease of NBE emission band energy were observed, depending on the mean size of NPs and their spatial density. The blue shift is generated by the filling of the ZnO CB states, known as the Burstein Moss effect.

Finally, NBE photoluminescence efficiency of ZnO is usually low. To enhance the NBE emission and suppress the defect related emission, the surface plasmon resonance in metal NPs was used to assist multiple electron transfer process. Varying the thickness and the SSD parameters, we can obtain the optimal NPs characteristics to reach the wanted optical properties.

6.6 References

[1] Özgür, Ü. , Alivov, Ya. I. , Liu, C. , Teke, A. , Reshchikov, M. A. , Doğan, S. , Avrutin, V. , Cho, S.-J. , and Morkoç, H. A comprehensive review of ZnO materials and devices. *Journal of Applied Physics* **2005**, 98, 041301.

[2] Lira-Cantu, M. The Future of Semiconductor Oxides in Next-Generation Solar Cells. Elsevier: 2017.

[3] Kelvii Kwok, Y. Methodologies for Achieving 1D ZnO Nanostructures Potential for Solar Cells. *In Renewable and Sustainable Composites*; B. Pereira, A., A. O. Fernandes, F., Eds.; IntechOpen, 2019;

[4] Shahi, K. , Singh, R. S. , Singh, J. , Aleksandrova, M. , and Singh, A. K. Synthesis of Ag Nanoparticle-Decorated ZnO Nanorods Adopting the Low-Temperature Hydrothermal Method. *Journal of Electronic Materials* **2020**, 49, 637–642.

[5] Chen, H. M. , Chen, C. K. , Chen, C.-J. , Cheng, L.-C. , Wu, P. C. , Cheng, B. H. , Ho, Y. Z. , Tseng, M. L. , Hsu, Y.-Y. , Chan, T.-S. , Lee, J.-F. , Liu, R.-S. , and Tsai, D. P. Plasmon Inducing Effects for Enhanced Photoelectrochemical Water Splitting: X-ray Absorption Approach to Electronic Structures. *ACS Nano* **2012**, 6, 7362–7372.

[6] Yoo, J. , Kim, J.-H. , Lee, K. , Lee, S. , Kim, S. , Park, H.-K. , Kim, S.-W. , Bae, J. , Park, J.-J. , and Choi, D. Dewetted gold nanoparticles on ZnO nanorods for three-dimensionally distributed plasmonic hot spots. *Scripta Materialia* **2013**, 69, 654–657.

[7] Lakowicz, J. R. Radiative decay engineering 5: metal-enhanced fluorescence and plasmon emission. *Analytical Biochemistry* **2005**, 337, 171–194.

[8] Kulakovich, O. , Strekal, N. , Yaroshevich, A. , Maskevich, S. , Gaponenko, S. , Nabiev, I. , Woggon, U. , and Artemyev, M. Enhanced Luminescence of CdSe Quantum Dots on Gold Colloids. *Nano Letters* **2002**, 2, 1449–1452.

[9] Matsuda, K. , Ito, Y. , and Kanemitsu, Y. Photoluminescence enhancement and quenching of single CdSe/ZnS nanocrystals on metal surfaces dominated by plasmon resonant energy transfer. *Applied Physics Letters* **2008**, 92, 211911.

[10] Zhou, X. D. , Xiao, X. H. , Xu, J. X. , Cai, G. X. , Ren, F. , and Jiang, C. Z. Mechanism of the enhancement and quenching of ZnO photoluminescence by ZnO-Ag coupling. *EPL (Europhysics Letters)* **2011**, 93, 57009.

[11] Dai, Y. , Lu, P. , Cao, Z. , Campbell, C. T. , and Xia, Y. The physical chemistry and materials science behind sinter-resistant catalysts. *Chemical Society Reviews* **2018**, 47, 4314–4331.

[12] Thiel, P. A. , Shen, M. , Liu, D.-J. , and Evans, J. W. Coarsening of Two-Dimensional Nanoclusters on Metal Surfaces. *The Journal of Physical Chemistry C* **2009**, 113, 5047–5067.

[13] Thøgersen, A. and Muntingh, G. Solar induced growth of silver nanocrystals. *Journal of Applied Physics* **2013**, 113, 144301.

[14] Simonsen, S. B. , Chorkendorff, I. , Dahl, S. , Skoglundh, M. , Sehested, J. , and Helveg, S. Direct Observations of Oxygen-induced Platinum Nanoparticle Ripening Studied by In Situ TEM. *Journal of the American Chemical Society* **2010**, 132, 7968–7975.

[15] Bojorge, C. D. , Cánepa, H. R. , Gilabert, U. E. , Silva, D. , Dalchiele, E. A. , and Marotti, R. E. Synthesis and optical characterization of ZnO and ZnO:Al nanocrystalline films obtained by the sol-gel dip-coating process. *Journal of Materials Science: Materials in Electronics* **2007**, 18, 1119–1125.

[16] Manzano, C. V. , Alegre, D. , Caballero-Calero, O. , Alén, B. , and Martín-González, M. S. Synthesis and luminescence properties of electrodeposited ZnO films. *Journal of Applied Physics* **2011**, 110, 043538.

[17] Zhang, M. , Averseng, F. , Krafft, J.-M. , Borghetti, P. , Costentin, G. , and Stankic, S. Controlled Formation of Native Defects in Ultrapure ZnO for the Assignment of Green Emissions to Oxygen Vacancies. *The Journal of Physical Chemistry C* **2020**, 124, 12696–12704.

[18] Zeng, H. , Duan, G. , Li, Y. , Yang, S. , Xu, X. , and Cai, W. Blue Luminescence of ZnO Nanoparticles Based on Non-Equilibrium Processes: Defect Origins and Emission Controls. *Advanced Functional Materials* **2010**, 20, 561–572.

[19] Biroju, R. K. and Giri, P. K. Strong visible and near infrared photoluminescence from ZnO nanorods/nanowires grown on single layer graphene studied using sub-band gap excitation. *Journal of Applied Physics* **2017**, 122, 044302.

[20] Venkatesh, P. S. , Ramakrishnan, V. , and Jeganathan, K. Investigations on the growth of manifold morphologies and optical properties of ZnO nanostructures grown by radio frequency magnetron sputtering. *AIP Advances* **2013**, 3, 082133.

[21] Pramanik, S. , Mondal, S. , Mandal, A. C. , Mukherjee, S. , Das, S. , Ghosh, T. , Nath, R. , Ghosh, M. , and Kuiri, P. K. Role of oxygen vacancies on the green photoluminescence of microwave-assisted grown ZnO nanorods. *Journal of Alloys and Compounds* **2020**, 849, 156684.

[22] Hong, R. , Song, X. , Tao, C. , Zhang, D. , and Zhang, D. Surface-enhanced Raman scattering of silver thin films on as-roughened substrate by reactive ion etching. *Applied Physics A* **2016**, 122, 178.

[23] Prajapati, K. N. , Johns, B. , Bandopadhyay, K. , Silva, S. R. P. , and Mitra, J. Interaction of ZnO nanorods with plasmonic metal nanoparticles and semiconductor quantum dots. *The Journal of Chemical Physics* **2020**, 152, 064704.

[24] Kuiri, P. K. and Pramanik, S. Large enhancement of UV luminescence emission of ZnO nanoparticles by coupling excitons with Ag surface plasmons. *Journal of Applied Physics* **2018**, 123, 154302.

[25] Sundararaman, R. , Narang, P. , Jermyn, A. S. , Goddard III, W. A. , and Atwater, H. A. Theoretical predictions for hot-carrier generation from surface plasmon decay. *Nature Communications* **2014**, 5, 5788.

[26] Zhou, J. , Zhang, J. , Yang, H. , Wang, Z. , Shi, J. , Zhou, W. , Jiang, N. , Xian, G. , Qi, Q. , Weng, Y. , Shen, C. , Cheng, Z. , and He, S. Plasmon-induced hot electron transfer in Au–ZnO heterogeneous nanorods for enhanced SERS. *Nanoscale* **2019**, 11, 11782–11788.

[27] Wu, K. , Chen, J. , McBride, J. R. , and Lian, T. Efficient hot-electron transfer by a plasmon-induced interfacial charge-transfer transition. *Science* **2015**, 349, 632–635.

[28] Su, L. , Qin, N. , Xie, W. , Fu, J. , and Bao, D. The surface-plasmon-resonance and band bending effects on the photoluminescence enhancement of Ag-decorated ZnO nanorods. *Journal of Applied Physics* **2014**, 116, 063108.

[29] Rahman, D. S. , Pal, S. K. , Singha, S. S. , Kundu, S. , Basu, S. , and Ghosh, S. K. Spectral characteristics upon harvesting plasmonic hot electrons at the Ag/ZnO heteromicrostructures. *Materials Advances* **2020**, 1, 2897–2907.

[30] Park, S. , An, S. , Mun, Y. , Kim, H. W. , and Lee, C. Enhanced luminescence of Ag-decorated ZnO nanorods. *Journal of Materials Science: Materials in Electronics* **2013**, 24, 4906–4912.

[31] Cheng, P. , Li, D. , Yuan, Z. , Chen, P. , and Yang, D. Enhancement of ZnO light emission via coupling with localized surface plasmon of Ag island film. *Applied Physics Letters* **2008**, 92, 041119.

[32] Sernelius, B. E. , Berggren, K.-F. , Jin, Z.-C. , Hamberg, I. , and Granqvist, C. G. Band-gap tailoring of ZnO by means of heavy Al doping. *Physical Review B* **1988**, 37, 10244–10248.

[33] Feneberg, M. , Osterburg, S. , Lange, K. , Lidig, C. , Garke, B. , Goldhahn, R. , Richter, E. , Netzel, C. , Neumann, M. D. , Esser, N. , Fritze, S. , Witte, H. , Bläsing, J. , Dadgar, A. , and Krost, A. Band gap renormalization and Burstein-Moss effect in silicon- and germanium-doped wurtzite GaN up to 10 20 cm − 3. *Physical Review B* **2014**, 90, 075203.

[34] Zhu, Q. , Lu, J. , Wang, Y. , Qin, F. , Shi, Z. , and Xu, C. Burstein-Moss Effect Behind Au Surface Plasmon Enhanced Intrinsic Emission of ZnO Microdisks. *Scientific Reports* **2016**, 6, 36194.

[35] Khan, R. , Yun, J.-H. , Bae, K.-B. , and Lee, I.-H. Enhanced photoluminescence of ZnO nanorods via coupling with localized surface plasmon of Au nanoparticles. *Journal of Alloys and Compounds* **2016**, 682, 643–646.

7 General Conclusions

2D silver NPs arrays were prepared by SSD process of Ag films on glass substrates. This process is possible because the initial thin film is in a meta-sable state and it is activated by a thermal treatment. To study the evolution of SSD in different steps, the interrupted annealing method was used. The observed results cannot be explained only by capillarity approaches and the poly-crystalline nature of the film has to taken into accounted.

The NPs mean lateral size of samples prepared with an initial thin film of nominal thickness of 40 nm, shows a decrease in function of the final temperature of the ramp. Whereas, density is almost constant. Therefore, the average NPs size, in the normal to the substrate direction, increases. For an initial thin film thickness of 80 nm, there are not clear trends. Although, both quantities look like constant

For samples whose thermal treatment ends in the plateau, two clear trends are observed for the two nominal thickness of the initial thin film (40 nm and 80 nm). They are an increase of NPs mean lateral size and a decrease of the density, both in function of the annealing plateau time. It can be explained by Ostwald ripening. At 60 min there is an abrupt change. This is also observed for stress, which is compressive at 51 min and tensile at 60 min. This can be attributed to the re-crystallization and removal of high energy grain boundaries. Therefore, varying the initial thin film nominal thickness, the working temperature and the plateau time, the NP mean lateral size and density can be modified but not independently.

The presence of silver oxide on the surface of nanoparticles has an important influence in the structural and optical characteristics. A big increase in the transmittance occurs for samples whose annealing was 1 hour and the working temperature were 450°C and 500°C. It is explained by the formation of silver oxide at these temperature, which is shown by XPS studies. The same change occurs when the OPC size begins to decrease, after reaching a maximum at 8-17 min of the annealing plateau time for a working temperature of 500°C and initial film nominal thickness of 80 nm. Thus, it can be an alternative explanation to the experimental observations attributed to Ostwald ripening.

The transmittance spectra of samples of Ag NPs prepared by SSD on glass substrates present a dip which is attributed to Surface Plasmon Resonance (SPR). It can be varied from 390 nm to 460 nm. The interaction between NPs is very important, so the SPR wavelength depends on the relation between d_{CC} (mean distance between nearest neighbours NPs) and D (size). A linear dependence of SPR wavelength with $\left(\frac{d_{CC}}{D}\right)^{-3}$ was observed. Although d_{CC} and D are not varied independently,

The ideal working temperatures of the annealing depend on the substrate and on the deposited metal. The suitable working temperature range, founded in this work, is from 300°C to 500°C. For temperatures above 500°C, the silver transform in silver oxide. The maximum suitable time is 1 hour. After that, the observed general trends collapse and it becomes difficult to control them.

3D plasmonic nanostructures were also prepared, using ZnO NWs. The size and density of NPs depends on thickness of the initial layer, working temperature and annealing plateau time. Unlike the 2D case, the support (ZnO NWs) does not admit coatings of arbitrary thickness or any thermal treatment process. For example, if the ICL thickness is 50 nm, a break of the ZnO NWs is observed after an annealing of 300°C for 1 hour. During the annealing process, atoms move and agglomerate in some places, breaking NWs.

For an ICL thickness of 12 nm or less and at a working temperature of 300°C, Ag NPs can be observed decorating the ZnO NWs, remaining the ZnO NWs self standing and not broken. Before and after the annealing process, XRD does not show diffraction peaks corresponding to silver, but the analyzing the HR-TEM micrographs, (111) oriented planes are observed in the Ag NPs. The size of the NPs presents a log-norm distribution.

The absorbance spectra of naked NWs present an absorption edge. The band gap energies of naked ZnO nanowires were calculated by Tauc plots. The obtained values are between 3.20 eV and 3.22 eV. For samples with ZnO NWs/Ag or ZnO NWs/Ag after SSD, the last absorption edge is visualized, but also a shoulder in the absorbance due to SPR between 400 nm and 500 nm is observed.

Room temperature photoluminescence presents bands in different regions of the spectra. The most important corresponds to the near band edge (NBE), which is attributed to the ZnO exciton. The bands in the visible region of the spectrum correspond to defects. The ratio between NBE integrated PL emission and defects integrated PL emission $\frac{I_{NBE}}{I_{def}}$ enlarges with respect to naked NWs in three cases: naked ZnO NWs submitted to a TT, ZnO NWs/Ag and ZnO NWs/Ag after SSD. Furthermore, the ratio is bigger for ZnO NWs/Ag and ZnO NWs/Ag after SSD than for naked ZnO NWs submitted to TT. An explanation is that silver NPs or roughness of the Ag coating are generating this enhancement because they harvest electrons and energy from defects. SPR can decay non-radiatively, generating excited carriers. They can be transferred to the ZnO conduction band and they become available to NBE transition.

Another related quantity is the NBE energy. For naked ZnO NWs, it exhibits a red shift if the sample is submitted to a TT. However if it is covered by Ag (ZnO/Ag) it present a blue shift. If the ZnO/Ag is submitted to a TT and the Solid State Dewetting occurs, increase and decrease of NBE energy were observed, depending of the mean size of NPs and their spatial density. The blue shift is generated by the filling of the ZnO CB states, known as the Burstein Moss effect.

NBE photoluminescence efficiency of naked ZnO NWs is usually low. To enhance the NBE emission and suppress the defect related emission, the surface plasmon resonance in metal NPs was used to assist multiple electron transfer process. Varying the thickness and the SSD parameters, we can obtain the optimal NPs characteristics to reach the desired optical properties.

Finally, a new vacuum thermal evaporation system was set up. Different evaporation sources can be used. There are two characteristics to define them: their shape (boat, basket, coil, etc) and their composition (tungsten, tantalum, etc). Each type of source is adequate to evaporate a specific material. The intensity and voltage of the power supply can be varied to modify the rate of evaporation. The last quantity and the thickness can be controlled by a quartz crystal monitor which was installed in the evaporation system. Also the distance between the source and the substrate holder can be varied as well as the angle between the substrate normal and the vertical direction. Therefore this system can be used in the future to prepare metal contacts for solar cells, metal or semiconductors thin films, coatings and nanostructures utilizing masks or oblique angle deposition.

8 Perspectives

In this work, a new vacuum thermal evaporation system was set up. Different evaporation sources can be used. There are two characteristics to define them: their shape (boat, basket, coil, etc) and their composition (tungsten, tantalum, etc). Each type of source is adequate to evaporate a specific material. The intensity and voltage of the power supply can be varied to modify the rate of evaporation. The last quantity and the thickness can be controlled by a quartz crystal. Also the distance between the source and the substrate holder can be varied as well as the angle between the substrate normal and the vertical direction. Therefore this system can be used in the future to prepare metal contacts for solar cells, metal or semiconductors thin films, coatings and nanostructures utilizing masks or oblique angle deposition.

Finally, Solid State Dewetting (SSD) give possibilities of future works, and some of them will be mention. It allows preparing different structures with application in nanophotonics. It can be induced by annealing, as demonstrated in this work or another techniques as pulsed laser [1] or an hybrid between them. Therefore, these methods should be further explored in the future. First, random arrays of metal particles can be synthesized by a SSD of an as deposited film on flat substrates. These arrays generate a broadband scattering, which is suitable for solar cells. Alloyed or core-shell bimetallic nanostructures [2] and hybrid nanostructures (semiconductor- metals), are also possible to be prepared by this method, or in a combination with others. An example of the hybrid nanostructures is the ZnO NWs decorated with Ag NPs studied in this work. The NBE emission enhances and suppress the defect level emission of ZnO. These properties are required for photodetectors, light emitting diodes and photocatalysis. When a high spatial order is necessary to vary precisely the optical responses, SSD in a pattern substrate can be used [3] [4] [5] [6]. This technique could be considered to practice. Also, another types of substrates, such as different semiconductors with different orientation, can be experimented.

The presence of oxides are important because they can change the optical properties of the metallic or hybrid nanostructures. Generally, it is a superficial effect, so XPS is a suitable technique to study it. Another technique which can be used is the Raman spectroscopy and should be explored in the future.

For a theoretical point of view, nowadays, modeling for simulate and predict the SSD have been developing [7] [8] [9] and it will continue in the future because SSD is very dependent on the conditions which is made.

8.1 References

[1] Garfinkel, D. A. , Pakeltis, G. , Tang, N. , Ivanov, I. N. , Fowlkes, J. D. , Gilbert, D. A. , and Rack, P. D. Optical and Magnetic Properties of Ag–Ni Bimetallic Nanoparticles Assembled via Pulsed Laser-Induced Dewetting. *ACS Omega* **2020**, 5, 19285–19292.

[2] Kvitek, O. , Havelka, V. , Vesely, M. , Reznickova, A. , and Svorcik, V. Preparation of alloyed and "core-shell" Au/Ag bimetallic nanostructures on glass substrate by solid state dewetting. *Journal of Alloys and Compounds* **2020**, 829, 154627.

[3] Jiang, R. , Li, W. , Li, Y. , Liu, Y. , Zhao, W. , Mao, R. , Deng, L. , and Zhou, P. Periodical distribution of Au nanoparticles through dewetting on patterned substrates. *Applied Physics Letters* **2020**, 116, 103106.

[4] Ruffino, F. and Grimaldi, M. G. Self-organized patterned arrays of Au and Ag nanoparticles by thickness-dependent dewetting of template-confined films. *J Mater Sci* **2014**, 49, 5714–5729.

[5] Jacquet, P. , Bouteille, B. , Dezert, R. , Lautru, J. , Podor, R. , Baron, A. , Teisseire, J. , Jupille, J. , Lazzari, R. , and Gozhyk, I. Periodic Arrays of Diamond Shaped Silver Nanoparticles: From Scalable Fabrication by Template Assisted Solid State Dewetting to Tunable Optical Properties. *Advanced Functional Materials* **2019**, 1901119.

[6] Le Bris, A. , Maloum, F. , Teisseire, J. , and Sorin, F. Self-organized ordered silver nanoparticle arrays obtained by solid state dewetting. *Applied Physics Letters* **2014**, 105, 203102.

[7] Jiang, W. , Zhao, Q. , and Bao, W. Sharp-Interface Model for Simulating Solid-State Dewetting in Three Dimensions. *SIAM Journal on Applied Mathematics* **2020**, 80, 1654–1677.

[8] Knavel, S. A. , Savina, T. V. , Mroz, M. V. , Kordesch, M. E. , Eads, C. N. , Sadowski, J. T. , and Tenney, S. A. A mathematical model of solid-state dewetting of barium thin films on *W* (112). *Mathematical Modelling of Natural Phenomena* **2020**, 15, 12.

[9] Verma, M. and Mukherjee, R. Nanoparticle formation through dewetting of a solid-state thin film on a substrate: A phase-field study. *Journal of Alloys and Compounds* **2020**, 835, 155163.

9 Publications

Until this moment, the results of this thesis work have generated the following publications:

Solid-state thermal dewetted silver nanoparticles onto electrochemically grown self-standing vertically aligned ZnO nanorods for three-dimensional plasmonic nanostructures; Juan Agustín Badán, Guillermo Jauregui , Elena Navarrete-Astorga , Rodrigo Henríquez , Francisco Martín Jiménez, Daniel Ariosa , Enrique A. Dalchiele. Submitted to Ceramic International.

Abstract: Three dimensional (3D) plasmonic nanostructures composed of silver nanoparticles decorated ZnO NRs arrays, have been fabricated by a process combining the electrochemical growth of ZnO NRs and further formation of Ag nanoparticles by the solid-state thermal dewetting (SSD) process. The effect of SSD parameters on the morphological, structural and optical properties of the Ag NPs decorated ZnO NRs arrays has been investigated. It is possible to tune the bandgap of the Ag NPs@ZnO nanorods array 3D plasmonic nanostructure by tailoring the Ag nanoparticle sizes, allowing light manipulation at the nanoscale. The silver nanoparticles attached to the ZnO NRs arrays experienced surface plasmonic coupling effect, causing enhancement in the room temperature photoluminescence (PL) UV emission and quenching the corresponding visible light one. An enhancement in the near band edge emission PL intensity of ZnO to the deep level emission PL intensity ratio after Ag NPs decoration of the ZnO nanostructures corresponding to ca. 11 folds has been observed, indicating that the defect emission is obviously suppressed.